Numerical Simulation of Blood Flow through Permeable Vascular Network Embedded in Tumour Porous Interstitium

SUN, Qiang

A dissertation submitted for the degree of

Doctor of Philosophy

Department of Mechanical Engineering

University College London

2011

Declaration

I, SUN Qiang, declare that the work delivered in this dissertation is my own. When information has been cited or derived from other sources, I confirm that it has been indicated in this thesis.

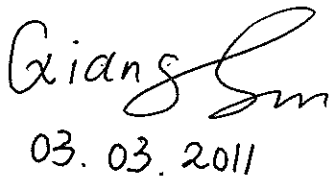

03. 03. 2011

Acknowledgements

I would like to express my sincere gratitude to my primary supervisor, Prof. Guo Xiong Wu, for introducing me to the computational fluid dynamics and for his contribution, kind and thoughtful criticism, valuable suggestions and discussions throughout this work. I also thank my secondary supervisor, Dr. Nick Ovenden, for introducing me to the biomedical fluid dynamics and for his helpful supervision. In addition to this, I am thankful for the help and expert advice of UCL Medical Modelling Group. Further to this, I gratefully acknowledge Overseas Research Students Awards Scheme (ORSAS) and K. C. Wong scholarship for the financial support during my study in UCL, and UCL Research Computing for the use of UCL HPC service — Legion. At last but not least, I owe appreciation to my family and friends for their consistent encouragement and generous support.

Abstract

Tumour blood flow plays a critical role in tumour growth and cancer therapies. Computational fluid dynamics is an efficient method to study blood behaviour by modelling fluid flow through numerical simulations. A mathematical model is developed to study the blood flow through a three-dimensional permeable vascular network embedded in a solid tumour, and its transvascular movement and spread within tumour interior in context with cancer therapies. The vasculature is described by the parametric equations in terms of vessel centre lines. The flow through each tumour vessel is approximated with the leading component in the longitudinal direction of the vessel, and its governing equation becomes an ordinary differential equation based on the parameter of the parametric equation for the vessel centre line. The pressure continuity and mass conservation conditions are imposed at every junction within tumour vascular network. The interstitial flow is described by the Darcy's law which is converted into the Laplace equation. The coupling effect between the flows through tumour vasculature and within tumour interstitial due to the vascular permeability is described by the Starling's law. A coupling mathematical model is then developed. Based on mass conservation, a differential equation for pressures on both sides of vascular surface is obtained. Transforming the Laplace equation into the boundary-integral form by using the Green's function offers another equation linking the pressures inside and outside vessels.

The numerical procedure is developed, and the discretised differential and integral equations are solved by finite difference method and boundary element method respectively. The model is applied to investigate how different types of physical parameters and special characters of tumour vasculature affect tumour blood flow. Finally, an approximation model by ignoring the term with small value of the fully coupling model is developed, and its validity and simulation efficiency are examined.

Nomenclature

a	radius of tumour vessel cross section
c_v	drug concentration in tumour vessel
l_v	length of tumour vessel measured from some reference point
p_0	peripheral pressure on tumour surface
p_a	inlet vascular flow pressure
p_c	vascular flow pressure
p_c^{J}	pressure at junction point J in vascular network
p_i	interstitial flow pressure
p_v	outlet vascular flow pressure
q_e	transmission flux over unit length along circumference of vessel cross section
$\mathbf{u}$	interstitial flow velocity
A_s	vascular surface area
D	Dean number
J_s	flux of molecules
L_p	permeability of tumour vessel

Continued on next page...

Continued

N_w	Womersley parameter
Q_a	inlet vascular flow flux
Q_c	flux through vessel
Q_{ex}	overall amount of extravasation flux
Q_v	outlet vascular flow flux
Re	Reynolds number
R_c	curvature radius of vessel centre line
U_0	peak velocity through vessel cross section
U_1, U_2, U_3	components of vascular flow velocity $\mathbf{U}$ in orthogonal curvilinear coordinate system (q_1, q_2, q_3)
U_x, U_y, U_z	components of vascular flow velocity $\mathbf{U}$ in Cartesian coordinate system $o - xyz$
U_r, U_θ, U_t	components of vascular flow velocity $\mathbf{U}$ in orthogonal curvilinear coordinate system (r, θ, t)
$\mathbf{U}$	vascular flow velocity
Z_g	geometrical resistance of vascular flow
Z_η	viscous resistance of vascular flow
γ_Q	ratio of extravasation flux over inlet vascular flow flux
κ	tumour tissue hydraulic conductivity parameter
μ	dynamic viscosity of blood
ω	heart pumping frequency
π_v	oncotic pressure in vascular fluid

Continued on next page...

Continued

π_i	oncotic pressure in interstitial fluid
ρ	density of blood
σ	oncotic reflection coefficient
$\sigma_{_F}$	plasmadrag reflection coefficient

Contents

List of Figures

List of Tables

Chapter 1

Introduction

Blood is a specialised bodily fluid flowing around human body through blood vessels driven by the pumping actions of heart. Blood flow plays a key role in maintaining body health. It delivers necessary nutrients and oxygen to body organs and cells, and takes waste products of metabolism away from the same organs or cells. Blood flow also signals tissue damages, maintains body temperatures, and transports therapeutic agents.

One of the main medical motivations behind the study of blood flow is the desire to process the fundamental understanding of pathology for blood flow system and apply it to help improve the effectiveness of resource transportation for life sustenance and/or disease treatment. Many methods can be adopted to undertake the research on the behaviour of blood flow. Fluid dynamics simulation offers good options to study blood flow when it is hard or dangerous to obtain *in vivo* measurement. Computational fluid dynamics (CFD) is a means to model fluid flow through numerical tools. It solves governing equations for mass and momentum conservations. It can make systematic analysis, and also allow local detailed study on fluid behaviour in areas which are not easy to access. With this kind of insightful information, one can ultimately deduce

some importance in physiological implications.

The study on blood flow from fluid dynamics point of view not only has the potential to bring medical benefit, but also poses many mathematical and numerical challenges. Applying mathematics for the research on blood flow has raised new types of problems, including an uncommon range of Reynolds number, pulsatile flow conditions, and unusual multiplicity and configuration of vascular networks [Lighthill (1972)]. In pursuit of meaningful results and useful analysis with physiologists, this cross-disciplinary subject is very active today.

In the work starting after this brief introduction, we will introduce and approach a CFD study on the blood flow in tumour which goes through a permeable vascular network embedded in tumour interstitium. Before that, it is beneficial to understand the foundation of tumour growth, the therapeutic effectiveness of cancer treatment and the special characters of tumour blood flow environment.

1.1 Cancer — the malignant tumours

Cancer is a fatal disease which can affect everyone in any age. It has already been one of the leading causes of world-wide death, and will be the most lethal disease within next few years. Globally, based on the recent available incidence and mortality data, it is estimated that there were more than 12 million new cancer cases in 2007, and the corresponding estimate for total cancer deaths in that year was 7.6 million [Garcia *et al.* (2007)]. This represents an increase of around 20% in cancer incidence and 13.4% in cancer mortality relative to the estimates in 2002, in which year, there were 10.9 million new cancer cases and 6.7 million deaths caused by cancer [Parkin *et al.* (2005)]. Fig.1.1a depicts the

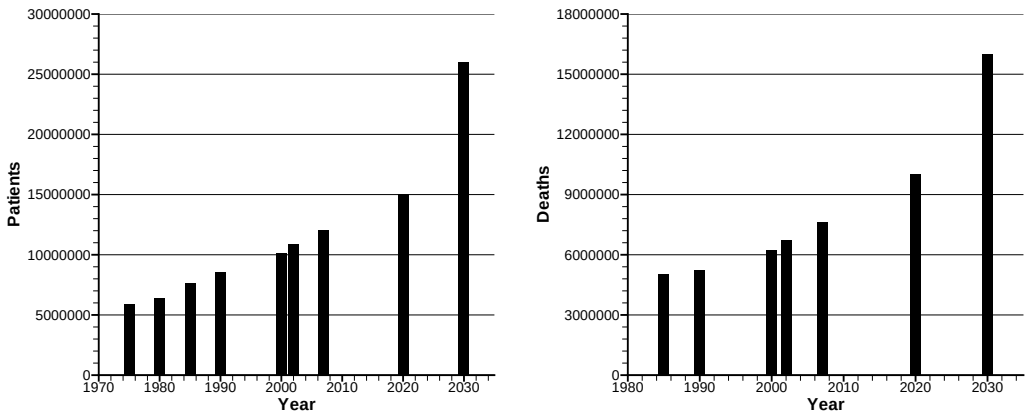

(a) **(b)**

Figure 1.1: Estimated global cancer burn: (a) number of cancer incidence per year; (b) number of cancer mortality per year [Boyle and Levin (2008), Garcia *et al.* (2007), Parkin *et al.* (1984, 1988, 1993, 1999), Parkin (2001), Parkin *et al.* (2005)].

estimates of subsequent new cancer cases for 1975 to 2030, and Fig.1.1b shows the cancer death cases estimated from 1985 to 2030. Adopting the current trends of cancer incidence and mortality, and taking the growth and ageing of world-wide population into account, it is predicted that there would be 15 million new cancer patients and 10 million cancer deaths in 2020 [Parkin (2001)]. Much worse, in 2030, the data will jump to 26 million and 16 million for cancer incidence and mortality respectively [Boyle and Levin (2008)]. This critical situation alerts us that cancer is becoming a much more dangerous global burden of disease and a major reason for losing lives.

Cancer is a disease beginning from somatic cells and their progeny. When cells begin to divide uncontrollably, they form an abnormal mass of tissue known as a tumour. A tumour can be either malignant or benign. Benign tumours [Sarg and Gross (2007)] imply a kind of mild and non-progressive disease. Although a benign tumour may cause some healthy problems depending

on its size and location, it does not infiltrate surrounding tissues or spread to distant organs. Benign tumours are seldom life-threatening (although some types of benign tumours are capable of becoming malignant). In fact, many kinds of benign tumours are harmless to human health.

On the contrary, malignant tumours, which are characterised with invasion and metastasis, are very harmful to human health [Sarg and Gross (2007)]. These two special characters, invasion and metastasis, differentiate malignant tumours from benign tumours. Invasion refers to a population of cells which grow from previously healthy genomic intact cells. However, these cells (malignant tumour cells) are different from normal cells as they disregard the normal controls of proliferation. They divide rapidly to replace old cells and damage normal cells without respect to normal limits, and multiply constantly to invade and destroy adjacent tissues and organs. Furthermore, malignant tumour cells can spread to distant anatomic sites along human body through circulatory system (both bloodstream and lymphatic system). This process is called metastasis. According to this peculiar character of metastasis, Hippocrates assigned the name of cancer or crab to malignant tumours because of their crab-like spreading behaviour within human bodies [Walter (1977)]. Hanahan and Weinberg (2000) summarised the following six characteristics of cancer: (1) ability to spontaneous proliferation; (2) discard of external inhibitory signals; (3) malfunction of apoptosis — immortalization; (4) capability to promote tumour angiogenesis; (5) unresponsiveness to the signal of differentiate; and (6) invasion and metastasis.

Though heart disease (HTD) is still the high risk for human beings, deaths from HTD have decreased significantly during the last three decades due to the great development of the knowledge and treatment on HTD possessed by us. In contrast, as shown in Fig.1.2, the overall death rate caused by cancer

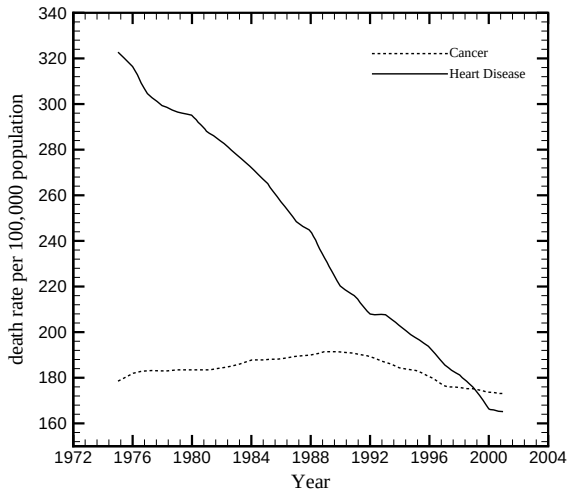

Figure 1.2: Death rate per year caused by cancer and heart disease [UCL Cancer Institute (2007)].

has not changed very much, since there are a lot of unknowns about cancer and its treatment. People can suffer with types of cancers at any age, and the risk for the more common varieties tends to increase with age. Cancer is now one of the major causes to lose lives, and very few patients with cancer are currently curable. Its treatment has become one of the major missions of science.

1.2 Therapeutic methods for cancer

1.2.1 Introduction on etiology of cancer and environmental carcinogenic factors

There are still many questions needed to be answered, though, a lot of evidence has been shown that the etiology of cancer is contributed to the variations in key gene activity caused by a series of genetic and epigenetic changes in human

bodies [Evan and Vousden (2001), Ponder (2001)]. Phrase "genetic changes" means mutations, while term "epigenetic changes" is regarded as the damage of DNA resulted from exogenous agents which can alter gene transcription pattern [Nagy (2005)]. Such key gene variations are induced by two categories of factors. One is the intrinsic influence, including the acquired and inherited defects of DNA repair and the variations in metabolic polymorphism inside and outside cells [Ponder (2001)]. The other is the extrinsic (exogenous) effect, which refers to the environmental carcinogenic factors.

A large number of environmental factors have been confirmed with carcinogenic or mutagenic properties. The Monographs Program on the Evaluation of Carcinogenic Risks to Humans of International Agency for Research on Cancer (IARC Monographs) identifies environmental factors which can increase the risk of human cancer. To date, this program has identified a total of 105 agents, mixtures and exposures classified in Group 1, or "carcinogenic to humans" [IARC (2008)]. Basically, these agents can be catalogued as life-style factors, radiation, virus, and pollution [Wogan *et al.* (2004)].

One of the leading life-style carcinogen factors is our daily diet. It has been estimated that nearly one third of all cancer cases are related with diet [Gabriel (2007)]. It causes 90% of colorectal cancer globally [Cartmel (1997)]. One main reason for this fact is that our diet becomes low in fibre, but high in animal fats nowadays. It is also well recognised that some significant sources from our diet can induce cancer. Through the application of well-validated biomarker in molecular epidemiology, aflatoxin has been proven as a strong liver carcinogen which is bloated contaminant of dietary staples in Asia and Africa [Wogan *et al.* (2004)]. The heterocyclic amines represent another important class of carcinogens in food products when meat is over cooked for a long period [Wogan *et al.* (2004)]. They are mutagens and carcinogens at

numerous organ sites.

Another clear life-style involving carcinogen exposure factor is tobacco. There are overwhelming proofs linking tobacco with many types of cancers [IARC (2004)]. Taking cigarette increases the risk of all histological types of lung cancers. It also induces cancers of oral cavity, especially when using smokeless tobacco or smoking together with drinking alcohol [IARC (1998)]. Furthermore, cigarette smoking is connected with other cancers, such as laryngeal, oropharyngeal, hypopharyngeal and nasopharyngeal cancers, as well as stomach, liver, and bladder carcinomata [Wogan *et al.* (2004)]. It has been confirmed that cigarettes and smokeless tobacco contain a mixture of carcinogens, tumour promoters and co-carcinogens. The coal tar in cigarette smoke can damage DNA directly to induce cancer [Nagy (2005)]. There are over one billion smokers and hundreds of millions of smokeless tobacco users all over the world. By far, tobacco use is the most widespread link between known carcinogens and death from cancer.

Radiation is another kind of carcinogenic sources. Ionising radiation releases enough energy to damage DNA within cells, which can lead to malignant changes taking place in later life. Exposure can be in the form of repeated doses or one isolated incident, such as the nuclear accident at Chernobyl in 1986 [Walter (1977)].

Viruses, bacteria and chemical pollution can place a premium on cancer as well. Chronic infection by hepatitis B (HBV) or hepatitis C (HVC) virus is a big risk for the great majority of hepatocellular carcinoma [IARC (1994)]. Exposure to asbestos is known to be responsible for inducing mesothelioma [Nagy (2005)].

1.2.2 Cancer therapeutic methods

At present, cancer is usually treated by surgery, chemotherapy (non-specific and/or targeted therapy such as monoclonal antibody therapy), radiotherapy, hormonal therapy, and hyperthermia therapy. The choice of treatment depends on the type, location and stage of cancer, as well as the general health of patients[i].

Removing cancerous tissues completely, but minimising the damage on the rest of body is the goal of cancer treatment. This can be accomplished by surgery to some extent when cancer is localised at a specific organ. But the propensity of cancer to invade adjacent tissues and/or metastasise to distant sites can limit its effectiveness [Beardsley (1994)].

Chemotherapy [Sarg and Gross (2007)] is one of the most important methods to treat cancer. In general sense, chemotherapy is the treatment or control of cancer by anti-cancer drugs, the highly toxic medications which can destroy cancer cells by interfering with their growth or preventing their reproduction. Chemotherapy works by interrupting cell cycle, preventing cells from reproducing, and killing the cells which divide rapidly. However, it also means that anti-cancer drugs may harm the cells that divide rapidly under normal circumstances, such as cells in bone marrow, digestive tract, and hair follicles, which leads to the most common side effect of chemotherapy. Targeted therapy is a developed form of chemotherapy. Unlike conventional chemotherapy, it targets specific processes and proteins unique to cancer cells, e.g. proteins which cause cell proliferation or invasion, or proteins which induce angiogenesis. As a result, target therapy usually has less adverse effects relative to the traditional chemotherapy.

[i]some knowledge in this section is obtained from Cancer Research UK (http://www.cancerresearchuk.org).

Most types of malignant tumours can be treated by radiotherapy (radiation therapy in North America) [Sarg and Gross (2007)] in some way. Radiotherapy may be used as the primary therapy, but it is usually combined with sugary, chemotherapy, hyperthermia therapy, or some mixture of them. The mechanism of radiotherapy is to damage the DNA of cells in the target cancerous tissues through the radiation beams ionising the atoms directly and indirectly to the DNA chain. The main side effects caused by radiotherapy are skin irritation which is like a mild to moderate sun burn, and physically exhausting of patients (fatigue) which could make patients lose appetite, weaken the immunologic system of patients to make them easily infected by some epidemic diseases, and even affect the mental health of patients. For example some patients feel low or depressed during radiotherapy.

Hormonal therapy [Sarg and Gross (2007)] is another popular therapeutic method for several types of cancers which derives from hormonally responsive tissues. It involves the manipulation of the endocrine system through exogenous administration of specific hormones or drugs which inhibit the production or activity of such hormones (hormone antagonists). Because some kinds of hormones are the powerful drivers of gene expression in certain cancer cells, changing the levels or activity of certain hormones can cause certain cancers to cease growing, or even undergo cell death.

Hyperthermia therapy [Sarg and Gross (2007)] is also a medical method to treat cancer, in which body tissues are exposed to high temperature to damage and kill cancer cells or make cancer cells more sensitive to the effects of radiation and/or certain anti-cancer drugs. Hyperthermia alone is only useful for certain kinds of cancers, and is not in widespread use. Most commonly, as an adjuvant therapy, hyperthermia is applied alongside with other therapies, such as surgery, radiation, chemotherapy, to increase the effectiveness of

therapies.

1.3 Role of tumour blood flow in cancer treatment

Most of conventional and novel cancer therapies, such as chemotherapy, radiotherapy, hormonal therapy, hyperthermia therapy, immunotherapy, and photodynamic therapy, are closely connected with the blood flow in tumour [Jain (1987a,b, 1988)]. As illustrated in Fig.1.3, for chemotherapy, no matter whether the anti-cancer drugs are taken orally (e.g. Glivec or Tarceva) or injected intravenously (e.g. Avastin and Rituximab), they are intended to travel by convection and diffusion along with blood circulation, across tumour vascular surface into surrounding cancerous tissues, and through tumour interstitial space to kill cancer cells [Jain (1989, 1994, 1997, 1998a,b, 2001)]. All these three major steps for the delivery of chemical anti-cancer drugs are closely related with tumour blood flow. This indicates that tumour blood flow is the key factor to determine the effectiveness of chemotherapy. In the meantime, the distribution of temperature within cancerous and surrounding normal tissues is affected by the convective heat transfer between blood and tissue media [Jain and Ward-Hartley (1984)]. As a result, in the process of hyperthermia, the ability to reach the desired temperature depends on the local perfusion rate [Jain *et al.* (1979)]. Meanwhile, the perfusion rate has strong effects on the effectiveness of radiotherapy, because the potent radiosensitiser — oxygen, which is able to increase the ability of a given dose of radiation by forming DNA-damaging free radicals, is transported into tumour tissues along with blood flow.

However, compared with the blood flow environment in normal tissues, the

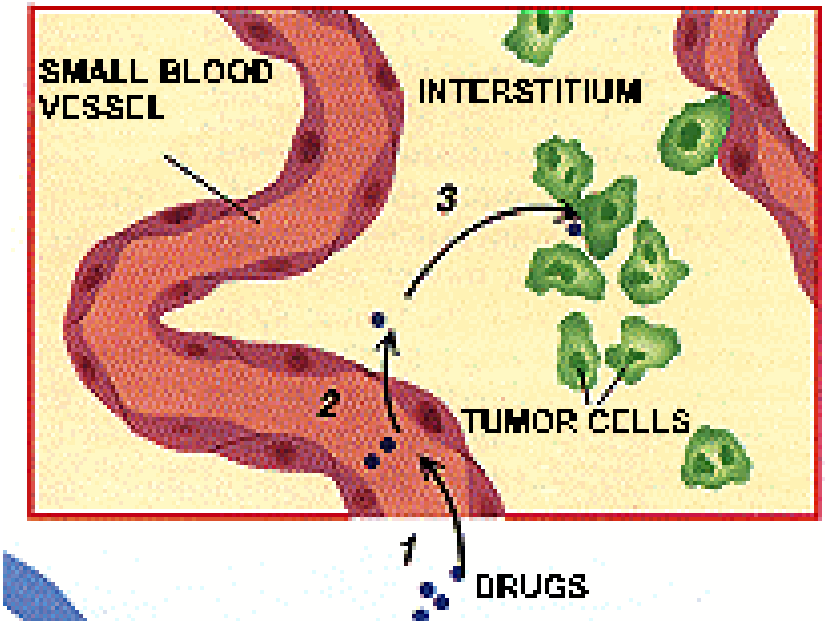

Figure 1.3: Path of drug delivery inside a solid tumour [Jain (1994)].

blood flow field inside a tumour is complicated, even chaotic [Fukumura and Jain (2007a,b)]. The abnormal flow environment severely constrains the delivery of anti-cancer agents into tumour interior, and limits the effectiveness of the non-surgical cancer treatments [Carmeliet and Jain (2000), Fukumura and Jain (2007a,b), Jain (1989, 1994, 1997, 1998a,b, 2001), Jang *et al.* (2003)].

The irregular structure and function of tumour vasculature are at the bottom of the abnormal blood flow field inside tumour [Carmeliet and Jain (2000), Fukumura and Jain (2007a)]. In order to support tumour growth, new vessels are recruited by vasculogenesis and angiogenesis to supply the nutrition when tumour extends beyond the critical size (in general, tumour diameters of 1 to 2 mm) [Folkman (1971, 1995, 2006)]. Angiogenesis changes the architecture of tumour vasculature significantly relative to the vasculature in normal tissues. In contrast to normal vessels, angiogenesis not only creates out of order vascular structures with excessive branches and loops inside tumour, but also

makes tumour vessels tortuous, dilated and with uneven diameters [Konerding *et al.* (1999), Less *et al.* (1991), Shubik (1982)].

Meanwhile, in the progress of angiogenesis (and/or required by angiogenesis), the vessels within tumour share another abnormal function: they are more permeable relative to the vessels in normal tissues [Gerlowski and Jain (1986), Yuan *et al.* (1993, 1994a,b)]. The tumour vascular walls have lots of "openings" (endothelial fenestrate, vesicles and transcellular pores), widened inter-endothelial junctions, and discontinuous or absent basement membranes. In addition, the endothelial cells of tumour vascular walls are abnormal in shape, growing on top of each other, and projecting into the lumen. These defects make tumour vessels permeable [Dvorak *et al.* (1995, 1999), Hashizume *et al.* (2000)]. The tumour vascular permeability plays a key role in forming the complicated blood flow environment in tumour because it induces higher interstitial pressure relative to normal tissues. Due to vascular permeability, when blood flows through tumour vessels, there are exchanges of flux between tumour vessels and interstitium. Because of the effects of tumour interstitial resistance for fluid, the extravasation flux cannot be transported throughout tumour interior instantly, which leads to blood flux accumulated in tumour interstitium. As a result, tumour interstitial pressure is elevated.

As described above, tumour vasculature is highly disorganised in architecture and abnormal in function. Vessels inside tumour are leaky, tortuous and dilated, and tumour vascular network contains excessive branches and loops. In addition, the elevated interstitial pressure caused by the permeability of tumour vessels compresses lymphatic vessels in tumour, which makes tumour lymphatic vessels not functional and impairs the lymphatic flow within tumour [Helmlinger *et al.* (1997), Leu *et al.* (2000)]. These structural and functional abnormalities of tumour vessels contribute to the heterogeneity of tumour blood

flow environment, which is characterised with interstitial hypertension (elevated hydrostatic pressure outside the blood vessels), hypoxia, and acidosis [Jain (2005), Maedaa *et al.* (2000)]. These features are very harmful to normal tissues. But, unfortunately, cancer cells are able to survive in this special environment.

Further to this, the chaotic tumour blood flow forms physiological barriers to compromise the effectiveness of cancer therapies [Jain (1994, 1997, 1998a,b, 1999b, 2001)]. Tumour blood environment hosts a low oxygen state known as hypoxia. This is a major cause for the failure of radiotherapy as tumour cells are deficient in oxygen [Fyles *et al.* (1998), Gatenby *et al.* (1988), Höckel *et al.* (1993)]. The heterogeneous blood flow leads to abnormal blood perfusion rates within tumour. This can harm the effectiveness of hyperthermia [Jain and Ward-Hartley (1984)]. For chemotherapy, the success is suspended because of the low transport rates into tumour interstitium across tumour vasculature and the small diffusion and convection of therapeutic macromolecules [Dykes *et al.* (1987), Kohler and Milstein (1975)]. This is contributed to the high interstitial pressure (interstitial hypertension) in tumour interior caused by the permeability of tumour vessels. The primary role of the elevated interstitial pressure is to reduce the driving force of transvascular exchange for both fluid and macromolecules, which is regarded as one of the major reasons for the low efficiency of drug delivery [Hobbs *et al.* (1998), Jain (1987a,b), Jain and Baxter (1988)]. The hypertension can also aggravate the side effects of chemotherapy and radiotherapy by purging toxic anti-cancer drugs and/or radiosensitiser from tumour interstitium to the surrounded normal tissues [Jain (1996)]. Meanwhile, the low efficiency and inadequate delivery of anti-cancer agents can also result in residual tumour cells, which would in turn lead to regrowth of tumour cells and development of drug resistant cells [Jang *et al.*

(2003)].

1.4 Aim of the project

1.4.1 Aim of the project

Blood flow is one of the key factors for tumour growth. But, what mainly concerns us in this work is its role in determination of the delivery profile and the effectiveness of therapeutic agents to cure cancer. Without blood flow, tumour cannot grow beyond a critical size or metastasise to other organs. On the other hand, with an efficient blood supply, we are able to deliver anti-cancer agents to all regions of tumour interstitium in optimal quantities.

In order to improve effectiveness of cancer treatment with minimal side effects to normal tissues, detailed studies on tumour blood flow are necessary. It will help us to achieve a better understanding of the path by which the therapeutic agents reach tumour cells. Statistically, the malignant solid tumour is responsible for over 85% human cancer mortality [Jain (2005), Jang *et al.* (2003)]. This motives us to investigate the blood flow in a solid tumour.

1.4.2 The problems

The following problems will be the focus of this PhD study:

1. How do the various physical parameters, such as vessel permeability, radius and curvature, the inlet and outlet vascular flow conditions, and the hydraulic conductivity of tumour interstitium, affect tumour blood flow?

2. What are the effects of periphery conditions on the blood environment

inside tumour?

3. When the configuration of tumour vasculature becomes complicated, for example a vascular network with branches and loops, what effects would it have on tumour blood flow?

1.5 Synopsis

In the present chapter, the basic physiology of cancer has been introduced, including the lethality, causes and therapeutical methods of cancer, the unusual characters of the blood flow environment in tumours, and the effects of those characters on cancer therapies. In addition, we have outlined the biomedical problems to be solved, which form the overall aim of this study. The contents in the following chapters are described below.

In Chapter 2, we go through briefly the previous research work on tumour blood flow. We focus on the existing mathematical models on the simulations of tumour blood flow, and highlight the blood pressure distributions inside tumour vessels and within tumour interstitium. In the meantime, the scope of our project is defined.

The chosen numerical simulation tools, finite difference method and boundary element method, are reviewed in Chapter 3. We derive finite difference method with non-uniform differencing schemes through the standard Taylor serious expansions. Then, by Green's identities, boundary element method in context of the blood flow in tumour interstitium is presented. The integral representative of the Green's function is derived at the end of Chapter 3, which is the key factor of applying boundary element method to do the simulations in this study.

According to flow continuity and momentum conservation, Chapter 4 fully

outlines the derivations of the governing equations for the blood flow in a solid tumour when the vasculature is represented by a single vessel. In Chapters 5 and 6, the governing equations derived in Chapter 4 are applied to investigate a simple but practical case for tumour blood flow, in which a single straight vessel with permeability is embedded in a solid tumour. The rationality of our mathematical model and the efficiency of the numerical procedure are examined, and the effects of different physical parameters on tumour blood flow are investigated, including the inlet and outlet vascular flow conditions, tumour hydraulic conductivity, and tumour peripheral pressure.

In Chapters 7 to 9, we undertake the research on how the particular characters of the irregular tumour vascular architecture affect tumour blood flow, including the disordered tumour vessel radius, vessel curvature, and out of order tumour vascular network with asymmetrical bifurcations and loops.

According to the observations on the results obtained in Chapters 6 to 9, an approximation model for the blood flow through tumour vessels is developed in Chapter 10. The validity and calculation efficiency of the approximation model are discussed.

Finally, in Chapter 11, this thesis is summarised with a discussion of the results and analysis.

Chapter 2

Literature Review

Our motivation to investigate tumour blood flow through CFD is to have a better understanding of tumour flow environment, potentially improve the effectiveness of existing therapies, and hopefully lead to the development of new cancer therapeutic methods. Before presenting our model and analysing the results, we briefly go through the previous studies on tumour blood flow. Following a short introduction on observing and measuring tumour blood flow through experimental techniques, we place our focus of this literature review on the existing mathematical models on simulating tumour blood flow. At the end of this chapter, the scope of this thesis is given.

2.1 Observation and measurement on tumour blood environment

Transparent chamber technique is an efficient and wide-used experimental method to observe tumour blood environment. From the author's knowledge, Algire (1943, 1945) and Chalkley (1948) were the first to apply transparent

chamber to study tumour vascular proliferation. Modified from the Sandiso-Clark chamber for the investigation on inflammation [Clark *et al.* (1930), Sandison (1924)], Algire (1943) and Chalkley (1948) designed a chamber as a transparent window inserted into the back of a mouse. This allowed them to observe vasculature of the transplantable tumours available in mice. From observation, they noticed the phenomenon of angiogenesis in tumour. Since then, the transparent chamber technique has been adopted and promoted to investigate tumour by many scholars. For example, Jain and his group applied the "window" technique (transparent chamber technique) to study the vasculature and blood flow in a tumour grown or transplanted in the ear of a rabbit or on the brain or dorsal skin of a rodent, when they put a glass over slip on the tumour [Jain (1994)]. By focusing a microscope on the visible tissue, they can directly investigate tumour blood environment.

Along with the transparent chamber technique for observation, many methods are developed to measure tumour blood flow. Jain and Ward-Hartley (1984) introduced the classification of various methods for tumour blood measurement on the basis of six categorisations, which are isolated tumour technique [Gullino and Grantham (1961)], microsphere technique [Peterso (1979)], uptake of radioactive tracers [Sapirstein (1958)], isotope clearance technique [Gump and White (1968)], thermal clearance [Eberhart *et al.* (1980)], and thermal probe techniques [Gibbs (1933)]. They also discussed the advantages and disadvantages of each method. Among these methods, isolated tumour technique and microsphere technique are the most popular ways to measure tumour blood flow. Later on, due to the development of high resolution imaging technology, more techniques could be applied alone and/or combined with the conventional techniques to observe and measure tumour blood flow, including magnetic resonances imagining (MRI) [Evelhoch (1992), Robinson *et al.*

(1998)], positron emission tomography (PET) [Anderson and Price (2002), Bacharach *et al.* (2000)], Doppler ultrasound imaging [Okihara *et al.* (1999), Peters-Engl *et al.* (1999)], and intravital microscopy method [Jain (2002), Leunig *et al.* (1992)].

A lot of research on observing and measuring tumour flow environment has been done through the methods mentioned above. For example, the study by Gullino *et al.* (1964) was one of the earliest to measure high interstitial tissue fluid pressures in tumours through isolated tumour technique. Peters *et al.* (1980) recorded the pressures in tumour vessels, which was summarised together with other tumour blood features by Jain (1988). Sevick and Jain (1989a) studied the geometrical resistance of blood flow in tumour vessels, and how it depended on tumour size and perfusion rate. Steinberg *et al.* (1990) observed the tumour vascular distribution and measured vascular density in a human xenotransplanted tumour. Less *et al.* (1991) was the first to report the quantitative measurement of vessel branching patterns and vascular dimensions in a mammary tumour.

Though MRI, PET and Doppler imaging techniques could be used *in vivo* measurement in human, most of the measurement methods listed above require harvesting tumours or surgical procedures which can be only conducted in experimental settings. However, a growing body of evidence has been shown that various physiological functions of tumour micro-environment, such as vascular permeability and vascular structure, are different in the original human tumour from the xenotransplanted tumour, even between the primary tumour and the metastatic tumour, because these physiological functions depend on the type of tumour and the host organ where the tumour is growing [Dellian *et al.* (1996), Fukumura *et al.* (1997), Jung *et al.* (2000), Monsky *et al.* (2002)]. For this reason, in many circumstances, experimental results would be declinational, even

opposite to actual *in vivo* physiological phenomena. Therefore, many efforts have been donated to study tumour blood flow through biomechanical models developed from fluid dynamics point of view, since biomechanical models can overcome the limitation of experiments on vascular configuration, and serve to test some biological aspects which are not easily accessible experimentally, especially when the highly adaptable computational fluid dynamics modelling is applied.

2.2 Mathematical models for blood flow in tumour

Jain and Baxter developed a model to study the interstitial fluid field in a spherical tumour [Baxter and Jain (1989, 1990), Jain and Baxter (1988)]. In their model, there was a continuously distributed vasculature and lymphatics in the tumour space. The flow pressure distribution in tumour space was described by the Darcy's law when regarding the tumour interstitium as a porous media. The vessels were taken as constant sources for extravasation flux due to their permeability, and the lymphatics as sinks because of their absorption ability. They assumed that the net flow transported into the interstitium was the balance of the flux exceeded from the vasculature by convection, the flux absorbed into the lymphatics, and the flux delivered from tumour interstitium into the surrounding normal tissues. Based on their model, Jain and Baxter (1988) showed that the interstitial fluid pressure was elevated in the centre of the tumour compared with normal tissues, which was equal to the average pressure in capillary, and was determined by the balance between flux flowing from the vasculature into the interstitium together with that from the interstitium into the surrounding normal tissues. El-Kareh and Secomb (1995)

applied a similar model to study the effects of tumour size and shape on the interstitial blood flow. They showed that the dependence of the flux exceeded from the vessels into tumour interior on tumour shape was much weaker than tumour size.

Adopting a similar approach to describe the vasculature in normal tissues proposed by Krogh (1919) and Apelblat *et al.* (1974), Netti *et al.* (1996) developed a model of steady-state tumour blood flow when applying a hypothetical vessel with permeability to represent the entire vascular network in tumour. In their model, the vascular elastic property was considered, and the dependence of steady-state cross-section area of tumour vessel on the transmural pressure difference was described mathematically based on a semi-empirical formula. The interstitial fluid pressure was assumed to be constant, and independent on the vascular flow pressure, vascular permeability, or tumour hydrodynamical property. They investigated how the arterial (inlet) and venous (outlet) vascular flow pressures affected the flux exceeded from vessels into tumour interstitium according to the conservation of blood mass.

Milosevic *et al.* (1999) modified the elastic vessel model developed by Netti *et al.* (1996) to investigate the unsteady property of tumour blood flow. They assumed that the variation of the vessel cross section with respect to time is directly proportional to the variation of transmural pressure difference with respect to time. The proportion coefficient was obtained through artificially differentiating the steady model proposed by Netti *et al.* (1996) with respect to the transmural pressure difference. Using this model, they calculated the elevated interstitial fluid pressure on the exterior surface of the permeable vessel which was embedded in a spherical solid tumour.

Another model was developed by Mollica *et al.* (2003) to study the temporal characters of tumour blood flow. They simplified the tumour vasculature as

a two-dimensional channel with permeability. The elastic property of the vessel was considered in their simulation, and the membrane theory was adopted to describe the vascular deformation. The tumour interstitial pressure was set to be constant and not related with the pressure in vessel. They investigated the blood pressure profile inside vessel based on the mass conservation, and concluded that the average vascular pressure was not necessarily equilibrating with the tumour interstitial pressure, and the tumour vessel performed a self-sustained oscillatory behaviour.

Baish *et al.* (1997) studied the steady-state coupling effects between tumour vascular and interstitial fluid flows through a model when replacing the vasculature by parallel rows of vessels which were spanned the full thickness of a hypothetical square tumour. The vessels were perfused by the blood entering along one edge of the tumour, and drained along the opposite edge. The direction of the tumour interstitial fluid flow was assumed to be perpendicular to the vascular blood flow. The model predicted uniformly elevated interstitial pressure in the central region of the tumour and a rapid reduce to low value at the periphery. Baish *et al.* (1997) themselves summarised that one obvious shortcoming of their model was the simplicity in vascular architecture. Having accepted that limitation, the model demonstrated redistribution of blood flow from the centre to the periphery of the tumour as a result of the interstitial pressure inducing constriction of the venous end of the vessels.

Fleischman *et al.* (1986a,b) developed a mathematical model to investigate the effects of pressure gradients on the exchange of flux exceeded from vessels into a tissue, who took into account of the coupling effects between the blood flow through the vessels and the flow field in the tissue. In their model, the tissue was assumed to be an infinite isotropic porous medium without lymph vessels, and the blood flow within it was governed by the Darcy's law. The

rigid vessels embedded in the tissue were straight with low permeability. The vascular flow was described by the Poiseuille's law, and the extravasation flux was controlled by the Starling's law. To solve the model, they converted the Darcy's law to a boundary-integral equation along the vessels, and then divided them into small cylinder sections along the vessel centre lines. In this numerical computation process, they only took the vessels as a set of sources, but ignored full interactions between the sections. However, in general, these interactions must be considered when the boundary-integral representative is applied to replace the original differential equations (see Sec.3.3).

Pozrikidis and Farrow (2003) improved the theoretical model developed by Fleischman *et al.* (1986a) to undertake the research on the blood flow in a solid tumour when the whole vasculature was replaced by a single straight vessel. They pointed out the weakness of the calculation in the work by Fleischman *et al.* (1986a). They included the full interactions between the sections when the boundary element method was applied, and showed that, though the error introduced by the approximation was not significant under physiological and physical conditions considered by Fleischman *et al.* (1986a), whereas for the blood flow through a vessel with high permeability in tumour tissue, the full interaction between the discretised cylinder sections has to be included. They also concluded that the assumption of uniform interstitial pressure along the outer surface of the vessel was not appropriate.

2.3 Scope of our project

Transporting anti-cancer therapeutic agents in optimal quantities is one of the critical problems for drug and gene delivery in solid tumours [Jain (1997)]. However, delivery of anti-cancer agents into solid tumours is always limited

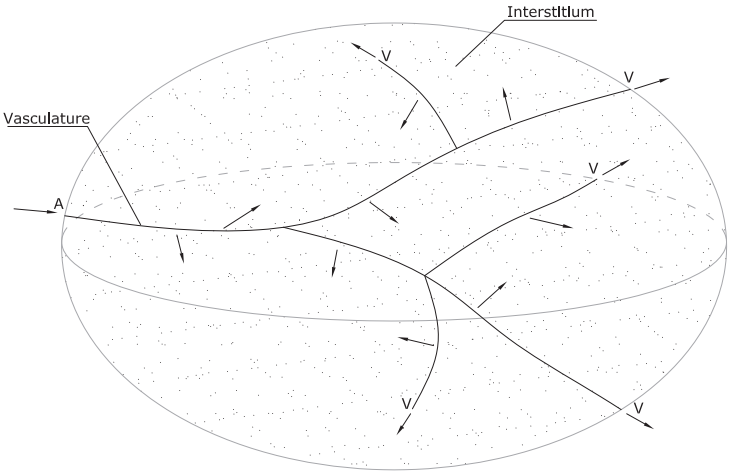

Figure 2.1: An illustration of blood flow through a 3D vascular network embedded in a solid tumour.

because of very slow diffusion [Boucher *et al.* (1998), Jain (1999a), Netti *et al.* (1999)] since most anti-cancer agents are molecules with large size and heavy weight [Costantini *et al.* (2000), Gabizon *et al.* (1998), Kulkarni *et al.* (1995)], and inadequate convective transport due to elevated interstitial fluid pressure [Jain (1997)]. Diffusive effects on molecules cannot be changed significantly unless chemical structures of therapeutic agents or tissues are modified substantially. However, convection can be adjusted through varying either systemic blood pressure gradients [Hori *et al.* (1994), Netti *et al.* (1997)], tumour interstitial hydraulic conductivity [Zhang *et al.* (2000)] or some other physical parameters. Therefore, it is relatively easy to process and control the convective effects in tumour, which can be investigated by fluid dynamics efficiently. This demarcates the scope of our study in this thesis.

The main objective of our study is to develop a mathematical model and numerical solution procedure for modelling the blood flow through a three-dimensional vascular network which is embedded in a solid tumour, as illustrated in Fig.2.1. The effects of different physical parameters on tumour blood

flow are investigated in context with the convective delivery of anti-cancer therapeutic agents. The results provided here are preliminarily to demonstrate the effectiveness of the method from computational point of view and their potential implications to the medical purpose, which are not yet at the stage to aim at direct clinical applications.

Chapter 3

Finite Difference Method and Boundary Element Method

3.1 Introduction

In this chapter, we present the numerical tools which are applied in this study. Finite difference method and boundary element method are chosen to undertake the required simulations. These two numerical methods are selected because they are believed to be convenient in programming and efficient for calculating the problems in our project.

Firstly, we introduce finite difference method (FDM). Among usual numerical simulation methods, including finite difference method, finite element method (FEM), finite volume method (FVM), and boundary element method (BEM), FDM is the most straightforward one in terms of its numerical discretisation procedure, which replaces the derivatives in differential equations with differencing schemes. It is easy to program, especially on solving ordinary differential equations. We are going to demonstrate the detailed differencing schemes based on the standard Taylor expansion in nonuniform meshes. In

our simulations, this method is mainly adopted to calculate the blood flow through tumour vessels.

Then, we step forward to present the details of boundary element method (BEM). In BEM, the governing differential equation in the calculation domain is converted, when possible, into a boundary-integral equation over the boundary of that domain. This procedure makes the dimensionality of the investigation problem lower by one order, and the discretised meshes are only generated on the boundary instead of the entire simulation domain. This feature can help us to significantly reduce the number of unknowns, especially for three-dimensional problems.

Finally, the integral representative of the free-space Green's function is derived. The Green's function is the key factor when applying BEM to solve the Laplace equation which is applied to describe the flow field within tumour interior in this project. The integral expression of the Green's function is convenient to solve the boundary-integral equation obtained in BEM, particularly for the present study.

3.2 Finite difference method

Finite difference method (FDM) is one of the most common numerical methods. The details of FDM may be found in the books by Anderson (1995), Chung (2002) and others. Compared with other popular numerical tools in computational fluid dynamics, such as finite element method (FEM), finite volume method (FVM), and boundary element method (BEM), FDM is the simplest one in terms of its numerical discretisation procedure. It is particularly powerful for ordinary differential equations or one-dimensional problems, since no mapping is needed between the physical domain and the computa-

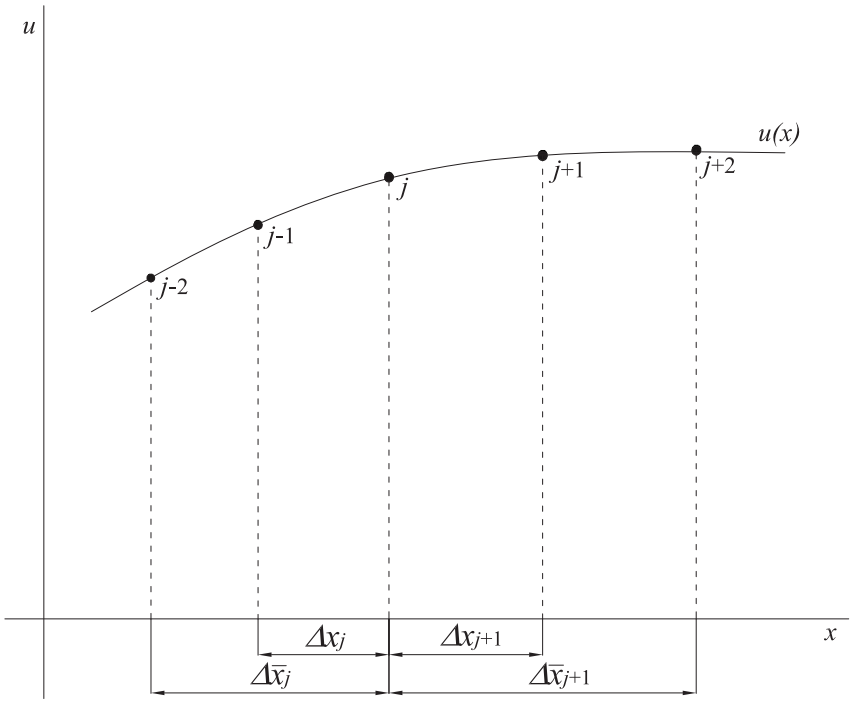

Figure 3.1: Illustration of behaviour in standard Taylor series expansion.

tional domain, which is usually required by partial differential equations. The basic principle of FDM is straightforward: using differencing schemes, the derivatives in differential equations are written in terms of discretised quantities of dependent and independent variables, resulting in simultaneous algebraic equations with all unknowns prescribed at discretised mesh points for the entire domain [Anderson (1995)].

In order to apply FDM to simulate fluid flow, we need to choose appropriate types of differencing schemes and suitable methods for solution. Normally, the choice for the proper type of finite differencing schemes depends on the particular physics of the flow, which may include inviscid/viscous, incompressible/compressible, subsonic/transonic/supersonic, irrotational/rotational, laminar/turbulent flow.

In this study, one-dimensional finite differencing schemes with nonuniform

spacing are used to investigate the blood flow through tumour vessels. This kind of differencing schemes can be obtained through the standard Taylor series expansion. As sketched in Fig.3.1, for some function $u(x)$, from the value of u_j at x_j, the value of u_{j+1} at x_{j+1} can be expressed in the form of the forward formula of the standard Taylor series as

$$\begin{aligned} u_{j+1} =& u_j + \Delta x_{j+1} \left(\frac{\partial u}{\partial x}\right)_j + \frac{\Delta x_{j+1}^2}{2} \left(\frac{\partial^2 u}{\partial x^2}\right)_j + \frac{\Delta x_{j+1}^3}{6} \left(\frac{\partial^3 u}{\partial x^3}\right)_j \\ & + O(h^4). \end{aligned} \tag{3.2.1}$$

Similarly, the value of u_{j-1} at x_{j-1} can be written by the backward formula of the standard Taylor series, which is

$$u_{j-1} = u_j - \Delta x_j \left(\frac{\partial u}{\partial x}\right)_j + \frac{\Delta x_j^2}{2} \left(\frac{\partial^2 u}{\partial x^2}\right)_j - \frac{\Delta x_j^3}{6} \left(\frac{\partial^3 u}{\partial x^3}\right)_j + O(h^4). \tag{3.2.2}$$

In both Eqs.(3.2.1) and (3.2.2), $\Delta x_j = x_j - x_{j-1}$, $\Delta x_{j+1} = x_{j+1} - x_j$, and h stands for a typical order of spacing.

The first order derivative from the central difference formula with the second order accuracy is obtained through combining Eqs.(3.2.1) and (3.2.2) as

$$\begin{aligned} \left(\frac{\partial u}{\partial x}\right)_j =& \frac{1}{\Delta x_j + \Delta x_{j+1}} \left[\frac{\Delta x_{j+1}}{\Delta x_j}(u_j - u_{j-1}) + \frac{\Delta x_j}{\Delta x_{j+1}}(u_{j+1} - u_j)\right] \\ & + O(h^2). \end{aligned} \tag{3.2.3}$$

The three-point central difference formula for the second order derivative has the form of

$$\left(\frac{\partial^2 u}{\partial x^2}\right)_j = \frac{2}{\Delta x_j + \Delta x_{j+1}} \left(\frac{u_{j+1} - u_j}{\Delta x_{j+1}} - \frac{u_j - u_{j-1}}{\Delta x_j}\right) + O(h). \tag{3.2.4}$$

The order of accuracy of Eq.(3.2.4) will be $O(h^2)$ if $\Delta x_{j+1} = \Delta x_j$.

Besides the central difference formulae, the forward and backward difference formulae are also applied in this study, for example, when we investigate the blood flow features at the junction points in the vascular network. According to the Taylor series expansion,

$$\begin{aligned} u_{j+2} =& u_j + \Delta\bar{x}_{j+1}\left(\frac{\partial u}{\partial x}\right)_j + \frac{\Delta\bar{x}_{j+1}^2}{2}\left(\frac{\partial^2 u}{\partial x^2}\right)_j + \frac{\Delta\bar{x}_{j+1}^3}{6}\left(\frac{\partial^3 u}{\partial x^3}\right)_j \\ &+ O(h^4), \end{aligned} \tag{3.2.5}$$

and

$$u_{j-2} = u_j - \Delta\bar{x}_j\left(\frac{\partial u}{\partial x}\right)_j + \frac{\Delta\bar{x}_j^2}{2}\left(\frac{\partial^2 u}{\partial x^2}\right)_j - \frac{\Delta\bar{x}_j^3}{6}\left(\frac{\partial^3 u}{\partial x^3}\right)_j + O(h^4), \tag{3.2.6}$$

in which $\Delta\bar{x}_{j+1} = x_{j+2} - x_j$ and $\Delta\bar{x}_j = x_j - x_{j-2}$ as depicted in Fig.3.1. Combining Eq.(3.2.1) with Eq.(3.2.5), we obtain the first order derivative from the three-point forward difference as

$$\begin{aligned} \left(\frac{\partial u}{\partial x}\right)_j =& \frac{\Delta x_{j+1}}{\Delta\bar{x}_{j+1}(\Delta x_{j+1} - \Delta\bar{x}_{j+1})}u_{j+2} - \frac{\Delta\bar{x}_{j+1}}{\Delta x_{j+1}(\Delta x_{j+1} - \Delta\bar{x}_{j+1})}u_{j+1} \\ &- \frac{(\Delta x_{j+1} + \Delta\bar{x}_{j+1})}{\Delta\bar{x}_{j+1}\Delta x_{j+1}}u_j + O(h^2), \end{aligned} \tag{3.2.7}$$

and the second order derivative from the three-point forward difference as

$$\begin{aligned} \left(\frac{\partial^2 u}{\partial x^2}\right)_j =& \frac{2}{\Delta\bar{x}_{j+1}(\Delta\bar{x}_{j+1} - \Delta x_{j+1})}u_{j+2} - \frac{2}{\Delta x_{j+1}(\Delta x_{j+1} - \Delta\bar{x}_{j+1})}u_{j+1} \\ &+ \frac{2}{\Delta\bar{x}_{j+1}\Delta x_{j+1}}u_j + O(h). \end{aligned} \tag{3.2.8}$$

Considering Eqs.(3.2.2) and (3.2.6), and following the same procedure stated above, we have the first order derivative from the three-point backward difference as

$$\left(\frac{\partial u}{\partial x}\right)_j = -\frac{\Delta x_j}{\Delta\bar{x}_j(\Delta x_j - \Delta\bar{x}_j)}u_{j-2} + \frac{\Delta\bar{x}_j}{\Delta x_j(\Delta x_j - \Delta\bar{x}_j)}u_{j-1} + \frac{(\Delta x_j + \Delta\bar{x}_j)}{\Delta\bar{x}_j\Delta x_j}u_j + O(h^2), \tag{3.2.9}$$

and the second order derivative from the three-point backward difference as

$$\left(\frac{\partial^2 u}{\partial x^2}\right)_j = \frac{2}{\Delta\bar{x}_j(\Delta\bar{x}_j - \Delta x_j)}u_{j-2} - \frac{2}{\Delta x_j(\Delta x_j - \Delta\bar{x}_j)}u_{j-1} + \frac{2}{\Delta\bar{x}_j\Delta x_j}u_j + O(h). \tag{3.2.10}$$

Now, we have obtained all the finite differencing schemes required in our project. In order to apply FDM to solve physical problems practically, we shall replace the differential derivatives in the governing equations with the finite difference schemes derived in this section. As a result, the original differential equations are transformed into a set of algebraic equations which can be solved efficiently by numerical programming. There are two common methods to improve the accuracy of FDM. One is to adopt more-point (more than three points) differencing schemes. The other is to decrease the value of typical spacing size h.

3.3 The boundary element method

3.3.1 Introduction

The procedure of boundary element method (BEM), which may be found in the books by Brebbia and Dominguez (1992), Pozrikidis (2002) and others, is introduced in this section. In BEM, the governing differential equation in the calculation domain is transformed into an integral equation over the boundary of the domain, after using a fundamental solution which satisfies the governing

differential equation inside the domain apart from some source point. The integral equation is calculated numerically over the boundary which is divided into small segments (boundary elements). Following the similar procedure in other numerical approaches, when the boundary conditions are satisfied, a set of linear algebraic equations emerges, for which the unique solution can be found through numerical programming.

3.3.2 Advantages of BEM

The most important feature of BEM is that it only requires discretisation on the boundary rather than in the whole calculation domain. The advantage of this feature is obvious: the dimensionality of the problem is reduced by one order, that is, only a surface instead of a volume discretisation is required. This indicates that the number of unknowns is reduced dramatically, especially for a three-dimensional problem, because unknowns occur only on the boundary. In the meantime, meshes for BEM can be easily generated and adjusted, but do not require a complete re-meshing. This factor also makes BEM conveniently accommodate geometrically complex boundaries and deal with an infinite continuum.

3.3.3 Basic integral equation

In this part, the basic process on how to derive the boundary-integral equation is presented. This boundary-integral equation can be obtained through some different ways, such as weighted residuals, Betti's reciprocal theorem, Green's identities, or fundamental principles. Here, Green's identities is chosen to present the process, because it is easy to understand, especially for the Laplace equation.

The three-dimensional Laplace equation

$$\nabla^2\phi(\mathbf{x}) = 0 \tag{3.3.1}$$

is adopted as the governing equation for the blood flow field within tumour interstitium in our project, in which $\phi(\mathbf{x})$ is a twice-differentiable function. The pressure distribution in tumour interior is described by Eq.(3.3.1), which is solved by BEM in this study.

Green's identities

Green's identities are a set of vector derivative/integral identities which can be derived from the vector derivative identities. For any two twice-differentiable functions f and g, we have

$$\nabla \cdot (f\nabla g) = f\nabla^2 g + \nabla f \cdot \nabla g. \tag{3.3.2}$$

When the divergence theorem

$$\int_{V_c} (\nabla \cdot \mathbf{F})\mathrm{d}V = \int_S \mathbf{F} \cdot \mathrm{d}\mathbf{S} = \int_S \mathbf{F} \cdot \mathbf{n}\mathrm{d}S \tag{3.3.3}$$

is applied to Eq.(3.3.2), the *first Green's identity* is derived as

$$\int_S f\nabla g \cdot \mathbf{n}\mathrm{d}S = \int_{V_c} (f\nabla^2 g + \nabla f \nabla g)\mathrm{d}V, \tag{3.3.4}$$

in which V_c is the calculation domain, S refers the boundary of V_c, and $\mathbf{n}$ is the unit vector normal to S pointing out of V_c.

Interchanging the roles of f and g, we have

$$\int_S g\nabla f \cdot \mathbf{n}\mathrm{d}S = \int_{V_c} (g\nabla^2 f + \nabla g \nabla f)\mathrm{d}V. \tag{3.3.5}$$

Subtracting Eq.(3.3.5) from Eq.(3.3.4), we obtain the *second Green's identity*, which is in the form of

$$\int_{V_c}(f\nabla^2 g - g\nabla^2 f)\mathrm{d}V = \int_S (f\nabla g - g\nabla f)\cdot \mathbf{n}\mathrm{d}S. \tag{3.3.6}$$

If both functions f and g are harmonic, the integrand on the left-hand side of Eq(3.3.6) vanishes, or

$$f\nabla^2 g - g\nabla^2 f = \nabla\cdot(f\nabla g - g\nabla f) = 0. \tag{3.3.7}$$

Then, an integral form is found as

$$\int_S f\nabla g\cdot\mathbf{n}\mathrm{d}S - \int_S g\nabla f\cdot\mathbf{n}\mathrm{d}S = 0. \tag{3.3.8}$$

Fundamental solution of the Laplace equation

One key issue of applying BEM is to choose a proper fundamental solution for the governing differential equation in the calculation domain. The three-dimensional Laplace equation

$$\nabla^2\phi(\mathbf{x}) = 0$$

shows that function ϕ is twice-differentiable and harmonic. The fundamental solution for the Laplace equation is a special harmonic function, or the Green's function

$$G(\mathbf{x},\mathbf{x}_0).$$

In $G(\mathbf{x},\mathbf{x}_0)$, $\mathbf{x}$ is a field point, and $\mathbf{x_0}$ is the location of a singularity.

The Green's function represents the field generated by a concentrated unit source acting at point $\mathbf{x}_0$. The effect of this source is from $\mathbf{x}_0$ to infinity without any consideration of boundary conditions. Thus,

$$\nabla^2 G(\mathbf{x}, \mathbf{x}_0) = \delta(\mathbf{x} - \mathbf{x}_0), \tag{3.3.9}$$

where

$$\delta(\mathbf{x} - \mathbf{x}_0) = \delta(x - x_0)\delta(y - y_0)\delta(z - z_0) \tag{3.3.10}$$

is the three-dimensional Direct Delta function. The solution for Eq.(3.3.9) is

$$G(\mathbf{x}, \mathbf{x}_0) = -\frac{1}{4\pi\,|\mathbf{r}|}, \tag{3.3.11}$$

in which

$$|\mathbf{r}| = |\mathbf{x} - \mathbf{x}_0| = \sqrt{(x - x_0)^2 + (y - y_0)^2 + (z - z_0)^2}. \tag{3.3.12}$$

Basic boundary-integral equation

When function f is replaced with $\phi(\mathbf{x})$ and g with $G(\mathbf{x}, \mathbf{x}_0)$, Eq.(3.3.7) is rewritten as

$$\nabla \cdot [\phi(\mathbf{x})\nabla G(\mathbf{x}, \mathbf{x}_0) - G(\mathbf{x}, \mathbf{x}_0)\nabla\phi(\mathbf{x})] = 0, \quad \mathbf{x} \neq \mathbf{x}_0. \tag{3.3.13}$$

In order to integrate Eq.(3.3.13) over a certain volume V_c and apply the divergence theorem, a small sphere of radius ϵ is excluded, whose centre is located

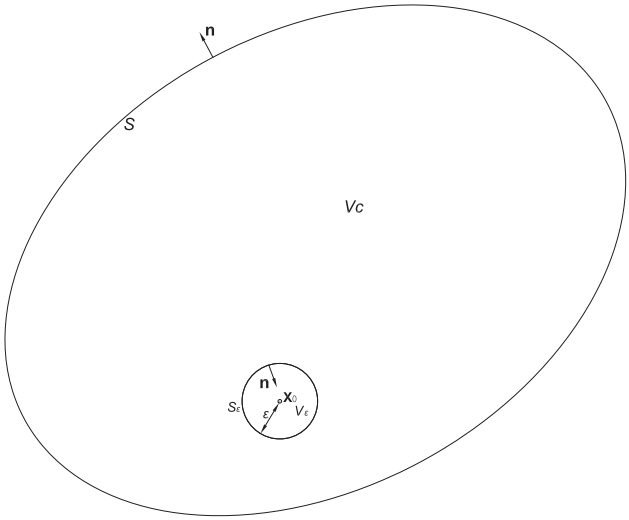

Figure 3.2: Sketch of a certain control volume V_c used to derive the boundary-integral equation of BEM when $\mathbf{x}_0$ is inside the volume.

at point $\mathbf{x}_0$, as shown in Fig.3.3.3. This leads to

$$\int_{S_\epsilon} \mathbf{n}(\mathbf{x}) \cdot [\phi(\mathbf{x}) \nabla G(\mathbf{x}, \mathbf{x}_0) - G(\mathbf{x}, \mathbf{x}_0) \nabla \phi(\mathbf{x})] \, \mathrm{d}S(\mathbf{x}) + \int_{S} \mathbf{n}(\mathbf{x}) \cdot [\phi(\mathbf{x}) \nabla G(\mathbf{x}, \mathbf{x}_0) - G(\mathbf{x}, \mathbf{x}_0) \nabla \phi(\mathbf{x})] \, \mathrm{d}S(\mathbf{x}) = 0. \tag{3.3.14}$$

Let us consider the integral over S_ϵ on the left-hand side of Eq.(3.3.14), or

$$\int_{S_\epsilon} \mathbf{n}(\mathbf{x}) \cdot [\phi(\mathbf{x}) \nabla G(\mathbf{x}, \mathbf{x}_0) - G(\mathbf{x}, \mathbf{x}_0) \nabla \phi(\mathbf{x})] \, \mathrm{d}S(\mathbf{x}). \tag{3.3.15}$$

Based on the definition of the Green's function in Eq.(3.3.11), we have

$$\nabla G(\mathbf{x}, \mathbf{x}_0) \cdot \mathbf{n}(\mathbf{x}) = -\frac{\partial G(\mathbf{x}, \mathbf{x}_0)}{\partial \left| \mathbf{r} \right|} = -\frac{\partial G(\mathbf{x}, \mathbf{x}_0)}{\partial \epsilon} = -\frac{1}{4\pi\epsilon^2}. \tag{3.3.16}$$

Introducing Eqs.(3.3.11) and (3.3.16) into Eq.(3.3.15), and letting $\epsilon \to 0$, we

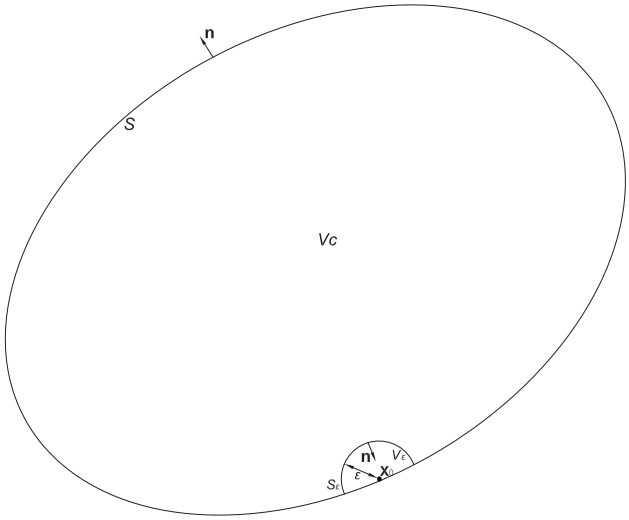

Figure 3.3: Sketch of a certain control volume V_c used to derive the boundary-integral equation of BEM when $\mathbf{x}_0$ tends to the surface of the volume.

obtain

$$\begin{aligned}
&\lim_{\epsilon\to 0}\int_{S_\epsilon}\mathbf{n}(\mathbf{x})\cdot[\phi(\mathbf{x})\nabla G(\mathbf{x},\mathbf{x}_0)-G(\mathbf{x},\mathbf{x}_0)\nabla\phi(\mathbf{x})]\,\mathrm{d}S(\mathbf{x})\\
=&\lim_{\epsilon\to 0}4\pi\epsilon^2\left[-\frac{1}{4\pi\epsilon^2}\phi(\mathbf{x}_0)+\frac{1}{4\pi\epsilon}\frac{\partial\phi(\mathbf{x}_0)}{\partial n}\right]\\
=&-\phi(\mathbf{x}_0). \qquad (3.3.17)
\end{aligned}$$

Substituting Eq.(3.3.17) into Eq.(3.3.14) yields the result as

$$\begin{aligned}
\phi(\mathbf{x}_0)=&-\int_S G(\mathbf{x},\mathbf{x}_0)\,[\mathbf{n}(\mathbf{x})\cdot\nabla\phi(\mathbf{x})]\,\mathrm{d}S(\mathbf{x})\\
&+\int_S\phi(\mathbf{x})\,[\nabla G(\mathbf{x},\mathbf{x}_0)\cdot\mathbf{n}(\mathbf{x})]\,\mathrm{d}S(\mathbf{x}). \qquad (3.3.18)
\end{aligned}$$

When point $\mathbf{x}_0$ tends to the surface of volume V_c, as plotted in Fig.3.3, only half sphere is left inside the volume if the surface is smooth at point $\mathbf{x}_0$. This

leads to

$$\frac{1}{2}\phi(\mathbf{x}_0) = -\int_S G(\mathbf{x},\mathbf{x}_0)\left[\nabla\phi(\mathbf{x})\cdot\mathbf{n}(\mathbf{x})\right]\mathrm{d}S(\mathbf{x}) + \int_S \phi(\mathbf{x})\left[\nabla G(\mathbf{x},\mathbf{x}_0)\cdot\mathbf{n}(\mathbf{x})\right]\mathrm{d}S(\mathbf{x}). \tag{3.3.19}$$

The Laplace equation is now transformed into an integral equation over the boundary of a certain control volume, as described in Eq.(3.3.19). This integral equation can be solved numerically when the boundary is divided into small elements. The unique solution is then obtained for unknowns if the boundary conditions are satisfied.

3.4 Integral representative of the free-space Green's function

As aforementioned in Section 3.1, the free-space Green's function is the key factor in applying BEM to solve the Laplace equation. In this section, we represent the free-space Green's function with its integral expression in Cartesian coordinate system (x, y, z). This integral representative is convenient to solve the boundary-integral equation (3.3.19) in our project. In a certain three-dimensional space with Cartesian coordinate system (x, y, z), the Green's function is defined as

$$G(\mathbf{x},\mathbf{x}_0) = -\frac{1}{4\pi\sqrt{(x-x_0)^2+(y-y_0)^2+(z-z_0)^2}}, \tag{3.4.1}$$

which satisfies

$$\nabla^2 G(\mathbf{x},\mathbf{x}_0) = \delta(\mathbf{x}-\mathbf{x}_0), \tag{3.4.2}$$

where $\delta(\mathbf{x}-\mathbf{x}_0)$ is the three-dimensional Dirac Delta function defined in Eq.(3.3.10).

Making the spatial Fourier Transformation [Bronshtein *et al.* (2007)] on both sides of Eq.(3.4.2), we have

$$\mathcal{F}_{\mathbf{x}}\left\{\nabla^2 G(\mathbf{x},\mathbf{x}_0)\right\} = \mathcal{F}_{\mathbf{x}}\left\{\delta(\mathbf{x}-\mathbf{x}_0)\right\}, \tag{3.4.3}$$

in which

$$\mathcal{F}_{\mathbf{x}}\{f\}(\mathbf{v}) \overset{def}{=} \int_{-\infty}^{+\infty}\int_{-\infty}^{+\infty}\int_{-\infty}^{+\infty} f(\mathbf{x})\mathrm{e}^{-\mathrm{i}(\mathbf{v}\cdot\mathbf{x})}\mathrm{d}x\mathrm{d}y\mathrm{d}z, \tag{3.4.4}$$

where $\mathrm{i}=\sqrt{-1}$, and $\mathbf{v}=(v_1,v_2,v_3)$. As

$$\mathcal{F}_{\mathbf{x}}\{f\}\left\{\nabla^2 G(\mathbf{x},\mathbf{x}_0)\right\} = [(\mathrm{i}v_1)^2+(\mathrm{i}v_2)^2+(\mathrm{i}v_3)^2]G_f(\mathbf{v},\mathbf{x}_0), \tag{3.4.5}$$

in which

$$G_f(\mathbf{v},\mathbf{x}_0) = \int_{-\infty}^{+\infty}\int_{-\infty}^{+\infty}\int_{-\infty}^{+\infty} G(\mathbf{x},\mathbf{x}_0)\mathrm{e}^{-\mathrm{i}(\mathbf{v}\cdot\mathbf{x})}\mathrm{d}x\mathrm{d}y\mathrm{d}z, \tag{3.4.6}$$

and noticing that the integral of Dirac delta function multiplied by any other function is equal to the value of the function at point $\mathbf{x}_0$, Eq.(3.4.3) can be rewritten as

$$[(\mathrm{i}v_1)^2+(\mathrm{i}v_2)^2+(\mathrm{i}v_3)^2]G_f(\mathbf{v},\mathbf{x}_0) = \mathrm{e}^{-\mathrm{i}v_1x_0-\mathrm{i}v_2y_0-\mathrm{i}v_3z_0}. \tag{3.4.7}$$

Then,

$$G_f(\mathbf{v},\mathbf{x}_0) = -\frac{\mathrm{e}^{-\mathrm{i}v_1x_0-\mathrm{i}v_2y_0-\mathrm{i}v_3z_0}}{(v_1^2+v_2^2+v_3^2)}. \tag{3.4.8}$$

According to the definition of the spatial Fourier Transformation in Eq.(3.4.4), the pair inverse spatial Fourier Transformation [Bronshtein *et al.* (2007)] is in the form of

$$\mathcal{F}_{\mathbf{v}}^{-1}\{f\}(\mathbf{x}) = \frac{1}{8\pi^3}\int_{-\infty}^{+\infty}\int_{-\infty}^{+\infty}\int_{-\infty}^{+\infty} f(\mathbf{v})\mathrm{e}^{\mathrm{i}(\mathbf{v}\cdot\mathbf{x})}\mathrm{d}v_1\mathrm{d}v_2\mathrm{d}v_3. \tag{3.4.9}$$

Applying Eq.(3.4.9) to Eq.(3.4.8), we have

$$G(\mathbf{x},\mathbf{x}_0) = \frac{1}{8\pi^3}\int_{-\infty}^{+\infty}\int_{-\infty}^{+\infty}\int_{-\infty}^{+\infty} -\frac{\mathrm{e}^{\mathrm{i}v_1(x-x_0)+\mathrm{i}v_2(y-y_0)+\mathrm{i}v_3(z-z_0)}}{v_1^2+v_2^2+v_3^2}\mathrm{d}v_1\mathrm{d}v_2\mathrm{d}v_3. \tag{3.4.10}$$

Following the procedure presented in the book by Ziomek (1995), the above equation is rewritten as

$$G(\mathbf{x},\mathbf{x}_0) = -\frac{1}{8\pi^3}\int_{-\infty}^{+\infty}\frac{\mathrm{e}^{\mathrm{i}v_1(x-x_0)}}{v_1^2+k_\rho^2}\mathrm{d}v_1\int_{-\infty}^{+\infty}\int_{-\infty}^{+\infty}\mathrm{e}^{\mathrm{i}v_2(y-y_0)+\mathrm{i}v_3(z-z_0)}\mathrm{d}v_2\mathrm{d}v_3, \tag{3.4.11}$$

where

$$k_\rho = \sqrt{v_2^2+v_3^2}. \tag{3.4.12}$$

Let us consider the first part of the integral on the right-hand side of Eq.(3.4.11), or

$$\int_{-\infty}^{+\infty}\frac{\mathrm{e}^{\mathrm{i}v_1(x-x_0)}}{v_1^2+k_\rho^2}\mathrm{d}v_1. \tag{3.4.13}$$

Based on the definition of complex function, and considering the parity of trigonometric functions, we have

$$\int_{-\infty}^{+\infty}\frac{\mathrm{e}^{\mathrm{i}v_1(x-x_0)}}{v_1^2+k_\rho^2}\mathrm{d}v_1 = \int_{-\infty}^{+\infty}\frac{\cos[v_1\,|x-x_0|]}{v_1^2+k_\rho^2}\mathrm{d}v_1 = \int_{-\infty}^{+\infty}\frac{\mathrm{e}^{\mathrm{i}v_1|x-x_0|}}{v_1^2+k_\rho^2}\mathrm{d}v_1. \tag{3.4.14}$$

The term on the right-hand side of Eq.(3.4.14) is an improper integral in an

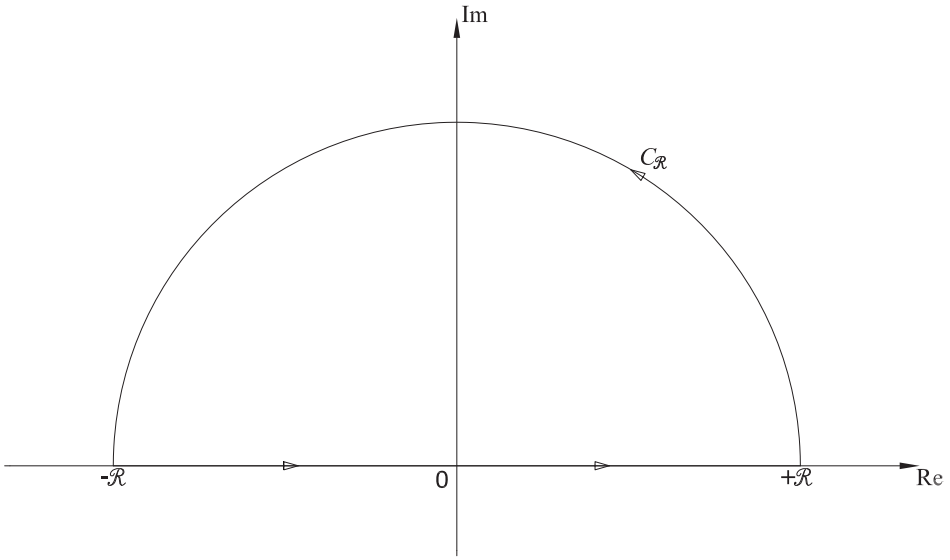

Figure 3.4: The closed integral path with half circle arch in a complex plane.

infinite domain. It can be calculated by Residue Theorem in association with Jordan's Lemma [Bronshtein *et al.* (2007)].

Considering an integral with the same integrand in the term on the right-hand side of Eq.(3.4.14) along a closed half-circle loop on a complex plane, or

$$\oint \frac{\mathrm{e}^{\mathrm{i}\varpi|x-x_0|}}{\varpi^2+k_\rho^2}\mathrm{d}\varpi,$$

we can rearrange the integral as

$$\oint \frac{\mathrm{e}^{\mathrm{i}\varpi|x-x_0|}}{\varpi^2+k_\rho^2}\mathrm{d}\varpi = \int_{-\mathcal{R}}^{+\mathcal{R}} \frac{\mathrm{e}^{\mathrm{i}\varpi|x-x_0|}}{\varpi^2+k_\rho^2}\mathrm{d}\varpi + \int_{C_\mathcal{R}} \frac{\mathrm{e}^{\mathrm{i}\varpi|x-x_0|}}{\varpi^2+k_\rho^2}\mathrm{d}\varpi, \tag{3.4.15}$$

where ϖ is the complex variable, $C_\mathcal{R}$ is a half-circle arc located on the upper half of the complex plane whose centre point is located at the origin, and $\mathcal{R}$ is

the radius of $C_{\mathcal{R}}$, as sketched in Fig.3.4. When $|\varpi| \to \infty$,

$$f(\varpi) = \frac{1}{\varpi^2 + k_\rho^2} \to 0$$

uniformly. Then, according to Jordan's Lemma [Bronshtein *et al.* (2007)],

$$\lim_{\mathcal{R} \to \infty} \int_{C_{\mathcal{R}}} \frac{\mathrm{e}^{\mathrm{i}\varpi|x-x_0|}}{\varpi^2 + k_\rho^2} \mathrm{d}\varpi = 0. \tag{3.4.16}$$

Thereby,

$$\int_{-\infty}^{+\infty} \frac{\mathrm{e}^{\mathrm{i}\varpi|x-x_0|}}{\varpi^2 + k_\rho^2} \mathrm{d}\varpi = \oint \frac{\mathrm{e}^{\mathrm{i}\varpi|x-x_0|}}{\varpi^2 + k_\rho^2} \mathrm{d}\varpi. \tag{3.4.17}$$

Applying Residue Theorem [Bronshtein *et al.* (2007)] to the integral on the right-hand side of Eq.(3.4.17), we have

$$\begin{aligned} \oint \frac{\mathrm{e}^{\mathrm{i}\varpi|x-x_0|}}{\varpi^2 + k_\rho^2} \mathrm{d}\varpi &= 2\pi\mathrm{i} \cdot \lim_{\varpi \to k_\rho \mathrm{i}} \left[(\varpi - k_\rho \mathrm{i}) \frac{\mathrm{e}^{\mathrm{i}\varpi|x-x_0|}}{\varpi^2 + k_\rho^2} \right] \\ &= \frac{\pi}{k_\rho} \mathrm{e}^{-k_\rho|x-x_0|}. \end{aligned} \tag{3.4.18}$$

Substituting Eq.(3.4.17) into Eq.(3.4.18), and introducing the result into Eq.(3.4.14), we obtain

$$\int_{-\infty}^{+\infty} \frac{\mathrm{e}^{\mathrm{i}v_1(x-x_0)}}{v_1^2 + k_\rho^2} dv_1 = \frac{\pi}{k_\rho} \mathrm{e}^{-k_\rho|x-x_0|}, \tag{3.4.19}$$

which indicates

$$\int_{-\infty}^{+\infty} G_f(v_1) \mathrm{e}^{\mathrm{i}v_1 x} \mathrm{d}v_1 = \frac{\pi}{k_\rho} \mathrm{e}^{-k_\rho|x-x_0|}. \tag{3.4.20}$$

When Eq.(3.4.20) is substituted into Eq.(3.4.11), we have

$$G(\mathbf{x},\mathbf{x}_0) = -\frac{1}{8\pi^2}\int_{-\infty}^{+\infty}\int_{-\infty}^{+\infty}\frac{\mathrm{e}^{-k_\rho|x-x_0|}}{k_\rho}\mathrm{e}^{[\mathrm{i}v_2(y-y_0)+\mathrm{i}v_3(z-z_0)]}\mathrm{d}v_2\mathrm{d}v_3. \tag{3.4.21}$$

In terms of Eq.(3.4.12), we can define

$$\begin{cases} v_2 = k_\rho\cos\theta, \\ v_3 = k_\rho\sin\theta. \end{cases} \tag{3.4.22}$$

Substituting Eq.(3.4.22) into Eq.(3.4.21), we successfully obtain the integral representative of the Green's function as

$$G(\mathbf{x},\mathbf{x}_0) = -\frac{1}{8\pi^2}\int_{0}^{+\infty}\int_{0}^{2\pi}\mathrm{e}^{-k_\rho|x-x_0|}\mathrm{e}^{\mathrm{i}k_\rho[\cos\theta(y-y_0)+\sin\theta(z-z_0)]}\mathrm{d}k_\rho\mathrm{d}\theta. \tag{3.4.23}$$

Chapter 4

Governing Equations for the flow through Vessels and in Tumour Interstitium

Fig.4.1 sketches a simple case when a single vessel with some curvature is embedded in a solid tumour, in which κ is the hydraulic conductivity parameter of tumour tissue, A stands for the connecting point of the vessel with the afferent arteriole (upstream blood flow), and V for the connecting point of the vessel with the efferent venule (downstream blood flow), as tumour vasculature does not begin or end suddenly in tumour interstitium. Along the vessel, the radius of vessel cross section is defined as $a(l)$, $L_p(l)$ donates the vessel permeability, and $q_e(l)$ is the extravasation flux over the unit length along the circumference of vessel cross section, where l is the length measured along the vessel centre line from some given reference point.

In this chapter, based on the case illustrated in Fig.4.1, we derive the governing equations for the blood flow through tumour vessels, the flow in tumour interstitium, and the coupling effects between those two flows caused

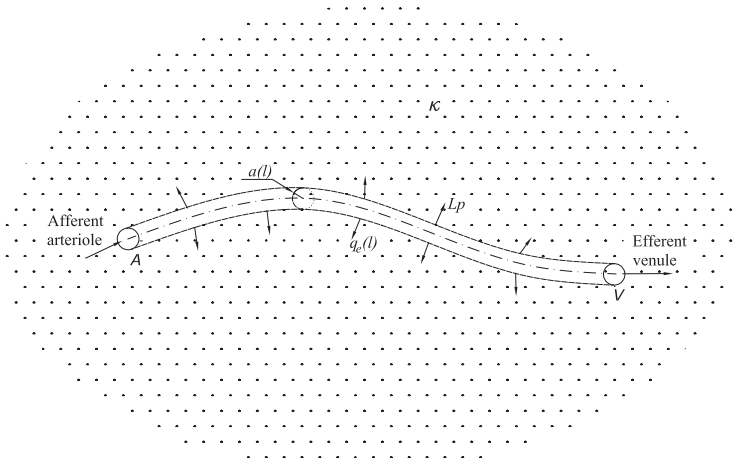

Figure 4.1: Sketch of a permeable vessel embedded in tumour interstitium.

by the permeability of tumour vessels. We start with the mathematical method to describe the position and shape of a tumour vessel. Then, according to flow continuity and momentum conservation, the governing equations for the blood flow through the vessel are derived. After that, the equation for the flow field in tumour interior and the relationship for the flux exceeded from tumour vessels into interstitium are given. In the meantime, the detailed procedure is presented on how to obtain the boundary-integral equation for tumour interstitial flow and calculate the key coefficients in that boundary-integral equation.

4.1 The parametric equation for vessel position

In order to describe the complicated configuration of tumour vasculature mathematically, each vessel within tumour vascular network is assumed to have circular cross section. As the length scale in the transverse direction of a tumour

vessel is usually much smaller than that in the longitudinal direction, the position and shape of a tumour vessel can be defined through the vessel centre line. One mathematical method to express the three-dimensional centre line of a tumour vessel is to use the parametric equation, for example

$$l : \{x(s), y(s), z(s)\}, \tag{4.1.1}$$

in which s is the parameter. For line l, the arc length starting from some reference point $l_o\,\{x(s_o), y(s_o), z(s_o)\}$ is

$$\int_{l_o} \mathrm{d}l = \int_{s_o} \sqrt{[x']^2 + [y']^2 + [z']^2}\ \mathrm{d}s, \tag{4.1.2}$$

in which

$$x' = \frac{\mathrm{d}x(s)}{\mathrm{d}s}, \qquad y' = \frac{\mathrm{d}y(s)}{\mathrm{d}s}, \qquad z' = \frac{\mathrm{d}z(s)}{\mathrm{d}s}. \tag{4.1.3}$$

Considering a certain differential function f defined based on space line $l(s)$, we have the following relationships:

$$\frac{\mathrm{d}f(l)}{\mathrm{d}l} = H_b(s)\frac{\mathrm{d}f(s)}{\mathrm{d}s}, \tag{4.1.4}$$

and

$$\frac{\mathrm{d}^2 f(l)}{\mathrm{d}l^2} = H_b(s)H_b(s)\frac{\mathrm{d}^2 f(s)}{\mathrm{d}s^2} + H_b(s)H_c(s)\frac{\mathrm{d}f(s)}{\mathrm{d}s}. \tag{4.1.5}$$

In the above two equations,

$$H_b(s) = \frac{1}{\sqrt{[x']^2 + [y']^2 + [z']^2}}, \tag{4.1.6}$$

and

$$H_c(s) = \frac{\mathrm{d}H_b}{\mathrm{d}s} = -\frac{x'x'' + y'y'' + z'z''}{\left\{[x']^2 + [y']^2 + [z']^2\right\}^{\frac{3}{2}}}, \tag{4.1.7}$$

where x', y', z' are defined in Eq.(4.1.3), and

$$x'' = \frac{\mathrm{d}x'}{\mathrm{d}s}, \qquad y'' = \frac{\mathrm{d}y'}{\mathrm{d}s}, \qquad z'' = \frac{\mathrm{d}z'}{\mathrm{d}s}. \tag{4.1.8}$$

The introduction of Eqs.(4.1.1) to (4.1.8) is essential when tumour vessels are not straight. They will significantly affect the development of the governing equations and solution procedure described below and in the following chapters.

4.2 Flow through tumour vasculature

The blood flow through vascular system is determined by the resulting actions of heart pulsating pumping together with vascular resistances. Whether the unsteady forces (pumping effects) are needed to be considered is determined by a non-dimensional parameter — the Womersley parameter [Ku (1997)]. This parameter, which represents the ratio of the unsteady forces over the viscous forces applied on the blood motion, is defined as

$$N_w = a\sqrt{\frac{\omega\rho}{\mu}}, \tag{4.2.1}$$

where ρ is the blood density, μ is the dynamic viscosity of blood, and ω is the frequency of heart pumping [Womersley (1955)]. When N_w is low, the viscous forces dominate the blood flow through a vessel, and the velocity value in that vessel is in direct proportion to pressure gradient along its centre line [Nichols and O'Rourke (2005), Womersley (1955)]. On the other hand, if the

Womersley parameter is larger than 10, the unsteady forces have to be involved. For the blood flow through a tumour vessel, whose diameter is between 10μm to 200μm under usual physical and physiological conditions in a solid tumour [Less *et al.* (1991)], the value of the Womersley parameter is quite small (less than 10) [Schmid-Schönbein (1999)]. Consequently, the pumping effects on the blood motion through tumour vasculature can be ignored. When blood is taken as incompressible Newtonian fluid, the vector form of continuity equation for the flow through a tumour vessel is

$$\mathrm{div}\mathbf{U} = 0, \tag{4.2.2}$$

and the momentum equation is

$$(\mathbf{U}\cdot\nabla)\mathbf{U} = -\frac{1}{\rho}\nabla p + \frac{\mu}{\rho}\nabla^2\mathbf{U}, \tag{4.2.3}$$

in which p is the flow pressure in the vessel, and $\mathbf{U}$ is the vascular flow velocity. The above two equations are independent on reference frames, but would have different scalar forms when different coordinate systems are chosen. For example, in Cartesian coordinate system $o-xyz$, Eqs.(4.2.2) and (4.2.3) can be expanded in the scalar forms of

$$\frac{\partial U_x}{\partial x} + \frac{\partial U_y}{\partial y} + \frac{\partial U_z}{\partial z} = 0, \tag{4.2.4}$$

and

$$\begin{cases} U_x\dfrac{\partial U_x}{\partial x} + U_y\dfrac{\partial U_x}{\partial y} + U_z\dfrac{\partial U_x}{\partial z} = -\dfrac{1}{\rho}\dfrac{\partial p}{\partial x} + \dfrac{\mu}{\rho}\left(\dfrac{\partial^2 U_x}{\partial x^2} + \dfrac{\partial^2 U_x}{\partial y^2} + \dfrac{\partial^2 U_x}{\partial z^2}\right), \\ U_x\dfrac{\partial U_y}{\partial x} + U_y\dfrac{\partial U_y}{\partial y} + U_z\dfrac{\partial U_y}{\partial z} = -\dfrac{1}{\rho}\dfrac{\partial p}{\partial y} + \dfrac{\mu}{\rho}\left(\dfrac{\partial^2 U_y}{\partial x^2} + \dfrac{\partial^2 U_y}{\partial y^2} + \dfrac{\partial^2 U_y}{\partial z^2}\right), \\ U_x\dfrac{\partial U_z}{\partial x} + U_y\dfrac{\partial U_z}{\partial y} + U_z\dfrac{\partial U_z}{\partial z} = -\dfrac{1}{\rho}\dfrac{\partial p}{\partial z} + \dfrac{\mu}{\rho}\left(\dfrac{\partial^2 U_z}{\partial x^2} + \dfrac{\partial^2 U_z}{\partial y^2} + \dfrac{\partial^2 U_z}{\partial z^2}\right), \end{cases} \tag{4.2.5}$$

respectively, where U_x, U_y, and U_z are the components of $\mathbf{U}$ in system $o-xyz$.

In many circumstances, in order to study the flow features conveniently, it is necessary for us to choose some orthogonal curvilinear coordinate (q_1, q_2, q_3) other than the regular Cartesian coordinate system (x, y, z). To convert the continuity and momentum equations from Cartesian coordinate system $o - xyz$ to orthogonal curvilinear coordinate system (q_1, q_2, q_3), we assume that coordinates x, y and z are related to quantities q_1, q_2 and q_3, as

$$x = x(q_1, q_2, q_3), \qquad y = y(q_1, q_2, q_3), \qquad z = z(q_1, q_2, q_3), \tag{4.2.6}$$

and the direct transformation functions in Eq.(4.2.6) are smooth functions. As a result, Jacobian determinant

$$\frac{\partial(q_1, q_2, q_3)}{\partial(x, y, z)} = \begin{vmatrix} \dfrac{\partial q_1}{\partial x} & \dfrac{\partial q_2}{\partial x} & \dfrac{\partial q_3}{\partial x} \\ \dfrac{\partial q_1}{\partial y} & \dfrac{\partial q_2}{\partial y} & \dfrac{\partial q_3}{\partial y} \\ \dfrac{\partial q_1}{\partial z} & \dfrac{\partial q_2}{\partial z} & \dfrac{\partial q_3}{\partial z} \end{vmatrix} \neq 0. \tag{4.2.7}$$

This means that the transformation in Eq.(4.2.6) is invertible according to the inverse function theorem, which gives

$$q_1 = q_1(x, y, z), \qquad q_2 = q_2(x, y, z), \qquad q_3 = q_3(x, y, z). \tag{4.2.8}$$

The condition that the Jacobian determinant is not zero reflects the fact that three surfaces from two different families of coordinate systems intersect in one and only one point, and thus determine the position of this point in a unique way [McConnell (1957)].

Then, three coefficients are defined as

$$\begin{cases} \mathcal{J}_1 = \sqrt{(\partial x/\partial q_1)^2 + (\partial y/\partial q_1)^2 + (\partial z/\partial q_1)^2}, \\ \mathcal{J}_2 = \sqrt{(\partial x/\partial q_2)^2 + (\partial y/\partial q_2)^2 + (\partial z/\partial q_2)^2}, \\ \mathcal{J}_3 = \sqrt{(\partial x/\partial q_3)^2 + (\partial y/\partial q_3)^2 + (\partial z/\partial q_3)^2}. \end{cases} \tag{4.2.9}$$

Based on the theory of curvilinear coordinates derived by Lamé [Wu (2004)], for pressure p in system (q_1, q_2, q_3), we have

$$\nabla p = \frac{1}{\mathcal{J}_1}\frac{\partial p}{\partial q_1}\mathbf{e}_1 + \frac{1}{\mathcal{J}_2}\frac{\partial p}{\partial q_2}\mathbf{e}_2 + \frac{1}{\mathcal{J}_3}\frac{\partial p}{\partial q_3}\mathbf{e}_3, \tag{4.2.10}$$

where $\mathbf{e}_1$, $\mathbf{e}_2$ and $\mathbf{e}_3$ stand for the unit vector of axes q_1, q_2 and q_3 respectively. For velocity vector $\mathbf{U}$ in system (q_1, q_2, q_3), we get

$$\mathrm{div}\mathbf{U} = \frac{1}{\mathcal{J}_1\mathcal{J}_2\mathcal{J}_3}\left[\frac{\partial(U_1\mathcal{J}_2\mathcal{J}_3)}{\partial q_1} + \frac{\partial(U_2\mathcal{J}_3\mathcal{J}_1)}{\partial q_2} + \frac{\partial(U_3\mathcal{J}_1\mathcal{J}_2)}{\partial q_3}\right], \tag{4.2.11}$$

$$\begin{aligned} &(\mathbf{U}\cdot\nabla)\mathbf{U} \\ = \quad &\mathbf{e}_1\left[\frac{U_1}{\mathcal{J}_1}\frac{\partial U_1}{\partial q_1} + \frac{U_2}{\mathcal{J}_2}\frac{\partial U_1}{\partial q_2} + \frac{U_3}{\mathcal{J}_3}\frac{\partial U_1}{\partial q_3} + \frac{U_2}{\mathcal{J}_1\mathcal{J}_2}\left(U_1\frac{\partial \mathcal{J}_1}{\partial q_2} - U_2\frac{\partial \mathcal{J}_2}{\partial q_1}\right)\right. \\ &\left. + \frac{U_3}{\mathcal{J}_1\mathcal{J}_3}\left(U_1\frac{\partial \mathcal{J}_1}{\partial q_3} - U_3\frac{\partial \mathcal{J}_3}{\partial q_1}\right)\right] \\ &+\mathbf{e}_2\left[\frac{U_1}{\mathcal{J}_1}\frac{\partial U_2}{\partial q_1} + \frac{U_2}{\mathcal{J}_2}\frac{\partial U_2}{\partial q_2} + \frac{U_3}{\mathcal{J}_3}\frac{\partial U_2}{\partial q_3} + \frac{U_3}{\mathcal{J}_2\mathcal{J}_3}\left(U_2\frac{\partial \mathcal{J}_2}{\partial q_3} - U_3\frac{\partial \mathcal{J}_3}{\partial q_2}\right)\right. \\ &\left. + \frac{U_1}{\mathcal{J}_1\mathcal{J}_2}\left(U_2\frac{\partial \mathcal{J}_2}{\partial q_1} - U_1\frac{\partial \mathcal{J}_1}{\partial q_2}\right)\right] \\ &+\mathbf{e}_3\left[\frac{U_1}{\mathcal{J}_1}\frac{\partial U_3}{\partial q_1} + \frac{U_2}{\mathcal{J}_2}\frac{\partial U_3}{\partial q_2} + \frac{U_3}{\mathcal{J}_3}\frac{\partial U_3}{\partial q_3} + \frac{U_1}{\mathcal{J}_1\mathcal{J}_3}\left(U_3\frac{\partial \mathcal{J}_3}{\partial q_1} - U_1\frac{\partial \mathcal{J}_1}{\partial q_3}\right)\right. \\ &\left. + \frac{U_2}{\mathcal{J}_2\mathcal{J}_3}\left(U_3\frac{\partial \mathcal{J}_3}{\partial q_2} - U_2\frac{\partial \mathcal{J}_2}{\partial q_3}\right)\right], \end{aligned} \tag{4.2.12}$$

and

$$
\begin{aligned}
&\nabla^2\mathbf{U} \\
= \;& \mathbf{e}_1\Bigg\{\frac{1}{\mathcal{J}_1}\frac{\partial}{\partial q_1}\Bigg\{\frac{1}{\mathcal{J}_1\mathcal{J}_2\mathcal{J}_3}\left[\frac{\partial(\mathcal{J}_2\mathcal{J}_3U_1)}{\partial q_1}+\frac{\partial(\mathcal{J}_3\mathcal{J}_1U_2)}{\partial q_2}+\frac{\partial(\mathcal{J}_1\mathcal{J}_2U_3)}{\partial q_3}\right]\Bigg\} \\
&\quad -\frac{1}{\mathcal{J}_2\mathcal{J}_3}\frac{\partial}{\partial q_2}\Bigg\{\frac{\mathcal{J}_3}{\mathcal{J}_1\mathcal{J}_2}\left[\frac{\partial(\mathcal{J}_2U_2)}{\partial q_1}-\frac{\partial(\mathcal{J}_1U_1)}{\partial q_2}\right]\Bigg\} \\
&\quad +\frac{1}{\mathcal{J}_2\mathcal{J}_3}\frac{\partial}{\partial q_3}\Bigg\{\frac{\mathcal{J}_2}{\mathcal{J}_3\mathcal{J}_1}\left[\frac{\partial(\mathcal{J}_1U_1)}{\partial q_3}-\frac{\partial(\mathcal{J}_3U_3)}{\partial q_1}\right]\Bigg\}\Bigg\} \\
&+\mathbf{e}_2\Bigg\{\frac{1}{\mathcal{J}_2}\frac{\partial}{\partial q_2}\Bigg\{\frac{1}{\mathcal{J}_1\mathcal{J}_2\mathcal{J}_3}\left[\frac{\partial(\mathcal{J}_2\mathcal{J}_3U_1)}{\partial q_1}+\frac{\partial(\mathcal{J}_3\mathcal{J}_1U_2)}{\partial q_2}+\frac{\partial(\mathcal{J}_1\mathcal{J}_2U_3)}{\partial q_3}\right]\Bigg\} \\
&\quad -\frac{1}{\mathcal{J}_3\mathcal{J}_1}\frac{\partial}{\partial q_3}\Bigg\{\frac{\mathcal{J}_1}{\mathcal{J}_2\mathcal{J}_3}\left[\frac{\partial(\mathcal{J}_3U_3)}{\partial q_2}-\frac{\partial(\mathcal{J}_2U_2)}{\partial q_3}\right]\Bigg\} \\
&\quad +\frac{1}{\mathcal{J}_3\mathcal{J}_1}\frac{\partial}{\partial q_1}\Bigg\{\frac{\mathcal{J}_3}{\mathcal{J}_1\mathcal{J}_2}\left[\frac{\partial(\mathcal{J}_2U_2)}{\partial q_1}-\frac{\partial(\mathcal{J}_1U_1)}{\partial q_2}\right]\Bigg\}\Bigg\} \\
&+\mathbf{e}_3\Bigg\{\frac{1}{\mathcal{J}_3}\frac{\partial}{\partial q_3}\Bigg\{\frac{1}{\mathcal{J}_1\mathcal{J}_2\mathcal{J}_3}\left[\frac{\partial(\mathcal{J}_2\mathcal{J}_3U_1)}{\partial q_1}+\frac{\partial(\mathcal{J}_3\mathcal{J}_1U_2)}{\partial q_2}+\frac{\partial(\mathcal{J}_1\mathcal{J}_2U_3)}{\partial q_3}\right]\Bigg\} \\
&\quad -\frac{1}{\mathcal{J}_1\mathcal{J}_2}\frac{\partial}{\partial q_1}\Bigg\{\frac{\mathcal{J}_2}{\mathcal{J}_3\mathcal{J}_1}\left[\frac{\partial(\mathcal{J}_1U_1)}{\partial q_3}-\frac{\partial(\mathcal{J}_3U_3)}{\partial q_1}\right]\Bigg\} \\
&\quad +\frac{1}{\mathcal{J}_1\mathcal{J}_2}\frac{\partial}{\partial q_2}\Bigg\{\frac{\mathcal{J}_1}{\mathcal{J}_2\mathcal{J}_3}\left[\frac{\partial(\mathcal{J}_3U_3)}{\partial q_2}-\frac{\partial(\mathcal{J}_2U_2)}{\partial q_3}\right]\Bigg\}\Bigg\}. \qquad (4.2.13)
\end{aligned}
$$

Since div$\mathbf{U} = 0$, Eq.(4.2.13) is reduced to

$$
\begin{aligned}
&\nabla^2\mathbf{U} \\
= \ & \mathbf{e}_1\Bigg\{ -\frac{1}{\mathcal{J}_2\mathcal{J}_3}\frac{\partial}{\partial q_2}\Bigg\{\frac{\mathcal{J}_3}{\mathcal{J}_1\mathcal{J}_2}\left[\frac{\partial(\mathcal{J}_2U_2)}{\partial q_1}-\frac{\partial(\mathcal{J}_1U_1)}{\partial q_2}\right]\Bigg\} \\
&\quad +\frac{1}{\mathcal{J}_2\mathcal{J}_3}\frac{\partial}{\partial q_3}\Bigg\{\frac{\mathcal{J}_2}{\mathcal{J}_3\mathcal{J}_1}\left[\frac{\partial(\mathcal{J}_1U_1)}{\partial q_3}-\frac{\partial(\mathcal{J}_3U_3)}{\partial q_1}\right]\Bigg\}\Bigg\} \\
&+\mathbf{e}_2\Bigg\{ -\frac{1}{\mathcal{J}_3\mathcal{J}_1}\frac{\partial}{\partial q_3}\Bigg\{\frac{\mathcal{J}_1}{\mathcal{J}_2\mathcal{J}_3}\left[\frac{\partial(\mathcal{J}_3U_3)}{\partial q_2}-\frac{\partial(\mathcal{J}_2U_2)}{\partial q_3}\right]\Bigg\} \\
&\quad +\frac{1}{\mathcal{J}_3\mathcal{J}_1}\frac{\partial}{\partial q_1}\Bigg\{\frac{\mathcal{J}_3}{\mathcal{J}_1\mathcal{J}_2}\left[\frac{\partial(\mathcal{J}_2U_2)}{\partial q_1}-\frac{\partial(\mathcal{J}_1U_1)}{\partial q_2}\right]\Bigg\}\Bigg\} \\
&+\mathbf{e}_3\Bigg\{ -\frac{1}{\mathcal{J}_1\mathcal{J}_2}\frac{\partial}{\partial q_1}\Bigg\{\frac{\mathcal{J}_2}{\mathcal{J}_3\mathcal{J}_1}\left[\frac{\partial(\mathcal{J}_1U_1)}{\partial q_3}-\frac{\partial(\mathcal{J}_3U_3)}{\partial q_1}\right]\Bigg\} \\
&\quad +\frac{1}{\mathcal{J}_1\mathcal{J}_2}\frac{\partial}{\partial q_2}\Bigg\{\frac{\mathcal{J}_1}{\mathcal{J}_2\mathcal{J}_3}\left[\frac{\partial(\mathcal{J}_3U_3)}{\partial q_2}-\frac{\partial(\mathcal{J}_2U_2)}{\partial q_3}\right]\Bigg\}\Bigg\}. \qquad (4.2.14)
\end{aligned}
$$

In Eqs.(4.2.11) to (4.2.14), U_1, U_2 and U_3 stand for the components of velocity $\mathbf{U}$ in reference frame (q_1, q_2, q_3). Substituting Eq.(4.2.11) into Eq.(4.2.2), and Eqs.(4.2.10), (4.2.12) and (4.2.14) into Eq.(4.2.3), we obtain the flow continuity and momentum equations in orthogonal curvilinear coordinate system (q_1, q_2, q_3) successfully.

As the vascular cross section is assumed to be circular, for the blood flow through a tumour vessel, the Reynolds number is defined as

$$Re = \frac{\rho a U_0}{\mu}, \qquad (4.2.15)$$

where U_0 is the peak velocity through vascular cross section. Under usual physical and physiological conditions in a solid tumour, the Reynolds number for the vascular flow is low [Sevick and Jain (1989a,b)]. Meanwhile, noticing

that the Womersley parameter is small [Schmid-Schönbein (1999)], and considering that the length scale in the transverse direction of a tumour vessel is much smaller than that in the longitudinal direction, one can conclude that the flow through a tumour vessel is laminar, and dominated by the pressure gradient along the vessel centre line.

To investigate the blood flow characters along the vessel centre line, we define a local cylindrical coordinate system (s, r, θ) on the cross section located at l, where l is the length measured along the vessel centre line from some given reference point l_0, as illustrated in Fig.4.2. In system (s, r, θ), unit axis vector $\mathbf{e}_s$ is along the tangential direction of the vessel centre line at l, unit axis vector $\mathbf{e}_r$ is along any radial direction on the cross section plane, and unit axis vector $\mathbf{e}_\theta$ is perpendicular to $\mathbf{e}_r$ on the cross section plane. Meanwhile, in order to get the relationship between the local coordinate system (s, r, θ) and the global Cartesian coordinate system $o - xyz$, we set up another local Cartesian coordinate system $\tilde{o} - \tilde{x}\tilde{y}\tilde{z}$ on the same cross section. For system $\tilde{o} - \tilde{x}\tilde{y}\tilde{z}$, origin $\tilde{o}$ is located at centre point C of the cross section corresponding to l, unit axis vector $\tilde{\mathbf{i}}$ is identical to $\mathbf{e}_s$, unit axis vector $\tilde{\mathbf{j}}$ is along one given radial direction on the cross section plane, and unit axis vector $\tilde{\mathbf{k}} = \tilde{\mathbf{i}} \times \tilde{\mathbf{j}}$ is along another radial direction on the cross section plane. Therefore, in local coordinate systems $\tilde{o} - \tilde{x}\tilde{y}\tilde{z}$ and (s, r, θ), for some point P on the cross section plane at l, we have

$$\mathbf{x}_P(\tilde{x}, \tilde{y}, \tilde{z}) = \mathbf{x}_P(0, r\cos\theta, r\sin\theta) \tag{4.2.16}$$

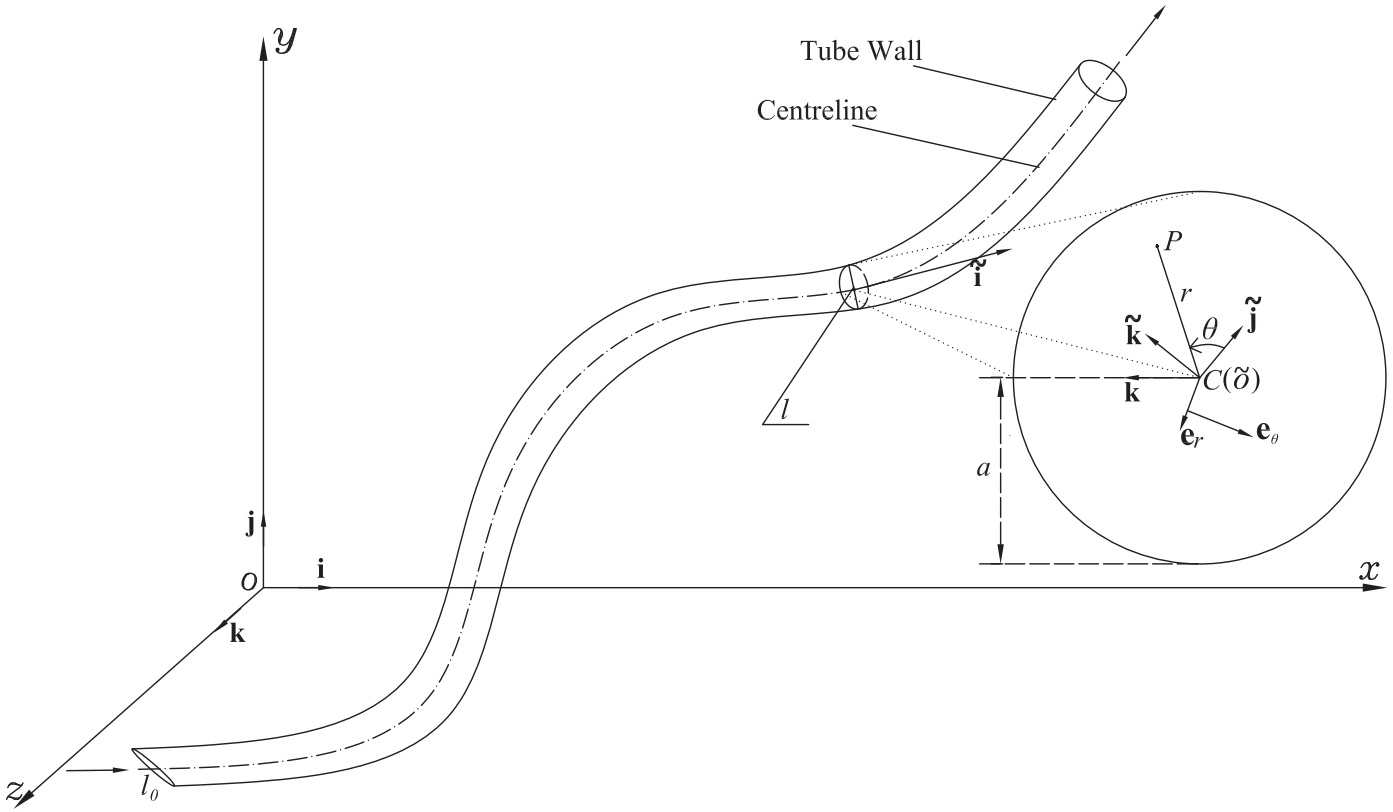

Figure 4.2: Sketch of a vessel with some curvature.

Supposing that the vessel centre line is defined by the parametric equation in Eq.(4.1.1), we have

$$\begin{aligned}\mathbf{e}_s = \tilde{\mathbf{i}} = &\frac{x'}{\sqrt{(x')^2+(y')^2+(z')^2}}\mathbf{i} \\ &+ \frac{y'}{\sqrt{(y')^2+(y')^2+(z')^2}}\mathbf{j} \\ &+ \frac{z'}{\sqrt{(x')^2+(y')^2+(z')^2}}\mathbf{k},\end{aligned} \tag{4.2.17}$$

where x', y' and z' are defined in Eq.(4.1.3). Since $\tilde{\mathbf{j}}$ is the unit vector along a given radius direction on the cross section plane corresponding to l, $\tilde{\mathbf{i}} \cdot \tilde{\mathbf{j}} = 0$. Therefore, it is easy for us to choose

$$\begin{aligned}\tilde{\mathbf{j}} = &\frac{y'+z'}{\sqrt{(y'+z')^2+2(x')^2}}\mathbf{i} \\ &- \frac{x'}{\sqrt{(y'+z')^2+2(x')^2}}\mathbf{j} \\ &- \frac{x'}{\sqrt{(y'+z')^2+2(x')^2}}\mathbf{k},\end{aligned} \tag{4.2.18}$$

As $\tilde{\mathbf{k}} = \tilde{\mathbf{i}} \times \tilde{\mathbf{j}}$, we have

$$\begin{aligned}\tilde{\mathbf{k}} = &\frac{x'z' - x'y'}{\sqrt{(x')^2(z'-y')^2+[(x')^2+z'(y'+z')]^2+[(x')^2+y'(y'+z')]^2}}\mathbf{i} \\ &+ \frac{(x')^2+z'(y'+z')}{\sqrt{(x')^2(z'-y')^2+[(x')^2+z'(y'+z')]^2+[(x')^2+y'(y'+z')]^2}}\mathbf{j} \\ &- \frac{(x')^2+y'(y'+z')}{\sqrt{(x')^2(z'-y')^2+[(x')^2+z'(y'+z')]^2+[(x')^2+y'(y'+z')]^2}}\mathbf{k},\end{aligned} \tag{4.2.19}$$

According to the forms of Eqs.(4.2.17) to (4.2.19), it is convenient for us to

write

$$\tilde{\mathbf{i}} = ll_1\mathbf{i} + mm_1\mathbf{j} + nn_1\mathbf{k}; \quad \tilde{\mathbf{j}} = ll_2\mathbf{i} + mm_2\mathbf{j} + nn_2\mathbf{k}; \quad \tilde{\mathbf{k}} = ll_3\mathbf{i} + mm_3\mathbf{j} + nn_3\mathbf{k}. \tag{4.2.20}$$

In the above equation, ll_1, mm_1, nn_1, ll_2, mm_2, nn_2, ll_3, mm_3 and nn_3 are the corresponding terms in Eqs.(4.2.17) to (4.2.19).

For a point $P(\tilde{x}_{_P}, \tilde{y}_{_P}, \tilde{z}_{_P})$ in system $\tilde{o}-\tilde{x}\tilde{y}\tilde{z}$, according to the relationships of transformation and rotation between two different families of coordinate systems, its coordinates in system $o - xyz$ are

$$\begin{cases} x_{_P} = x(s) + ll_1 \cdot \tilde{x}_{_P} + ll_2 \cdot \tilde{y}_{_P} + ll_3 \cdot \tilde{z}_{_P}, \\ y_{_P} = y(s) + mm_1 \cdot \tilde{x}_{_P} + mm_2 \cdot \tilde{y}_{_P} + mm_3 \cdot \tilde{z}_{_P}, \\ z_{_P} = z(s) + nn_1 \cdot \tilde{x}_{_P} + nn_2 \cdot \tilde{y}_{_P} + nn_3 \cdot \tilde{z}_{_P}. \end{cases} \tag{4.2.21}$$

Introducing Eq.(4.2.16) into Eq.(4.2.21), we have

$$\begin{cases} x_{_P} = x(s) + \dfrac{(y'+z')r\cos\theta}{\sqrt{(y'+z')^2+2(x')^2}} \\ \qquad + \dfrac{(x'z'-x'y')r\sin\theta}{\sqrt{(x')^2(z'-y')^2+[(x')^2+z'(y'+z')]^2+[(x')^2+y'(y'+z')]^2}}, \\ y_{_P} = y(s) - \dfrac{x'r\cos\theta}{\sqrt{(y'+z')^2+2(x')^2}} \\ \qquad + \dfrac{[(x')^2+z'(y'+z')]r\sin\theta}{\sqrt{(x')^2(z'-y')^2+[(x')^2+z'(y'+z')]^2+[(x')^2+y'(y'+z')]^2}}, \\ z_{_P} = z(s) - \dfrac{x'r\cos\theta}{\sqrt{(y'+z')^2+2(x')^2}} \\ \qquad - \dfrac{[(x')^2+y'(y'+z')]r\sin\theta}{\sqrt{(x')^2(z'-y')^2+[(x')^2+z'(y'+z')]^2+[(x')^2+y'(y'+z')]^2}}. \end{cases} \tag{4.2.22}$$

Substituting Eq.(4.2.22) into Eq.(4.2.9), we obtain

$$\begin{cases} \mathcal{J}_r = \mathcal{J}_1 = 1, \\ \mathcal{J}_\theta = \mathcal{J}_2 = r, \\ \mathcal{J}_s = \mathcal{J}_3 = \sqrt{\left(\dfrac{\partial x_p}{\partial s}\right)^2 + \left(\dfrac{\partial y_p}{\partial s}\right)^2 + \left(\dfrac{\partial z_p}{\partial s}\right)^2}. \end{cases} \tag{4.2.23}$$

Introducing Eq.(4.2.23) into Eqs.(4.2.10), (4.2.11), (4.2.12) and (4.2.14), and rearranging the results according to Eqs.(4.2.2) and (4.2.3), we obtain, for the blood flow through a three-dimensional curved tumour vessel, the continuity equation as

$$\frac{\partial U_r}{\partial r} + \frac{1}{r}U_r + \frac{U_r}{\mathcal{J}_s}\frac{\partial \mathcal{J}_s}{\partial r} + \frac{1}{r}\frac{\partial U_\theta}{\partial \theta} + \frac{U_\theta}{r\mathcal{J}_s}\frac{\partial \mathcal{J}_s}{\partial \theta} + \frac{1}{\mathcal{J}_s}\frac{\partial U_s}{\partial s} = 0, \tag{4.2.24}$$

and the momentum equations as

$\mathbf{e}_r$:

$$\begin{aligned} &U_r\frac{\partial U_r}{\partial r} + \frac{U_\theta}{r}\frac{\partial U_r}{\partial \theta} + \frac{U_s}{\mathcal{J}_s}\frac{\partial U_r}{\partial s} - \frac{U_\theta^2}{r} - \frac{U_s^2}{\mathcal{J}_s}\frac{\partial \mathcal{J}_s}{\partial r} \\ =& -\frac{1}{\rho}\frac{\partial p_c}{\partial r} - \frac{\mu}{\rho}\left[\frac{1}{r\mathcal{J}_s}\frac{\partial}{\partial \theta}\left(\frac{\mathcal{J}_s U_\theta}{r} + \mathcal{J}_s\frac{\partial U_\theta}{\partial r} - \frac{\mathcal{J}_s}{r}\frac{\partial U_r}{\partial \theta}\right)\right. \\ &\left. -\frac{1}{\mathcal{J}_s}\frac{\partial}{\partial s}\left(\frac{1}{\mathcal{J}_s}\frac{\partial U_r}{\partial s} - \frac{\partial U_s}{\partial r} - \frac{U_s}{\mathcal{J}_s}\frac{\partial \mathcal{J}_s}{\partial r}\right)\right]; \end{aligned} \tag{4.2.25}$$

$\mathbf{e}_\theta$:

$$\begin{aligned} &U_r\frac{\partial U_\theta}{\partial r} + \frac{U_\theta}{r}\frac{\partial U_\theta}{\partial \theta} + \frac{U_s}{\mathcal{J}_s}\frac{\partial U_\theta}{\partial s} - \frac{U_s^2}{\mathcal{J}_s}\frac{\partial \mathcal{J}_s}{\partial \theta} + \frac{U_r U_\theta}{r} \\ =& -\frac{1}{r\rho}\frac{\partial p_c}{\partial \theta} - \frac{\mu}{\rho\mathcal{J}_s}\left[\frac{\partial}{\partial s}\left(\frac{U_s}{r\mathcal{J}_s}\frac{\partial \mathcal{J}_s}{\partial \theta} + \frac{1}{r}\frac{\partial U_s}{\partial \theta} - \frac{1}{\mathcal{J}_s}\frac{\partial U_\theta}{\partial s}\right)\right. \\ &\left. -\frac{\partial}{\partial r}\left(\frac{U_\theta \mathcal{J}_s}{r} + \mathcal{J}_s\frac{\partial U_\theta}{\partial r} - \frac{\mathcal{J}_s}{r}\frac{\partial U_r}{\partial \theta}\right)\right]; \end{aligned} \tag{4.2.26}$$

and

$\mathbf{e}_s$:

$$
\begin{aligned}
&U_r\frac{\partial U_s}{\partial r}+\frac{U_\theta}{r}\frac{\partial U_s}{\partial \theta}+\frac{U_s}{\mathcal{J}_s}\frac{\partial U_s}{\partial s}+\frac{U_rU_s}{\mathcal{J}_s}\frac{\partial \mathcal{J}_s}{\partial r}+\frac{U_\theta U_s}{r\mathcal{J}_s}\frac{\partial \mathcal{J}_s}{\partial \theta}\\
=&-\frac{1}{\rho\mathcal{J}_s}\frac{\partial p_c}{\partial s}-\frac{\mu}{\rho r}\left[\frac{\partial}{\partial r}\left(\frac{r}{\mathcal{J}_s}\frac{\partial U_r}{\partial s}-r\frac{\partial U_s}{\partial r}-\frac{rU_s}{\mathcal{J}_s}\frac{\partial \mathcal{J}_s}{\partial r}\right)\right.\\
&\left.-\frac{\partial}{\partial \theta}\left(\frac{1}{r}\frac{\partial U_s}{\partial \theta}+\frac{U_s}{r\mathcal{J}_s}\frac{\partial \mathcal{J}_s}{\partial \theta}-\frac{1}{\mathcal{J}_s}\frac{\partial U_\theta}{\partial s}\right)\right].
\end{aligned}
\tag{4.2.27}
$$

Since the above Eqs.(4.2.24) to (4.2.27) are derived in system (s, r, θ), $\mathcal{J}_1$, $\mathcal{J}_2$, $\mathcal{J}_3$, U_1, U_2 and U_3 are replaced with $\mathcal{J}_r$, $\mathcal{J}_\theta$, $\mathcal{J}_s$, U_r, U_θ and U_s respectively.

Applying mathematical analysis on Eqs.(4.2.24) to (4.2.27) directly would be highly complex, but they can be simplified according to the explicit expression of the parametric equation for the vessel centre line and the assumptions of the microcirculation based on the physiological and physical characters of tumour blood flow, which will be presented in detail in the following chapters.

4.3 Flow in tumour interstitium

4.3.1 Flow in tumour space

Tumour interstitial space is composed of cancer cells and tumour extracellular matrix. From flow dynamics point of view, tumour interstitium can be regarded as porous media. In the meantime, though lymphatic vessels can be detected in tumour interior [Guillino (1975), Jain and Fenton (2002)], the lymphatic effects are excluded in our model, since lymphatic vessels in tumour are impaired and/or not functional [Helmlinger *et al.* (1997), Leu *et al.* (2000)] due to the over proliferation of cancer cells and tumour interstitial hypertension [Jain (1994)]. As a result, the blood flow within tumour interstitium can be

described by the Darcy's law, which indicates that the fluid velocity in tumour interstitium is proportional to the gradient of interstitial pressure, as

$$\mathbf{u} = -\kappa \nabla p_i, \tag{4.3.1}$$

where $\mathbf{u}$ is the flow velocity in tumour interstitium, κ is the hydraulic conductivity of tumour interstitium, and p_i is the interstitial blood pressure. Substituting Eq.(4.3.1) into flow continuity equation

$$\text{div}\mathbf{u} = 0, \tag{4.3.2}$$

and assuming that κ is constant in tumour interstitium, we find that tumour interstitial pressure satisfies the Laplace equation, or

$$\nabla^2 p_i(\mathbf{x}) = 0. \tag{4.3.3}$$

4.3.2 Extravascular flux through vessel walls

Through observing the flow absorbed from the connective tissues by blood vessels, Starling (1896) concluded that the exchange of fluid and large molecules between tissues and vessels is determined primarily by the difference of hydrostatic pressure in association with oncotic pressure. Named as the Starling's law, this conclusion can be written in the mathematical form of

$$q_e(l) = L_p(l)[p_c(l) - p_i(l) - \sigma(\pi_v(l) - \pi_i(l))], \tag{4.3.4}$$

where $q_e(l)$ is the transmission flux over the unit length along the circumference of the vessel cross section at l, $L_p(l)$ is the vessel permeability, $p_c(l)$ is the blood pressure inside vessel, $p_i(l)$ is the interstitial pressure evaluated on the

exterior vascular surface, $\pi_v(l)$ and $\pi_i(l)$ are the oncotic pressures in vessel fluid and tumour interstitial fluid respectively, and σ is the oncotic reflection coefficient. σ is used to correct the magnitude of the measured gradient for the ineffectiveness of the oncotic pressure gradient, whose value varies from 0 up to 1 [Curry (1984)].

Landis (1927) emphasised that increased vascular permeability would reduce the effects of colloid osmotic pressure. Considering the high permeability of tumour vessels, Jain and co-workers proposed a hypothesis that the oncotic pressures in tumour vessels and interstitium are similar [Boucher and Jain (1992), Jain (1987a,b)]. Stohrer *et al.* (2000) confirmed the above hypothesis through directly measuring the oncotic pressures in solid tumours. As a result, Eq.(4.3.4) is reduced to

$$q_e(l) = L_p(l)[p_c(l) - p_i(l)]. \tag{4.3.5}$$

Eq.(4.3.5) has assumed that both p_c and p_i are the functions of locations along vessel centre line. According to the foregoing analysis in Section 4.2, the flow through a tumour vessel is mainly dominated by pressure gradient along the vessel centre line, then p_c can be regarded as a function of vessel centre line, and it does not vary in the radial direction measured by r or in the circumferential direction by θ. Interstitial pressure p_i on the external vascular surface, on the other hand, does vary along θ since the direction of interstitial flow is unconstrained. There is therefore a mismatch for the pressures in Eq.(4.3.5). To avoid that, p_i is expanded into a Fourier series in the circumferential direction of vessel cross section, as

$$p_i(l,\theta) = p_{i_0}(l) + \sum_{n=1}^{+\infty} p_{i_n}^a(l)\cos n\theta + \sum_{n=1}^{+\infty} p_{i_n}^b(l)\sin n\theta, \tag{4.3.6}$$

in which p_{i_0} is the mean value of p_i along the circumferential direction of vessel cross section, or

$$p_{i_0}(l) = \frac{1}{2\pi}\int_0^{2\pi} p_i(l,\theta)\mathrm{d}\theta. \tag{4.3.7}$$

As tumour vessel radius is much smaller relative to the size of tumour, it can be regarded that the interstitial pressure on the exterior vascular surface is nearly independent on the angular position around vessel cross section, or mean value p_{i_0} is the main component of p_i. Consequently, p_{i_0} is the target of our solution. To make it concise, p_{i_0} will be written as p_i in the following equations.

Based on mass conservation, the flux transported into tumour interior from each section of a tumour vessel must be equal to the gradient of flux $Q_c(l)$ flowing along the longitudinal direction of the vessel, or

$$\frac{\mathrm{d}[Q_c(l)]}{\mathrm{d}l} + 2\pi a(l) q_e(l) = 0, \tag{4.3.8}$$

in which the assumption of circular vessel cross section has been applied. Substituting Eq.(4.3.5) into Eq.(4.3.8), and considering that the vessel centre line is defined by parametric equation $l : \{x(s), y(s), z(s)\}$, we obtain a differential governing equation for the coupling effect between the flow flux through a tumour vessel and the exceeded flux from its surface into tumour interstitium as

$$H_b(s)\frac{\mathrm{d}[Q_c(s)]}{\mathrm{d}s} + 2\pi a(s) L_p(s)\left[p_c(s) - p_i(s)\right] = 0, \tag{4.3.9}$$

in which the relationship in Eq.(4.1.4) is applied, and $H_b(s)$ is defined in Eq.(4.1.6).

4.3.3 Boundary-integral representative of the governing equation for the flow in tumour interstitium

Let us consider a study case for tumour blood flow, in which a single permeable vessel is embedded in a solid tumour whose surface is far away from the blood vessel. The boundary condition requires interstitial pressure p_i to be equal to peripheral pressure p_0 at the tumour surface, or

$$p_i(\mathbf{x}) = p_0 \quad \text{at} \quad \mathbf{x} \to \infty. \tag{4.3.10}$$

Following the procedure described in Section 3.3, the Laplace equation in Eq.(4.3.3) is converted into a boundary-integral equation. This gives an expression for the interstitial pressure at point $\mathbf{x}_0$ according to the values of the pressure and its normal derivative on boundary $S(\mathbf{x})$ of a certain calculation domain V_c, which is

$$\begin{aligned} p_i(\mathbf{x}_0) - p_0 = &- \int_S G(\mathbf{x}, \mathbf{x}_0) \left[\mathbf{n}(\mathbf{x}) \cdot \nabla p_i(\mathbf{x})\right] \mathrm{d}S(\mathbf{x}) \\ &+ \int_S \left[p_i(\mathbf{x}) - p_0\right] \left[\nabla G(\mathbf{x}, \mathbf{x}_0) \cdot \mathbf{n}(\mathbf{x})\right] \mathrm{d}S(\mathbf{x}), \end{aligned} \tag{4.3.11}$$

where $\mathbf{n}(\mathbf{x})$ is the unit normal vector of $S(\mathbf{x})$ pointing out of V_c, and $G(\mathbf{x}, \mathbf{x_0})$ is the Green's function which is defined in Eq.(3.3.11).

In the case that the tumour is virtually infinitely large, S refers to vascular surface S_v only as the contribution for infinity in Eq.(4.3.11) is zero. When $\mathbf{x}_0$ is on the surface of the vessel which is assumed to be smooth, we have

$$\begin{aligned} \frac{1}{2}\left[p_i(\mathbf{x}_0) - p_0\right] = &- \int_{S_v} G(\mathbf{x}, \mathbf{x}_0) \left[\mathbf{n}(\mathbf{x}) \cdot \nabla p_i(\mathbf{x})\right] \mathrm{d}S(\mathbf{x}) \\ &+ \int_{S_v} \left[p_i(\mathbf{x}) - p_0\right] \left[\nabla G(\mathbf{x}, \mathbf{x}_0) \cdot \mathbf{n}(\mathbf{x})\right] \mathrm{d}S(\mathbf{x}). \end{aligned} \tag{4.3.12}$$

According to flow continuity, combining the Darcy's law and the Starling's law on the vessel surface, and considering that the vessel centre line is defined by $l : \{x(s), y(s), z(s)\}$, we have

$$\mathbf{n}(\mathbf{x}) \cdot \nabla p_i(\mathbf{x}) = \frac{L_p(l)}{\kappa} \left[p_c(l) - p_i(l)\right] = \frac{L_p(s)}{\kappa} \left[p_c(s) - p_i(s)\right], \tag{4.3.13}$$

where $\mathbf{n}(\mathbf{x})$ is the unit vector normal to the vessel surface pointing out of tumour interstitium. As vascular cross section is assumed to be circular, and noticing the relationship described in Eq.(4.1.4), we have

$$\mathrm{d}S(x) = \int_0^{2\pi} a(l)\mathrm{d}l\mathrm{d}\theta = \int_0^{2\pi} \frac{a(s)}{H_b(s)}\mathrm{d}s\mathrm{d}\theta, \tag{4.3.14}$$

in which $H_b(s)$ is defined in Eq.(4.1.6). Introducing Eqs.(4.3.13) and (4.3.14) into Eq.(4.3.12), integrating the result at point $\mathbf{x}_0$ over $0 \leq \theta_0 \leq 2\pi$, and then dividing 2π on both sides of the equation, we obtain

$$\begin{aligned}
&\frac{1}{2}\left[p_i(\mathbf{x}_0) - p_0\right] \\
=& -\frac{1}{2\pi}\int_{l_v(s)}\int_0^{2\pi}\int_0^{2\pi} \frac{a(s)}{H_b(s)}\frac{L_p(s)}{\kappa}\left[p_c(s) - p_i(s)\right] G(\mathbf{x}, \mathbf{x}_0)\mathrm{d}\theta_0\mathrm{d}\theta\mathrm{d}s \\
&+ \frac{1}{2\pi}\int_{l_v(s)}\int_0^{2\pi}\int_0^{2\pi} \frac{a(s)}{H_b(s)}\left[p_i(s) - p_0\right] \nabla G(\mathbf{x}, \mathbf{x}_0)\mathbf{n}(\mathbf{x})\mathrm{d}\theta_0\mathrm{d}\theta\mathrm{d}s,
\end{aligned} \tag{4.3.15}$$

where $l_v(s)$ donates the length of the vessel.

Eq.(4.3.15) is now a one-dimensional integral equation, which can be solved numerically together with Eq.(4.3.9). After the solution for $p_c(s)$ and $p_i(s)$ along the vessel is found, the pressure distribution in tumour can be obtained. In fact, this can be achieved by introducing the coordinates of a point inside tumour space into Eq.(4.3.12), after Eqs.(4.3.13) and (4.3.14) have been

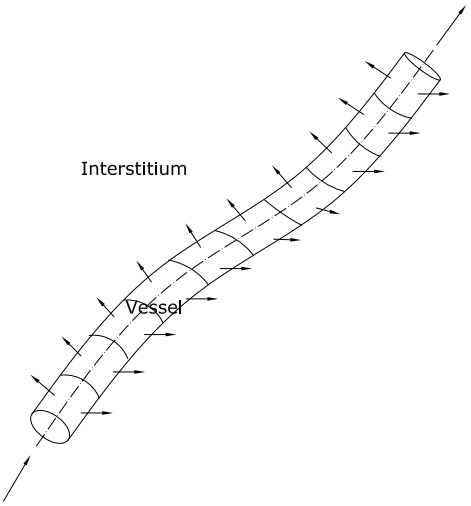

Figure 4.3: Discretisation of a vessel into cylindrical elements along its centre line.

substituted into it and 1/2 on its left-hand side has been deleted, which is

$$\begin{aligned} p_i =& p_0 - \frac{1}{2\pi}\int_{l_v(s)}\int_0^{2\pi} \frac{a(s)}{H_b(s)}\frac{L_p(s)}{\kappa}\left[p_c(s) - p_i(s)\right] G(\mathbf{x},\mathbf{x}_0)\mathrm{d}\theta\mathrm{d}s \\ &+ \frac{1}{2\pi}\int_{l_v(s)}\int_0^{2\pi} \frac{a(s)}{H_b(s)}\left[p_i(s) - p_0\right]\nabla G(\mathbf{x},\mathbf{x}_0)\mathbf{n}(\mathbf{x})\mathrm{d}\theta\mathrm{d}s. \end{aligned} \tag{4.3.16}$$

4.3.4 Numerical procedure on solving Eq.(4.3.15)

In order to solve Eq.(4.3.15) numerically, the vessel is divided into N_E cylindrical elements along its centre line, as presented in Fig.4.3. The segments can be distributed in nonuniform schemes. Within each element, the vessel permeability, the pressures in vessel, and the interstitial pressures on the exterior vascular surface are approximated to be constant, expressed by $L_p^{[j]}$, $p_c^{[j]}$, and $p_i^{[j]}$ respectively. The continuity condition is then imposed at the middle of every element. For the nth segment, where $n = 1, \cdots, N_E$, Eq.(4.3.15) is

discretised as

$$\frac{1}{2}\left(p_i^{[n]} - p_0\right) = -\sum_{j=1}^{N_E} \frac{L_p^{[j]}}{\kappa}\left(p_c^{[j]} - p_i^{[j]}\right)\bar{A}_n^{[j]} + \sum_{j=1}^{N_E}\left(p_i^{[j]} - p_0\right)\bar{B}_n^{[j]}, \quad (4.3.17)$$

where

$$\bar{A}_n^{[j]} = \frac{1}{2\pi}\int_0^{2\pi} A_n^{[j]} \mathrm{d}\theta_0, \quad (4.3.18)$$

and

$$\bar{B}_n^{[j]} = \frac{1}{2\pi}\int_0^{2\pi} B_n^{[j]} \mathrm{d}\theta_0, \quad (4.3.19)$$

in which

$$A_n^{[j]} = \int_{-\frac{\delta s_j}{2}}^{\frac{\delta s_j}{2}} \frac{a_j}{H_b^{[j]}} \mathrm{d}s \int_0^{2\pi} G(\mathbf{x}, \mathbf{x}_0)\mathrm{d}\theta, \quad (4.3.20)$$

and

$$B_n^{[j]} = \int_{-\frac{\delta s_j}{2}}^{\frac{\delta s_j}{2}} \frac{a_j}{H_b^{[j]}} \mathrm{d}s \int_0^{2\pi} \left[\nabla G(\mathbf{x}, \mathbf{x}_0) \cdot \mathbf{n}(\mathbf{x})\right] \mathrm{d}\theta. \quad (4.3.21)$$

In the above two equations, δs_j donates the longitudinal length of the jth segment. Rearranging terms in Eq.(4.3.17), we get

$$\begin{aligned} &\sum_{j=1}^{N_E}\left\{\delta_{nj} - 2\bar{B}_n^{[j]} - \frac{2L_p^{[j]}}{\kappa}\bar{A}_n^{[j]}\right\} p_i^{[j]} \\ &= -\sum_{j=1}^{N_E} \frac{2L_p^{[j]}}{\kappa}\bar{A}_n^{[j]} p_c^{[j]} + p_0\left\{1 - \sum_{j=1}^{N_E} 2\bar{B}_n^{[j]}\right\}, \end{aligned} \quad (4.3.22)$$

where δ_{nj} is Kronecker's delta function which is defined as

$$\delta_{nj} = \begin{cases} 1 & n = j, \\ 0 & n \neq j. \end{cases} \tag{4.3.23}$$

The major issue to construct the computing matrix in Eq.(4.3.22) is to obtain the values of influence coefficients $\bar{A}_n^{[j]}$ and $\bar{B}_n^{[j]}$ which are defined in Eqs.(4.3.18) and (4.3.19) respectively. The key feature to obtain $\bar{A}_n^{[j]}$ and $\bar{B}_n^{[j]}$ is to calculate $A_n^{[j]}$ and $B_n^{[j]}$ in Eqs.(4.3.20) and (4.3.21) respectively. In order to calculate $A_n^{[j]}$ and $B_n^{[j]}$, the integral representative of the Green's function derived in Section 3.4 is applied. This allows us to calculate the integrals with respect to θ analytically. As a result, the Green's function will be written through the complete elliptical integrals of first and second kind, which can be calculated for each pair of given $\mathbf{x}$ and $\mathbf{x}_0$ according to the polynomial schemes in Abramowitz and Stegun (1972) efficiently. Once $A_n^{[j]}$ and $B_n^{[j]}$ are obtained, the integrals with respect to θ_0 in $\bar{A}_n^{[j]}$ and $\bar{B}_n^{[j]}$ can be calculated through numerical methods, e.g. the Simpson's method.

According to the definitions in Eqs.(4.3.20) and (4.3.20), $A_n^{[j]}$ and $B_n^{[j]}$ are determined by the values of the Green's function and its derivative along the normal direction of tumour vascular surface. As stated in Section 3.3, the Green's function is

$$G(\mathbf{x}, \mathbf{x}_0) = -\frac{1}{4\pi\sqrt{(x-x_0)^2 + (y-y_0)^2 + (z-z_0)^2}}. \tag{4.3.24}$$

It is worth to be noticed that the Green's function in the above equation depends only on the distance between field point $\mathbf{x}$ and source point $\mathbf{x}_0$, which indicates that its value is independent on the reference coordinate frames. As a result, we are free to choose any convenient coordinate system to calculate

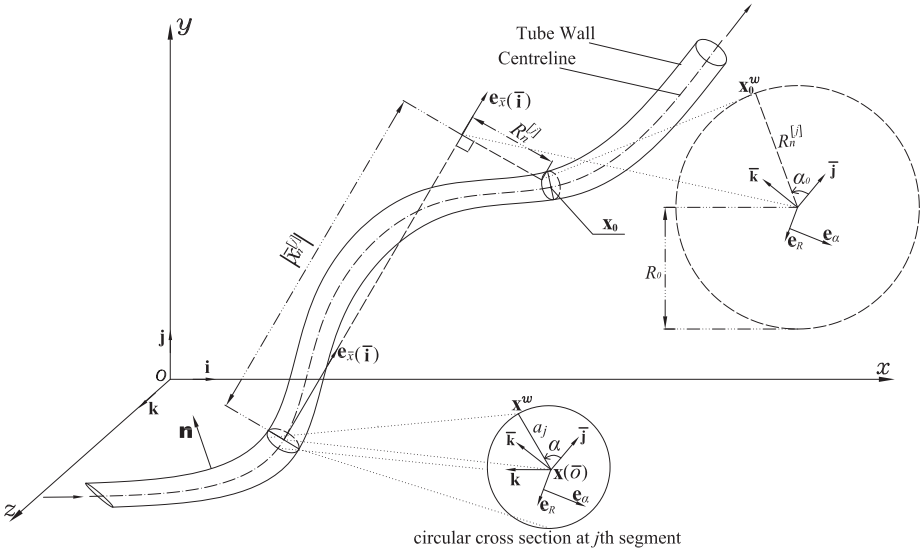

Figure 4.4: Sketch of a vessel inside tumour interstitium.

the values of the Green's function and its derivative. Two local reference coordinate frames are set up at the jth segment corresponding to point $\mathbf{x}$, as sketched in Fig.4.4. One local reference frame is a Cartesian coordinate system $\bar{o} - \bar{x}\bar{y}\bar{z}$, which has the same definition as system $\tilde{o} - \tilde{x}\tilde{y}\tilde{z}$ defined in Section 4.2. The other local reference frame is a cylinder coordinate system $(\bar{x}, R, \alpha)$ similar to system (s, r, θ), in which $\mathbf{e}_{\bar{x}}$ is identical to $\bar{\mathbf{i}}$, $\mathbf{e}_R$ is along any radial direction on the cross section plane, and $\mathbf{e}_\alpha = \mathbf{e}_{\bar{x}} \times \mathbf{e}_R$.

In coordinate systems $\bar{o}-\bar{x}\bar{y}\bar{z}$ and $(\bar{x}, R, \alpha)$, we have the following relationship for a point $\mathbf{x}^w$ on the vascular surface at the jth segment corresponding to point $\mathbf{x}$, which is

$$\mathbf{x}^w(\bar{x}, \bar{y}, \bar{z}) = \mathbf{x}^w(0, a_j \cos\alpha, a_j \sin\alpha), \tag{4.3.25}$$

where a_j is the radius of the vessel cross section at the jth segment. Similarly,

for a point $\mathbf{x}_0^w$ on the vascular surface of the nth segment corresponding to point $\mathbf{x}_0$, we have

$$\mathbf{x}_0^w(\bar{x}_0, \bar{y}_0, \bar{z}_0) = \mathbf{x}_0^w \left(\bar{x}_n^{[j]}, R_n^{[j]} \cos\alpha_0, R_n^{[j]} \sin\alpha_0\right). \tag{4.3.26}$$

According to the foregoing outcome obtained in Section 3.4, the integral expression of the Green's function is

$$G(\mathbf{x}, \mathbf{x}_0) = -\frac{1}{8\pi^2} \int_0^{+\infty} \int_0^{2\pi} \mathrm{e}^{-k_\rho |x-x_0|} \mathrm{e}^{\mathrm{i}k_\rho[\cos\theta(y-y_0)+\sin\theta(z-z_0)]} \mathrm{d}k_\rho \mathrm{d}\theta. \tag{4.3.27}$$

Introducing Eqs.(4.3.25) and (4.3.26) into Eq.(4.3.27), we get

$$G(\mathbf{x}^w, \mathbf{x}_0^w) = -\frac{1}{8\pi^2} \int_0^{+\infty} \int_0^{2\pi} \mathrm{e}^{-k_\rho \left|\bar{x}_n^{[j]}\right|} \mathrm{e}^{\mathrm{i}k_\rho[a_j \cos(\theta-\alpha) - R_n^{[j]} \cos(\theta-\alpha_0)]} \mathrm{d}k_\rho \mathrm{d}\theta. \tag{4.3.28}$$

Based on the definition of complex function, it follows

$$\begin{aligned}
&\mathrm{e}^{\mathrm{i}k_\rho[a_j \cos(\theta-\alpha) - R_n^{[j]} \cos(\theta-\alpha_0)]} \\
=&\left\{\cos[k_\rho a_j \cos(\theta-\alpha)] + \mathrm{i}\sin[k_\rho a_j \cos(\theta-\alpha)]\right\} \\
&\times \left\{\cos[k_\rho R_n^{[j]} \cos(\theta-\alpha_0)] - \mathrm{i}\sin[k_\rho R_n^{[j]} \cos(\theta-\alpha_0)]\right\}.
\end{aligned} \tag{4.3.29}$$

According to the expansions in Abramowitz and Stegun (1972), the terms on the right-hand side of Eq.(4.3.29) can be further expanded to

$$\begin{aligned}
&\cos[k_\rho a_j \cos(\theta-\alpha)] + \mathrm{i}\sin[k_\rho a_j \cos(\theta-\alpha)] \\
=&J_0(k_\rho a_j) + 2\sum_{m=1}^{\infty} (-1)^m J_{2m}(k_\rho a_j) \cos[2m(\theta-\alpha)] \\
&+ \mathrm{i}2\sum_{m=0}^{\infty} (-1)^m J_{2m+1}(k_\rho a_j) \cos[(2m+1)(\theta-\alpha)],
\end{aligned} \tag{4.3.30}$$

and

$$\begin{aligned}
&\cos[k_\rho R_n^{[j]}\cos(\theta-\alpha_0)]-\mathrm{i}\sin[k_\rho R_n^{[j]}\cos(\theta-\alpha_0)]\\
=&J_0\left(k_\rho R_n^{[j]}\right)+2\sum_{m=1}^{\infty}(-1)^m J_{2m}\left(k_\rho R_n^{[j]}\right)\cos[2m(\theta-\alpha_0)]\\
&-\mathrm{i}2\sum_{m=0}^{\infty}(-1)^m J_{2m+1}\left(k_\rho R_n^{[j]}\right)\cos[(2m+1)(\theta-\alpha_0)],
\end{aligned}\tag{4.3.31}$$

respectively, in which J_k $(k=0,1,2,\cdots)$ are the Bessel functions. Substituting Eqs.(4.3.30) and (4.3.31) into Eq.(4.3.29), we then introduce the result into Eq.(4.3.28). Due to the orthogonality of trigonometric function, when the integral with respect to variable θ is considered, Eq.(4.3.28) is reduced to

$$\begin{aligned}
G(\mathbf{x}^w,\mathbf{x}_0^w)=-\frac{1}{4\pi}\int_0^{+\infty}\mathrm{e}^{-k_\rho\left|\bar{x}_n^{[j]}\right|}\Bigg\{&2\sum_{m=1}^{\infty}J_{2m}\left(k_\rho a_j\right)J_{2m}\left(k_\rho R_n^{[j]}\right)\cos[2m(\alpha-\alpha_0)]\\
&+2\sum_{m=0}^{\infty}J_{2m+1}\left(k_\rho a_j\right)J_{2m+1}\left(k_\rho R_n^{[j]}\right)\cos[(2m+1)(\alpha-\alpha_0)]\\
&+J_0\left(k_\rho a_j\right)J_0\left(k_\rho R_n^{[j]}\right)\Bigg\}\mathrm{d}k_\rho.
\end{aligned}\tag{4.3.32}$$

After substituting Eq.(4.3.32) into Eqs.(4.3.20) and (4.3.21), we follow the steps mentioned in the beginning of this section. Eqs.(4.3.20) and (4.3.21) can be calculated by performing the integrals with respect to the meridional angle around a cylindrical element first. Considering the orthogonality of trigonometric function with respect to variable α, we have

$$A_n^{[j]}=-\frac{1}{2}\int_{-\frac{\delta s_j}{2}}^{\frac{\delta s_j}{2}}\frac{a_j}{H_b^{[j]}}\mathrm{d}s\int_0^{+\infty}\mathrm{e}^{-k_\rho\left|\bar{x}_n^{[j]}\right|}J_0\left(k_\rho a_j\right)J_0\left(k_\rho R_n^{[j]}\right)\mathrm{d}k_\rho,\tag{4.3.33}$$

$$B_n^{[j]} = -\frac{1}{2}\int_{-\frac{\delta s_j}{2}}^{\frac{\delta s_j}{2}} \frac{a_j}{H_b^{[j]}} \mathrm{d}s \int_0^{+\infty} \mathrm{e}^{-k_\rho \left|\bar{x}_n^{[j]}\right|} k_\rho J_1\left(k_\rho a_j\right) J_0\left(k_\rho R_n^{[j]}\right) \mathrm{d}k_\rho, \tag{4.3.34}$$

in which

$$\nabla G \cdot \mathbf{n}(\mathbf{x}) = -\left.\frac{\partial G}{\partial r}\right|_{r=a_j},$$

and

$$J_0^{'}\left(k_\rho a_j\right) = \left.\frac{\mathrm{d}\left[J_0(k_\rho r)\right]}{\mathrm{d}r}\right|_{r=a_j} = -k_\rho J_1\left(k_\rho a_j\right)$$

have been used.

It has been showed by Eason *et al.* (1955) that

$$\int_0^{+\infty} \mathrm{e}^{-k_\rho \left|\bar{x}_n^{[j]}\right|} J_0\left(k_\rho a_j\right) J_0\left(k_\rho R_n^{[j]}\right) \mathrm{d}k_\rho = \frac{\sqrt{\hat{m}}}{2\sqrt{a_j R_n^{[j]}}} F(\hat{m}), \tag{4.3.35}$$

and

$$\begin{aligned}
&\int_0^{+\infty} \mathrm{e}^{-k_\rho \left|\bar{x}_n^{[j]}\right|} k_\rho J_1\left(k_\rho a_j\right) J_0\left(k_\rho R_n^{[j]}\right) \mathrm{d}k_\rho \\
=&\frac{\sqrt{\hat{m}}}{4a_j\sqrt{a_j R_n^{[j]}}} F(\hat{m}) + \frac{\hat{m}^{3/2}\left[\left(a_j\right)^2 - \left(R_n^{[j]}\right)^2 - \left(\bar{x}_n^{[j]}\right)^2\right]}{16 a_j \hat{m}_1 \left(a_j R_n^{[j]}\right)^{3/2}} E(\hat{m}),
\end{aligned} \tag{4.3.36}$$

where

$$E(\hat{m}) = \frac{2}{\pi}\int_0^{\pi/2} (1 - \hat{m}\sin^2\xi)^{1/2} \mathrm{d}\xi, \tag{4.3.37}$$

$$F(\hat{m}) = \frac{2}{\pi}\int_0^{\pi/2} (1 - \hat{m}\sin^2\xi)^{-1/2} \mathrm{d}\xi, \tag{4.3.38}$$

Table 4.1: Coefficients within $\hat{u}_1(\hat{m}_1)$, $\hat{u}_2(\hat{m}_1)$, $\hat{v}_1(\hat{m}_1)$ and $\hat{v}_2(\hat{m}_1)$

k	$\hat{a}_k$	$\hat{b}_k$	$\hat{c}_k$	$\hat{d}_k$
0	1.38629436112	0.5	—	—
1	0.09666344259	0.12498593597	0.44325141463	0.24998368310
2	0.03590092383	0.06880248576	0.06260601220	0.09200180037
3	0.03742563713	0.03328355346	0.04757383546	0.04069697526
4	0.01451196212	0.00441787012	0.01736506451	0.00526449639

$$\hat{m} = \frac{4a_j R_n^{[j]}}{\left(a_j + R_n^{[j]}\right)^2 + \left(\bar{x}_n^{[j]}\right)^2}, \tag{4.3.39}$$

and

$$\hat{m}_1 = 1 - \hat{m} = \frac{\left(a_j - R_n^{[j]}\right)^2 + \left(\bar{x}_n^{[j]}\right)^2}{\left(a_j + R_n^{[j]}\right)^2 + \left(\bar{x}_n^{[j]}\right)^2}. \tag{4.3.40}$$

$F(\hat{m})$ and $E(\hat{m})$ are the complete elliptic integrals of the first and second kind respectively. There are two popular ways to calculate these two integrals. One method is to adopt the efficient polynomial approximations [Abramowitz and Stegun (1972)]. The other is to use the recursive formulae, as presented in Appendix A (also in the book by Pozrikidis (1997)). Abramowitz and Stegun (1972) provided that

$$\int_0^{\pi/2} (1 - \hat{m}\sin^2\xi)^{-1/2} \mathrm{d}\xi = \hat{u}_1(\hat{m}_1) + \hat{u}_2(\hat{m}_1) + \epsilon(\hat{m}) \qquad |\epsilon(\hat{m})| \leq 2 \times 10^{-8},$$

where

$$\hat{u}_1(\hat{m}_1) = \hat{a}_0 + \hat{a}_1 \cdot \hat{m}_1 + \hat{a}_2 \cdot \hat{m}_1^2 + \hat{a}_3 \cdot \hat{m}_1^3 + \hat{a}_4 \cdot \hat{m}_1^4,$$

and

$$\hat{u}_2(\hat{m}_1) = \left(\hat{b}_0 + \hat{b}_1 \cdot \hat{m}_1 + \hat{b}_2 \cdot \hat{m}_1^2 + \hat{b}_3 \cdot \hat{m}_1^3 + \hat{b}_4 \cdot \hat{m}_1^4\right) \cdot \ln\left(\frac{1}{\hat{m}_1}\right),$$

in which the values of $\hat{a}_k$ and $\hat{b}_k$ $(k = 0, 1, \cdots, 4)$ are listed in Table4.1. Also,

$$\int_0^{\pi/2} (1 - \hat{m}\sin^2\xi)^{1/2} \mathrm{d}\xi = \hat{v}_1(\hat{m}_1) + \hat{v}_2(\hat{m}_1) + \epsilon(\hat{m}) \qquad |\epsilon(\hat{m})| \leq 2 \times 10^{-8},$$

where

$$\hat{v}_1(\hat{m}_1) = 1 + \hat{c}_1 \cdot \hat{m}_1 + \hat{c}_2 \cdot \hat{m}_1^2 + \hat{c}_3 \cdot \hat{m}_1^3 + \hat{c}_4 \cdot \hat{m}_1^4,$$

and

$$\hat{v}_2(\hat{m}_1) = \left(\hat{d}_1 \cdot \hat{m}_1 + \hat{d}_2 \cdot \hat{m}_1^2 + \hat{d}_3 \cdot \hat{m}_1^3 + \hat{d}_4 \cdot \hat{m}_1^4\right) \cdot \ln\left(\frac{1}{\hat{m}_1}\right),$$

in which the values of $\hat{c}_k$ and $\hat{d}_k$ $(k = 1, 2, 3, 4)$ are presented in Table4.1. As a result,

$$A_n^{[j]} = -\int_{-\frac{\delta s_j}{2}}^{\frac{\delta s_j}{2}} \frac{a_j\sqrt{\hat{m}}}{2\pi H_b^{[j]}\sqrt{a_j R_n^{[j]}}} \left[\hat{u}_1(\hat{m}_1) + \hat{u}_2(\hat{m}_1)\right] \mathrm{d}s, \tag{4.3.41}$$

and

$$\begin{aligned} B_n^{[j]} = &-\int_{-\frac{\delta s_j}{2}}^{\frac{\delta s_j}{2}} \frac{\sqrt{\hat{m}}}{4\pi H_b^{[j]}\sqrt{a_j R_n^{[j]}}} \left[\hat{u}_1(\hat{m}_1) + \hat{u}_2(\hat{m}_1)\right] \mathrm{d}s \\ &-\int_{\delta s_j} \frac{\hat{m}^{3/2}\left[(a_j)^2 - \left(R_n^{[j]}\right)^2 - \left(\bar{x}_n^{[j]}\right)^2\right]}{16\pi H_b^{[j]}\hat{m}_1\left(a_j R_n^{[j]}\right)^{3/2}} \left[\hat{v}_1(\hat{m}_1) + \hat{v}_2(\hat{m}_1)\right] \mathrm{d}s. \end{aligned} \tag{4.3.42}$$

We, now, proceed to calculate the integrals with respect to the distance along the element (regarding it as a straight section) axis on the right-hand

sides of Eqs.(4.3.41) and (4.3.42). There are two kinds of situations for the integrals. One is that the evaluation point does not lie on the host element, or $j \neq n$. In this situation, the integrals in both Eqs.(4.3.41) and (4.3.42) do not contain any singularity. The integrals on the right-hand sides of Eqs.(4.3.41) and (4.3.42) can be solved easily and efficiently by Gauss-Legendre Quadrature [Zwillinger (2003)] as

$$I^{[j]}_{\{A_n^{[j]},B_n^{[j]}\}} \cong \frac{\delta s_j}{2} \sum_{k=1}^{n} \hat{c}_k^g \cdot f_{\{A_n^{[j]},B_n^{[j]}\}} \left(\frac{\delta s_j}{2} \hat{x}_k^g \right), \tag{4.3.43}$$

where $I_{\{A_n^{[j]},B_n^{[j]}\}}$ stands for a certain integral term on the right-hand side of Eq.(4.3.41) or (4.3.42), $f_{\{A_n^{[j]},B_n^{[j]}\}}$ represents the integrand of that term, and $\hat{c}_k^g$ and $\hat{x}_k^g$ are the Gauss-Legendre Quadrature parameters whose values are listed in Table.4.2. When the evaluation point is on the host segment as $j = n$, $R_n^{[j]} = a_j$ and $\bar{x}_n^{[j]} = 0$ in the middle of the element. This leads to a logarithmic singularity with term

$$\ln \left[\left(a_j - R_n^{[j]} \right)^2 + \left(\bar{x}_n^{[j]} \right)^2 \right]$$

in $\hat{u}_2(\hat{m}_1)$. The singularity can be dealt analytically as

$$\int_{-\frac{\delta s_j}{2}}^{\frac{\delta s_j}{2}} \frac{1}{H_b^{[j]}} \ln \left[\left(\frac{\xi}{H_b^{[j]}} \right)^2 \right] \mathrm{d}\xi = 2 \left[\ln \left(\frac{\delta s_j}{2 H_b^{[j]}} \right) - 1 \right] \frac{\delta s_j}{H_b^{[j]}}. \tag{4.3.44}$$

Consequently, when $n = j$, the singularities within $A_n^{[j]}$ and $B_n^{[j]}$ should be calculated according to Eq.(4.3.44) together with integral mean value theorem. The rest of integral terms in $A_n^{[j]}$ and $B_n^{[j]}$ are calculated by Gauss-Legendre Quadrature. In this way, $A_n^{[j]}$ and $B_n^{[j]}$ are found. Using the results, we are now able to calculate $\bar{A}_n^{[j]}$ and $\bar{B}_n^{[j]}$ by numerical integration methods, e.g. the Simpson's Rule.

Table 4.2: Six-point Gauss-Legendre Quadrature

k	Roots	Coefficients
1	$\hat{x}_1^g = 0.23861919$	$\hat{c}_1^g = 0.46791393$
2	$\hat{x}_2^g = 0.66120939$	$\hat{c}_2^g = 0.36076157$
3	$\hat{x}_3^g = 0.93246951$	$\hat{c}_3^g = 0.17132449$
4	$\hat{x}_4^g = -0.23861919$	$\hat{c}_4^g = 0.46791393$
5	$\hat{x}_5^g = -0.66120939$	$\hat{c}_5^g = 0.36076157$
6	$\hat{x}_6^g = -0.93246951$	$\hat{c}_6^g = 0.17132449$

However, values of $\left|\bar{x}_n^{[j]}\right|$ and $R_n^{[j]}$ are also needed to be calculated. $R_n^{[j]}$ is the distance of point $\mathbf{x}_0^w$ to the line which passes through point $\mathbf{x}$ in the direction of $\mathbf{e}_{\bar{\mathbf{x}}}$, where $\mathbf{e}_{\bar{\mathbf{x}}}$ is the unit vector along the tangential direction of the vessel centre line at point $\mathbf{x}$, as shown in Fig.4.5. $\left|\bar{x}_n^{[j]}\right|$ has the following relationship with $R_n^{[j]}$:

$$\left|\bar{x}_n^{[j]}\right| = \sqrt{|\mathbf{x} - \mathbf{x}_0^w|^2 - \left(R_n^{[j]}\right)^2}. \tag{4.3.45}$$

$\left|\bar{x}_n^{[j]}\right|$ and $R_n^{[j]}$ are independent on the coordinate systems. To calculate them, two local reference coordinate systems are defined at the nth segment corresponding to point $\mathbf{x}_0$. As depicted in Fig.4.5, one is Cartesian coordinate system $\tilde{o} - \tilde{x}\tilde{y}\tilde{z}$ which has the same definition as system $\tilde{o} - \tilde{x}\tilde{y}\tilde{z}$ defined in Section 4.2. The other one is cylinder coordinate system $(\tilde{x}, r_0, \theta_0)$ which is similar to system $(\bar{x}, R, \alpha)$. In $(\tilde{x}, r_0, \theta_0)$, $\mathbf{e}_{\tilde{x}}$ is identical to $\tilde{\mathbf{i}}$, $\mathbf{e}_{r_0}$ is along any radial direction on the cross section plane corresponding to point $\mathbf{x}_0$, and $\mathbf{e}_{\theta_0} = \mathbf{e}_{\tilde{x}} \times \mathbf{e}_{r_0}$. On the vessel surface at the nth segment corresponding to

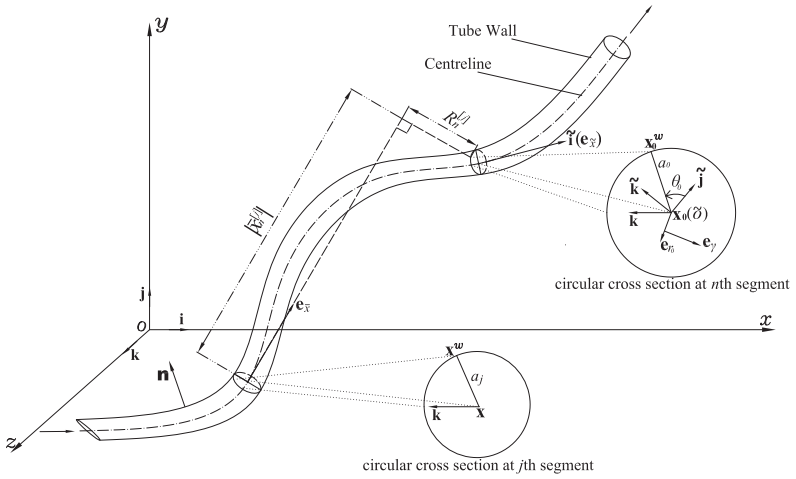

Figure 4.5: Sketch of a vessel inside tumour interstitium.

point $\mathbf{x}_0$, we have

$$\mathbf{x}_0^w(\tilde{x}^w, \tilde{y}^w, \tilde{z}^w) = \mathbf{x}_0^w(0, a_0 \cos\theta_0, a_0 \sin\theta_0), \tag{4.3.46}$$

where a_0 is the radius of the vessel cross section at the nth segment. Similar to the procedure described in Section 4.2, in the original coordinate system $o - xyz$, we have

$$\begin{aligned}\tilde{\mathbf{i}} =& \frac{x_0'}{\sqrt{(x_0')^2 + (y_0')^2 + (z_0')^2}}\mathbf{i} + \frac{y_0'}{\sqrt{(x_0')^2 + (y_0')^2 + (z_0')^2}}\mathbf{j} \\ &+ \frac{z_0'}{\sqrt{(x_0')^2 + (y_0')^2 + (z_0')^2}}\mathbf{k},\end{aligned} \tag{4.3.47}$$

$$\begin{aligned}\tilde{\mathbf{j}} =& \frac{y_0' + z_0'}{\sqrt{(y_0' + z_0')^2 + 2(x_0')^2}}\mathbf{i} - \frac{x_0'}{\sqrt{(y_0' + z_0')^2 + 2(x_0')^2}}\mathbf{j} \\ &- \frac{x_0'}{\sqrt{(y_0' + z_0')^2 + 2(x_0')^2}}\mathbf{k},\end{aligned} \tag{4.3.48}$$

and

$$\begin{aligned}\tilde{\mathbf{k}} =&\frac{x_0'z_0' - x_0'y_0'}{\sqrt{(x_0')^2(z_0'-y_0')^2 + [(x_0')^2 + z_0'(y_0'+z_0')]^2 + [(x_0')^2 + y_0'(y_0'+z_0')]^2}}\mathbf{i}\\ &+\frac{(x_0')^2 + z_0'(y_0'+z_0')}{\sqrt{(x_0')^2(z_0'-y_0')^2 + [(x_0')^2 + z_0'(y_0'+z_0')]^2 + [(x_0')^2 + y_0'(y_0'+z_0')]^2}}\mathbf{j}\\ &-\frac{(x_0')^2 + y_0'(y_0'+z_0')}{\sqrt{(x_0')^2(z_0'-y_0')^2 + [(x_0')^2 + z_0'(y_0'+z_0')]^2 + [(x_0')^2 + y_0'(y_0'+z_0')]^2}}\mathbf{k},\end{aligned} \tag{4.3.49}$$

in which

$$x_0 = x(s_0), \qquad y_0 = y(s_0), \qquad z_0 = z(s_0),$$

and

$$x_0' = \left.\frac{\mathrm{d}x}{\mathrm{d}s}\right|_{s=s_0}, \qquad y_0' = \left.\frac{\mathrm{d}y}{\mathrm{d}s}\right|_{s=s_0}, \qquad z_0' = \left.\frac{\mathrm{d}z}{\mathrm{d}s}\right|_{s=s_0},$$

where s_0 is position for point $\mathbf{x}_0$ along the vessel centre line. According to Eq.(4.3.46), in Cartesian coordinate system $o - xyz$, we have

$$\begin{cases} x_0^w =x_0 + \dfrac{(y_0'+z_0')a_0\cos\theta_0}{\sqrt{(y_0'+z_0')^2 + 2(x_0')^2}} \\ \qquad + \dfrac{(x_0'z_0' - x_0'y_0')a_0\sin\theta_0}{\sqrt{(x_0')^2(z_0'-y_0')^2 + [(x_0')^2 + z_0'(y_0'+z_0')]^2 + [(x_0')^2 + y_0'(y_0'+z_0')]^2}}, \\ y_0^w =y_0 - \dfrac{x_0'a_0\cos\theta_0}{\sqrt{(y_0'+z_0')^2 + 2(x_0')^2}} \\ \qquad + \dfrac{[(x_0')^2 + z_0'(y_0'+z_0')]a_0\sin\theta_0}{\sqrt{(x_0')^2(z_0'-y_0')^2 + [(x_0')^2 + z_0'(y_0'+z_0')]^2 + [(x_0')^2 + y_0'(y_0'+z_0')]^2}}, \\ z_0^w =z_0 - \dfrac{x_0'a_0\cos\theta_0}{\sqrt{(y_0'+z_0')^2 + 2(x_0')^2}} \\ \qquad - \dfrac{[(x_0')^2 + y_0'(y_0'+z_0')]a_0\sin\theta_0}{\sqrt{(x_0')^2(z_0'-y_0')^2 + [(x_0')^2 + z_0'(y_0'+z_0')]^2 + [(x_0')^2 + y_0'(y_0'+z_0')]^2}}. \end{cases} \tag{4.3.50}$$

Based on the definition of the distance from a point to a line [Bronshtein

et al. (2007)], we get

$$R_n^{[j]} = \Big\{ \left[(x_j - x_0^w)y_j' - (y_j - y_0^w)x_j'\right]^2 + \left[(x_j - x_0^w)z_j' - (z_j - z_0^w)x_j'\right]^2 + \left[(z_j - z_0^w)y_j' - (y_j - y_0^w)z_j'\right]^2 \Big\}^{\frac{1}{2}} \left[(x_j')^2 + (y_j')^2 + (z_j')^2\right]^{-\frac{1}{2}}. \quad (4.3.51)$$

In terms of the definition in Eq.(4.3.45), we have

$$\left|\bar{x}_n^{[j]}\right| = \frac{\left|(x_j - x_0^w)x_j' + (y_j - y_0^w)y_j' + (z_j - z_0^w)z_j'\right|}{\sqrt{(x_j')^2 + (y_j')^2 + (z_j')^2}}. \quad (4.3.52)$$

In Eqs.(4.3.51) and (4.3.52), x_j, y_j and z_j are the coordinates of point $\mathbf{x}$ in system $o - xyz$, and

$$x_j' = \left.\frac{\mathrm{d}x}{\mathrm{d}s}\right|_{s=s_j}, \qquad y_j' = \left.\frac{\mathrm{d}y}{\mathrm{d}s}\right|_{s=s_j}, \qquad z_j' = \left.\frac{\mathrm{d}z}{\mathrm{d}s}\right|_{s=s_j},$$

where s_j is the position for point $\mathbf{x}$ along the vessel centre line. Introducing Eq.(4.3.50) into Eqs.(4.3.51) and (4.3.52), $\left|\bar{x}_n^{[j]}\right|$ and $R_n^{[j]}$ are calculated successfully.

4.4 Summary

In this chapter, the governing equations for tumour blood flow are derived based on a case when a single permeable vessel is embedded in a solid tumour to some large extent. The vessel centre line is expressed by the parametric equation. According to the parameter in that parametric equation, a one-dimensional differential equation and a one-dimensional integral equation which include the coupling effect between the flows inside and outside the tumour vessel are obtained, as described in Eqs.(4.3.9) and (4.3.15) respectively.

Those two equations establish the mathematical basis of our project, which are discretised and solved by FDM and BEM respectively. The detailed numerical procedure on solving Eq.(4.3.15) by BEM has been presented in Section 4.3.4, while for Eq.(4.3.9), the numerical procedure will be discussed in the following chapters in detail when the explicit expression of the parametric equation for the vessel centre line is given.

Chapter 5

Flow through a Single Straight Permeable Vessel in a Solid Tumour

In the present and next chapters, we apply the governing equations derived in the previous chapter to investigate a simple case for tumour blood flow when tumour vasculature is represented by a single straight permeable vessel which is embedded in a solid tumour whose surface is far away from the vessel. The simplicity of this tumour vasculature allows us to examine the rationality of our model and the efficiency of the numerical procedure (in the present chapter), and study in detail how different types of physical parameters affect tumour blood flow (in Chapter 6), including the inlet and outlet vascular flow conditions, vessel permeability, tumour hydraulic conductivity, and tumour peripheral pressure.

Though using a single straight vessel to represent the entire tumour vasculature may be an idealised model, it provides us a good platform to study the effects of various physical parameters on the distributions of the blood

pressures inside and outside the vessel and the flux exceeded from vessel into tumour interstitium. The results obtained here have useful and important implications on medical applications. As stated in Section 2.3, convective effect is our major concern in this study, because it is the leading mechanism for the delivery of the therapeutic anti-cancer agents with heavy weight and large size from tumour vessels into interstitium to kill cancer cells. Netti *et al.* (1999) described the transvascular delivery of molecules by convection as

$$J_s = L_p A_s[(p_c - p_i) - \sigma(\pi_v - \pi_i)](1 - \sigma_{_F})c_v, \tag{5.0.1}$$

where J_s is the flux of molecules, L_p is the vessel permeability, A_s is the vascular surface area, p_c and p_i are the hydrostatic pressures in vessel and interstitium respectively, σ and $\sigma_{_F}$ are the oncotic and plasmadrag reflection coefficients respectively, π_v and π_i are the oncotic pressures in vascular and interstitial fluid respectively, and c_v is the drug concentration in the vessel fluid. Since oncotic gradient $\pi_v - \pi_i$ in tumours is almost zero as stated in Section 4.3.2, the transvascular movement of macromolecules would rely mostly on the extravasation flux driven by hydrostatic pressure gradient $p_c - p_i$. Since vascular cross section is assumed to be circular in our model, vascular surface area A_s can be written as

$$A_s = 2\pi \int_{l_v} a(l)\mathrm{d}l, \tag{5.0.2}$$

in which $a(l)$ is vessel radius, and l_v is the length of the vessel. Then, Eq.(5.0.1) is reduced to

$$J_s = 2\pi \int_{l_v} a(l)L_p(l)\left[p_c(l) - p_i(l)\right](1 - \sigma_{_F})c_v\mathrm{d}l. \tag{5.0.3}$$

Some conclusions have been drawn that elevated tumour interstitial flow pressure (IFP) is the major physiological barrier to macromolecular uptake in solid tumours, for example in the papers by Jain (1994), Jain and Baxter (1988). However, based on the above discussions, we notice that extravasation flux $L_p a(p_c - p_i)$ dominates the transvascular delivery of macromolecules in tumour, while interstitial flow pressure p_i is one of the factors which have influence on the extravasation flux. In this thesis, we assume drug concentration c_v and plasmadrag reflection coefficient $\sigma_{_F}$ are constant. Our investigation then focuses on how other various physical parameters affect extravasation flux $L_p a(p_c - p_i)$ in tumour.

Another feature that we are interested in is the relative flux coefficient $\gamma_{_Q}$, which is the ratio of blood flux exceeded from the vessel into tumour interstitium over the flux perfused into the vessel, or

$$\gamma_{_Q} = \frac{Q_a - Q_v}{Q_a}, \tag{5.0.4}$$

where Q_a stands for the inlet afferent blood flux perfused into the vessel, and Q_v is the outlet efferent blood flux flowing out of the vessel. Transporting therapeutic anti-cancer agents throughout vascular surface into tumour interior is one aspect of our concerns. Meanwhile, we hope to delivery the agents with high efficiency. Here, $\gamma_{_Q}$ represents the efficiency of flux exceeded into tumour interstitium from the vessel. High value of $\gamma_{_Q}$ means that relatively more blood flux is delivered into tumour interior throughout vascular surface rather than transported through the vessel into other parts of human body, e.g. normal organs and tissues. When we choose radiotherapy and/or chemotherapy to treat cancer, if the radiosensitiser and/or the anti-cancer chemical drugs are uniformly dissolved in blood, we shall make ways to increase the value of $\gamma_{_Q}$, as we prefer more anti-cancer agents are exceeded out of the vessel into

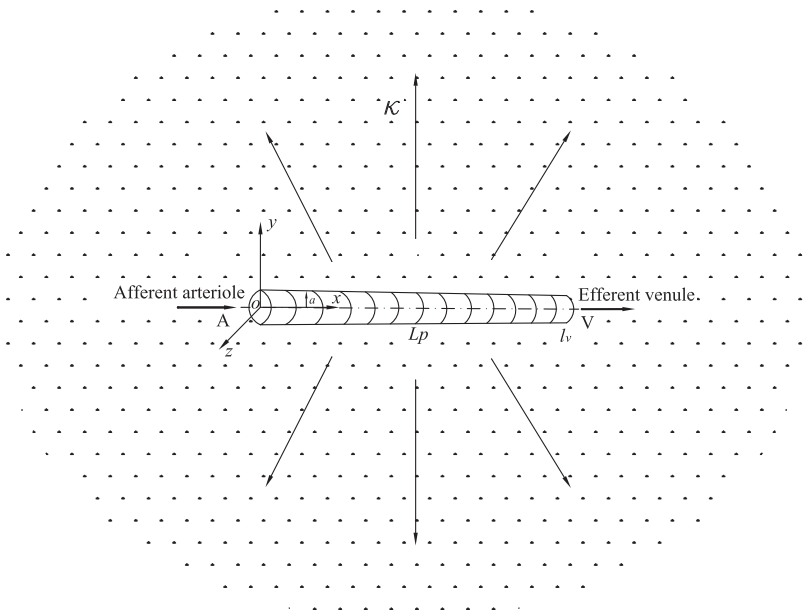

Figure 5.1: Sketch of a single vessel embedded in a solid tumour

tumour interstitium along with blood flow. Lowering γ_Q not only reduces the effectiveness of radiotherapy and chemotherapy, but also aggravates the side effects of these two treatments, because relatively more radiosensitiser and/or anti-cancer chemical drugs are transported to the surrounding normal tissues rather than into tumour. This leads to that tumour is more likely survive from the therapies, whereas the normal tissues are more likely to be killed by radiation and/or toxic anti-cancer chemical drugs.

5.1 Governing equations for the flow and numerical simulation procedure

Similar to the case illustrated in Fig.4.1, Fig.5.1 sketches a case when a single straight permeable vessel is embedded in tumour interior. For this case, it is

natural for us to choose the following parametric equation

$$x(s) = s, \qquad y(s) = 0, \qquad z(s) = 0, \tag{5.1.1}$$

to describe the vessel centre line. We then have

$$x'(s) = 1, \qquad y'(s) = 0, \qquad z'(s) = 0, \tag{5.1.2}$$

and

$$x''(s) = 0, \qquad y''(s) = 0, \qquad z''(s) = 0. \tag{5.1.3}$$

Introducing Eqs.(5.1.2) and (5.1.3) into Eqs.(4.1.6) and (4.1.7), we obtain

$$H_b(s) = 1, \qquad H_c(s) = 0. \tag{5.1.4}$$

Substituting Eqs.(5.1.2) to (5.1.4) into Eq.(4.2.23), we get

$$\mathcal{J}_r = 1, \qquad \mathcal{J}_\theta = r, \qquad \mathcal{J}_s = 1. \tag{5.1.5}$$

Introducing Eq.(5.1.5) into Eqs.(4.2.10), (4.2.11), (4.2.12) and (4.2.14), and rearranging the results according to mass- and momentum-conservation formulations in Eqs.(4.2.3) and (4.2.2), we obtain the continuity equation for the blood flow through a straight vessel as

$$\frac{\partial U_r}{\partial r} + \frac{1}{r}U_r + \frac{1}{r}\frac{\partial U_\theta}{\partial \theta} + \frac{\partial U_s}{\partial s} = 0, \tag{5.1.6}$$

and the momentum equations as

$$
\begin{aligned}
&U_r\frac{\partial U_r}{\partial r}+\frac{U_\theta}{r}\frac{\partial U_r}{\partial \theta}+U_s\frac{\partial U_r}{\partial s}-\frac{U_\theta^2}{r}\\
=&-\frac{1}{\rho}\frac{\partial p}{\partial r}-\frac{\mu}{\rho}\left(\frac{1}{r^2}\frac{\partial^2 U_r}{\partial \theta^2}-\frac{1}{r^2}\frac{\partial U_\theta}{\partial \theta}-\frac{1}{r}\frac{\partial^2 U_\theta}{\partial r\partial \theta}+\frac{\partial^2 U_r}{\partial s^2}-\frac{\partial^2 U_s}{\partial r\partial s}\right),
\end{aligned}
\tag{5.1.7}
$$

$$
\begin{aligned}
&U_r\frac{\partial U_\theta}{\partial r}+\frac{U_\theta}{r}\frac{\partial U_\theta}{\partial \theta}+U_s\frac{\partial U_\theta}{\partial s}+\frac{U_rU_\theta}{r}\\
=&-\frac{1}{\rho r}\frac{\partial p}{\partial \theta}-\frac{\mu}{\rho}\left(\frac{\partial^2 U_\theta}{\partial s^2}-\frac{1}{r}\frac{\partial^2 U_s}{\partial \theta\partial s}+\frac{1}{r}\frac{\partial U_\theta}{\partial r}\right.\\
&\left.-\frac{1}{r^2}U_\theta+\frac{\partial^2 U_\theta}{\partial r^2}-\frac{1}{r}\frac{\partial^2 U_r}{\partial \theta\partial r}+\frac{1}{r^2}\frac{\partial U_r}{\partial \theta}\right),
\end{aligned}
\tag{5.1.8}
$$

and

$$
\begin{aligned}
&U_r\frac{\partial U_s}{\partial r}+\frac{U_\theta}{r}\frac{\partial U_s}{\partial \theta}+U_s\frac{\partial U_s}{\partial s}\\
=&-\frac{1}{\rho}\frac{\partial p}{\partial s}-\frac{\mu}{\rho}\left(\frac{1}{r}\frac{\partial U_s}{\partial r}-\frac{1}{r}\frac{\partial U_r}{\partial s}+\frac{\partial^2 U_s}{\partial r^2}\right.\\
&\left.-\frac{\partial^2 U_r}{\partial s\partial r}+\frac{1}{r^2}\frac{\partial^2 U_s}{\partial \theta^2}-\frac{1}{r}\frac{\partial^2 U_\theta}{\partial s\partial \theta}\right).
\end{aligned}
\tag{5.1.9}
$$

As aforementioned in Section 4.3.2, under the usual physical and physiological conditions in tumour, the blood flow through a tumour vessel is steady, fully developed, laminar, and dominated by the pressure gradient along the vessel centre line. As a result, we are able to assume that $U_r = U_\theta = 0$, and $U_s = U_s(s)$, $p = p_c(s)$. Noticing that $H_b(s) = 1$, the flux Q_c flowing through a single straight tumour vessel can be described by the Poiseuille's law [Nichols and O'Rourke (2005)] as

$$
Q_c(s) = -\frac{\pi a^4(s)}{8\mu}\frac{\mathrm{d}p_c(s)}{\mathrm{d}s}. \tag{5.1.10}
$$

Substituting Eq.(5.1.10) into Eq.(4.3.9), and considering that $H_b(s) = 1$ and

$H_c(s) = 0$, we get

$$\frac{\mathrm{d}^2 p_c}{\mathrm{d}s^2} + \frac{4}{a(s)} \frac{\mathrm{d}a}{\mathrm{d}s} \frac{\mathrm{d}p_c}{\mathrm{d}s} = \frac{16\mu L_p(s)}{a^3(s)} \left[p_c(s) - p_i(s)\right]. \tag{5.1.11}$$

Similarly, another equation linking the blood pressures on both sides of vascular surface, or Eq.(4.3.15), becomes

$$\begin{aligned} &\frac{1}{2}\left[p_i(\mathbf{x}_0) - p_0\right] \\ =& -\frac{1}{2\pi} \int_{l_v} \int_0^{2\pi} \int_0^{2\pi} a(s) \frac{L_p(s)}{\kappa} \left[p_c(s) - p_i(s)\right] G(\mathbf{x}, \mathbf{x}_0) \mathrm{d}\theta_0 \mathrm{d}\theta \mathrm{d}s \\ &+ \frac{1}{2\pi} \int_{l_v} \int_0^{2\pi} \int_0^{2\pi} a(s) \left[p_i(s) - p_0\right] \nabla G(\mathbf{x}, \mathbf{x}_0) \mathbf{n}(\mathbf{x}) \mathrm{d}\theta_0 \mathrm{d}\theta \mathrm{d}s. \end{aligned} \tag{5.1.12}$$

Together with the inlet and outlet vascular flow conditions, we obtain a set of self-contained equations to calculate vascular blood flow pressure $p_c(s)$ and interstitial pressure $p_i(s)$ on the external vascular surface.

In Section 4.3.4, we have stated that, during the numerical procedure of our simulation, the vessel is divided into N_E cylindrical elements along its centre line, as shown in Fig.4.3. Within each element, all the physical variables are approximated to be constant. This makes the continuity condition imposed at the middle of every element. Based on the segments generated along the vessel, the differential equation (5.1.11) can be discretised by finite difference method. Both the first and second order derivatives in Eq.(5.1.11) are replaced with the three-point central difference formulae. This gives us a set of linear equations for the pressures inside and outside the vessel as

$$\sum_{j=1}^{N_E} T_{jn} p_c^{[j]} = -\frac{16\mu L_p^{[n]}}{(a_n)^3} p_i^{[n]}, \qquad n = 2, 3, \cdots, N_E - 1, \tag{5.1.13}$$

where T_{jn} is the finite difference computing matrix. According to Eqs.(3.2.2)

and (3.2.4), we have

$$T_{jn} = \begin{cases} -\dfrac{\Delta s_{n+1}}{(\Delta s_n + \Delta s_{n+1})\Delta s_n}\left(\dfrac{4a'_n}{a_n}\right) + \dfrac{2}{(\Delta s_n + \Delta s_{n+1})\Delta s_n} & j = n-1, \\ \dfrac{\Delta s_{n+1} - \Delta s_n}{\Delta s_n \Delta s_{n+1}}\left(\dfrac{4a'_n}{a_n}\right) - \dfrac{2}{\Delta s_n \Delta s_{n+1}} - \dfrac{16\mu L_p^{[n]}}{(a_n)^3} & j = n, \\ \dfrac{\Delta s_n}{(\Delta s_n + \Delta s_{n+1})\Delta s_{n+1}}\left(\dfrac{4a'_n}{a_n}\right) + \dfrac{2}{(\Delta s_n + \Delta s_{n+1})\Delta s_{n+1}} & j = n+1, \\ 0 & \text{else}, \end{cases} \tag{5.1.14}$$

in which

$$a'_n = \left(\frac{\mathrm{d}a}{\mathrm{d}s}\right)_n = \frac{\Delta s_{n+1}(a_n - a_{n-1})}{\Delta s_n(\Delta s_{n+1} + \Delta s_n)} + \frac{\Delta s_n(a_{n+1} - a_n)}{\Delta s_{n+1}(\Delta s_{n+1} + \Delta s_n)}, \tag{5.1.15}$$

$$\Delta s_n = s_n - s_{n-1}, \qquad \Delta s_{n+1} = s_{n+1} - s_n, \tag{5.1.16}$$

and s_n donates the mid-point position of the nth segment. Eqs.(5.1.13) to (5.1.16) are available for the segments when $2 \leq n \leq N_E - 1$. For the segments on the two ends of the vessel, i.e. $n = 1$ or $n = N_E$, Eq.(5.1.13) is solved together with the inlet and outlet vascular flow conditions respectively. In our model, the vessel is set to be connected with the arterial (upstream) and the venous (downstream) ends. As the afferent arteriole and efferent venule are not included in our simulations, the coupling effects between the inlet and outlet vascular flow conditions and tumour interstitial flow are ignored. As a result, the inlet and outlet vascular flow conditions can be introduced into Eq.(5.1.13) directly. If inlet vascular flow pressure p_a is given at the afferent

connecting point of the vessel, for segment $n = 1$, Eq.(5.1.13) is reduced to

$$\sum_{j=1}^{N_E} T_{j1} p_c^{[j]} = -\frac{16\mu L_p^{[1]}}{(a_1)^3} p_i^{[1]} - T_a p_a, \tag{5.1.17}$$

where

$$T_{j1} = \begin{cases} \dfrac{\Delta s_2 - \Delta s_a}{\Delta s_a \Delta s_2}\left(\dfrac{4a_1'}{a_1}\right) - \dfrac{2}{\Delta s_a \Delta s_2} - \dfrac{16\mu L_p^{[1]}}{(a_1)^3} & j = 1, \\ \dfrac{\Delta s_a}{(\Delta s_a + \Delta s_2)\Delta s_2}\left(\dfrac{4a_1'}{a_1}\right) + \dfrac{2}{(\Delta s_a + \Delta s_2)\Delta s_2} & j = 2, \\ 0 & \text{else}, \end{cases} \tag{5.1.18}$$

and

$$T_a = -\frac{\Delta s_2}{(\Delta s_a + \Delta s_2)\Delta s_a}\left(\frac{4a_1'}{a_1}\right) + \frac{2}{(\Delta s_a + \Delta s_2)\Delta s_a}. \tag{5.1.19}$$

In Eqs.(5.1.18) and (5.1.19),

$$\Delta s_a = s_1 - s_a, \tag{5.1.20}$$

where s_a stands for the afferent arterial connection point of the vessel; and a_1' is calculated through the three-point forward difference formula as

$$\begin{aligned} a_1' = \left(\frac{\mathrm{d}a}{\mathrm{d}s}\right)_1 =& \frac{\Delta s_2}{\Delta \bar{s}_2(\Delta s_2 - \Delta \bar{s}_2)} a_3 - \frac{\Delta \bar{s}_2}{\Delta s_2(\Delta s_2 - \Delta \bar{s}_2)} a_2 \\ & - \frac{(\Delta s_2 + \Delta \bar{s}_2)}{\Delta \bar{s}_2 \Delta s_2} a_1, \end{aligned} \tag{5.1.21}$$

in which

$$\Delta \bar{s}_2 = s_3 - s_1. \tag{5.1.22}$$

Similarly, when outlet vascular flow pressure p_v is given at the efferent connecting point of the vessel, for segment $n = N_E$, Eq.(5.1.13) is reduced to

$$\sum_{j=1}^{N_E} T_{jN_E} p_c^{[j]} = -\frac{16\mu L_p^{[N_E]}}{\left(a_{N_E}\right)^3} p_i^{[N_E]} - T_v p_v, \tag{5.1.23}$$

where

$$T_{jN_E} = \begin{cases} \dfrac{2}{(\Delta s_{N_E} + \Delta s_v)\Delta s_{N_E}} - \dfrac{\Delta s_v}{(\Delta s_{N_E} + \Delta s_v)\Delta s_{N_E}} \left(\dfrac{4a'_{N_E}}{a_{N_E}}\right) & j = N_E - 1, \\ \dfrac{\Delta s_v - \Delta s_{N_E}}{\Delta s_{N_E} \Delta s_v} \left(\dfrac{4a'_{N_E}}{a_{N_E}}\right) - \dfrac{2}{\Delta s_{N_E} \Delta s_v} - \dfrac{16\mu L_p^{[N_E]}}{\left(a_{N_E}\right)^3} & j = N_E, \\ 0 & \text{else}, \end{cases} \tag{5.1.24}$$

and

$$T_v = \frac{\Delta s_{N_E}}{(\Delta s_{N_E} + \Delta s_v)\Delta s_v} \left(\frac{4a'_{N_E}}{a_{N_E}}\right) + \frac{2}{(\Delta s_{N_E} + \Delta s_v)\Delta s_v}. \tag{5.1.25}$$

In Eqs.(5.1.24) and (5.1.25),

$$\Delta s_v = s_v - s_{N_E}, \tag{5.1.26}$$

where s_v stands for the efferent venous connection point of the vessel, and a'_{N_E} is calculated through the three-point backward difference formula as

$$\begin{aligned} a'_{N_E} = \left(\frac{\mathrm{d}a}{\mathrm{d}s}\right)_{N_E} =& \frac{(\Delta s_{N_E} + \Delta \bar{s}_{N_E})}{\Delta \bar{s}_{N_E} \Delta s_{N_E}} a_{N_E} + \frac{\Delta \bar{s}_{N_E}}{\Delta s_{N_E}(\Delta s_{N_E} - \Delta \bar{s}_{N_E})} a_{N_E - 1} \\ & - \frac{\Delta s_{N_E}}{\Delta \bar{s}_{N_E}(\Delta s_{N_E} - \Delta \bar{s}_{N_E})} a_{N_E - 2}, \end{aligned} \tag{5.1.27}$$

in which

$$\Delta\bar{s}_{N_E} = s_{N_E} - s_{N_E-2}. \tag{5.1.28}$$

If the inlet vascular flow condition at the arterial point is given by the perfused flux Q_a rather than pressure p_a, according to the Poiseuille's law, when adopting the three-point forward difference formula in Eq.(3.2.7) for the first order derivative, we have

$$p_a = \frac{8\mu Q_a H_b^{[1]} \Delta\bar{s}_a \Delta s_a}{\pi (a_1)^4 (\Delta s_a + \Delta\bar{s}_a)} + \frac{(\Delta s_a)^2 p_c^{[2]}}{(\Delta s_a)^2 - (\Delta\bar{s}_a)^2} - \frac{(\Delta\bar{s}_a)^2 p_c^{[1]}}{(\Delta s_a)^2 - (\Delta\bar{s}_a)^2}, \tag{5.1.29}$$

in which

$$\Delta\bar{s}_a = s_2 - s_a. \tag{5.1.30}$$

Substituting Eq.(5.1.29) into Eq.(5.1.17), and rearranging the terms, for segment $n = 1$, we have

$$\sum_{j=1}^{N_E} \hat{T}_{j1} p_c^{[j]} = -\frac{16\mu L_p^{[1]}}{(a_1)^3} p_i^{[1]} - \frac{8\mu Q_a T_a \Delta\bar{s}_a \Delta s_a}{\pi (a_1)^4 (\Delta s_a + \Delta\bar{s}_a)}, \tag{5.1.31}$$

where

$$\hat{T}_{j1} = \begin{cases} \dfrac{\Delta s_2 - \Delta s_a}{\Delta s_a \Delta s_2}\left(\dfrac{4a_1'}{a_1}\right) - \dfrac{2}{\Delta s_a \Delta s_2} - \dfrac{16\mu L_p^{[1]}}{(a_1)^3} + \dfrac{T_a (\Delta\bar{s}_a)^2}{(\Delta s_a)^2 - (\Delta\bar{s}_a)^2} & j = 1, \\ \dfrac{\Delta s_a}{(\Delta s_a + \Delta s_2)\Delta s_2}\left(\dfrac{4a_1'}{a_1}\right) + \dfrac{2}{(\Delta s_a + \Delta s_2)\Delta s_2} - \dfrac{T_a (\Delta s_a)^2}{(\Delta s_a)^2 - (\Delta\bar{s}_a)^2} & j = 2, \\ 0 & \text{else}, \end{cases} \tag{5.1.32}$$

As derived in Section 4.3.4, Eq.(5.1.12) is discretised as

$$\sum_{j=1}^{N_E}\left\{\delta_{nj}-2\bar{B}_n^{[j]}-\frac{2L_p^{[j]}}{\kappa}\bar{A}_n^{[j]}\right\}p_i^{[j]}$$
$$=-\sum_{j=1}^{N_E}\frac{2L_p^{[j]}}{\kappa}\bar{A}_n^{[j]}p_c^{[j]}+p_0\left\{1-\sum_{j=1}^{N_E}2\bar{B}_n^{[j]}\right\}. \tag{5.1.33}$$

Then, when the inlet and outlet vascular flow pressures are given, we can solve Eqs.(5.1.13), (5.1.17), (5.1.23) and (5.1.33) together through iteration to obtian the solution for the pressures inside the vessel and on the external vascular surface. The detailed procedure is summarised as below:

1) Set initial guess for blood pressure $p_c(s)$ inside the vessel.

2) Evaluate the right-hand side of Eq.(5.1.33).

3) Solve Eq.(5.1.33) to obtain tumour interstitial pressure $p_i(s)$ on the external surface of the vessel.

4) Evaluate the right-hand sides of Eqs.(5.1.13), (5.1.17), and (5.1.23).

5) Solve Eqs.(5.1.13), (5.1.17), and (5.1.23) together to obtain p_c.

6) Go back to step 2 and repeat the procedure until convergence has been achieved, or the difference in either $p_c(s)$ or $p_i(s)$ from two successive steps is sufficiently small.

If the vascular inlet condition at the arterial point is given by Q_a instead of p_a, we only need to adjust the fourth step in the above numerical procedure correspondingly.

In order to check the convergence of our simulations, we define a relative

round error function as

$$Er = \mathrm{Max}\left\{ \frac{\left| p_k^{[j]} - p_{k-1}^{[j]} \right|}{p_k^{[j]}} \right\} \quad 1 \leq j \leq N_E, \tag{5.1.34}$$

in which, $p_k^{[j]}$ represents the iterative result for either p_i or p_c at the kth iteration step when $k \geq 2$. We are able to adopt the relative round error function Er in our simulations because the value of $\left| p_k^{[j]} \right|$ is always larger than zero in our model. If $Er \to 0$, the solution would approach to the exact one. However, in practical, when Er is less than a very small positive value ϵ, we conclude that our simulations are successful, and the obtained results are accurate and consistent with all the physical and constrain conditions.

5.2 Convergence and validation study

Before investigating tumour blood flow by our model, we have to be sure that our numerical procedure is mesh independent and convergent. A test case is set up, in which a single straight permeable vessel with length l_v = 1 cm is embedded in a solid tumour to a large extent with peripheral pressure $p_0 = 6.666 \times 10^2$ g cm^{-1}s^{-2}. The vessel radius is set as $a = 0.01$ cm, vessel permeability as $L_p = 1 \times 10^{-9}$ g^{-1}cm^{2}s, and tumour interstitial hydraulic conductivity as $\kappa = 1 \times 10^{-10}$ g^{-1}cm^{3}s. In the meantime, the inlet vascular flow condition is given as $p_a = 5.59952 \times 10^4$ g cm^{-1}s^{-2}, and the outlet condition as $p_v = 1.19990 \times 10^4$ g cm^{-1}s^{-2}. Since we regard the blood as incompressible Newtonian fluid, blood density $\rho = 1.05$ g cm^{-3} and dynamic viscosity μ = 4 g cm^{-1}s^{-1} remain constant in this thesis.

Fig.5.2a plots the dependence of the relative flux coefficient γ_Q[i] on number

[i] the relative flux coefficient γ_Q is plotted on a linear-log$_{10}$ scale. The same scale for γ_Q

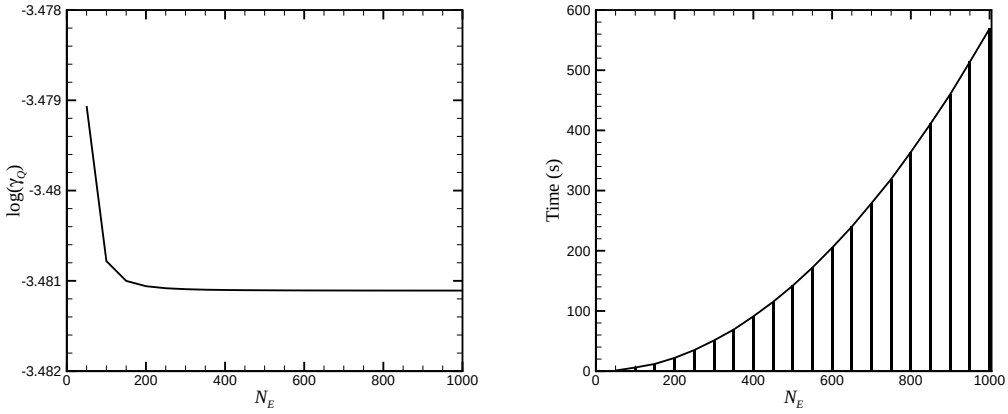

(a) **(b)**

Figure 5.2: Dependence of (a) the relative flux coefficient γ_Q and (b) calculation time on N_E when $Er = 1. \times 10^{-6}$.

of discretised segments N_E when $Er = 1. \times 10^{-6}$. The results in Fig.5.2a indicate that the value of γ_Q converges to a constant (mesh independent) rapidly when N_E increases. However, an increase of N_E induce the calculation time or CPU time[ii] to rise dramatically, as depicted in Fig.5.2b. The numerical simulation time can be affected by some factors. To take the present study case as an example, since the vessel is rigid, all of the elements in the coefficient matrices derived by FDM and BEM are constant throughout the entire simulation. Therefore, these two matrices can be composed and stored before the iteration. The coefficient matrix obtained in FDM is a tridiagonal system, which costs computer $3N_E$ FLOPS (Floating point Operations Per Second) to construct it. However, the global matrix derived in BEM is fully populated, which takes the computer $(N_E)^2$ FLOPS to calculate all the coefficients in it. When the iteration starts, within each step, the tridiagonal system in FDM can be solved

is used throughout this thesis.

[ii]CPU time (calculation or simulation time) on a personal laptop with 2.00 GHz Intel Centrino Duo processor. The same definition for simulation time is used throughout this thesis.

by Thomas' Algorithm [Anderson (1995)], which requires $O(N_E)$ FLOPS to do the calculation [Hamming (1986)]. As to the fully populated matrix in BEM, Gauss-Seidel method [Schilling and Harris (2000)] can be adopted to solve it. Gauss-Seidel method is an iterative method, and the calculation time taken by each iterative step of it is $O(N_E)^2$ FLOPS [Schilling and Harris (2000)]. The convergence of Gauss-Seidel method is guaranteed when the matrix is either diagonally dominant or symmetric and positive definite. Though sometimes the Gauss-Seidel method may be convergent even though neither of the above two conditions is satisfied, the convergence rate could be very slow and the number of iteration could be larger than N_E FLOPS. Under this circumstance, we can apply Gauss Elimination method [Schilling and Harris (2000)] to solve the matrix, whose calculation time is in the order of $(N_E)^3$ FLOPS [Schilling and Harris (2000)]. All these features indicate that, along the increasing of N_E, the calculation time spent on calculating the coefficient matrices and every step of iteration increases rapidly. Moreover, when N_E increases, the number of iterative steps to achieve the convergence normally grows, because the convergence rate of simulation usually slows down along the decreasing of the size of discretised segment. Under such a circumstance, multigrid method [Briggs *et al.* (2000)] can be adopted to accelerate the convergence rate. The basic idea of multigrid method is to use the results obtained from coarser grids as the initial solution for the finer grids through interpolation. In this way, the number of iterative steps for the finer grids could be reduced. Considering that the convergence rate with coarser grids is usually faster, the convergence rate for the entire simulation procedure can be accelerated.

For some other cases which will be investigated later in this thesis, the simulation time varies significantly compared with the present test case. For example, if the vessel is compliant, the vessel radius relies on the transmural

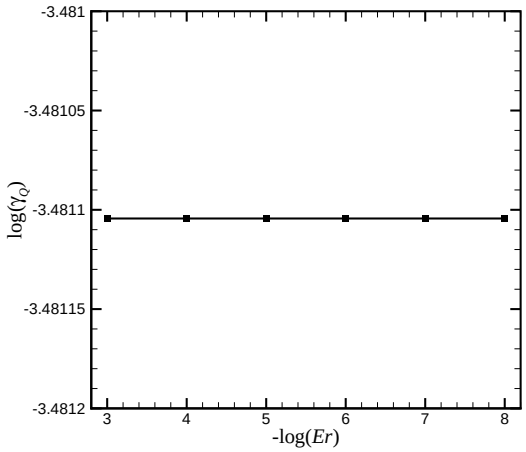

Figure 5.3: Dependence of the relative flux coefficient $\gamma_{_Q}$ on Er when element size $\delta s_j = 0.2a$ $(j = 1, 2, \cdots, N_E)$

pressure difference monotonically along the vessel. Then, there would be another iteration external to the numerical procedure, which is stated in Section 5.1, to calculate vessel radius. Furthermore, in each step of this new iteration, the coefficient matrices of FDM and BEM have to be updated. Thus, it can be expected that there would be a tremendous increase of computation time for that case relative to the current study case (Section 7.2). Another situation is that the configuration of tumour vasculature becomes complicated, such as it contains branches with multiple generations. This could lead to billions of coefficients in FDM and BEM, which might cause our simulation to encounter with prohibitive computer memory and CPU, mainly because the global matrix of BEM is fully populated. A realistic approach is therefore to use domain decomposition method [Wu and Taylor (2003)] which has been adopted in water wave problems (Section 9.1).

Fig.5.3 plots the dependence of the relative flux coefficient $\gamma_{_Q}$ on Er when $N_E = 500$. It shows that there is no significant difference in our simulation results when Er decreases from $1. \times 10^{-3}$ to $1. \times 10^{-8}$. Therefore, for the present

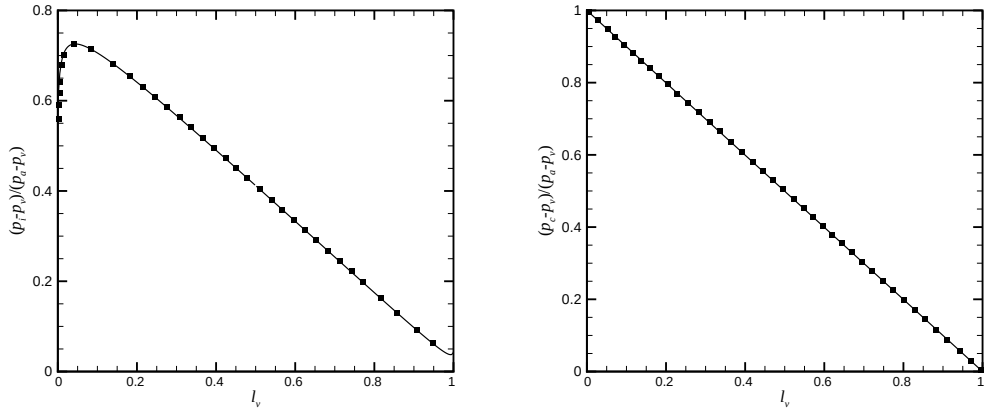

(a) **(b)**

Figure 5.4: Distributions of (a) interstitial pressures on the external vascular surface and (b) vascular flow pressures. Solid line: present results; square symbols: Pozrikidis and Farrow (2003).

study case, taking the simulation time into account, our calculation solution is accurate enough when we choose the relative error as $Er = 1. \times 10^{-6}$, and the segment size as $\delta s_j = 0.2a$ $(j = 1, 2, \cdots, N_E)$ which corresponds to $N_E = 500$.

In the work conducted by Pozrikidis and Farrow (2003), they investigated the case when the tumour vessel has the same geometrical sizes as here, while they let $L_p = 2.5 \times 10^{-10}$ g^{-1}cm^{2}s and $\kappa = 2.5 \times 10^{-11}$ g^{-1}cm^{3}s. They set the tumour peripheral pressure to be equal to the outlet vascular flow pressure, or $p_0 = p_v$. Their results provide a good bench mark to validate our model. Fig.5.4 presents the pressures inside the vessel and the interstitial pressures along the external vascular surface obtained by Pozrikidis and Farrow (2003) and by our model. It shows that the results are in excellent agreement.

Chapter 6

Effects of Physical Variables on the Blood Flow Environment in Tumour

Having validated the rationality of our model and examined the efficiency of the numerical procedure, we proceed to investigate the effects of different physical parameters on tumour blood flow. The study case in this chapter is a single straight permeable vessel embedded in a solid tumour whose surface is far away from the vessel. The vessel radius and length are set as $a = 0.01$ cm and $l_v = 1$ cm respectively. For the tumour vessel with radius $a = 0.01$ cm ($a \geq 0.003$ cm), the physiological and physical parameters relative to tumour blood flow are summarised in Table6.1, which provide us the reference range of our simulations. In order to present our simulation results clearly, we choose three basic physical parameters, pressure $\check{p} = 1.33322 \times 10^4$ g cm^{-1}s^{-2}, vascular permeability $\check{L}_p = 10^{-8}$ g^{-1}cm^{2}s, and vessel radius $\check{a} = 0.01$ cm, as the characteristic units (natural units). For the simulation results, the physiological and physical parameters relative to tumour blood flow, including blood

Table 6.1: Physical parameters of tumour blood flow when $a \geq 0.003$ cm

Parameter (dimensional)	Value
Arterial pressure p_a (g cm^{-1}s^{-2})	$(5.93283 \pm 1.29322) \times 10^4$ [Jain (1988), Wiig (1982)]
Venous pressure p_v (g cm^{-1}s^{-2})	$(1.19990 \pm 0.33331) \times 10^4$ [Jain (1988), Wiig (1982)]
Blood density ρ (g cm^{-3})	1.05 [Pedley (1980)]
Blood dynamic viscosity μ (g cm^{-1}s^{-1})	4×10^{-2} [Pedley (1980)]
Tissue hydraulic conductivity κ (g^{-1}cm^{3}s)	$3 \times 10^{-11} \sim 1.5 \times 10^{-10}$ [Swabb *et al.* (1974)]
Vascular Permeability L_p (g^{-1}cm^{2}s)	$2.7 \times 10^{-10} \sim 2.1 \times 10^{-9}$ [Baish *et al.* (1997)]

pressure, vessel radius, vessel length, vessel permeability, tumour interstitial hydraulic conductivity parameter, and flow flux, are divided by the dimensional normalisation constants derived according to the above three natural units, and represented by $p^{\mathbf{n}}$, $a^{\mathbf{n}}$, $l_v^{\mathbf{n}}$, $L_p^{\mathbf{n}}$, $\kappa^{\mathbf{n}}$, and $Q^{\mathbf{n}}$ respectively. The values of the dimensional normalisation constants are listed in Table6.2.

6.1 Influence of systemic pressure gradients on tumour blood flow

Pressure gradient is the prime force to drive blood flow through tumour vessels and transport flux from vessels into tumour interstitium. The flow through a

tumour vessel is dominated by the pressure difference between inlet vascular flow pressure p_a at the arterial end and outlet vascular flow pressure p_v at the venous end of the vessel, the transvascular flux is driven by the transmural pressure difference of pressure $p_c(s)$ in the vessel and interstitial pressure $p_i(s)$ on the external vascular surface, and the tumour interstitial blood flow is driven by the pressure difference between $p_i(s)$ and tumour peripheral pressure p_0. Therefore, pressure difference $p_a - p_v$ and $p_a - p_0$ are the two determinant issues for tumour blood flow.

6.1.1 Effects of inlet outlet vascular flow pressures on tumour blood flow

For the investigations in this section, we let tumour tissue hydraulic coefficient $\kappa = 10^{-10}$ g^{-1}cm^{3}s and vessel permeability $L_p = 10^{-9}$ g^{-1}cm^{2}s remain constant. When we set the inlet vascular flow pressure as $p_a = 5.93283 \times 10^4$ g cm^{-1}s^{-2}, and the tumour peripheral pressure as $p_0 = 6.666 \times 10^2$ g cm^{-1}s^{-2}, the distributions of vascular flow pressure $p_c(s)$ with different outlet vascular flow pressure p_v are plotted in Fig.6.1a. Along the increasing of p_v, $p_c(s)$ is elevated, and the variation of $p_c(s)$ near the venous end is more significant than that around the arterial end. The vascular flow pressure at the arterial point remains the same under different p_v since the inlet vascular flow pressure p_a is not changed. According to the coupling effect relationship between the vascular flow and tumour interstitial flow in Eq.(4.3.13), which is

$$\kappa \frac{\partial p_i(s)}{\partial n} = L_p(s) \left[p_c(s) - p_i(s) \right], \tag{6.1.1}$$

along the increasing of pressure $p_c(s)$ in the vessel, transmural pressure difference $p_c(s) - p_i(s)$ is elevated. Consequently, the interstitial pressure gradient

Table 6.2: Normalisation formulae for physical and physiological parameters

Normalisation formula	Normalisation parameter value
Vessel typical length $l_v^{\mathbf{n}} = \dfrac{l_v}{\check{a}}$	$\check{a} = 0.01$ cm
Vessel radius $a^{\mathbf{n}} = \dfrac{a}{\check{a}}$	$\check{a} = 0.01$ cm
Pressure $p^{\mathbf{n}} = \dfrac{p}{\check{p}}$	$\check{p} = 1.33322 \times 10^4$ g cm^{-1}s^{-2}
Tissue hydraulic parameter $\kappa^{\mathbf{n}} = \dfrac{\kappa}{\check{\kappa}}$	$\check{\kappa} = \check{a}\check{L}_p = 10^{-10}$ g^{-1}cm^{3}s
Vascular permeability $L_p^{\mathbf{n}} = \dfrac{L_p}{\check{L}_p}$	$\check{L}_p = 10^{-8}$ g^{-1}cm^{2}s
Blood flow velocity $U^{\mathbf{n}} = \dfrac{U}{\check{U}}$	$\check{U} = \check{p}\check{L}_p = 1.33322 \times 10^{-4}$ cm s^{-1}
Flow flux $Q^{\mathbf{n}} = \dfrac{Q}{\check{Q}}$	$\check{Q} = \check{a}^2\check{p}\check{L}_p = 1.33322 \times 10^{-8}$ cm^{3}s^{-1}

$\partial p_i(s)/\partial n$ on the exterior vascular surface is increased since vascular permeability L_p and tumour tissue hydraulic conductivity coefficient κ are constant. In Figs.6.1c and 6.1d, we present the distributions of transmural pressure difference $p_c - p_i$ and extravasation flux $L_p a\,(p_c - p_i)$ along the vessel together. Due to that vessel permeability and radius remain constant in the current investigation, the transmural pressure difference and the extravasation flux share the same curve, but with different scales. Noticing that the interstitial pressures on the exterior vascular surface are elevated, and considering that the vascular flow pressures do not change significantly around the arterial point of the vessel due to the fixed inlet vascular flow pressure p_a, the extravasation flux in that area is decreased along the increasing of outlet vascular flow

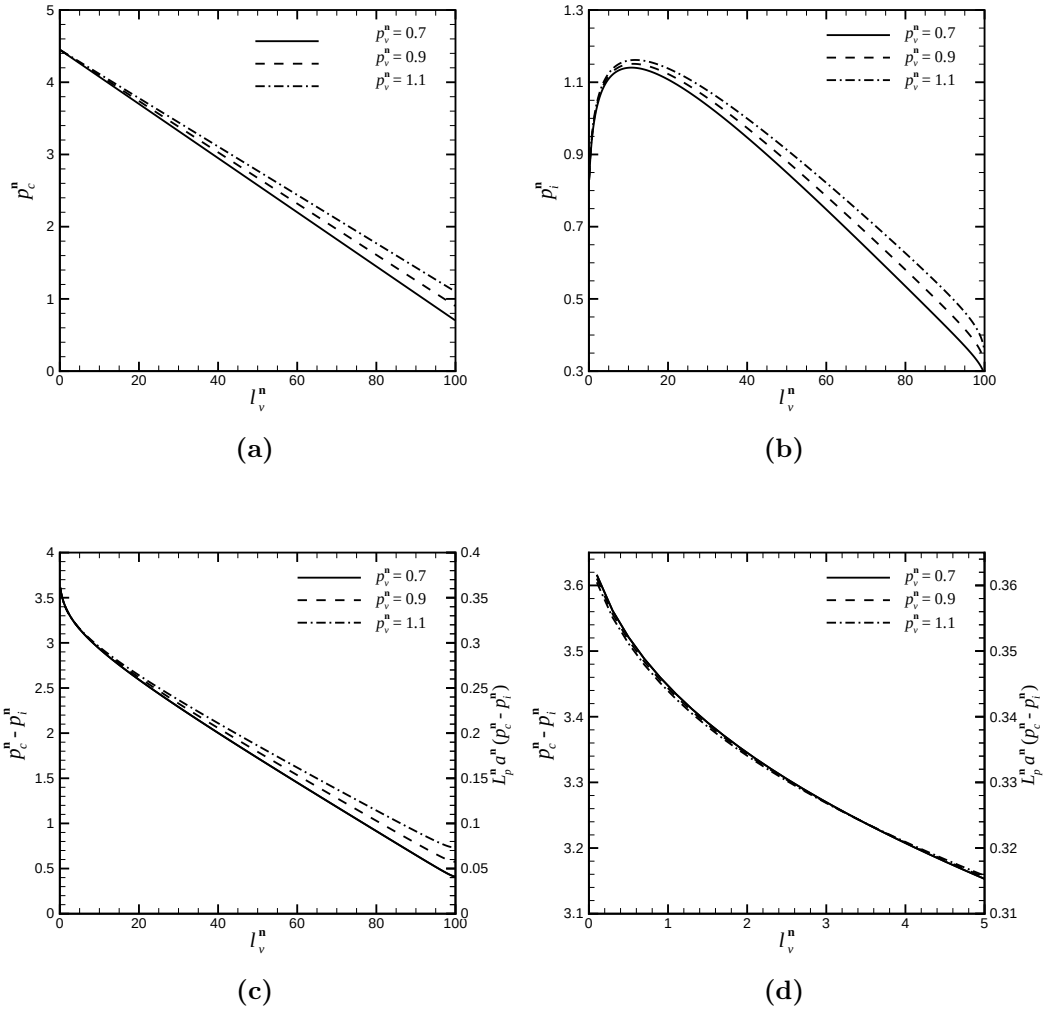

Figure 6.1: Distributions of (a) vascular flow pressures, (b) interstitial pressures on the external vascular surface, and (c) (d) extravasation flux and transmural pressure difference, when $p_a^{\mathbf{n}} = 4.45$ and $p_0^{\mathbf{n}} = 0.05$.

pressure p_v (Fig6.1d). However, the results in Fig.6.1c indicate that, when the outlet vascular flow pressure is raised at given inlet vascular flow pressure and tumour peripheral pressure, the average amount of the extravasation flux over the entire vessel is improved despite the elevated interstitial pressures.

Supposing that outlet vascular flow pressure p_v could be elevated to the

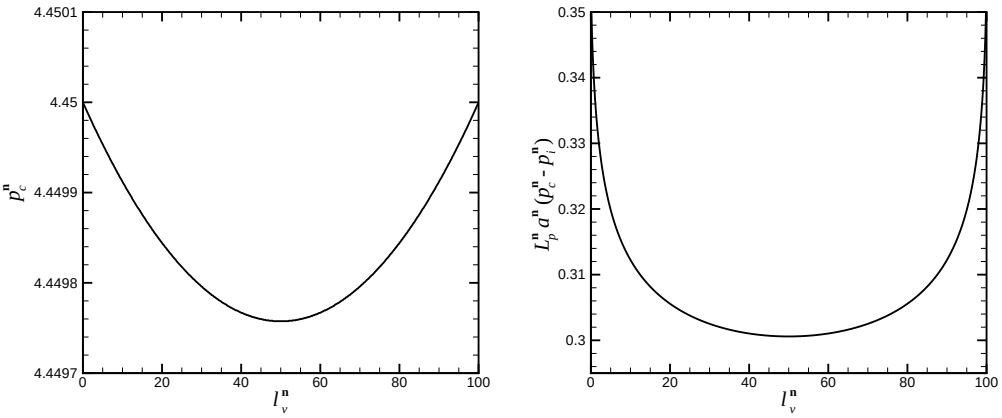

(a) **(b)**

Figure 6.2: Distributions of (a) vascular flow pressures, and (b) extravasation flux, when $p_a^{\mathbf{n}} = p_v^{\mathbf{n}} = 4.45$ and $p_0^{\mathbf{n}} = 0.05$.

special situation as $p_v \to p_a$, there would be no flux flowing through the vessel according to the Poiseuille's law if the vessel is not leaky, and pressure $p_c(s)$ in the vessel is equal to p_a. However, when the vessel is permeable, due to the difference between inlet vascular flow pressure p_a and tumour peripheral pressure p_0, there would be some flux exceeded from the vessel into the tumour interior, as displayed in Fig.6.2b. Furthermore, because $p_v = p_a$, the blood would flow into tumour from both arterial and venous ends of the vessel (Fig.6.2b). Under such a special circumstance, p_c decreases from p_a at the arterial point to reach the minimum at the middle point of the vessel, then rises up to p_v (p_a) at the venous point, as plotted in Fig.6.2a. Meanwhile, the value of the relative flux coefficient γ_Q defined in Eq.(5.0.4) would be higher than 100%. However, we should be aware that, under such a special situation, the Poiseuille's law in Eq.(5.1.10) for the vascular flow in our model is not accurate enough as it requires the velocity of the flow along the radius direction to be much smaller than the velocity along the vessel centre line. To

get accurate calculation results for this particular case, the governing equation for the vascular blood flow has to be revised. Nevertheless, it is necessary for us to notice that this special case of $p_a = p_v$ is very rare in practical tumour blood flow environment. The investigation presented here is for the purpose of illustrating the particular flow phenomena for such an extreme case.

If we let the outlet vascular flow pressure decrease to reach the tumour peripheral pressure as $p_v \to p_0$, there would be some flux transported back into the vessel from tumour interior near the venous end (intravascular flow), as shown in Fig.6.3b. This is because the flux exceeded from the upstream part of the vessel into tumour interior elevates the interstitial pressures within the entire tumour interior, which are higher than the pressures near the venous end in the vessel, as shown in Fig.6.3a. The intravascular flow is very harmful for cancer treatment as it reduces the extravasation flux. It may also induce metastasis of tumour cells since some of them might be transported together with the intravascular flow into circulation system and delivered to other healthy organs.

When outlet venous pressure $p_v = 1.19990 \times 10^4$ g cm^{-1}s^{-2} and tumour peripheral pressure $p_0 = 6.666 \times 10^2$ g cm^{-1}s^{-2} remain constant, along the increasing of p_a, vascular flow pressure $p_c(s)$ is increased, as shown in Fig.6.4a. In this circumstance, the variation of vascular flow pressure near the arterial point is more remarkable relative to that near the venous end of the vessel. According to the same mechanism as the case investigated above, the interstitial pressures along the external vascular surface are elevated, and the average transmural pressure difference and extravasation flux over the whole vessel are improved, as presented in Figs.6.5b and 6.4 respectively.

When we increase p_a and p_v together but letting pressure difference $p_a - p_v$ remain unchanged at a given tumour peripheral pressure, vascular flow pres-

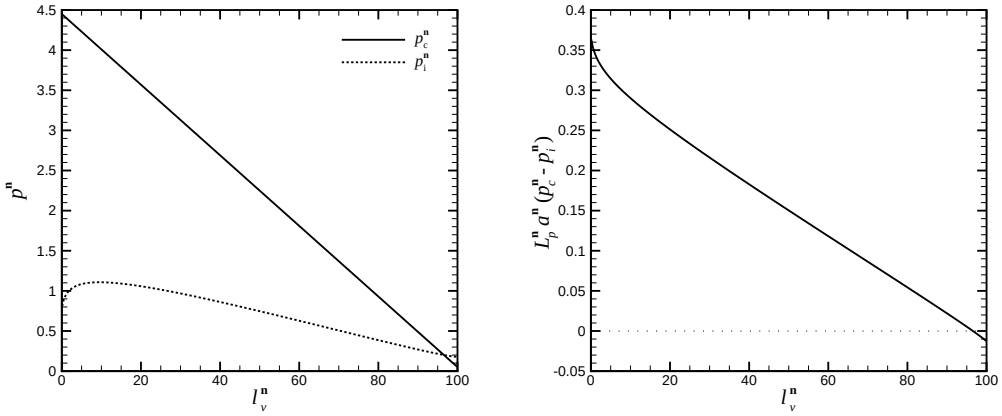

(a) **(b)**

Figure 6.3: Distributions of (a) vascular flow pressures, interstitial pressures on the external vascular surface, and (b) extravasation flux, when $p_a^{\mathbf{n}} = p_0^{\mathbf{n}} = 0.05$ and $p_a^{\mathbf{n}} = 4.45$.

sures almost increase uniformly along the vessel. This leads to the interstitial pressures on the external vascular surface, the transmural pressure difference, and the extravasation flux all elevated along the vessel, as presented in Fig.6.5.

The results presented above indicate that increasing the inlet vascular flow pressure and/or the outlet vascular flow pressure at a given tumour peripheral pressure can improve the amount of the extravasation flux, which would be beneficial for the delivery of anti-cancer agents with heavy weight through vessel surface into tumour interior.

Fig.6.6 presents the dependence of the relative flux coefficient γ_Q on p_a and p_v at a given tumour peripheral pressure p_0. We observe that γ_Q displays an upward trend along the increasing of outlet vascular flow pressure p_v, when p_v is within the range in the figure and inlet vascular flow pressure p_a is constant. However, γ_Q presents a downward trend along the increasing of p_a when p_v is fixed. At a given p_0, when p_a is constant, elevating p_v lowers pressure difference $p_a - p_v$, which causes the perfused flux into the vessel, Q_a, to decrease according

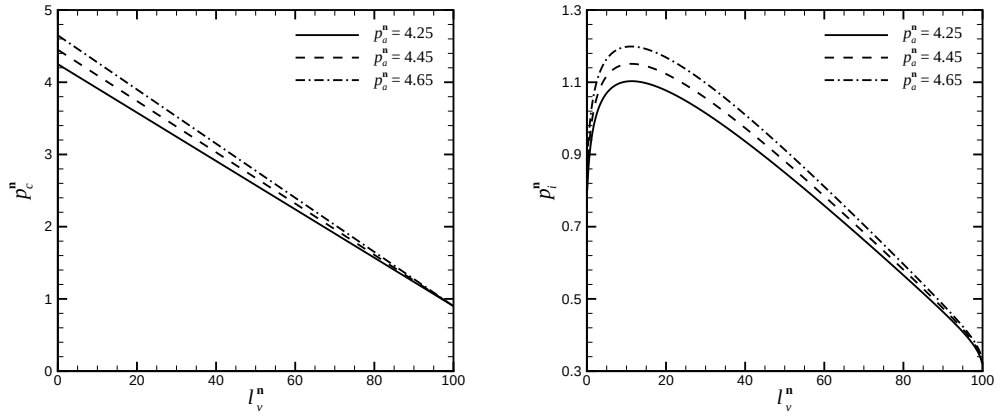

(a) **(b)**

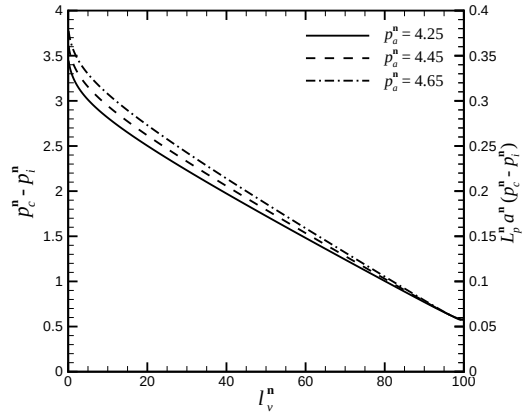

(c)

Figure 6.4: Distributions of (a) vascular flow pressures, (b) interstitial pressures on the external vascular surface, and (c) extravasation flux and transmural pressure differences along vessel, when $p_v^{\mathbf{n}} = 0.9$ and $p_0^{\mathbf{n}} = 0.05$.

to the Poiseuille's law. However, in this circumstance, the extravasation flux is increased (Fig.6.1c). As a result, the relative flux coefficient γ_Q is improved, as shown in Fig.6.6a. On the contrary, when p_v is fixed, increasing p_a leads to pressure gradient $p_a - p_v$ elevated, which causes relatively more flux flowing through the vessel. Under such a circumstance, though the extravasation flux

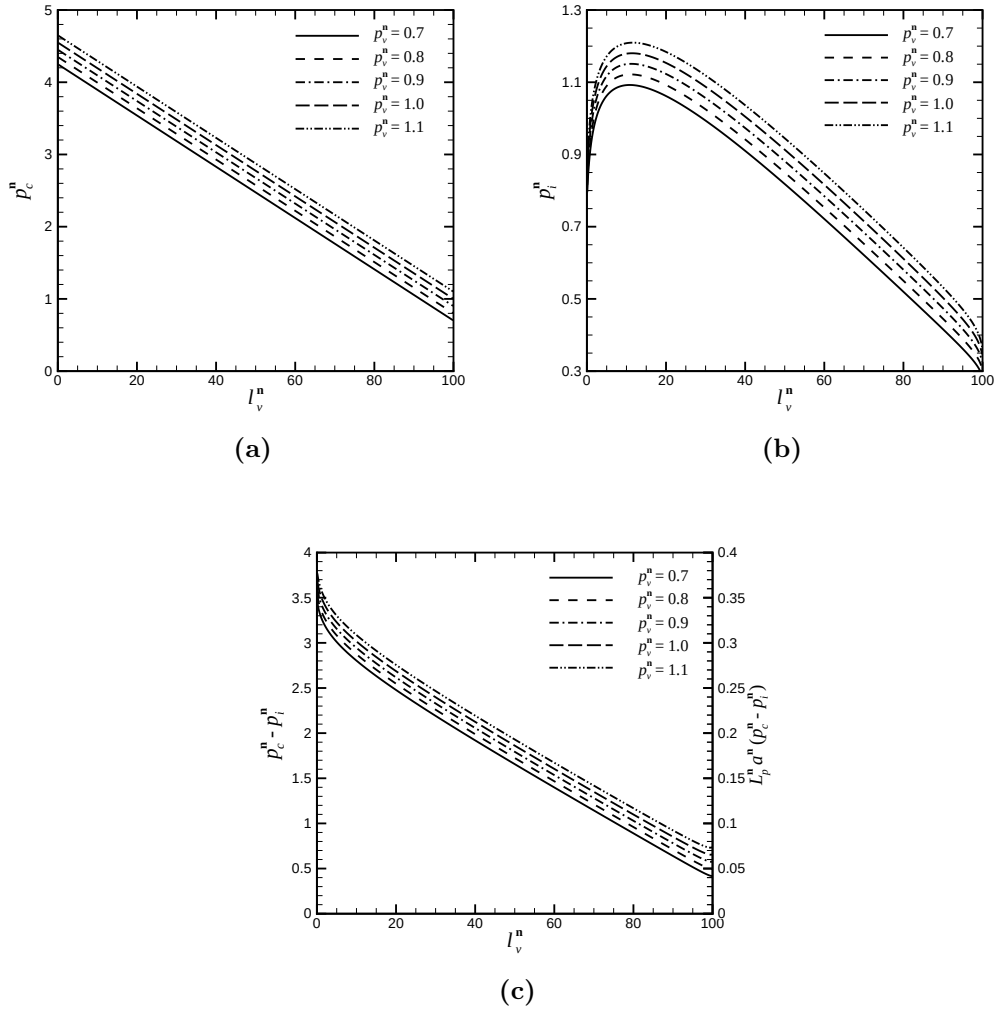

Figure 6.5: Distributions of (a) vascular flow pressures, (b) interstitial pressures on the external vascular surface, and (c) extravasation flux and transmural pressure difference, when $p_a^{\mathbf{n}} - p_v^{\mathbf{n}} = 3.55$ and $p_0^{\mathbf{n}} = 0.05$.

is improved (Fig.6.4c), γ_Q decreases, as shown in Fig.6.6b. When p_a and p_v are raised together while pressure difference $p_a - p_v$ remains constant, the extravasation flux is increased (Fig.6.5c), whereas the flux flowing through the vessel is almost unchanged, since we notice that the distribution curves for the pressures in the vessel are parallel with each other, as plotted in Fig.6.5a.

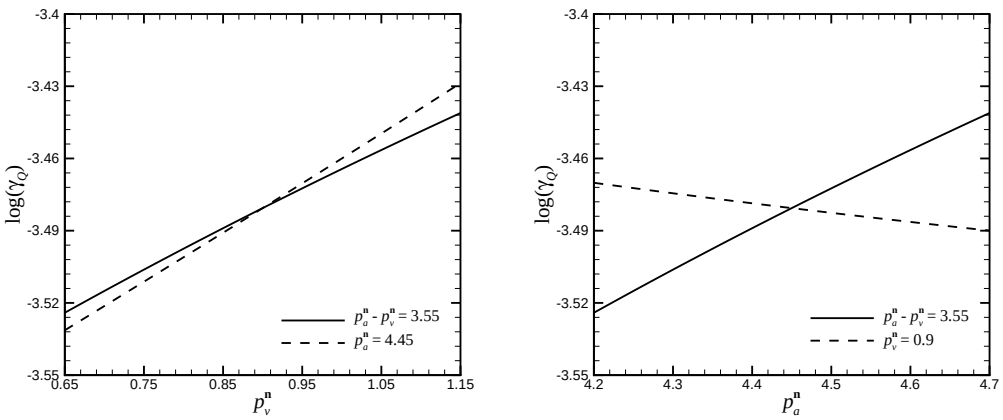

Figure 6.6: Dependence of the relative flux coefficient γ_Q on (a) outlet vascular flow pressure p_v and (b) inlet vascular flow pressure p_a when $p_0^{\mathbf{n}} = 0.05$.

Then, γ_Q is improved in this situation.

Based on the above discussions, if we would like to improve the effectiveness of radiotherapy and chemotherapy as well as to reduce their side effects, elevating the tumour outlet venous pressure within reasonable ranges is a good option to achieve the goal. However, venous pressure p_v in tumour is always lower compared with that in normal tissues [Jain (1988)]. Lowered p_v not only deceases the extravasation flux and the value of the relative flux coefficient γ_Q, but also might cause intravascular flow from the tumour interior into the vessel when it is decreased to some level, for example when p_v tends to tumour peripheral pressure p_0 in our model. This could cause tumour cells to be transported into circulation system and delivered to other normal tissues (metastasis). These factors indicate that the abnormal tumour blood environment forms physiological barriers for cancer treatment, and plays an important role in tumour growth.

Our results and conclusions presented here is supported by the previously

study by Netti *et al.* (1999). They have shown that angiotensin II can increase systemic vessel blood pressure in mice and can create an increase of pressure gradient across tumour vessel walls, which can improve the delivery of specific antibodies in solid tumors. However, elevating the systemic vascular flow pressure in human body is very critical because it might lead to tachycardia, stroke and some other hypertension related disease. Nevertheless, once these side effects are carefully monitored, our results still have potential in practical applications.

6.1.2 Influence of tumour peripheral pressure on tumour blood flow

As aforementioned in the beginning of Section 6.1, the tumour interstitial blood flow is driven by the pressure difference between interstitial pressure $p_i(s)$ on the external vascular surface and tumour peripheral pressure p_0. Considering the symmetrical geometry of the study case in this chapter, and noticing that the blood flow is dependent on the pressure gradients linearly in our model, one can conclude that the variation of the extravasation flux along the increasing of p_0 at given p_a and p_v is similar to the situation when we decrease p_a and p_v together with constant pressure difference $p_a - p_v$ at a given p_0. In the later situation, the vascular flow pressures are affected by the variations of p_a and p_v, then the interstitial pressures, the transmural pressure difference, and the extravasation flux are changed correspondingly. However, if we increase p_0 at given p_a and p_v, the interstitial pressure gradients are reduced. This requires transmural pressure difference $p_c(s) - p_i(s)$ to decrease according to the coupling effect relationship defined in Eq.(6.1.1). Since the inlet and outlet vascular flow pressures are constant, the variation of vascular flow pressure $p_c(s)$ is insignificant along the variation of p_0, as presented in Fig.6.7a.

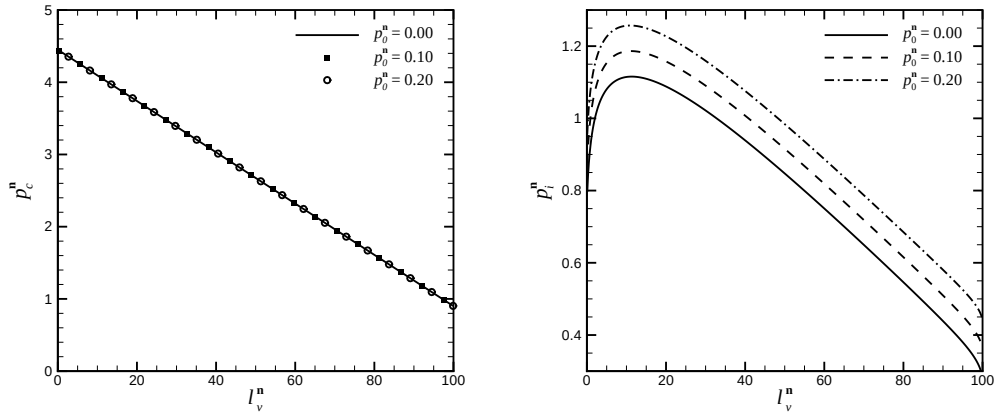

(a) **(b)**

Figure 6.7: Distributions of (a) vascular flow pressures and (b) interstitial pressures on the external surface along vessel when $p_a^{\mathbf{n}} = 4.45$ and $p_v^{\mathbf{n}} = 0.9$.

Consequently, interstitial pressure $p_i(s)$ on the exterior vascular surface is elevated, as displayed in Fig.6.7b. Meanwhile, the decreasing of the transmural pressure difference makes the extravasation flux decreased. This leads to that the relative flux coefficient γ_Q is reduced along the increasing of p_0 because the perfused flux into the vessel is almost unchanged, as plotted in Fig.6.8. In Fig.6.8b, we present the dependence of γ_Q on p_0 at given p_a and p_v (solid line), and the dependence on p_v when $p_a - p_v$ is constant at a given p_0. They are parallel with each other, which confirms the above analysis that these two situations have the similar effects on tumour blood flow. The results presented here indicate that the elevated peripheral pressure is harmful for transporting macromolecules with heavy weight from vessel into tumour interior and the effectiveness of radiotherapy and chemotherapy.

In the foregoing investigations, we have separately studied the effects of inlet vascular arterial pressure p_a, outlet vascular venous pressure p_v and tumour peripheral pressure p_0 on tumour blood flow, whereas we are aware that

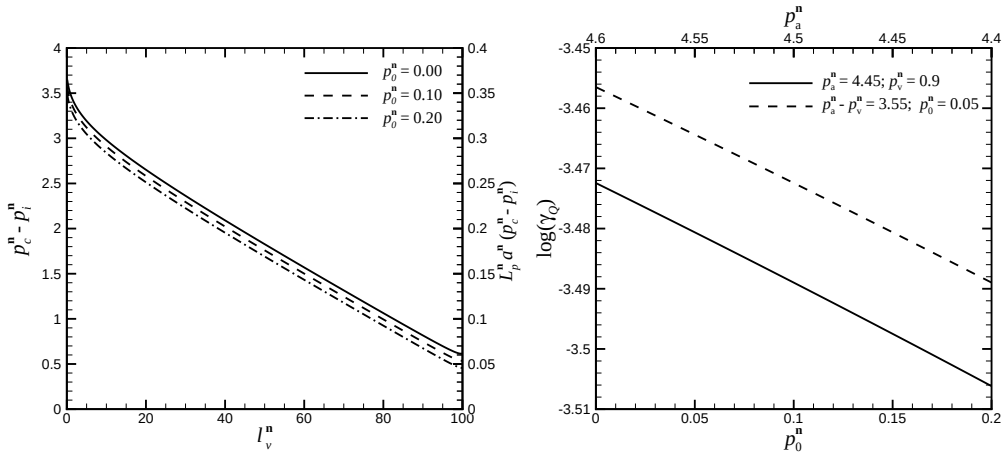

(a) **(b)**

Figure 6.8: (a) Distributions of extravasation flux and transmural pressure difference; (b) dependence of the relative flux coefficient γ_Q on tumour peripheral pressure p_0.

flow is driven by pressure difference $p_a - p_0$ and $p_v - p_0$ (or $p_a - p_v$ and $p_a - p_0$), not these parameters individually. For the previous study cases, either $p_a - p_0$, $p_v - p_0$ or both of them has been modified as we varied p_a, p_v, p_0 or some combinations of them. When $p_a - p_0$ and $p_v - p_0$ remain constant, the pressure itself will of course change when p_a, p_v and p_0 vary together. If we set $p_a - p_0 = 5.86617 \times 10^4$ g cm^{-1}s^{-2} and $p_v - p_0 = 1.1332 \times 10^3$ g cm^{-1}s^{-2}, the distributions of vascular flow pressure $p_c(s)$ and interstitial pressure $p_i(s)$ on the exterior vascular surface with different p_0 (p_a and p_v) are presented in Fig.6.9. However, when we check Eqs.(5.1.11) and (5.1.12), we notice that, if p_c and p_i are the solution for given p_a, p_v and p_0, $p_c + \Delta p$ and $p_i + \Delta p$ will be the solution for $p_a + \Delta p$, $p_v + \Delta p$ and $p_0 + \Delta p$. As a result, when we vary p_a, p_v and p_0 together but fix pressure difference $p_a - p_0$ and $p_v - p_0$, the transmural pressure difference, the extravasation flux, and the relative flux coefficient γ_Q remain unchanged, as shown in Fig.6.10. This indicates that, if pressure difference $p_a - p_0$ and $p_v - p_0$ remain constant, there would be no

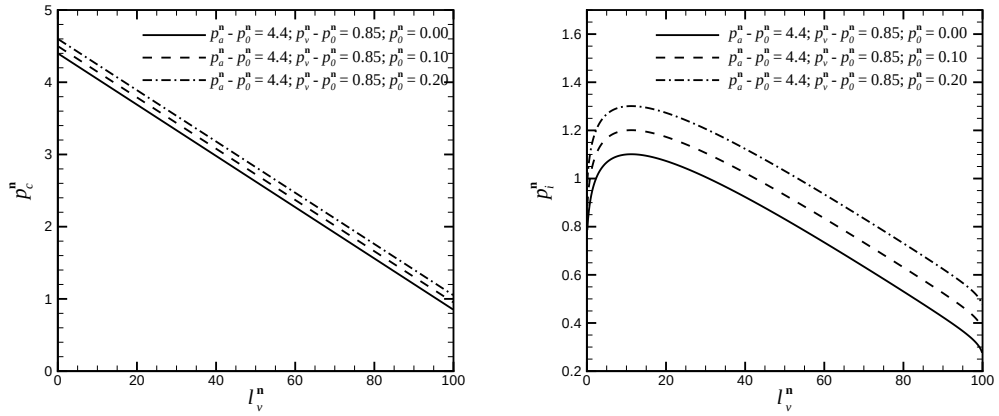

Figure 6.9: Distributions of (a) vascular flow pressures and (b) interstitial pressures on the external vascular surface.

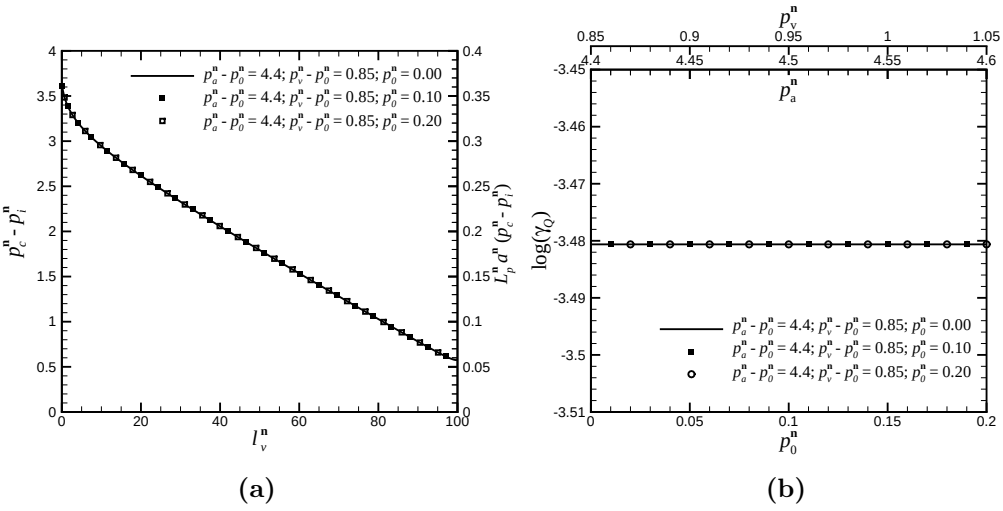

Figure 6.10: (a) Distributions of extravasation flux and transmural pressure difference; (b) dependence of the relative flux coefficient γ_Q.

effects on the transvascular movement of anti-cancer agents or the effectiveness of radiotherapy and chemotherapy when we adjust p_a, p_v and p_0. Therefore, the conclusion can be drawn that the variations of pressure difference $p_a - p_0$ and $p_v - p_0$ are the primary mechanics to affect tumour flow flied. According

to the foregoing observations and analysis, we find that elevating the pressure difference $p_a - p_0$ and $p_v - p_0$, but reducing $p_a - p_v$ within some reasonable limits can be beneficial for the delivery of anti-cancer agents with heavy weight through vascular surface into tumour interior, and improving the effectiveness of chemotherapy and radiotherapy.

Our results are consistent with some previous investigations, for example the papers by Hori *et al.* (1994), Netti *et al.* (1997, 1999). However, adjusting blood pressure itself can lead to some danger for human health. As aforementioned, elevating systemic vascular flow pressure can lead to hypertension related disease. Meanwhile, increasing pressure gradient in tumour interstitium may cause tissue compression, which can cause a significant increase in the interstitial resistance to convective transport [Kroll *et al.* (1996)], because biological tissues are viscoelastic materials [Fung (1981)]. Nevertheless, if these adverse effects are carefully controlled, our results can still be applied practically.

6.2 Effects of tumour hydraulic conductivity parameter on tumour blood flow

Though tumour blood flow is driven by the pressure gradients, it is also affected by other characters of tumour blood environment. Tumour tissue hydraulic conductivity coefficient κ is one of the factors which have effects on tumour blood flow. If the value of κ is very low, for example tending to zero, blood would hardly be able to move within tumour interstitium due to the high resistance. Under such a circumstance, according to the coupling effect relationship in Eq.(6.1.1), flux cannot be transported from the vessel into tumour interior even if the vessel is permeable. As a result, transmural

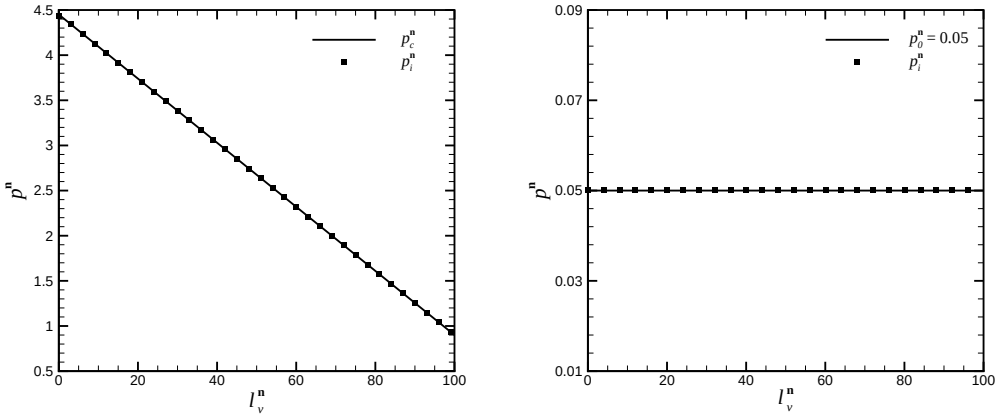

(a) $\kappa^{\mathbf{n}} = 10^{-4}$ **(b)** $\kappa^{\mathbf{n}} = 10^{4}$

Figure 6.11: Distributions of interstitial pressures on the external vascular surface.

pressure difference $p_c(s) - p_i(s)$ would tend to zero, which indicates that interstitial pressure $p_i(s)$ on the exterior vascular surface is equal to pressure $p_c(s)$ in the vessel. Along the increasing of κ, the resistance for the blood flow inside tumour interior is lowered, and blood can be transported through tumour interstitium more easily. If the value of κ is very high, the blood can be delivered through tumour interior freely, and no flux would be accumulated inside tumour interstitium. In such a case, the interstitial pressures, including the interstitial pressures on the external vascular surface, would be equal to the tumour peripheral pressure, as $p_i(\mathbf{x}) = p_0$. This indicates that the high interstitial pressure within tumour interior would disappear. Letting $L_p = 10^{-9}$ g^{-1}cm^{2}s, $p_a = 5.93283 \times 10^4$ g cm^{-1}s^{-2}, $p_v = 1.19990 \times 10^4$ g cm^{-1}s^{-2}, and $p_0 = 6.666 \times 10^2$ g cm^{-1}s^{-2}, the results in Fig.6.11 reflect the foregoing discussions. Fig.6.12 displays the pressure distributions along the vessel under different values of κ. The results in Fig.6.12a show that κ has insignificant effects on the vascular flow pressures as the inlet and outlet vascular flow pres-

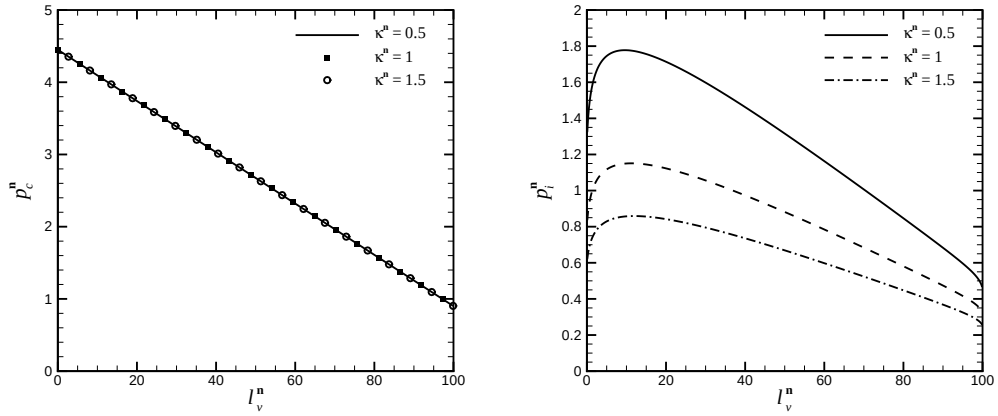

Figure 6.12: Distributions of (a) vascular flow pressures and (b) interstitial pressures on the external vascular surface.

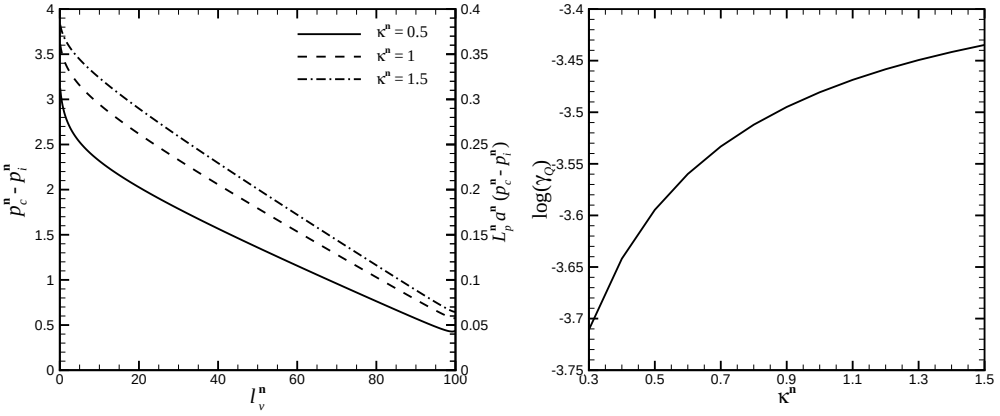

Figure 6.13: (a) Distributions of extravasation flux and transmural pressure differences along vessel; (b) dependence of the relative flux coefficient γ_Q on tumour tissue hydraulic conductivity coefficient κ.

sures are fixed, whereas it has clear influence on tumour interstitial pressures (Fig.6.12b). Based on the coupling effect relationship in Eq.(6.1.1), when κ

is raised, the interstitial pressures on the external vascular surface decrease (Fig.6.12b), which leads to the increase of the transmural pressure difference and the extravasation flux, as presented in Fig.6.13a. As a result, the value of the relative flux coefficient γ_Q is improved because the perfused flux into the vessel is almost unchanged, as displayed in Fig.6.13b. These results indicate that we can adjust tumour tissue hydraulic conductivity parameter κ to achieve better efficiency of drug delivery in tumour. When the tumour interstitial hydrodynamic conductibility is poor, raising κ is helpful to transport macromolecules out of tumour vessels into interstitium and improve the effectiveness of chemotherapy and radiotherapy. The results and conclusions obtained in this section are consistent with the previous study in the paper by Zhang *et al.* (2000), in which they investigated interstitial hydraulic conductivity and gave a brief implication for drug and gene delivery through controlling interstitial hydraulic conductivity.

6.3 Influence of vessel permeability on tumour blood flow

The tumour vasculature owns a unique functional abnormality as which it is more permeable compared with the vasculature in normal tissues. This special abnormal function of tumour vessels plays a critical role in forming the disordered tumour flow environment, which has strong effects on tumour growth and cancer therapies. Tumour vessel permeability induces high interstitial pressure in tumour, which is one of the primary features contributing to the abnormal blood flow field within tumour interior. When the vessel is not permeable, or $L_p = 0$, there would be no flux transported through vascular surface into tumour interstitium. Under this circumstance,

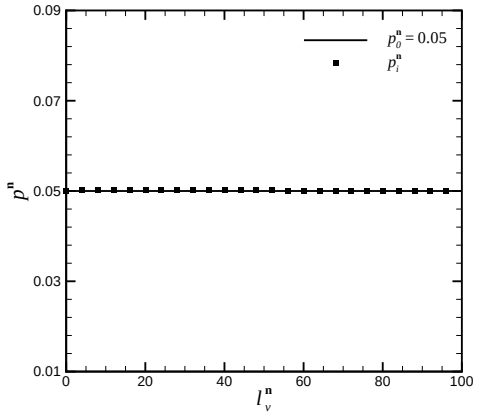

Figure 6.14: Distribution of interstitial pressures on the external vascular surface when $L_p^{\mathbf{n}} = 10^{-5}$.

according to the coupling effect relationship defined in Eq.(6.1.1), interstitial pressure gradient $\partial p_i(s)/\partial n = 0$. Since the interstitial pressure satisfies the Laplace equation, or $\nabla^2 p_i(\mathbf{x}) = 0$, this gives $p_i(\mathbf{x}) = p_0$ everywhere within tumour interior, including the interstitial pressures on the external vascular surface. When we let $\kappa = 5 \times 10^{-8}$ g^{-1}cm^{3}s, $p_a = 5.93283 \times 10^4$ g cm^{-1}s^{-2}, $p_v = 1.19990 \times 10^4$ g cm^{-1}s^{-2}, and $p_0 = 6.666 \times 10^2$ g cm^{-1}s^{-2}, the results in Fig.6.14 reflect the above discussions. Fig.6.15 displays the dependence of tumour blood flow on vessel permeability. According to the results in Fig.6.15a, we notice that the vascular flow pressures are almost unaffected when vessel permeability L_p varies. However, the variation of L_p has significant effects on the pressures in tumour interstitium. Based on the coupling effect relationship in Eq.(6.1.1), along the increasing of vessel permeability L_p, the interstitial pressure gradient $\partial p_i(s)/\partial n$ on the external vascular surface is elevated. This indicates that the interstitial pressure $p_i(s)$ on the exterior vascular surface is increased since the tumour peripheral pressure remains constant. Due to the elevated $p_i(s)$ and unchanged $p_c(s)$, transmural pressure difference $p_c(s) - p_i(s)$ decreases. However, the increasing of L_p makes the extravasation flux raised,

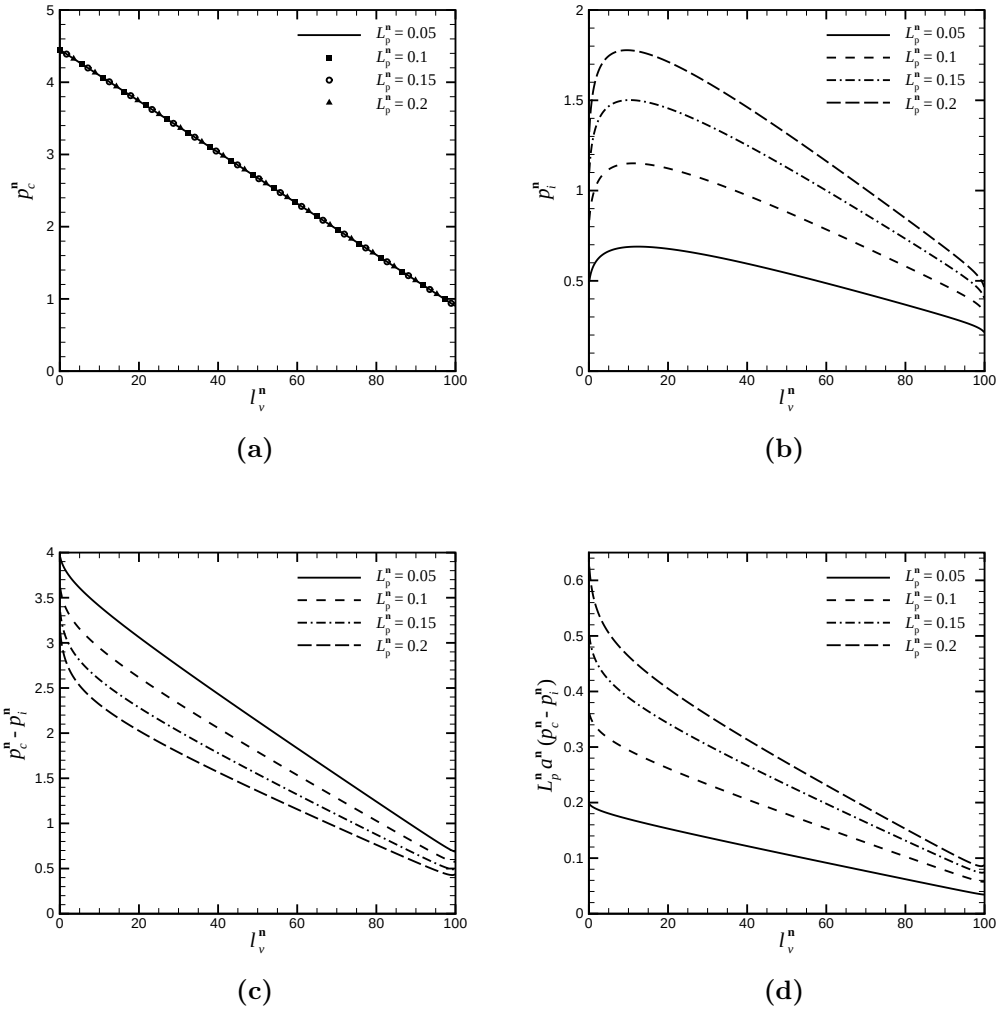

Figure 6.15: Distributions of (a) vascular flow pressures, (b) interstitial pressures on the external vascular surface, (c) transmural pressure difference, and (d) extravasation flux.

which also leads to the relative flux coefficient γ_Q improved. When the value of L_p is raised to some high level, the tumour interstitial pressures on the external vascular surface would be elevated until they are balanced with the pressures inside the vessel, as shown in Fig.6.17. In such a case, the transmural pressure difference would tend to zero, and there would be no difference for

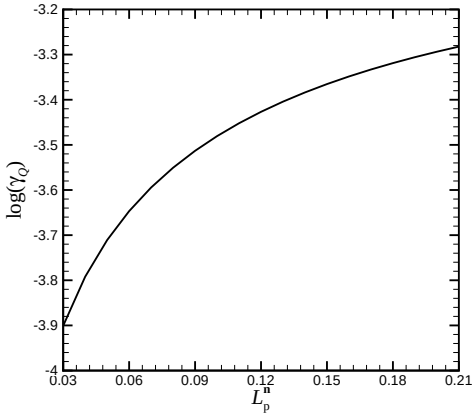

Figure 6.16: Dependence of relative flux coefficient γ_Q on vessel permeability L_p.

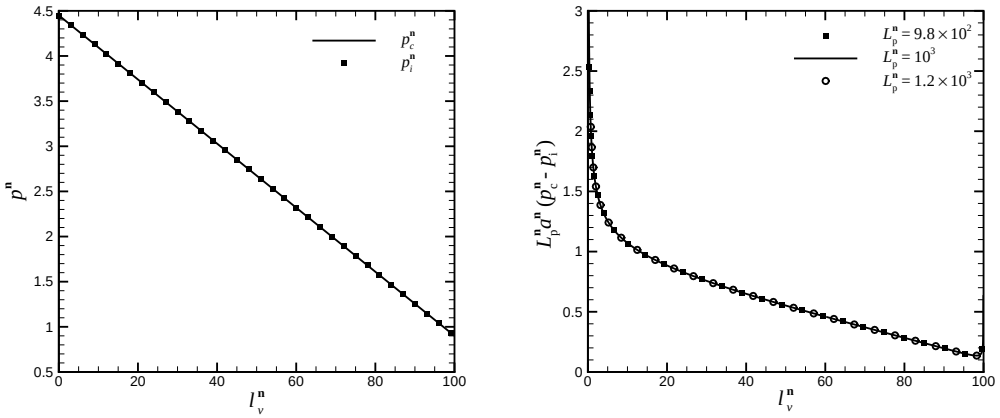

(a) $L_p^n = 10^3$ **(b)**

Figure 6.17: Distributions of (a) interstitial pressures on the external vascular surface and (b) extravasation flux along vessel.

the extravasation flux if we keep increasing L_p, as plotted in Fig.6.17b. From the above discussions, we can conclude that if the value of vascular permeability L_p is quite low, we can improve the ability of transvascular movement of macromolecules with heavy weight and the effectiveness of radiotherapy and chemotherapy by elevating the permeability of tumour vessel.

Our conclusions in this section may not be consistent with some previous study, for example the paper by Tong *et al.* (2004). The experimental observations in Tong *et al.* (2004) indicated that a drop of tumour vessel permeability can improve delivery of anti-cancer agents in solid tumours. However, there is some clear difference between our investigation case and theirs. Our study in this section is based on a simplified case, in which tumour vasculature is represented by a single straight vessel and the tumour is regarded to be virtually large. However, for the case investigated by Tong *et al.* (2004), the vasculature is a fully developed three-dimensional vascular network and tumour is within a certain finite size. In their case, the interstitial pressure is high, even close to the pressure inside tumour vessels. That situation is similar to our investigation case presented in Fig.6.17. As a result, Tong *et al.* (2004) decreased vessel permeability to make a drop of interstitial pressure, which can consequently increase the transmural pressure difference. This feature is consistent with our findings. When the interstitial pressure is lowered, considering our simulation results, for a practical tumour as illustrated by Tong *et al.* (2004), we might be able to propose a strategy to make periodic modulations of vessel permeability, which can induce cycles of fluid exchange between vascular and interstitial space, to optimise the delivery of anti-cancer agents in solid tumours.

Chapter 7

Influence of Vessel Radius on Tumour Blood Flow

In the previous chapter, adopting the governing equations derived in Chapters 4 and 5, we have studied the blood flow in a solid tumour when tumour vasculature is represented by a single straight vessel. Taking the advantage of the simplicity of the vasculature, we have obtained some insightful results on how the inlet and outlet vascular flow pressures, tumour peripheral pressure and tumour interstitial hydraulic conductivity coefficient affect tumour blood flow. Further to this, we have investigated the effects of vessel permeability, the functional abnormality of tumour vessels compared with the vessels in normal tissues, on tumour blood flow. Nevertheless, there is another special feature of tumour vasculature relative to normal vasculature, which is the irregular vascular architecture in tumour. As summarised in Section 1.3, and also described in the literatures by Konerding *et al.* (1999), Less *et al.* (1991), Ryschich *et al.* (2004) and Shubik (1982), unlike normal vessels, the vascular architecture in tumour is characterised with disordered vessel radius, curved vessels, and out of order vascular network with excessive branches and loops. From the present

chapter to Chapter 9, we will orderly investigate how the above three abnormal characters of tumour vascular architecture affect tumour blood flow.

In this chapter, we investigate how dilated and uneven vessel radius affects tumour blood flow. Vessel radius has strong influence on tumour blood flow. In our model, for the vascular flow, the Poiseuille's law in Eq.(5.1.10) states that the flow flux through a tumour vessel is in direct proportion to the forth power of vessel radius. In the discretised equation (5.1.12) for the vascular flow pressures and the interstitial pressures on the external vascular surface, influence coefficients $\bar{A}_n^{[j]}$ and $\bar{B}_n^{[j]}$ depend on vessel radius. Furthermore, as described in Eq.(5.0.3), flux of molecules J_s is also correlative with vessel radius.

7.1 Dilated tumour vessel

One of the special characters of tumour vasculature is that vessel radius in tumour is dilated compared with the vessels in normal tissues [Ryschich *et al.* (2004)]. The vessel radius in our previous investigations is set as $a = 0.01$ cm, which is within practical tumour physiological ranges. However, tumour vessel radius varies stage by stage along tumour growth, because the angiogenesis process normally requires tumour vessels to dilate to support tumour growth [Ryschich *et al.* (2004)]. The variation of vessel radius has clear effects on tumour blood environment, especially on the vascular flow. In order to investigate the influence of dilated vessel on tumour blood flow, we set up a study case, in which a single straight vessel with length $l_v = 1.0$ cm and leakage $L_p = 10^{-9}$ g^{-1}cm^{2}s is embedded in a solid tumour to a large extent whose hydraulic conductivity coefficient $\kappa = 10^{-10}$ g^{-1}cm^{3}s and peripheral pressure $p_0 = 6.666 \times 10^2$ g cm^{-1}s^{-2}. The cross section radius is uniform along the

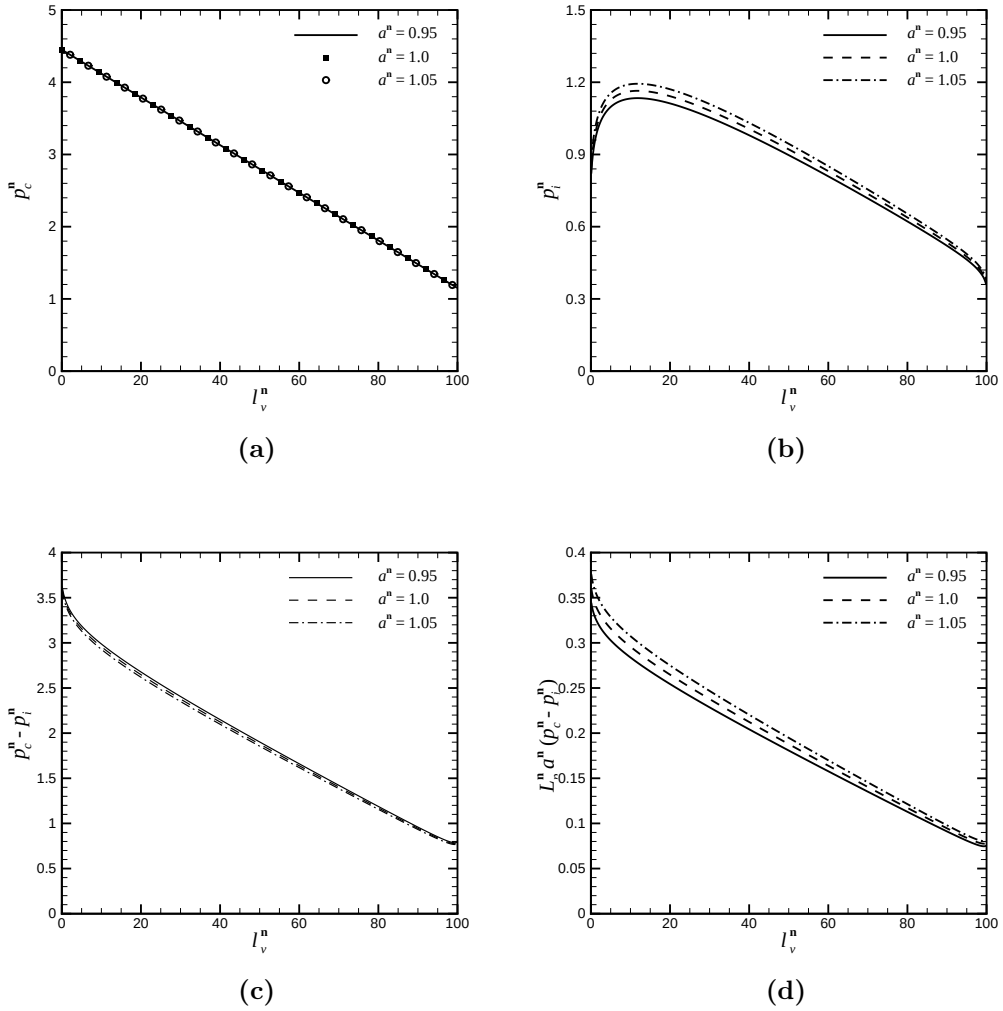

Figure 7.1: Distributions of (a) vascular flow pressures, (b) interstitial pressures on the external vascular surface, (c) transmural pressure difference, and (d) extravasation flux when $p_a^{\mathbf{n}} = 4.7$ and $p_v^{\mathbf{n}} = 1.15$.

vessel.

When the inlet and outlet pressures for the vascular flow are given, the dilated vessel leads to a rapid increase of flux Q_a at the arterial point in the vessel since the flow flux through a tumour vessel is in direct proportion to the forth power of vessel radius as described by the Poiseuille's law

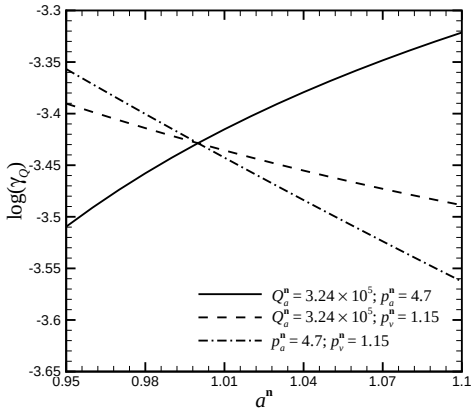

Figure 7.2: Dependence of the relative flux coefficient γ_Q on vessel radius a.

in Eq.(5.1.10). Though the enlarged vessel radius also makes the vascular surface area broadened, which can induce more extravasation flux, the value of the relative flux coefficient γ_Q is reduced as the increasing rate of Q_a is much higher than that of the extravasation flux. Fig.7.1 displays the variation of tumour blood flow along the dilated vessel when the inlet vascular flow pressure is set as $p_a = 5.93283 \times 10^4$ g cm^{-1}s^{-2} and the outlet pressure as $p_v = 1.19990 \times 10^4$ g cm^{-1}s^{-2}. The results in Fig.7.1a show that the effect of the variation of vessel radius on vascular flow pressure $p_c(s)$ is insignificant. However, interstitial pressure $p_i(s)$ on the external vascular surface is elevated when the vessel radius is enlarged, as displayed in Fig.7.1b. Consequently, transmural pressure difference $p_c(s) - p_i(s)$ is reduced (Fig.7.1c). Due to that the vascular surface area is extended because of the enlarged vessel radius, the extravasation flux is increased despite the drop of transmural pressure difference, as presented in Fig.7.1d. However, based on the foregoing discussions, the relative flux coefficient γ_Q is reduced in the current case, as plotting in Fig.7.2 by the dash dot line. This indicates that, under this circumstance, though it can be beneficial for the delivery of anti-cancer agents with heavy weight

through vascular surface into tumour interstitium when vessel is dilated, one has to consider the possibility of losing the effectiveness and aggravating the side effects of chemotherapy and radiotherapy.

Since the variation of vessel radius has powerful effects on vascular flow, when different types of inlet and outlet vascular flow conditions are given, there will be different phenomena of tumour blood flow caused by the dilated tumour vessel. For example, when we set the perfused vascular flow flux as $Q_a = 4.3196 \times 10^{-3}$ cm^{3}s^{-1} and the inlet vascular flow pressure as $p_a = 5.93283 \times 10^4$ g cm^{-1}s^{-2} at the arterial connecting point of the vessel, while outlet vascular flow pressure p_v is part of unknowns, transmural pressure difference $p_a - p_v$ is reduced when the vessel radius is enlarged, which indicates that p_v is elevated. As a result, vascular flow pressure $p_c(s)$ is increased, as plotted in Fig.7.3a. Due to the increased vascular flow pressures and enlarged vessel radius, though the interstitial pressures on the exterior vascular surface are elevated, the average transmural pressure difference over the whole vessel is raised. Multiplying the broadened vascular surface area caused by the dilated vessel, the extravasation flux through the vessel surface is increased, as displayed in Fig.7.3. In Section 6.1.1, we have investigated the case when p_v is elevated while the vessel radius remains unchanged. The results in the current case look similar to the results of that case, as shown in Figs.6.1 and 6.2a. However, there are some difference between these two cases, especially for the interstitial pressures and extravasation flux near the arterial point of the vessel, which is mainly due to the variation of vessel radius. As Q_a is fixed, and noticing that the extravasation flux is increased, the relative flux coefficient γ_Q is improved under the present circumstance, as plotted in Fig.7.2 by the solid line.

For the same reason, when $Q_a = 4.3196 \times 10^{-3}$ cm^{3}s^{-1} and $p_v = 1.19990 \times$

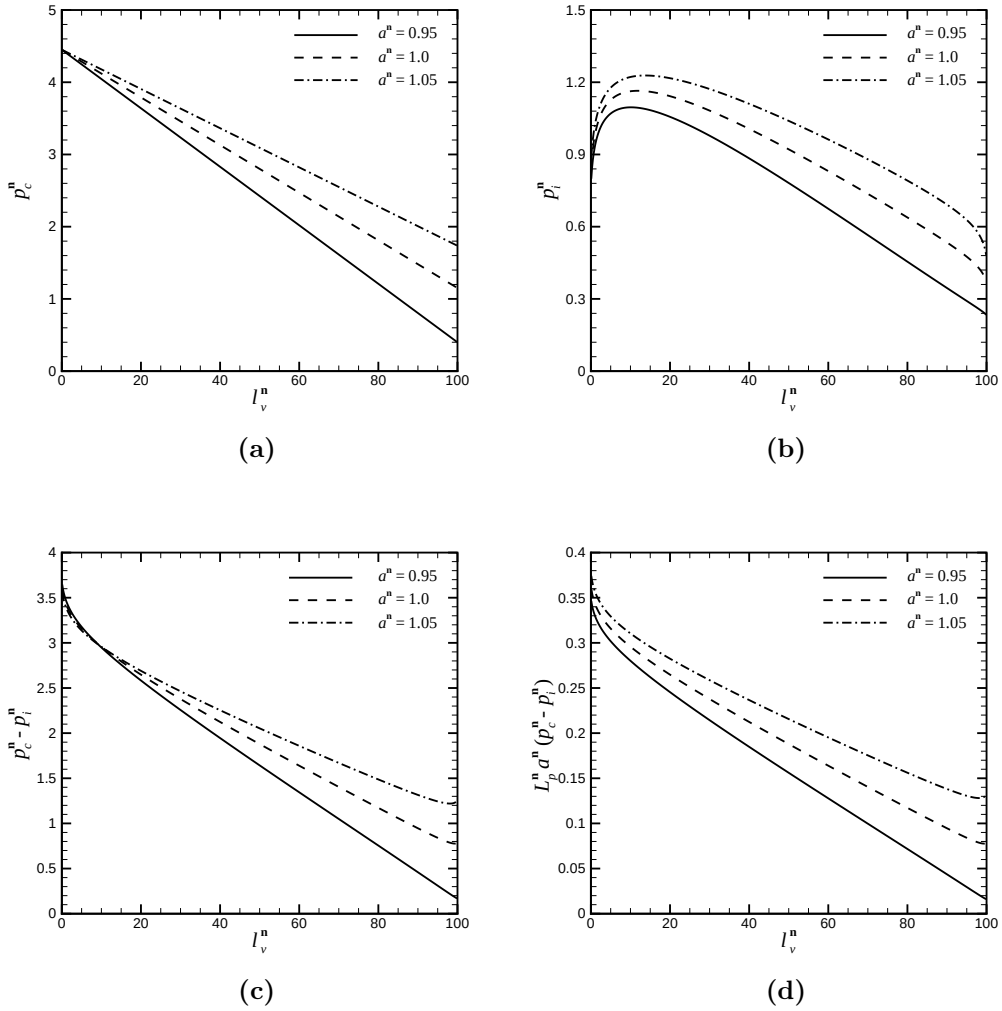

Figure 7.3: Distributions of (a) vascular flow pressures, (b) interstitial pressures on the external vascular surface, (c) transmural pressure difference, and (d) extravasation flux when $Q_a^{\mathbf{n}} = 3.24 \times 10^5$ and $p_a^{\mathbf{n}} = 4.7$.

10^4 g cm^{-1}s^{-2} are given but p_a is part of unknowns, the dilated vessel cross section makes the pressure gradient in the vessel decreased, which leads to a drop of arterial pressure p_a. As a result, the vascular flow pressures are lowered, the interstitial pressures on the external vascular surface are decreased, and the average transmural pressure difference is reduced, as shown in Figs.7.4a,

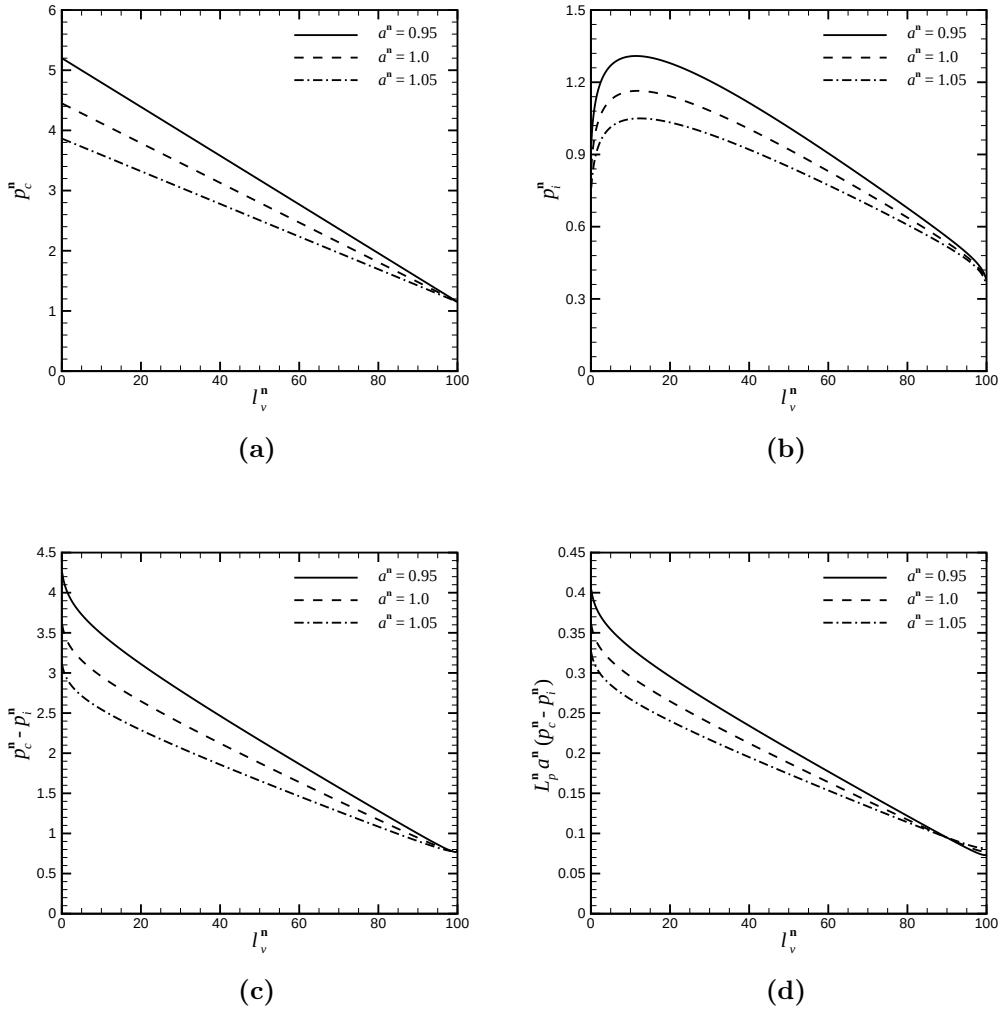

Figure 7.4: Distributions of (a) vascular flow pressures, (b) interstitial pressures on the external vascular surface, (c) transmural pressure difference, and (d) extravasation flux when $Q_a^{\mathbf{n}} = 3.24 \times 10^5$ and $p_v^{\mathbf{n}} = 1.15$.

7.4b and 7.4c respectively. Even though the vascular surface area is extended, the average extravasation flux along the whole vessel is decreased, as presented in Fig.7.4d. Consequently, the relative flux coefficient γ_Q is reduced since Q_a is constant, as plotted in Fig.7.2 by the dash line.

Based on the above results, we find that the effects of dilated vessel on

tumour blood flow are complicated, which rely on the inlet and outlet vascular flow conditions strongly. When Q_a and p_a are given, dilated tumour vessel can improve the efficacy of transporting anti-cancer agents with heavy weight through vascular surface into tumour interior, and the effectiveness of chemotherapy and radiotherapy. However, if Q_a and p_v are fixed, enlarged tumour vessel diameter has negative effects on transvascular delivery of heavy macromolecules in tumour or the effectiveness of chemotherapy and/or radiotherapy. On the other hand, if we can control and fix the inlet and outlet vascular flow pressures, enlarged tumour vessel can be beneficial for transporting anti-cancer agents with heavy weight through vascular surface into tumour interior, but would have to sacrifice the effectiveness of chemotherapy and radiotherapy.

7.2 Effects of vessel elastic property on tumour blood flow

Another character of disordered tumour vessel radius is that it is not always uniform along the vessel. One major reason for uneven diameters along tumour vessels is due to the elastic property of tumour vascular walls together with the abnormal interstitial pressure distributions within tumour. However, the elastic behaviour of blood vessels is complicated. A mathematical model capable of exactly describing the elastic behaviour of vessels would not only require a complete understanding of the coupling effects between vascular, transvascular and interstitial flows, but also need full knowledge about the elastic properties of vascular walls. So far, based on the best of author's knowledge, there is yet a precise mathematical model to describe the elastic behaviour of blood vessels, although some efforts have been donated in this area, such as the literatures

by Baish *et al.* (1997) and Lee and Schmid-Schönbein (1996).

We investigate a case for tumour blood flow, in which a single straight compliant vessel is embedded in a solid tumour whose surface is far away from the vessel. For the elastic behaviour of the vessel, the empirical constitutive equation developed by Baish *et al.* (1997) is adopted, which describes the functional relationship between vessel radius and transmural pressure difference as

$$a(s) = a_0 \left[\frac{p_c(s) - p_i(s)}{E_{cl}} + \frac{p_{cl}}{E_{cl}} \right]^{\frac{b_r}{2}}, \tag{7.2.1}$$

where a_0 is the vessel radius in the reference state, E_{cl} is the compliance coefficient, b_r is the compliance exponent, p_{cl} is the collapse pressure, and the values of these parameters are listed in Table7.1. This model is suitable for the tumour vessels when a_0 is around 5 μm. Hence, the geometrical sizes of the vessel are assigned as followings: $l_v = 200$ μm and radius $a_0 = 5$ μm in the reference state. The vessel permeability $L_p = 10^{-9}$ g^{-1}cm^{2}s, interstitial hydraulic conductivity coefficient $\kappa = 10^{-10}$ g^{-1}cm^{3}s, and tumour peripheral pressure $p_0 = 666.61$ gcm^{-1}s^{-2} are set to remain constant for the present case. Meanwhile, using all the same physical parameters, we simulate another case for comparison, in which the vessel is rigid, and its radius and length are set as $a = 5$ μm and $l_v = 200$ μm respectively.

For the current study case, though the vessel is compliant, the vascular cross section is assumed to remain circular. Therefore, the governing equations for tumour blood flow derived in Section 5.1 are still available. Due to that the vessel radius relies on the transmural pressure difference as described in Eq.(7.2.1), the numerical procedure for the present case is modified by adding another iteration external to the numerical procedure stated in Section 5.1 to calculate the vessel radius. The detailed procedure is summarised as below:

Table 7.1: Physiological parameter values when $5\mu\text{m} \leq a \leq 10\mu\text{m}$

Parameter (dimensions)	Value
Arterial pressure p_a (g cm^{-1}s^{-2})	$(1.58653 \pm 0.25331) \times 10^4$ [Jain (1988), Peters *et al.* (1980)]
Venous pressure p_v (g cm^{-1}s^{-2})	$(8.9326 \pm 2.4531) \times 10^3$ [Jain (1988), Peters *et al.* (1980)]
Tissue hydraulic conductivity κ (g^{-1}cm^{3}s)	$3 \times 10^{-11} \sim 1.5 \times 10^{-10}$ [Swabb *et al.* (1974)]
Vascular Permeability L_p (g^{-1}cm^{2}s)	$2.7 \times 10^{-10} \sim 2.1 \times 10^{-9}$ [Baish *et al.* (1997)]
Collapse pressure p_{cl} (g cm^{-1}s^{-2})	3.99966×10^3 [MacPhee and Michel (1995)]
Compliance coefficient E_{cl} (g cm^{-1}s^{-2})	8.66593×10^3 [Mason (1975)]
Compliance exponent b_r	0.2 [Mason (1975)]

1) Adopt radius a_0 in the reference state as the initial value for vessel radius.

2) Set initial guess for blood pressure $p_c(s)$ inside the vessel.

3) Evaluate the right-hand side of Eq.(5.1.33).

4) Solve Eq.(5.1.33) to obtain tumour interstitial pressure $p_i(s)$ on the external vascular surface.

5) Evaluate the right-hand sides of Eqs.(5.1.13), (5.1.17) and (5.1.23).

6) Solve Eqs.(5.1.13), (5.1.17) and (5.1.23) together to obtain $p_c(s)$.

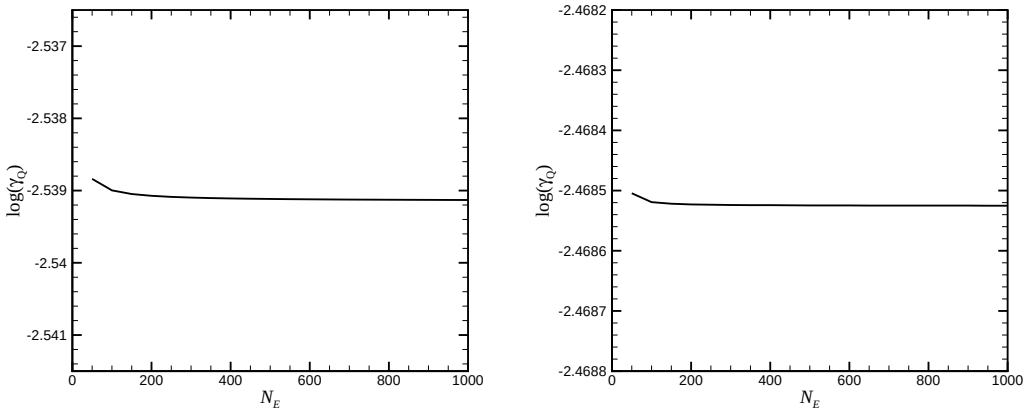

(a) compliant vessel **(b)** rigid vessel

Figure 7.5: Dependence of the relative flux coefficient γ_Q on number of discretised segments N_E when the relative round error function $Er = 1. \times 10^{-6}$.

7) Repeat the procedure between step 2 and 6 until the difference in either p_c or p_i from two successive steps is sufficiently small.

8) Get new vessel radius according to Eq.(7.2.1).

9) Repeat the procedure between step 2 and 8 until the convergence for the vessel radius has been achieved.

Fig.7.5 displays the dependence of the relative flux coefficient γ_Q on number of discretised segments N_E when the relative round error function is set as $Er = 1. \times 10^{-6}$. The results in Fig.7.5 indicate that for either compliant vessel or rigid vessel, the value of γ_Q becomes mesh independent when N_E is sufficiently large. The comparison results of simulation time for the case of compliant vessel and rigid vessel under different N_E are listed in Table7.2. These results have confirmed our foregoing analysis in Section 5.1, which states that there is a significant increase (one order higher) of the computation time for the case of compliant vessel relative to the case of rigid vessel. Therefore,

Table 7.2: Calculation time for compliant vessel and rigid vessel

	N_E	300	450	600	750	900
Rigid vessel	Time (s)	76	170	303	474	684
Compliant vessel	Time (s)	690	1438	2550	4016	5733

for the case of compliant vessel, based on the results in Fig.7.5, and considering the simulation time, our calculation results are accurate enough when the element size is chosen as $\delta s_j = 0.066667 a_0$ $(j = 1, 2, \cdots, N_E)$.

Since compliance exponent $b_r = 0.2$ as listed in Table7.1, according to the relationship between the vessel radius and the transmural pressure difference in Eq.(7.2.1), we notice that the vessel radius relies on the transmural pressure difference monotonically along the vessel. In the meantime, when transmural pressure difference $p_c(s) - p_i(s) > (E_{cl} - p_{cl}) = 0.35 \cdot \check{p}$, the vessel is dilated compared with radius a_0 in the reference state, while if $p_c(s) - p_i(s) < 0.35 \cdot \check{p}$, the vessel is compressed relative to a_0. If tumour vessel is not permeable, based on the discussions in Section 6.3, tumour interstitial pressure $p_i(\mathbf{x})$ would be constant, and equal to tumour peripheral pressure p_0. Under this circumstance, when inlet and outlet vascular flow pressures p_a and p_v are given, pressure $p_c(s)$ in the vessel decreases from p_a to p_v monotonically according to the Poiseuille's law. As a result, the transmural pressure difference descends monotonically along the vessel. According to the relationship in Eq.(7.2.1), we can conclude that the vessel radius near the arterial point is larger than that around the venous point. Since there is no flux exceeded from the vessel into tumour interior, the perfused flux into the vessel at the arterial point, Q_a, is equal to Q_v, which is the flux flowing out of the vessel at the venous end. Consequently,

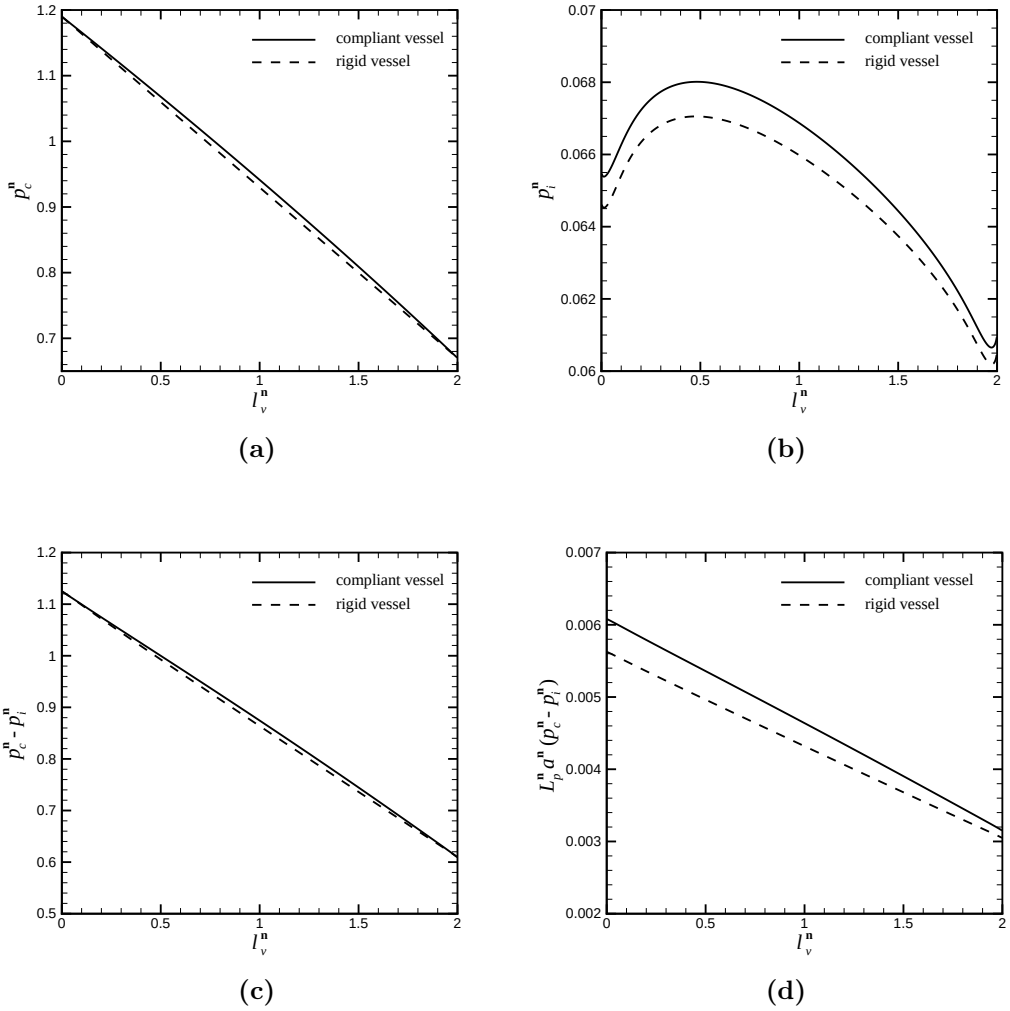

Figure 7.6: Comparison of distributions of (a) vascular flow pressures, (b) interstitial pressures on the external vascular surface, (c) transmural pressure difference, and (d) extravasation flux for the cases of compliant vessel and rigid vessel.

according to the Poiseuille's law, the vascular pressure gradient at the upstream part of the vessel is lower than that at the downstream part of the vessel, which indicates that the vascular flow pressures along the compliant vessel are higher than the pressures in the rigid vessel. Since the effects of vessel permeability on the vascular flow pressures are insignificant based on the foregoing discussions

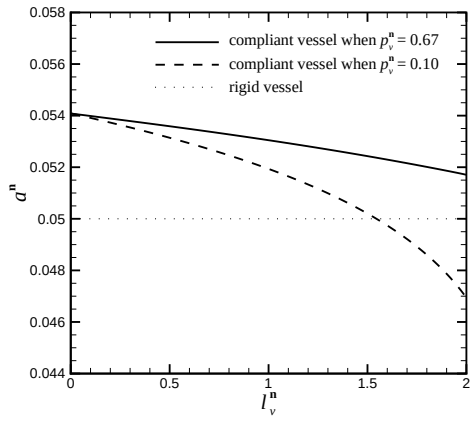

Figure 7.7: Distributions of vessel radius.

in Section 6.3, the above analysis is also available for tumour blood flow, as shown in Fig.7.6a, when we let $p_a = 1.58653 \times 10^4$ g cm^{-1}s^{-2} and $p_v = 8.9326 \times 10^3$ g cm^{-1}s^{-2}. Similar to the results in Section 6.1.1, we observe that, in the present case, though the elevated vascular flow pressures induce the interstitial pressures on the exterior vascular surface to increase, the average transmural pressure difference over the entire vessel is raised, as shown in Figs.7.6b and 7.6c respectively. For the current study case, as $p_c(s) - p_i(s) > 0.35 \cdot \check{p}$ along the vessel, the vessel radius is enlarged along the entire vessel relative to radius a_0 in the reference state, as plotted in Fig.7.7 by the solid line. This leads to the vascular surface area extended. Under this circumstance, considering the increased transmural pressure difference, the extravasation flux transported from the compliant vessel is higher than that from the rigid vessel, as displayed in Fig.7.6d. However, since the enlarged vessel radius leads to the rapid increasing of Q_a as p_a and p_v are fixed, the relative flux coefficient $\gamma_{_Q}$ is lowered when the vessel is compliant relative to that when the vessel is rigid, as shown in Fig.7.8.

The simulation results on tumour blood flow are displayed in Fig.7.9, when

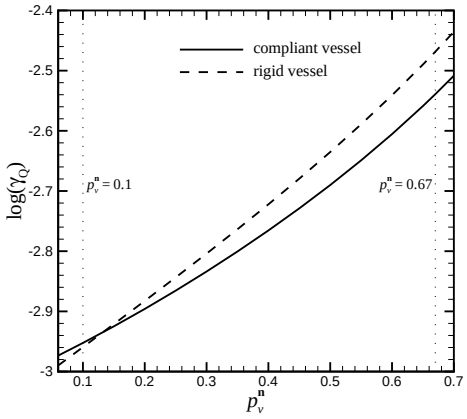

Figure 7.8: Dependence of the relative flux coefficient $\gamma_{_Q}$ on outlet vascular flow pressure p_v.

we decrease the outlet vascular flow pressure to $p_v = 1.3332 \times 10^3$ g cm^{-1}s^{-2} but let $p_a = 1.58653 \times 10^4$ g cm^{-1}s^{-2} remain unchanged. Fig.7.9a and 7.9b show that the distributions of inner and outer pressures along the vessel present the similar aspects to the results obtained above. However, under the current inlet and outlet vascular flow conditions, transmural pressure difference $p_c(s) - p_i(s) > 0.35 \cdot \check{p}$ at the upstream part of the vessel, but at the downstream part of the vessel, $p_c(s) - p_i(s) < 0.35 \cdot \check{p}$, as plotted in Fig.7.9c. Consequently, the vessel is dilated at the upstream part of the vessel but compressed at the downstream part of the vessel relative to radius a_0 in the reference state, as shown in Fig.7.7 by the dash line. Since the inlet and outlet pressures for the vascular flow are given, the compressed vessel radius near the venous end makes the flux flowing out of the vessel reduced, which respectively requires flux Q_a at the arterial point to decrease. As a result, the relative flux coefficient $\gamma_{_Q}$ is improved when the vessel is compliant compared with that when the vessel is rigid, as shown in Fig.7.8. This figure also plots the dependence of $\gamma_{_Q}$ on outlet vascular flow pressure p_v when the vessel is either compliant or rigid. Though there is some difference in the value of $\gamma_{_Q}$ between these two cases,

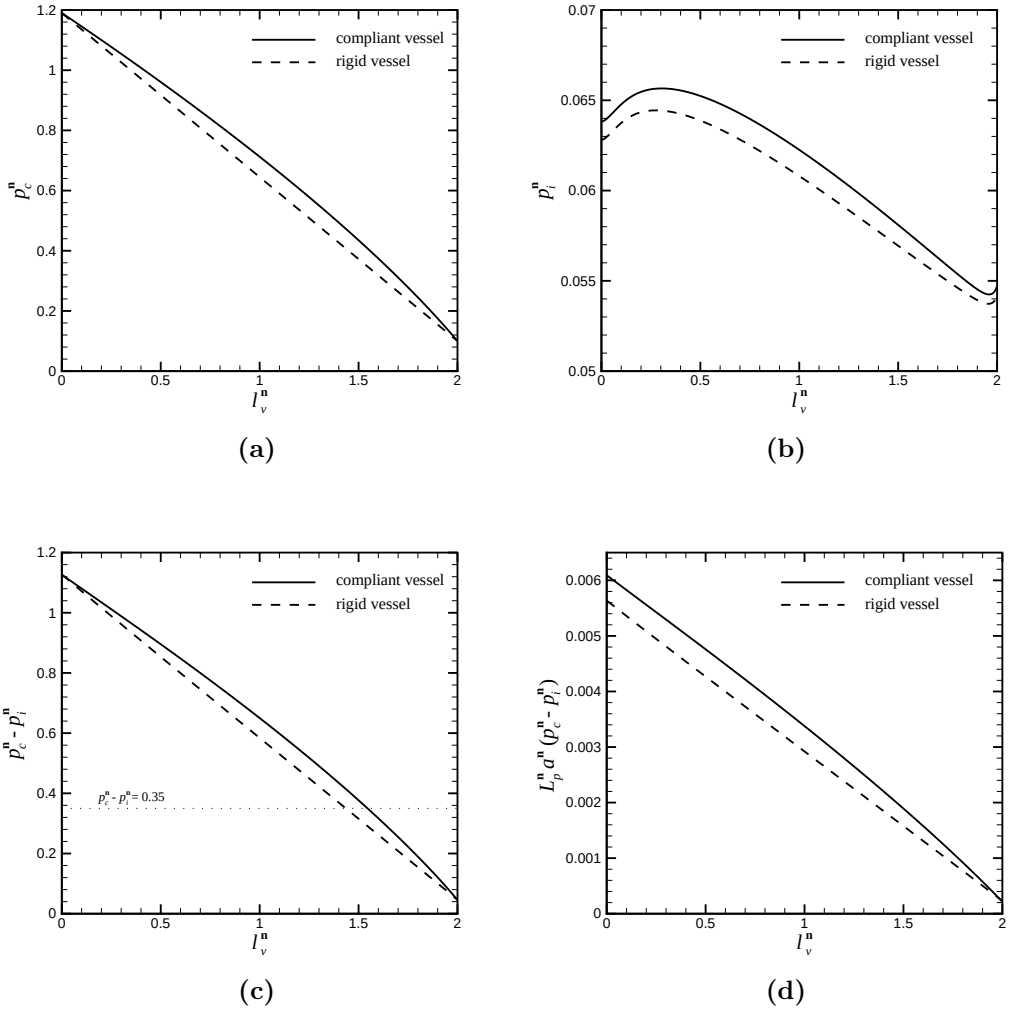

Figure 7.9: Comparison of distributions of (a) vascular flow pressures, (b) interstitial pressures on the external vascular surface, (c) transmural pressure difference, and (d) extravasation flux for the cases of compliant vessel and rigid vessel.

the trends of the variation of γ_Q along the variation of the outlet vascular flow pressure are similar to each other.

Chapter 8

Effects of Vessel Curvature on Tumour Blood Flow

In Chapter 7, we have studied how disordered tumour vessel radius, which is regarded as one of the abnormal characters of tumour vascular architecture, affects tumour blood flow. Except for the disordered vessel radius, there are some other particular characters of tumour vascular configuration compared with the vessels in normal tissues. One of these special characters is that, unlike the normal vessels, the practical vessels within tumour are not in good shapes, but with curvature. Obviously, vessel curvature has clear effects on tumour blood flow. It also induces new difficulty in our mathematical model. For a curved vessel, the detailed expression of the parametrical equation for the vessel centre line becomes more complex relative to that for a straight vessel, which consequently leads to significant variations of vascular shape functions $H_b(s)$ and $H_c(s)$, which are defined in Eqs.(4.1.6) and (4.1.7) respectively. This results in the rapid changes of the continuity and momentum equations in Eqs.(4.2.10) to (4.2.12) for the vascular flow, which further affects the equations linking the blood flows in the vessel and tumour interstitium, such as

Eqs.(4.3.9) and (4.3.15). In this chapter, we investigate the mathematical difficulty mentioned above and the influence of vessel curvature on tumour blood flow in detail through a case, in which a single curved vessel is embedded in a large solid tumour whose surface is far away from the vessel. The vessel is permeable, and bent with constant curvature in a plane. It is assumed that the vascular walls are rigid, vessel cross section is circular, and vessel radius is uniform along the vessel centre line. In the meantime, we set the vessel length as $l_v = 1.0$ cm, the vessel permeability as $L_p = 10^{-9}$ g^{-1}cm^{2}s, the tumour hydraulic conductivity coefficient as $\kappa = 10^{-10}$ g^{-1}cm^{3}s, and the tumour peripheral pressure as $p_0 = 6.666 \times 10^2$ g cm^{-1}s^{-2}. All of these parameters remain constant in this chapter.

8.1 Governing equations and numerical simulation procedure

In Fig.8.1, we sketch a case of a curved vessel with constant curvature radius R_c embedded in a solid tumour. The arterial point of the vessel is located at the origin of Cartesian coordinate system $o - xyz$. As a result, we can choose parametric equation

$$x(s) = R_c \sin s, \quad y(s) = R_c - R_c \cos s, \quad z(s) = 0, \tag{8.1.1}$$

to describe the vessel centre line, which gives us

$$x'(s) = R_c \cos s, \qquad y'(s) = R_c \sin s, \qquad z'(s) = 0; \tag{8.1.2}$$

$$x''(s) = -R_c \sin s, \qquad y''(s) = R_c \cos s, \qquad z''(s) = 0; \tag{8.1.3}$$

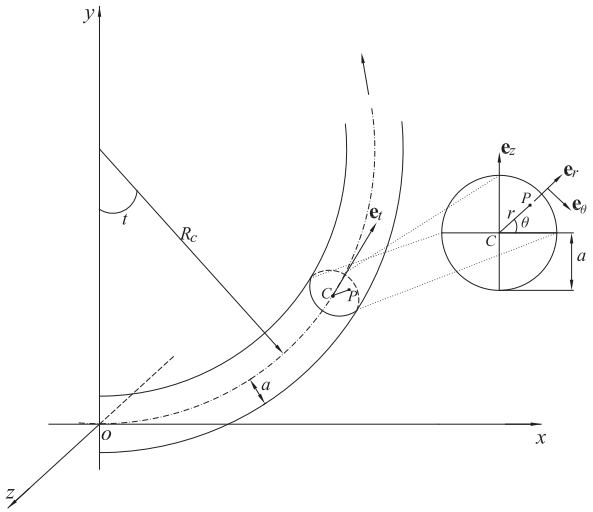

Figure 8.1: Sketch of a tumour vessel with constant curvature.

and

$$H_b(s) = \frac{1}{R_c}, \qquad H_c(s) = 0. \tag{8.1.4}$$

Introducing Eqs.(8.1.2) to (8.1.4) into Eq.(4.2.23), we get

$$\begin{cases} \mathcal{J}_r = 1, \\ \mathcal{J}_\theta = r, \\ \mathcal{J}_s = R_c - r\cos\theta. \end{cases} \tag{8.1.5}$$

Substituting Eq.(8.1.5) into Eqs.(4.2.10), (4.2.11), (4.2.12), and introducing the results into Eqs.(4.2.3) and (4.2.2), we obtain the continuity equation for the flow through a curved tumour vessel as

$$\begin{aligned} &\frac{\partial U_r}{\partial r} + \frac{U_r}{r} - \frac{U_r\cos\theta}{R_c - r\cos\theta} + \frac{1}{r}\frac{\partial U_\theta}{\partial\theta} \\ &+ \frac{U_\theta\sin\theta}{R_c - r\cos\theta} + \frac{1}{R_c - r\cos\theta}\frac{\partial U_s}{\partial s} = 0, \end{aligned} \tag{8.1.6}$$

and the momentum equations as

$$
\begin{aligned}
&U_r\frac{\partial U_r}{\partial r}+\frac{U_\theta}{r}\frac{\partial U_r}{\partial \theta}+\frac{U_s}{R_c-r\cos\theta}\frac{\partial U_r}{\partial s}-\frac{U_\theta^2}{r}+\frac{U_s^2\cos\theta}{R_c-r\cos\theta}\\
=&-\frac{1}{\rho}\frac{\partial p}{\partial r}-\frac{\mu}{\rho}\Bigg[\frac{1}{r(R_c-r\cos\theta)}\frac{\partial}{\partial r}\left(r\frac{\partial U_s}{\partial s}\right)\\
&-\frac{R_c}{r\left(R_c-r\cos\theta\right)^2}\frac{\partial U_s}{\partial s}-\frac{1}{\left(R_c-r\cos\theta\right)^2}\frac{\partial^2 U_r}{\partial s^2}\\
&+\left(\frac{1}{r}\frac{\partial}{\partial\theta}+\frac{\sin\theta}{R_c-r\cos\theta}\right)\left(\frac{\partial U_\theta}{\partial r}+\frac{U_\theta}{r}-\frac{1}{r}\frac{\partial U_r}{\partial\theta}\right)\Bigg],
\end{aligned}
\tag{8.1.7}
$$

$$
\begin{aligned}
&U_r\frac{\partial U_\theta}{\partial r}+\frac{U_\theta}{r}\frac{\partial U_\theta}{\partial \theta}+\frac{U_s}{R_c-r\cos\theta}\frac{\partial U_\theta}{\partial s}-\frac{U_s^2\sin\theta}{R_c-r\cos\theta}+\frac{1}{r}U_rU_\theta\\
=&-\frac{1}{\rho}\frac{1}{r}\frac{\partial p}{\partial\theta}+\frac{\mu}{\rho}\Bigg[\frac{1}{\left(R-r\cos\theta\right)^2}\frac{\partial^2 U_\theta}{\partial s^2}-\frac{\sin\theta}{\left(R-r\cos\theta\right)^2}\frac{\partial U_s}{\partial s}\\
&+\left(\frac{\partial}{\partial r}+\frac{\sin\theta}{R_c-r\cos\theta}\right)\left(\frac{\partial U_\theta}{\partial r}+\frac{U_\theta}{r}-\frac{1}{r}\frac{\partial U_r}{\partial\theta}\right)\Bigg],
\end{aligned}
\tag{8.1.8}
$$

and

$$
\begin{aligned}
&U_r\frac{\partial U_s}{\partial r}+\frac{U_\theta}{r}\frac{\partial U_s}{\partial \theta}+\frac{U_s}{R_c-r\cos\theta}\left(\frac{\partial U_s}{\partial s}-U_r\cos\theta+U_\theta\sin\theta\right)\\
=&-\frac{1}{\rho}\frac{1}{R_c-r\cos\theta}\frac{\partial p}{\partial s}+\frac{\mu}{\rho}\Bigg\{\frac{R_c}{r^2(R_c-r\cos\theta)^2}\frac{\partial U_r}{\partial s}-\frac{U_s}{(R_c-r\cos\theta)^2}\\
&-\frac{\sin\theta}{(R_c-r\cos\theta)^2}\frac{\partial U_\theta}{\partial s}-\frac{1}{r(R_c-r\cos\theta)}\frac{\partial^2 U_\theta}{\partial\theta\partial s}-\frac{1}{R_c-r\cos\theta}\frac{\partial^2 U_r}{\partial r\partial s}\\
&+\frac{\partial^2 U_s}{\partial r^2}+\frac{1}{r}\frac{\partial U_s}{\partial r}+\frac{R_c-r\cos\theta}{r^2}\frac{\partial}{\partial\theta}\left[\frac{1}{R_c-r\cos\theta}\frac{\partial U_s}{\partial\theta}\right]\Bigg\}.
\end{aligned}
\tag{8.1.9}
$$

As aforementioned in Section 4.3.2, the blood flow through tumour vessels is fully developed, steady and laminar. When the vessel curvature is mild, which means that the value of the ratio of vessel cross section radius a over

vessel curvature radius R_c, or a/R_c, is small, following the procedure illustrated by Dean (1928) (also in the book by Pedley (1980)), we can presume that U_r, U_θ, U_s and $\partial p/\partial s$ are independent of s. We can further replace term

$$R_c - r\cos\theta$$

with R_c, and term

$$\partial/\partial r + \sin\theta/(R_c - r\cos\theta)$$

with $\partial/\partial r$ respectively. In this way, Eqs.(8.1.6) to (8.1.9) are reduced to

$$\frac{\partial U_r}{\partial r} + \frac{U_r}{r} + \frac{1}{r}\frac{\partial U_\theta}{\partial \theta} = 0. \tag{8.1.10}$$

$$\begin{aligned} &U_r\frac{\partial U_r}{\partial r} + \frac{U_\theta}{r}\frac{\partial U_r}{\partial \theta} - \frac{U_\theta^2}{r} + \frac{U_s^2\cos\theta}{R_c} \\ =&-\frac{1}{\rho}\frac{\partial p}{\partial r} - \frac{1}{r}\frac{\mu}{\rho}\frac{\partial}{\partial \theta}\left(\frac{\partial U_\theta}{\partial r} + \frac{U_\theta}{r} - \frac{1}{r}\frac{\partial U_r}{\partial \theta}\right), \end{aligned} \tag{8.1.11}$$

$$\begin{aligned} &U_\theta\frac{\partial U_\theta}{\partial \theta} + rU_r\frac{\partial U_\theta}{\partial r} + U_rU_\theta - r\frac{U_s^2\sin\theta}{R_c} \\ =&-\frac{1}{\rho}\frac{\partial p}{\partial \theta} + r\frac{\mu}{\rho}\frac{\partial}{\partial r}\left(\frac{\partial U_\theta}{\partial r} + \frac{U_\theta}{r} - \frac{1}{r}\frac{\partial U_r}{\partial \theta}\right), \end{aligned} \tag{8.1.12}$$

and

$$\begin{aligned} &U_r\frac{\partial U_s}{\partial r} + \frac{U_\theta}{r}\frac{\partial U_s}{\partial \theta} \\ =&-\frac{1}{\rho}\frac{1}{R_c}\frac{\partial p}{\partial s} + \frac{\mu}{\rho}\left\{\frac{\partial^2 U_s}{\partial r^2} + \frac{1}{r^2}\frac{\partial^2 U_s}{\partial \theta^2} + \frac{1}{r}\frac{\partial U_s}{\partial r}\right\}. \end{aligned} \tag{8.1.13}$$

Since U_r, U_θ, U_s, and $\partial p/\partial s$ are independent of s, pressure p can be assumed in the form of $sf_1(r,\theta) + f_2(r,\theta)$. Based on Eqs.(8.1.11) and (8.1.12),

we are able to conclude that $f_1(r,\theta)$ is a constant. As a result, the mean pressure gradient along the vessel centre line,

$$-\frac{1}{R_c}\frac{\partial p}{\partial s}, \tag{8.1.14}$$

is a constant.

According to Eq.(8.1.10), we set

$$U_r = -\frac{1}{r}\frac{\partial f_c}{\partial \theta}, \qquad U_\theta = \frac{\partial f_c}{\partial r}, \tag{8.1.15}$$

in which f_c is a function of r and θ. Introducing the expressions in Eq.(8.1.15) into Eqs.(8.1.11) to (8.1.13), and eliminating p from Eqs.(8.1.11) and (8.1.12), we obtain

$$\left(\frac{\partial f_c}{\partial r}\frac{\partial}{\partial \theta} - \frac{\partial f_c}{\partial \theta}\frac{\partial}{\partial r}\right)\nabla_1^2 f_c - \frac{2U_s}{R_c}\left(r\frac{\partial U_s}{\partial r}\sin\theta + \frac{\partial U_s}{\partial \theta}\cos\theta\right) = \frac{r\mu}{\rho}\nabla_1^4 f_c, \tag{8.1.16}$$

and

$$\frac{1}{r}\left(\frac{\partial f_c}{\partial r}\frac{\partial U_s}{\partial \theta} - \frac{\partial f_c}{\partial \theta}\frac{\partial U_s}{\partial r}\right) = -\frac{1}{\rho}\frac{1}{R_c}\frac{\partial p}{\partial s} + \frac{\mu}{\rho}\nabla_1^2 U_s, \tag{8.1.17}$$

where

$$\nabla_1^2 \equiv \frac{\partial}{\partial r^2} + \frac{1}{r}\frac{\partial}{\partial r} + \frac{1}{r^2}\frac{\partial}{\partial \theta^2}. \tag{8.1.18}$$

Three non-dimensional relationships are defined as

$$f_c = \frac{\mu}{\rho}\hat{\phi}_c, \qquad U_s = U_0\hat{w}, \qquad r = a\hat{r}, \tag{8.1.19}$$

where U_0 is the dimensional peak velocity in a straight vessel with the same

cross-section radius of the curved vessel which is driven by the pressure gradient defined in Eq.(8.1.14) as

$$U_0 = -\frac{1}{R_c}\frac{a^2}{4\mu}\frac{\partial p_c}{\partial s}. \tag{8.1.20}$$

Applying the definitions to Eq.(8.1.19), Eqs.(8.1.16) and (8.1.17) can be rewritten in non-dimensional form, which are

$$\left(\frac{\partial\hat{\phi}_c}{\partial\hat{r}}\frac{\partial}{\partial\theta} - \frac{\partial\hat{\phi}_c}{\partial\theta}\frac{\partial}{\partial\hat{r}}\right)\nabla_1^2\hat{\phi}_c + D\hat{w}\left(\hat{r}\frac{\partial\hat{w}}{\partial\hat{r}}\sin\theta + \frac{\partial\hat{w}}{\partial\theta}\cos\theta\right) = \hat{r}\nabla_1^4\hat{\phi}_c, \tag{8.1.21}$$

and

$$\frac{1}{\hat{r}}\left(\frac{\partial\hat{\phi}_c}{\partial\hat{r}}\frac{\partial\hat{w}}{\partial\theta} - \frac{\partial\hat{\phi}_c}{\partial\theta}\frac{\partial\hat{w}}{\partial\hat{r}}\right) = 4 + \nabla_1^2 U_s, \tag{8.1.22}$$

where

$$D = \frac{2U_0^2a^3\rho^2}{\mu^2R_c} = \frac{\rho^2a^7}{8\mu^4R_c^3}\left(\frac{\partial p_c}{\partial s}\right)^2, \tag{8.1.23}$$

in which Eq.(8.1.20) has been used. In Eqs.(8.1.21) and (8.1.22), ∇_1^2 has the same form of the expression in Eq.(8.1.18) through replacing r with $\hat{r}$.

Dean (1928) obtained the approximate analytic solution for Eqs.(8.1.21) and (8.1.22) in powers of constant D (also in the book by Pedley (1980)). The main application of his work is to calculate the flow rate through the curved vessel corresponding to the particular value of D, which is

$$Q_c = \mathcal{C}_D\bar{Q}_c, \tag{8.1.24}$$

where Q_c and $\bar{Q}_c$ represent the flow rates due to a given pressure gradient in two vessels with the same cross section which are respectively curved and

straight, and

$$\mathcal{C}_D = 1 - 0.03058 \cdot \left[\frac{D}{576}\right]^2 + 0.01195 \cdot \left[\frac{D}{576}\right]^4 + O(D^6). \tag{8.1.25}$$

Though the expression in Eq.(8.1.24) is for the flow through an impermeable vessel with constant curvature, we can assume for certain that Eq.(8.1.24) is available for our model, since we have noticed that the permeability of tumour vessel has insignificant effects on the vascular flow, as stated in Section 6.3.

When the high order terms in the perturbation are ignored, Eq.(8.1.24) is adopted to describe the blood flow through a curved tumour vessel. Substituting the Poiseuille's law for the flow flux through a straight vessel in Eq.(5.1.10) into Eq.(8.1.24), introducing the result into Eq.(4.3.9), and noticing that $H_b(s) = 1/R_c$ and $H_c(s) = 0$, we get a differential equation for the vascular flow as

$$\mathcal{C}_D \frac{\mathrm{d}^2 p_c}{\mathrm{d}s^2} + \mathcal{C}_D \frac{4}{a(s)} \frac{\mathrm{d}a}{\mathrm{d}s} \frac{\mathrm{d}p_c}{\mathrm{d}s} + \frac{\mathrm{d}\mathcal{C}_D}{\mathrm{d}s} \frac{\mathrm{d}p_c}{\mathrm{d}s} = \frac{16\mu R_c^2 L_p(s)}{a^3(s)} \left[p_c(s) - p_i(s)\right]. \tag{8.1.26}$$

Another equation, or Eq.(4.3.15), which links the vascular flow pressures and the interstitial pressures on the outer vascular surface, is modified to

$$\begin{aligned} &\frac{1}{2}\left[p_i(\mathbf{x}_0) - p_0\right] \\ =& -\frac{1}{2\pi} \int_{l_v} \int_0^{2\pi} \int_0^{2\pi} R_c a(s) \frac{L_p(s)}{\kappa} \left[p_c(s) - p_i(s)\right] G(\mathbf{x}, \mathbf{x}_0) \mathrm{d}\theta_0 \mathrm{d}\theta \mathrm{d}s \\ &+ \frac{1}{2\pi} \int_{l_v} \int_0^{2\pi} \int_0^{2\pi} R_c a(s) \left[p_i(s) - p_0\right] \nabla G(\mathbf{x}, \mathbf{x}_0) \mathbf{n}(\mathbf{x}) \mathrm{d}\theta_0 \mathrm{d}\theta \mathrm{d}s. \end{aligned} \tag{8.1.27}$$

Together with the inlet and outlet conditions for the vascular flow, we obtain a set of self-contained equations to simulate tumour blood flow when a curved permeable vessel is embedded in tumour interstitium.

Following the discretisation procedure stated in Section 4.3.4, the vessel is divided into N_E cylindrical elements along its centre line, and all the physical variables are approximated to be constant within each element. The continuity condition is imposed at the middle of every element. Therefore, Eq.(8.1.26) can be discretised and solved by FDM as

$$\sum_{j=1}^{N_E} T_{jn}^{c} p_c^{[j]} = -\frac{16\mu R_c^2 L_p^{[n]}}{(a_n)^3} p_i^{[n]}. \tag{8.1.28}$$

In the meantime, Eq.(8.1.28) can be discretised and solved by BEM as

$$\begin{aligned} &\sum_{j=1}^{N_E} \left\{ \delta_{nj} + 2\bar{B}_n^{[j]} - \frac{2L_p^{[j]}}{\kappa} \bar{A}_n^{[j]} \right\} p_i^{[j]} \\ &= -\sum_{j=1}^{N_E} \frac{2L_p^{[j]}}{\kappa} \bar{A}_n^{[j]} p_c^{[j]} + p_0 \left\{ 1 + \sum_{j=1}^{N_E} 2\bar{B}_n^{[j]} \right\}. \end{aligned} \tag{8.1.29}$$

By analogy with the numerical procedure in Section 5.1, we are able to solve Eqs.(8.1.28) and (8.1.29) through iteration. The detailed procedure is described as following:

1) Set initial guess for pressure $p_c(s)$ inside the vessel, and let coefficient $\mathcal{C}_D = 1.0$.

2) Evaluate the right-hand side of Eq.(8.1.29).

3) Solve Eq.(8.1.29) to obtain interstitial pressure $p_i(s)$ on the vascular exterior surface.

4) Evaluate the right-hand side of Eq.(8.1.28).

5) Solve Eq.(8.1.28) to obtain $p_c(s)$, and update the value of coefficient $\mathcal{C}_D$ according to Eq.(8.1.25).

6) Go back to step 2 and repeat the procedure until convergence has been achieved, or the difference in either $p_c(s)$, $p_i(s)$ or $\mathcal{C}_D$ from two successive steps is sufficiently small.

8.2 Results and analysis

For a straight vessel, its curvature radius $R_c \to \infty$, which leads to Dean number $D = 0$ according to the definition in Eq.(8.1.23). In such a circumstance, flux ratio parameter $\mathcal{C}_D = 1$, and the vascular flow is described by the Poiseuille's law. If the curvature of the vessel with the same cross-section area is increased, one can conclude for certain that the flow rate driven by the same pressure gradient will decrease. As a result, along the increasing of the value of ratio a/R_c, the value of flux ratio parameter $\mathcal{C}_D$ drops, and will reach to the minimum value when the value of D is roughly 650. Therefore, Eq.(8.1.24) will not be available when D exceeds that critical value due to limit of perturbation analysis.

Based on the definition in Eq.(8.1.23), vessel radius a has the most powerful effects on D, since D is in direct proportion to the seventh power of a. Given that inlet pressure for the vascular flow $p_a = 5.93283 \times 10^4$ g cm^{-1}s^{-2}, the outlet vascular flow pressure $p_v = 1.19990 \times 10^4$ g cm^{-1}s^{-2}, vessel length $l_v = 1.0$ cm and vessel curvature $l_v/R_c = 4\pi/3$, when D tends to 650, vessel radius $a \approx 0.02$ cm. However, under usual physical and physiological conditions in a solid tumour, vessel radius is within the range between 5 μm to 100 μm [Less *et al.* (1991)]. Therefore, the expression in Eq.(8.1.24) is suitable for our simulations. Fig.8.2 displays the dependence of the relative flux coefficient γ_Q on number of discretised segments N_E, when we adopt the geometric sizes and physical parameters stated above and set the relative round error as

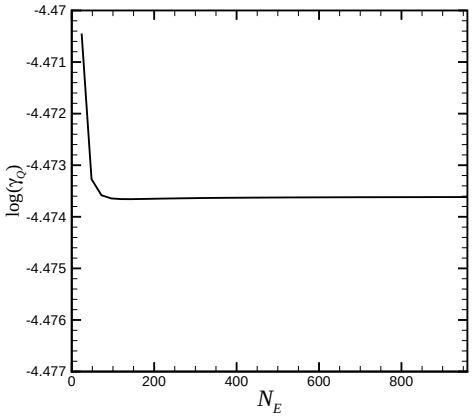

Figure 8.2: Dependence of γ on number of segments N_E.

$E_r = 1. \times 10^{-6}$. The results in Fig.8.2 show that the value of $\gamma_{_Q}$ becomes mesh independent as N_E increases, and indicate that $\gamma_{_Q}$ is accurate enough when the element size is chosen as $\delta s_j = 0.2a/R_c$.

For the case of a curved vessel with radius $a = 0.01$ cm, the inner and outer pressure distributions along the vessel with difference curvatures are plotted in Fig.8.3, when the same inlet and outlet vascular flow conditions stated above are used. Along the increase of vessel curvature, the variation of vascular flow pressures is insignificant, while the interstitial pressures on the external vascular surface are clearly elevated. This is mainly because the relative positions of vessel cross sections have changed because of the vessel curvature, which affects the interactions of the transmural flow among these cross sections. As a result, the extravasation flux is decreased since the vessel permeability and radius remain constant, which leads to a drop of the relative flux coefficient $\gamma_{_Q}$, as presented in Fig.8.4. These results show that vessel curvature is harmful for the transvascular movement of anti-cancer agents with heavy weight and the effectiveness of chemotherapy and radiotherapy. However, we should be aware that the governing equations presented in this chapter are available for the

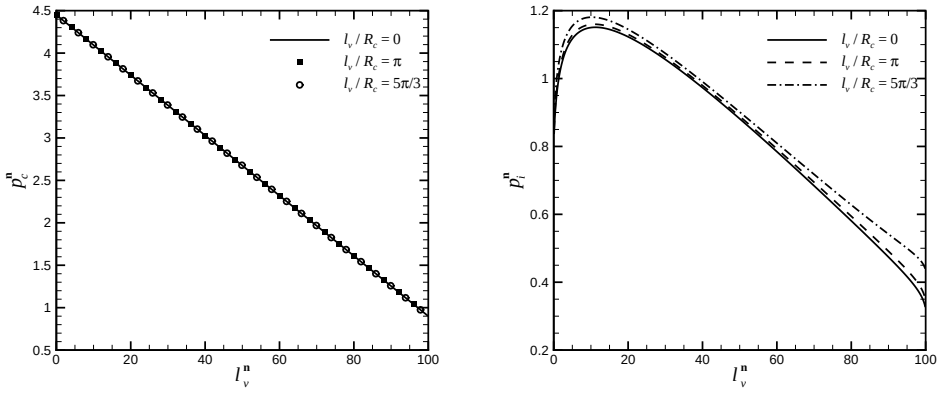

(a) **(b)**

Figure 8.3: Distributions of (a) vascular flow pressures, and (b) interstitial pressures on the external vascular surface.

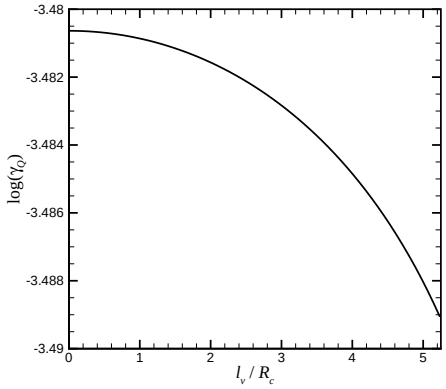

Figure 8.4: Dependence of γ on the vessel curvature.

vessel with mild curvature, or the value of ratio a/R_c is low. For large vascular curvature, or high value of ratio a/R_c, a different model may be needed, and conditions might be different.

In the meantime, the complex shape of tumour vessel has strong influence on the distributions of the interstitial pressure and the flow fluid within tumour interior. Figs.8.5 and 8.6 display the three-dimensional simulation results for

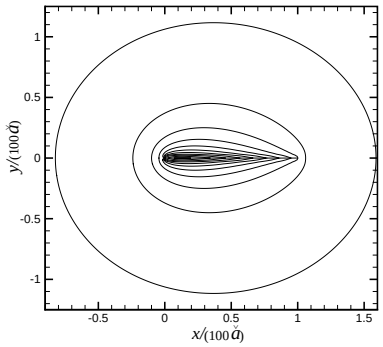

(a) when $l_v/R_c = 0$

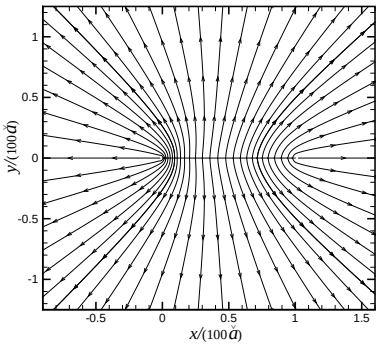

(b) when $l_v/R_c = 0$

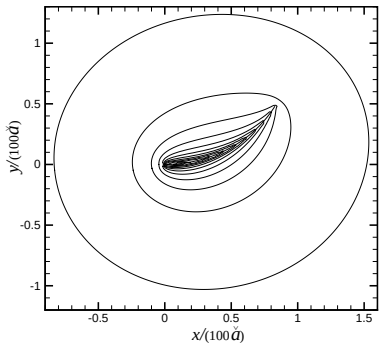

(c) when $l_v/R_c = \pi/3$

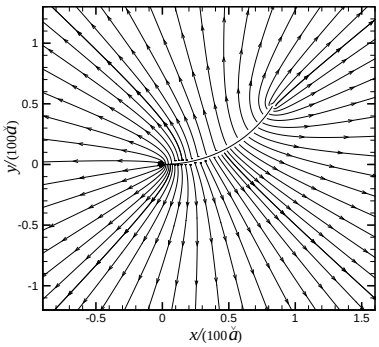

(d) when $l_v/R_c = \pi/3$

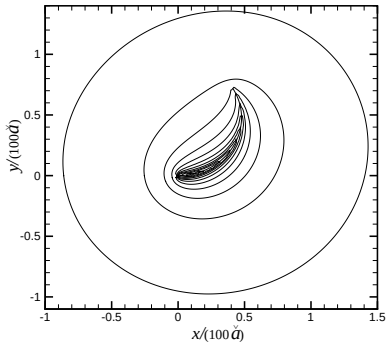

(e) when $l_v/R_c = 2\pi/3$

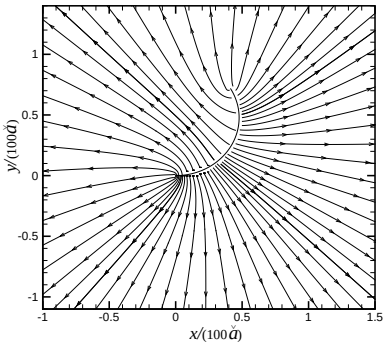

(f) when $l_v/R_c = 2\pi/3$

Figure 8.5: Slides of 3D simulation results for (a, c, e) pressure contours and (b, d, f) blood flow velocity streamlines on the vessel located plane.

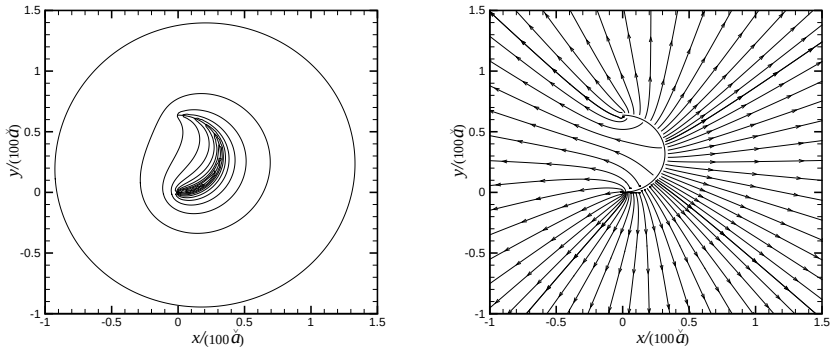

(a) when $l_v/R_c = \pi$ **(b)** when $l_v/R_c = \pi$

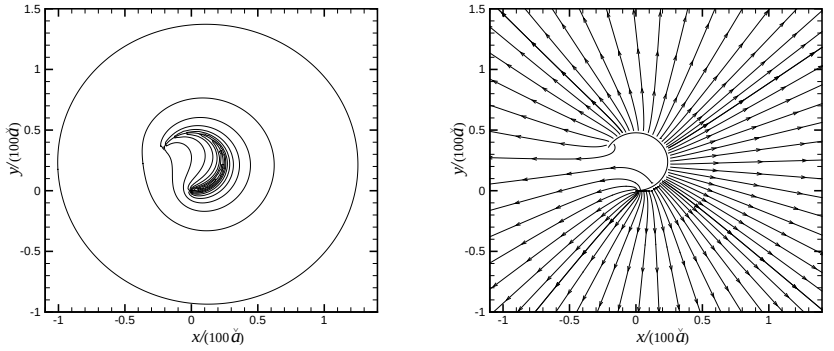

(c) when $l_v/R_c = 4\pi/3$ **(d)** when $l_v/R_c = 4\pi/3$

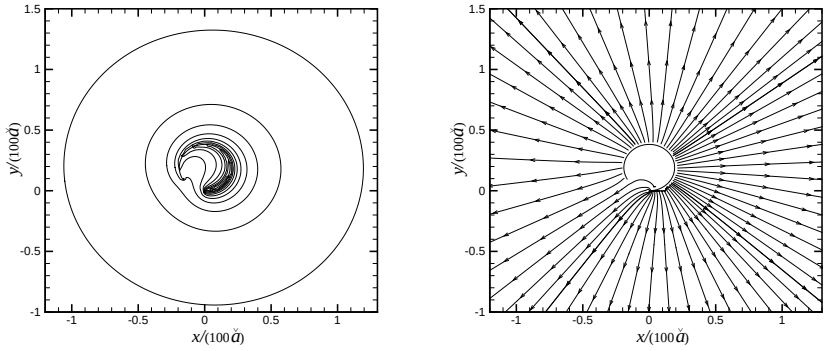

(e) when $l_v/R_c = 5\pi/3$ **(f)** when $l_v/R_c = 5\pi/3$

Figure 8.6: Slides of 3D simulation results for (a, c, e) pressure contours and (b, d, f) blood flow velocity streamlines on the vessel located plane.

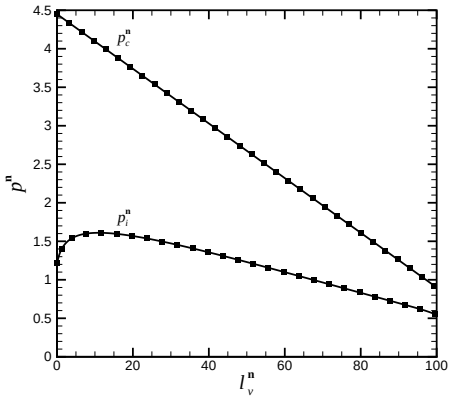

Figure 8.7: Distributions of vascular flow pressures and interstitial pressures on the external vascular surface when $D = 647$. Solid line: results obtained by Eq.(8.1.24); symbol: results calculated by Eq.(5.1.10)

the interstitial pressure contours and the flow velocity streamlines when the vessel is bent with different curvatures. The shapes of pressure contours vary rapidly near the vessel, but tend to be circle away from the vessel. This indicates that the effects of vessel curvature are more significant on the blood flow field around the vessel than that far away from the vessel. Meanwhile, the results of the interstitial flow velocity streamlines show that the interstitial flow on the concave side of the vessel is less active than that on the convex side, and this phenomena becomes more visible along the increasing of vessel curvature. This can lead to uneven distribution of flow flux within tumour space, which would cause insufficient, maybe no supply of anti-cancer agents in some area of tumour interior. As a result, the cancerous cells might not be removed thoroughly within the entire interstitium, which may induce tumour regrowth, and/or develop drug resistance tumour cells. All these results prove that vessel curvature, which is one of the special characters of tumour vascular configuration relative to normal vessels, forms physiological barriers for cancer treatment.

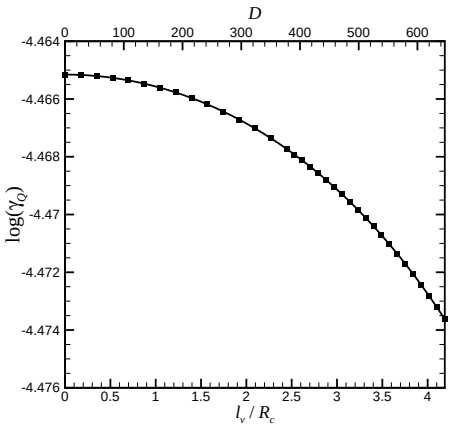

Figure 8.8: Dependence of the relative flux coefficient γ_Q on vessel curvature. Solid line: results obtained by Eq.(8.1.24); symbol: results calculated by Eq.(5.1.10)

According to the results in Fig.8.3a, we notice that the change of the vascular flow pressures is insignificant along the variation of vessel curvature. Eq.(8.1.24) describes that the flux through a curved vessel with given cross-section area and pressure gradient is equal to the flow rate through a straight vessel with the identical geometric and physical conditions multiplying flux ratio parameter $\mathcal{C}_D$. When the Dean number is with the critical value as $D = 650$, $\mathcal{C}_D = 0.98044$. This indicates that, when the vessel curvature is mild, the flux through a curved vessel obtained by the expression in Eq.(8.1.24) is very close to that calculated by the Poiseuille's law directly. Therefore, we can assume that for the blood flow through a curved vessel in tumour, the Poiseuille's law in Eq.(5.1.10) can be applied to replace Eq.(8.1.24). Fig.8.7 shows that when $D = 647$, the results obtained by the Poiseuille's law (symbols) are in good agreement with the results calculated by Eq.(8.1.24) (solid line). Meanwhile, the results in Fig.8.8, which present the dependence of γ_Q on Dean number D, also confirm our assumption.

Chapter 9

Flow through a Permeable Vascular Network in a Solid Tumour

In Chapters 7 and 8, adopting the governing equations derived in Chapter 4, we have investigated the effects of two abnormal characters of tumour vascular architecture, which are the disordered vessel radius and vessel curvature, on tumour blood flow when tumour vasculature is represented as a single vessel. Nevertheless, the practical tumour vasculature is a three-dimensional vascular network characterised with excessive branches and loops. The tumour vascular configuration is complex and disorganised relative to the vasculature in normal tissues. The normal vasculature forms a well-organized, regulated and functional architecture featured by symmetrical dichotomous branching [Jain (2003)]. In contrast, the vascular architecture in tumour is disordered and has atypical bifurcations, trifurcations, self loops and true loops [Less *et al.* (1991)]. Such a kind of complicated vascular network has strong effects on tumour blood flow, which can significantly affect the delivery of anti-cancer agents in tumour.

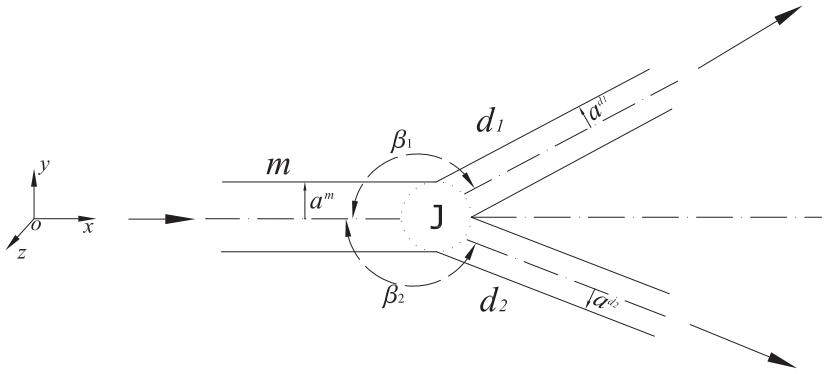

Figure 9.1: Sketch of vascular configuration around the junction point when one mother vessel splits into two daughter vessels.

In this chapter, we study three representative vascular structures of tumour vasculature, including symmetrical dichotomous branching, asymmetrical bifurcation with uneven radius of daughter vessels, and trifurcation. Under most circumstances, the practical tumour vascular network can be decomposed into these three types of structures, which is the motivation of the investigations in this chapter.

For tumour vasculature with complicated configuration, some new challenges are presented in both our mathematical model and the numerical procedure compared with the case in which tumour vasculature is represented by a single vessel. For example, when vessels meet together at a junction point, such as a structure of bifurcation (Fig.9.1), it is required to establish the mathematical description for the flow pattern around the junction. The features of the vascular flow at the junction can affect the flow inside each vessel connecting with it, and eventually have effects on the entire tumour

blood flow. In the meantime, for the complicated vascular network, along the increasing of the number of vessels, the total number of discretised segments generated within the whole vascular network will increase. As aforementioned in Section 5.1, this can make the size of the global fully populated coefficient matrix in BEM enlarged rapidly, which would lead to our numerical simulation encountering with prohibitiveness of computer memory and CPU. Under such a circumstance, some special numerical methods, the domain decomposition method [Wu and Taylor (2003)] for instance, are applied to solve the problem. These issues will be investigated in detail in the following sections.

9.1 Continuity conditions for the flow at the junction in vascular network

Based on the analysis in Section 8.2, under the usual physical and physiological conditions, we can directly apply the Poiseuille's law,

$$Q_c = -\frac{\pi a^4(l)}{8\mu}\frac{\mathrm{d}p_c}{\mathrm{d}l}, \tag{9.1.1}$$

to describe the blood flow through a tumour vessel even if the vessel is not straight.

Within a vascular network in either normal or tumour tissues, a typical configuration with junction is that mother vessel m with radius a^m separates into two daughter vessels d_1 and d_2 with radii a^{d_1} and a^{d_2} respectively at junction point J, as illustrated in Fig.9.1. The outside angle between the mother vessel centre line and the centre line of the kth daughter vessel (d_k) is represented by β_k ($k = 1, 2$ for the case in Fig.9.1). In our model, it is assumed that all the vessels are perfectly matched at the junction. Consequently, at

junction point J, the pressure for the flow in vascular network is continuous, or

$$p_c^m(l) = p_c^{d_k}(l) = p_c^{\mathrm{J}}, \tag{9.1.2}$$

and the mass conservation holds, or

$$Q_c^m(l) = \sum_{k=1}^{N_d} Q_c^{d_k}(l), \tag{9.1.3}$$

in which p_c^{J} is the vascular flow pressure at junction point J, and N_d ($N_d = 2$ for the case in Fig.9.1) is the number of the daughter vessels connecting with the junction. Introducing Eq.(9.1.1) into Eq.(9.1.3), we get

$$[a_{\mathrm{J}}^m(l)]^4 \left.\frac{\mathrm{d}}{\mathrm{d}l}\right|_{\mathrm{J}} [p_c^m(l)] = \sum_{k=1}^{N_d} \left[a_{\mathrm{J}}^{d_k}(l)\right]^4 \left.\frac{\mathrm{d}}{\mathrm{d}l}\right|_{\mathrm{J}} \left[p_c^{d_k}(l)\right]. \tag{9.1.4}$$

Eq.(9.1.4) offers us a mathematical relationship to calculate p_c^{J}. Similar to Eq.(5.1.11), the flow through each vessel within the vascular network is described by

$$\begin{aligned} &[H_b(s)]^2 \frac{\mathrm{d}^2 p_c}{\mathrm{d}s^2} + \left\{ \frac{4[H_b(s)]^2}{a(s)} \frac{\mathrm{d}a(s)}{\mathrm{d}s} + H_c(s) H_b(s) \right\} \frac{\mathrm{d}p_c}{\mathrm{d}s} \\ =&\frac{16\mu L_p(s)}{a^3(s)} \left[p_c(s) - p_i(s)\right]. \end{aligned} \tag{9.1.5}$$

In the above equation, $H_b(s)$ and $H_c(s)$ are kept to represent the effects of vessel shape on the vascular flow, which are defined in Eqs.(4.1.6) and (4.1.7) respectively. Meanwhile, at junction point J, the pressure gradient condition in Eq.(9.1.4) is rewritten as

$$[a_{\mathrm{J}}^m(s)]^4 H_b^m(s) \left.\frac{\mathrm{d}}{\mathrm{d}s}\right|_{\mathrm{J}} [p_c^m(s)] = \sum_{k}^{N_d} \left[a_{\mathrm{J}}^{d_k}(s)\right]^4 H_b^{d_k}(s) \left.\frac{\mathrm{d}}{\mathrm{d}s}\right|_{\mathrm{J}} \left[p_c^{d_k}(s)\right]. \tag{9.1.6}$$

Another relationship linking the vascular internal and external pressures is described in Eq.(4.3.15). Eq.(4.3.15) is available for the case when the vasculature is represented by a single vessel. If there are more than one vessel embedded in tumour interstitium, the whole coupling effects of all vessels should be included, Eq.(4.3.15) is then modified to

$$\begin{aligned}
&\frac{1}{2}\left[p_i(\mathbf{x}_0)-p_0\right] \\
=&-\sum_{k=1}^{N_V}\frac{1}{2\pi}\int_{l_v^{[k]}(s)}\int_0^{2\pi}\int_0^{2\pi}\frac{a(s)}{H_b(s)}\frac{L_p(s)}{\kappa}\left[p_c(s)-p_i(s)\right]G(\mathbf{x},\mathbf{x}_0)\mathrm{d}\theta_0\mathrm{d}\theta\mathrm{d}s \\
&+\sum_{k=1}^{N_V}\frac{1}{2\pi}\int_{l_v^{[k]}(s)}\int_0^{2\pi}\int_0^{2\pi}\frac{a(s)}{H_b(s)}\left[p_i(s)-p_0\right]\nabla G(\mathbf{x},\mathbf{x}_0)\mathbf{n}(\mathbf{x})\mathrm{d}\theta_0\mathrm{d}\theta\mathrm{d}s, \quad (9.1.7)
\end{aligned}$$

in which N_V stands for the number of the vessels within the entire tumour vascular network.

Similar to the discretisation procedure described in Section 4.3.4, every vessel within tumour vasculature is divided into small cylindrical elements along its centre line, and all the physical variables are approximated to remain constant within each element. The continuity condition is then imposed at the middle of every element. As a result, Eq.(9.1.7) can be discretised and calculated by BEM as

$$\begin{aligned}
&\sum_{j=1}^{\bar{N}_E}\left\{\delta_{nj}+2\bar{B}_n^{[j]}-\frac{2L_p^{[j]}}{\kappa}\bar{A}_n^{[j]}\right\}p_i^{[j]} \\
=&-\sum_{j=1}^{\bar{N}_E}\frac{2L_p^{[j]}}{\kappa}\bar{A}_n^{[j]}p_c^{[j]}+p_0\left\{1+\sum_{j=1}^{\bar{N}_E}2\bar{B}_n^{[j]}\right\}, \quad (9.1.8)
\end{aligned}$$

where $\bar{N}_E$ is the number of discretised segments for the whole tumour vascular network.

In the meantime, along the kth daughter vessel, for segment $2 \leq n \leq$

$N_E^{d_k}-1$, Eq.(9.1.5) can be discretised and calculated by FDM as

$$\sum_{j=1}^{N_E^{d_k}} T_{jn}^{d_k} {p_c}^{[j]} = -\frac{16\mu {L_p}^{[n]}}{\left(a_n\right)^3} {p_i}^{[n]}, \qquad n=2,3,\cdots,N_E^{d_k}-1, \tag{9.1.9}$$

where $N_E^{d_k}$ is the number of elements on the kth daughter vessel, and

$$T_{jn}^{d_k} = \begin{cases} \dfrac{2\left({H_b}^{[n]}\right)^2}{(\Delta s_n+\Delta s_{n+1})\Delta s_n} - \dfrac{\Delta s_{n+1}\left({H_b}^{[n]}\right)^2}{(\Delta s_n+\Delta s_{n+1})\Delta s_n}\left(\dfrac{4a_n'}{a_n}+\dfrac{{H_c}^{[n]}}{{H_b}^{[n]}}\right) & j=n-1, \\ \dfrac{(\Delta s_{n+1}-\Delta s_n)\left({H_b}^{[n]}\right)^2}{\Delta s_n \Delta s_{n+1}}\left[\dfrac{4a_n'}{a_n}+\dfrac{{H_c}^{[n]}}{{H_b}^{[n]}}\right] - \dfrac{2\left({H_b}^{[n]}\right)^2}{\Delta s_n \Delta s_{n+1}} - \dfrac{16\mu {L_p}^{[n]}}{\left(a_n\right)^3} & j=n, \\ \dfrac{2\left(H_b^{[n]}\right)^2}{(\Delta s_n+\Delta s_{n+1})\Delta s_{n+1}} + \dfrac{\Delta s_n\left(H_b^{[n]}\right)^2}{(\Delta s_n+\Delta s_{n+1})\Delta s_{n+1}}\left(\dfrac{4a_n'}{a_n}+\dfrac{H_c^{[n]}}{H_b^{[n]}}\right) & j=n+1, \\ 0 & \text{else.} \end{cases} \tag{9.1.10}$$

The pressure continuity condition in Eq.(9.1.2) is used as the inlet boundary condition for the flow inside each daughter vessel. Therefore, for segment $n=1$ on the kth daughter vessel, Eq.(9.1.9) is reduced to

$$\sum_{j=1}^{N_E^k} T_{j1}^{d_k} p_c^{[j]} = -\frac{16\mu L_p^{[1]}}{\left(a_1\right)^3} p_i^{[1]} - T_{\text{J}}^{d_k} p_c^{\text{J}}, \tag{9.1.11}$$

where

$$T_{j1}^{d_k} = \begin{cases} \dfrac{\Delta s_2 - \Delta s_{\text{J}}}{\Delta s_{\text{J}} \Delta s_2}\left(\dfrac{4a_1'}{a_1}+\dfrac{H_c^{[1]}}{H_b^{[1]}}\right) - \dfrac{2\left(H_b^{[1]}\right)^2}{\Delta s_{\text{J}} \Delta s_2} - \dfrac{16\mu L_p^{[1]}}{\left(a_1\right)^3} & j=1, \\ \dfrac{\Delta s_{\text{J}}}{(\Delta s_{\text{J}}+\Delta s_2)\Delta s_2}\left(\dfrac{4a_1'}{a_1}+\dfrac{H_c^{[1]}}{H_b^{[1]}}\right) + \dfrac{2\left(H_b^{[1]}\right)^2}{(\Delta s_{\text{J}}+\Delta s_2)\Delta s_2} & j=2, \\ 0 & \text{else,} \end{cases} \tag{9.1.12}$$

and

$$T_{\text{J}}^{d_k} = -\frac{\Delta s_2}{(\Delta s_{\text{J}} + \Delta s_2)\Delta s_{\text{J}}}\left(\frac{4a_1'}{a_1} + \frac{H_c^{[1]}}{H_b^{[1]}}\right) + \frac{2\left(H_b^{[1]}\right)^2}{(\Delta s_{\text{J}} + \Delta s_2)\Delta s_{\text{J}}}, \tag{9.1.13}$$

in which $\Delta s_{\text{J}} = s_1 - s_{\text{J}}$, and s_{J} reflects the position of junction J. When outlet pressure p_v for the vascular flow is given at the venous point of every daughter vessel, for segment $n = N_E^k$ on the kth daughter vessel, Eq.(9.1.9) is reduced to

$$\sum_{j=1}^{N_E^k} T_{jN_E^k}^{d_k} p_c^{[j]} = -\frac{16\mu L_p^{[N_E^k]}}{\left(a_{N_E^k}\right)^3} p_i^{[N_E^k]} - T_v^{d_k} p_v, \tag{9.1.14}$$

where

$$T_{jN_E^k}^{d_k} = \begin{cases} \dfrac{2\left(H_b^{[N_E^k]}\right)^2}{(\Delta s_{N_E^k} + \Delta s_v)\Delta s_{N_E^k}} - \dfrac{\Delta s_v}{(\Delta s_{N_E^k} + \Delta s_v)\Delta s_{N_E^k}}\left(\dfrac{4a'_{N_E^k}}{a_{N_E^k}} + \dfrac{H_c^{[N_E^k]}}{H_b^{[N_E^k]}}\right) & j = N_E^k - 1, \\ \dfrac{\Delta s_v - \Delta s_{N_E^k}}{\Delta s_{N_E^k}\Delta s_v}\left(\dfrac{4a'_{N_E^k}}{a_{N_E^k}} + \dfrac{H_c^{[N_E^k]}}{H_b^{[N_E^k]}}\right) - \dfrac{2\left(H_b^{[N_E^k]}\right)^2}{\Delta s_{N_E^k}\Delta s_v} - \dfrac{16\mu L_p^{[N_E^k]}}{\left(a_{N_E^k}\right)^3} & j = N_E^k, \\ 0 & \text{else}, \end{cases} \tag{9.1.15}$$

and

$$T_v^{d_k} = \frac{\Delta s_{N_E^k}}{(\Delta s_{N_E^k} + \Delta s_v)\Delta s_v}\left(\frac{4a'_{N_E^k}}{a_{N_E^k}} + \frac{H_c^{[N_E^k]}}{H_b^{[N_E^k]}}\right) + \frac{2\left(H_b^{[N_E^k]}\right)^2}{(\Delta s_{N_E^k} + \Delta s_v)\Delta s_v}. \tag{9.1.16}$$

The governing equations for the flow inside the mother vessel can be discretised in the same manner. However, the flux conservation condition in Eq.(9.1.3) instead of the pressure is imposed at the junction. The flux condition is given through the pressure derivatives in Eq.(9.1.6), and the three-point back and

forward difference formulae are applied to replace the derivatives on the left- and right-hand sides of that equation respectively. Eq.(9.1.6) then becomes

$$\sum_{j=0}^{1}\left(T_{j+2}^{m}\right)p_{c}^{[N_{E}^{m}-j]}+T_{1}^{m}p_{c}^{\mathrm{J}}=\sum_{k=1}^{N_{E}^{k}}\left[T_{1}^{d_{k}}p_{c}^{\mathrm{J}}+\sum_{j=1}^{2}T_{j+1}^{d_{k}}p_{c}^{d_{k}[j]}\right], \tag{9.1.17}$$

where N_E^m is the number of elements generated along the mother vessel,

$$\begin{cases} T_{1}^{m}=-\dfrac{H_{b}^{[N_{E}^{m}]}}{\left(a_{N_{E}^{m}}\right)^{4}}\dfrac{2s_{\mathrm{J}}-s_{N_{E}^{m}}-s_{N_{E}^{m}-1}}{\left(s_{\mathrm{J}}-s_{N_{E}^{m}}\right)\left(s_{\mathrm{J}}-s_{N_{E}^{m}-1}\right)}, \\ T_{2}^{m}=\dfrac{H_{b}^{[N_{E}^{m}]}}{\left(a_{N_{E}^{m}}\right)^{4}}\dfrac{s_{\mathrm{J}}-s_{N_{E}^{m}-1}}{\left(s_{\mathrm{J}}-s_{N_{E}^{m}}\right)\left(2s_{\mathrm{J}}-s_{N_{E}^{m}}-s_{N_{E}^{m}-1}\right)}, \\ T_{3}^{m}=-\dfrac{H_{b}^{[N_{E}^{m}]}}{\left(a_{N_{E}^{m}}\right)^{4}}\dfrac{s_{\mathrm{J}}-s_{N_{E}^{m}}}{\left(s_{\mathrm{J}}-s_{N_{E}^{m}-1}\right)\left(2s_{\mathrm{J}}-s_{N_{E}^{m}}-s_{N_{E}^{m}-1}\right)}, \end{cases} \tag{9.1.18}$$

and

$$\begin{cases} T_{1}^{d_{k}}=-\dfrac{H_{b}^{d_{k}[1]}}{\left(a_{1}^{d_{k}}\right)^{4}}\dfrac{s_{1}^{d_{k}}+s_{2}^{d_{k}}-2s_{\mathrm{J}}}{\left(s_{1}^{d_{k}}-s_{\mathrm{J}}\right)\left(s_{2}^{d_{k}}-s_{\mathrm{J}}\right)}, \\ T_{2}^{d_{k}}=\dfrac{H_{b}^{d_{k}[1]}}{\left(a_{1}^{d_{k}}\right)^{4}}\dfrac{s_{2}^{d_{k}}-s_{\mathrm{J}}}{\left(s_{1}^{d_{k}}-s_{\mathrm{J}}\right)\left(s_{1}^{d_{k}}+s_{2}^{d_{k}}-2s_{\mathrm{J}}\right)}, \\ T_{3}^{d_{k}}=-\dfrac{H_{b}^{d_{k}[1]}}{\left(a_{1}^{d_{k}}\right)^{4}}\dfrac{s_{1}^{d_{k}}-s_{\mathrm{J}}}{\left(s_{2}^{d_{k}}-s_{\mathrm{J}}\right)\left(s_{1}^{d_{k}}+s_{2}^{d_{k}}-2s_{\mathrm{J}}\right)}. \end{cases} \tag{9.1.19}$$

If inlet vascular flow pressure p_a is given at the arterial point of the mother vessel, for segment $n = 1$ on the mother vessel, the discretised equation is in the same form of Eq.(9.1.11) but replacing p_c^{J} and s_{J} with p_a and s_a respectively.

The above set of equations can be solved through iteration. Similar to the numerical procedure in Section 5.1, the detailed procedure for blood flow through a vascular network is summarised as below:

1) Set up initial guess for interstitial pressure $p_i(s)$ on the exterior vascular surface.

2) Guess the vascular pressure p_c^{J} at the junction.

3) Evaluate the right-hand sides of Eqs.(9.1.9), (9.1.11) and (9.1.14).

4) Solve Eqs.(9.1.9), (9.1.11) and (9.1.14) for the pressures inside the daughter vessels.

5) Solve the equations similar to Eqs.(9.1.9) and (9.1.11) for the pressures inside the mother vessel by applying the flux conservation condition in Eq.(9.1.17) at the junction.

6) Use the solution of the pressures inside the mother vessel to get new p_c^{J}.

7) Repeat step 3 to step 6 until the pressures for the vascular flow have converged.

8) Evaluate the right-hand side of Eq.(9.1.8).

9) Solve Eq.(9.1.8) for the interstitial pressures on the exterior vascular surface.

10) Repeat step 2 to step 9 until the pressures both inside the vascular network and on the outside vascular walls have converged.

Compared with the computation procedure for the case of a single vessel as stated in Section 5.1, only steps 1, 3, 4, 9 and 10 mentioned above are previously involved.

To verify the mathematical model and the numerical procedure for the case of tumour vasculature with branches, we artificially divide the single straight vessel in the case which was investigated in the beginning of Section 5.2 into two separated parts. Each part of the vessel is solved independently, and the conditions of pressure continuity and flux conservation are imposed

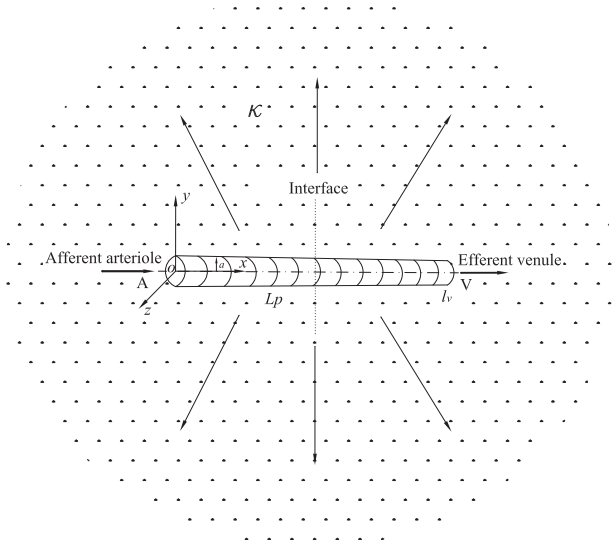

Figure 9.2: Sketch of a single straight vessel splits into two connecting straight vessels.

at the junction or the interface, as sketched in Fig.9.2. Adopting the physical parameters of that test case, the pressures inside the vessel, the interstitial pressures on the external vascular surface, and the extravasation flux obtained by the one-whole-vessel simulation and by the two-separated-vessel simulation are presented in Fig.9.3, when the mesh size is set as $\delta s_j = 0.2a$ and the relative round error as $Er = 1 \times 10^{-6}$ for these two simulations. Fig.9.3 shows that the results are in excellent agreement, which indicates that our matching conditions at the junction and the numerical procedure are rational. The calculation time by the one-whole-vessel simulation is 142s, while the time by the two-separated-vessel simulation is 160s. The clear difference of the simulation time is due to that the numerical procedure in the two-separated-vessel simulation is more complicated than that in the one-whole-vessel simulation.

According to the foregoing analysis in Section 5.2, the domain decomposition method [Wu and Taylor (2003)] can be adopted to avoid the prohibitiveness of computer CPU and memory when the size of the global fully

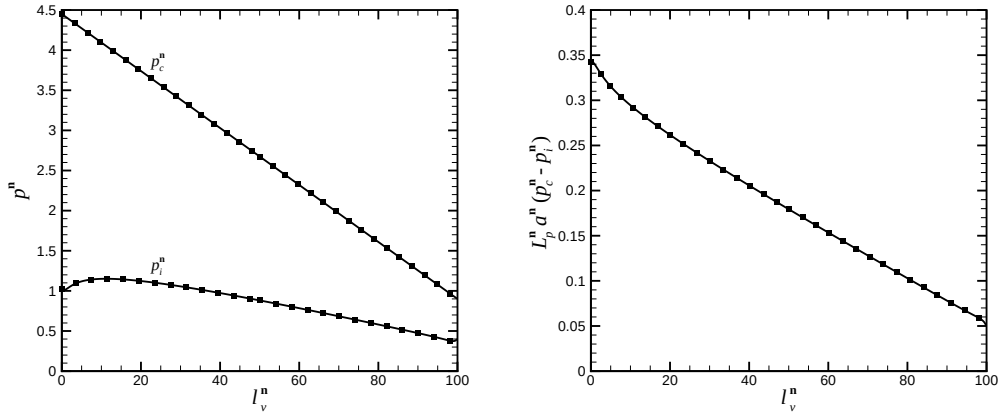

(a) **(b)**

Figure 9.3: Distributions of (a) vascular flow pressures and interstitial pressures on the external vascular surface, (b) extravasation flux along vessel. Solid line: results with one-vessel-simulation; symbols: results with two-vessel-simulation.

populated matrix in BEM is too large. Mathematically, the basic idea of the domain decomposition method is to separate the fully populated matrix into sub-matrices with small sizes along its principal diagonal as

$$\left[\mathrm{Mx}_{\mathrm{BEM}}^{\bar{N}_E \bar{N}_E}\right] = \begin{bmatrix} \mathrm{Mx}_{\mathrm{BEM}}^{11} & \mathrm{Mx}_{\mathrm{BEM}}^{12} & \cdots & \mathrm{Mx}_{\mathrm{BEM}}^{1s} \\ \mathrm{Mx}_{\mathrm{BEM}}^{21} & \mathrm{Mx}_{\mathrm{BEM}}^{22} & \cdots & \mathrm{Mx}_{\mathrm{BEM}}^{2s} \\ \vdots & \vdots & \vdots & \vdots \\ \mathrm{Mx}_{\mathrm{BEM}}^{k1} & \mathrm{Mx}_{\mathrm{BEM}}^{k2} & \cdots & \mathrm{Mx}_{\mathrm{BEM}}^{kk} \end{bmatrix}. \tag{9.1.20}$$

As a result, the original large-size set of discretised equations derived by BEM, for example Eq.(9.1.8), is divided into some sets of discretised equations with smaller size based on the sub-matrices $\mathrm{Mx}_{\mathrm{BEM}}^{ii} \quad (i = 1, 2, \cdots, k)$ along the principal diagonal of the matrix on the right-hand side of Eq.(9.1.20). These sets of equations can be solved through iteration. In this way, only part of coefficients within the original global fully populated matrix in BEM are

Table 9.1: Calculation time by two-separated-vessel simulation

Method		Time(s)
size of $\mathrm{Mx}^{ii}_{\mathrm{BEM}} = 250 \times 250$	$i = 1, 2$	4839
size of $\mathrm{Mx}^{ii}_{\mathrm{BEM}} = 125 \times 125$	$i = 1, 2, 3, 4$	7190
one domain method		160

stored during the entire numerical simulation, which can help us to avoid the prohibitiveness of personal computer CPU and memory. However, adopting the domain decomposition method has to sacrifice simulation time, since there is one more inner iteration to be added into the numerical procedure stated above, and the unrecorded BEM coefficients are required to be calculated in every step of this inner iteration. Table9.1 shows that there is a significant increase of calculation time for the test case by the domain decomposition method compared with the original one domain method.

9.2 Symmetrical dichotomous branching

Having verified the model, we take our study to the next step to consider the cases as tumour vasculature with branches. Firstly, we investigate a case of a symmetrical structure of vasculature when a straight mother vessel splits into two straight daughter vessels with the same radius, and both two outside angles at the junction are equal to each other, or $\beta_1 = \beta_2 = \beta$. This kind of symmetrical dichotomous branching configuration is not only common in normal tissues, but also can be found in tumour tissues. In this case, the vascular network is permeable and embedded in a large solid tumour whose

surface is far away from the network. All the vessel centre lines are placed on one plane (oxy), and the afferent connecting point (arterial point) of mother vessel m is located at origin o of reference frame $o-xyz$ whose centre line is along axis x, as illustrated in Fig.9.1. According to the patterns of tumour vascular network summarised by Less *et al.* (1991), if the outside angles of two daughter vessels are equal with each other, the radii of both daughter vessels are one order lower than that of the mother vessel. Therefore, we can define the geometrical sizes of the vascular network in the present case as followings: lengths of all three vessels $l_v^m = l_v^{d_1} = l_v^{d_2} = 0.5$ cm, radius of mother vessel $a^m = 0.01$ cm, radii of two daughter vessels $a^{d_1} = a^{d_2} = 0.004$ cm, and outside angle $\beta = 2\pi/3$ at junction point J. Meanwhile, we set the tumour hydraulic conductivity parameter as $\kappa = 10^{-10}$ g^{-1}cm^{3}s, the tumour peripheral pressure as $p_0 = 6.666 \times 10^2$ g cm^{-1}s^{-2}, the permeable parameters of all three vessels as $L_p^m = L_p^{d_1} = L_p^{d_2} = 10^{-9}$ g^{-1}cm^{2}s, the inlet vascular flow pressure in the mother vessel as $p_a = 5.93283 \times 10^4$ g cm^{-1}s^{-2}, and the outlet venous pressures for the flow in both daughter vessels as $p_v^{d_1} = p_v^{d_2} = 1.19990 \times 10^4$ g cm^{-1}s^{-2}. According to the symmetry of the geometrical and physical data in this case, we are able to predict that the flow patterns in two daughter vessels are identical to each other, and the tumour interstitial flow field is symmetrical, as shown in Figs.9.4 and 9.5 respectively. In Fig.9.4, we display the vascular flow pressures and the interstitial pressures on the exterior vascular surface along all three vessels together by placing the daughter vessels as the extension of the mother vessel after the junction. The results in Fig.9.4a directly reflect the pressure continuity condition for the vascular flow at junction point J as defined in Eq.(9.1.2). This figure also shows that pressure $p_c(s)$ in both daughter vessels decreases faster than that in the mother vessel. Generally speaking, the blood

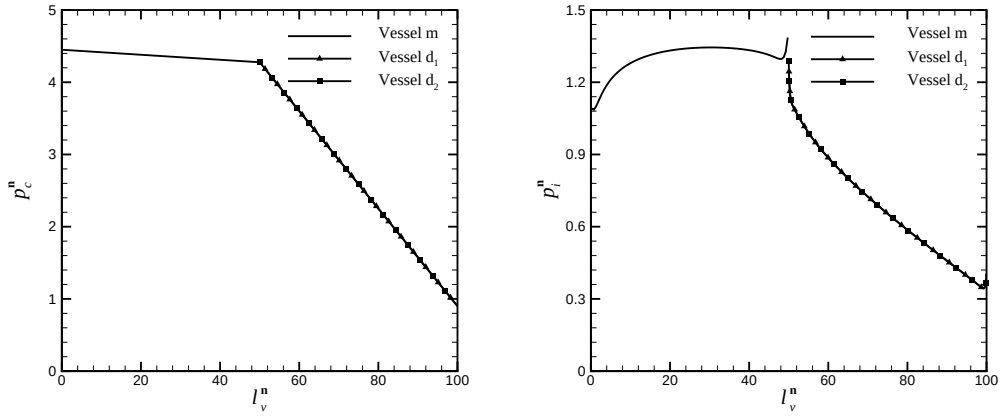

(a) **(b)**

Figure 9.4: Distributions of (a) vascular flow pressures and (b) interstitial pressures on the exterior vascular surface.

flow through a vascular network can be described as

$$Q = \frac{\nabla p_c}{Z_\eta Z_g}, \tag{9.2.1}$$

in which Z_η and Z_g reflect the viscous and the geometrical resistances for the vascular flow respectively. Viscous resistance Z_η can be taken as a constant since the blood viscosity is fixed throughout this work, while geometrical resistance Z_g varies according to the structure and geometrical sizes of the vascular network. Z_g depends on the geometrical sizes of vessels strongly, particularly on vessel radius. For example, when the vasculature is represented by a single straight vessel, Z_g is in inverse proportion to the forth power of vessel radius as described by the Poiseuille's law in Eq.(9.1.1). In the present case, noticing that the outlet venous pressures for the flow in both daughter vessels are equal to each other, and taking into account the matching conditions for the vascular flow at the junction defined in Eqs.(9.1.2) and (9.1.3), we can regard the daughter vessels as two resistances which are connected in parallel, and

the mother vessel and the daughter vessels as two resistances which are connected in series at junction point J. As a consequence, the overall geometrical resistance for the vascular flow can be written as

$$Z_g = Z_g^m + Z_g^d, \tag{9.2.2}$$

where Z_g^m is the geometrical resistance of mother vessel m, and

$$Z_g^d = \frac{1}{\frac{1}{Z_g^{d_1}} + \frac{1}{Z_g^{d_2}}}, \tag{9.2.3}$$

in which $Z_g^{d_1}$ and $Z_g^{d_2}$ represent the geometrical resistances of daughter vessels d_1 and d_2 respectively. For our current case, since the geometrical sizes of the two daughter vessels are identical to each other, we have

$$Z_g^d = \frac{1}{2} Z_g^{d_1}. \tag{9.2.4}$$

As the mother vessel and the daughter vessels are all straight, and they are identical in length, we can conclude that Z_g^m is much lower than Z_g^d as the radius of the mother vessel is larger than that of the daughter vessel. As a result, the pressure gradient in the mother vessel is lower than that in the daughter vessel.

Meanwhile, the pattern of the pressures inside vessels affects the interstitial pressures on the exterior vascular surface significantly, as displayed in Fig.9.4b. The results in this figure also show that the interstitial pressures on the external vascular surface have some rapid variation near the junction. Strictly speaking, for the interstitial pressures on the exterior vascular surface near the junction, the present model may not be sufficiently accurate, since there are sharp corners where the vessels meet. As a result, the normal vector

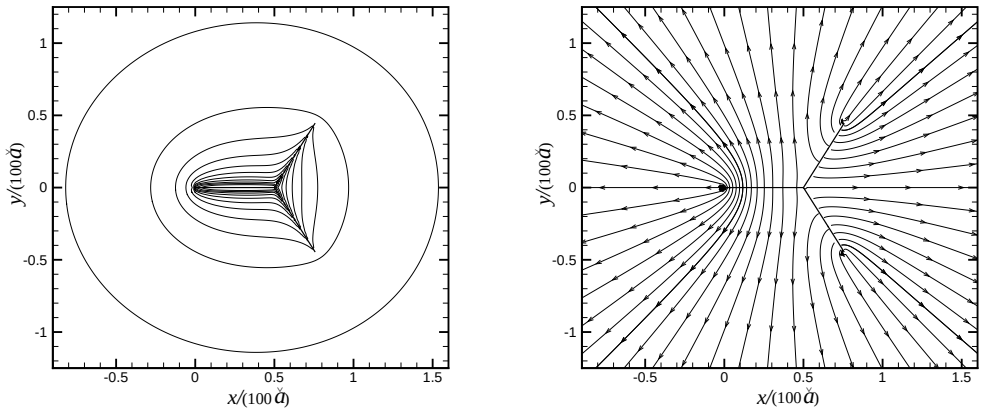

Figure 9.5: Slides of 3D simulation results for (a) pressure contours and (b) blood flow velocity streamlines on the vascular network located plane.

of the vascular surface at junction point J is not continuous. Ideally, it may be required to obtain a local solution for the interstitial flow around the junction referring to the research work in the area of naval and ocean engineering as illustrated by Faltinsen and Pettersen (1987). However, when our interest lies in the global results, the present model is still highly relevant (Fig.9.5).

The symmetrical flow can be easily disturbed when there are some perturbations on physical parameters, such as the unequal outlet venous pressures, or the unequal vascular permeable coefficients of two daughter vessels. Permeability is one of the particular features of tumour vasculature relative to the vessels in normal tissues. As have been discussed in Section 6.3, the effects of vessel permeability on vascular flow are insignificant. Consequently, when we adjust permeability $L_p^{d_2}$ of daughter vessel d_2 while let the rest of physical parameters remain unchanged, the pressure at the junction in the vascular network almost remains constant, as shown in Fig.9.6. However, vessel permeability has strong influence on the interstitial pressures on the external vascular surface and the

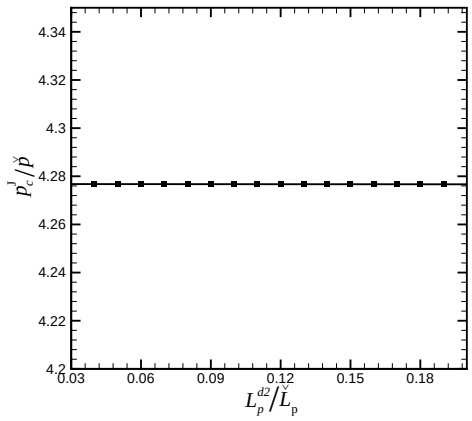

Figure 9.6: Dependence of pressure p_c^{J} on permeability $L_p^{d_2}$ of daughter vessel d_2.

extravasation flux. Along the increasing of $L_p^{d_2}$, interstitial pressure $p_i(s)$ on the exterior surface of the entire vascular network is elevated, as shown in Figs.9.7a, 9.7b and 9.7c. The distribution of extravasation flux along the vascular network is complicated. For either mother vessel m or daughter vessel d_1, as their permeability does not vary, the extravasation flux along either of them is decreased since $p_i(s)$ is elevated while pressure $p_c(s)$ inside vessels almost remains unchanged, as presented in Figs.9.7a and 9.7b. On the other hand, for daughter vessel d_2, due to the increasing of vessel permeability $L_p^{d_2}$, the extravasation flux is increased despite the elevated $p_i(s)$, as shown in Fig.9.7c. The results in Fig.9.8a indicate that the relative flux coefficient $\gamma_{_Q}$ is improved when $L_p^{d_2}$ increases, where the definition of $\gamma_{_Q}$ has been modified to

$$\gamma_{_Q} = \frac{Q_a - \sum_{k=1}^{N_d} Q_v^k}{Q_a}. \tag{9.2.5}$$

Consequently, the whole amount of the extravasation flux for the entire vascular network is improved when $L_p^{d_2}$ is raised, since the flow through the vascular

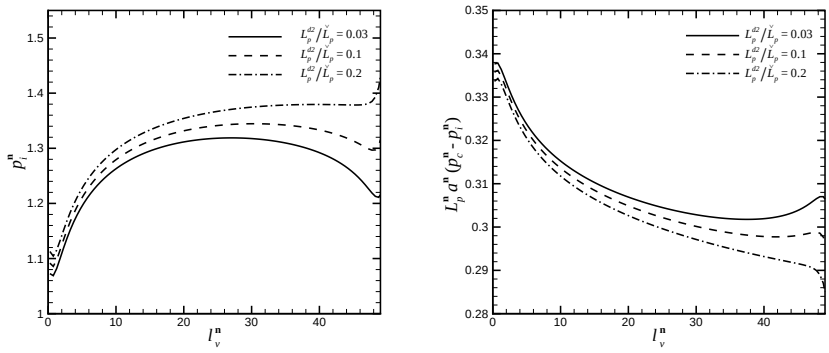

(a) mother vessel m

(b) mother vessel m

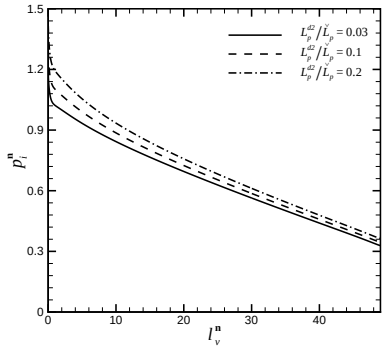

(c) daughter vessel d_1

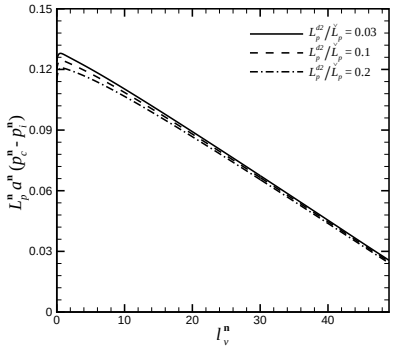

(d) daughter vessel d_1

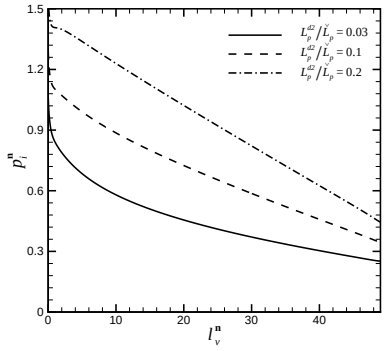

(e) daughter vessel d_2

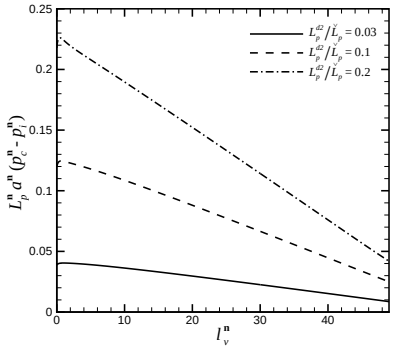

(f) daughter vessel d_2

Figure 9.7: Distributions of (a, c, e) interstitial pressures on the external vascular surface and (b, d, f) extravasation flux along vascular network.

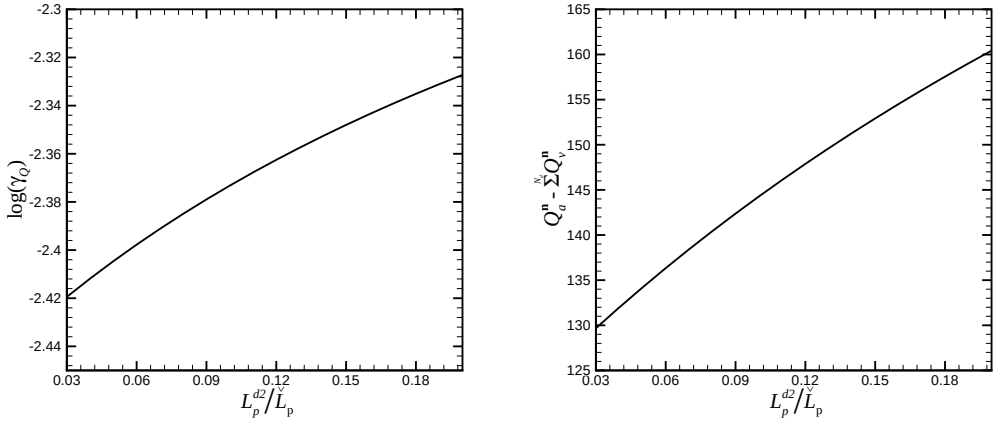

Figure 9.8: Dependence of the relative flux coefficient γ_Q and extravasation flux on vessel permeability $L_p^{d_2}$ of daughter vessel d_2.

network is barely affected, as plotted in Fig.9.8b. Meanwhile, the asymmetrical interstitial pressures on the external vascular surface and the uneven extravasation flux caused by the unequal permeability of the two daughter vessels have some clear effects on the flow in tumour interstitium. Fig.9.9 shows that near the vascular network, the daughter vessel with higher permeability generates higher interstitial pressures around it, which pushes blood flow to the daughter vessel with lower permeability. Nevertheless, away from the vasculature, the shapes of the interstitial pressure contours tend to be circular. Therefore, one can conclude that vessel permeability can affect the extravasation flux, the relative flux coefficient, and the blood flow field within tumour interior at some level. If part vessel permeability can be adjusted, the overall ability of transvascular delivery of macromolecules with heavy weight and the effectiveness of radiotherapy and chemotherapy could be improved by raising that part of the vascular permeability.

The unequal outlet venous pressures for the flow in two daughter vessels can also disturb the symmetrical flow field within tumour interstitium even

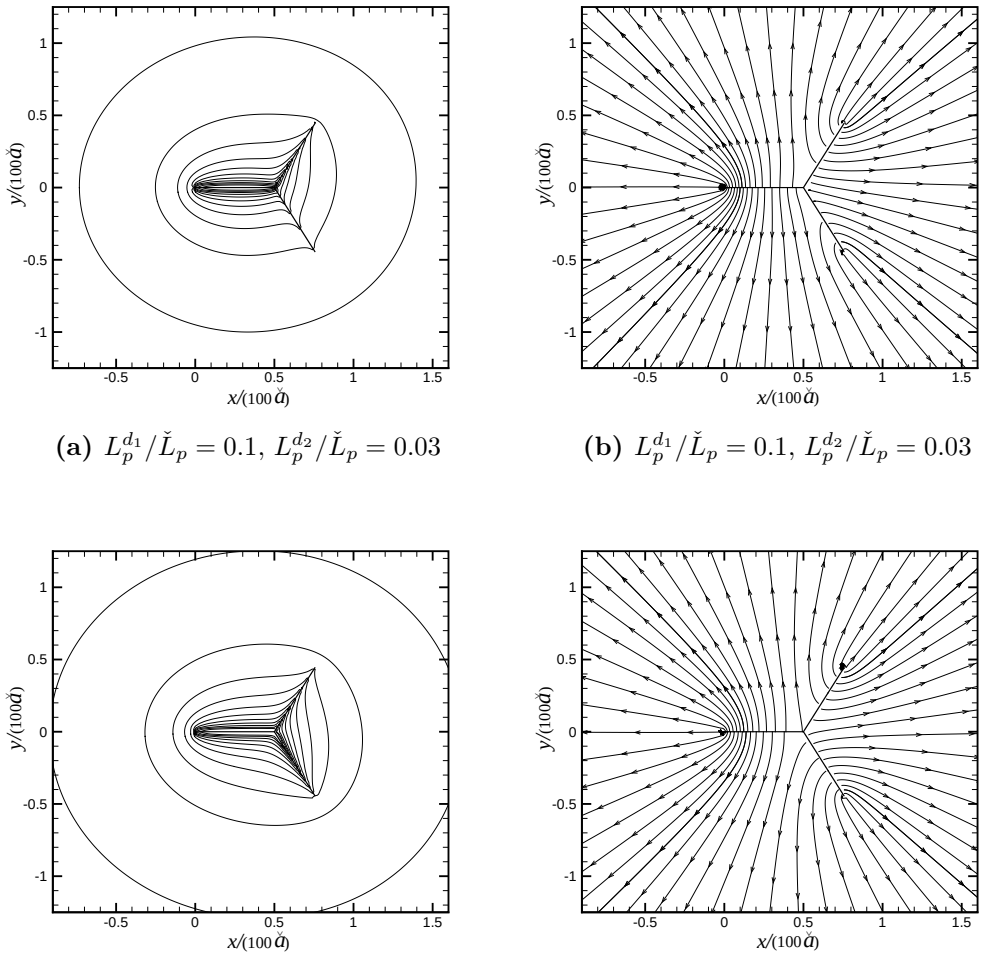

(a) $L_p^{d_1}/\check{L}_p = 0.1$, $L_p^{d_2}/\check{L}_p = 0.03$ **(b)** $L_p^{d_1}/\check{L}_p = 0.1$, $L_p^{d_2}/\check{L}_p = 0.03$

(c) $L_p^{d_1}/\check{L}_p = 0.1$, $L_p^{d_2}/\check{L}_p = 0.2$ **(d)** $L_p^{d_1}/\check{L}_p = 0.1$, $L_p^{d_2}/\check{L}_p = 0.2$

Figure 9.9: Slides of 3D simulation results for (a, c) pressure contours and (b, d) blood flow velocity streamlines on the vascular network located plane.

though the vasculature is symmetrical. If we increase outlet venous pressure $p_v^{d_2}$ for the flow in daughter vessel d_2, but keep the other physical flow parameters to remain constant, vascular flow pressure p_c^{J} at the junction is raised, and interstitial pressure $p_i(s)$ on the external vascular surface is elevated, as shown in Figs.9.10 and 9.11 respectively. In the meantime, the results in Fig.9.11

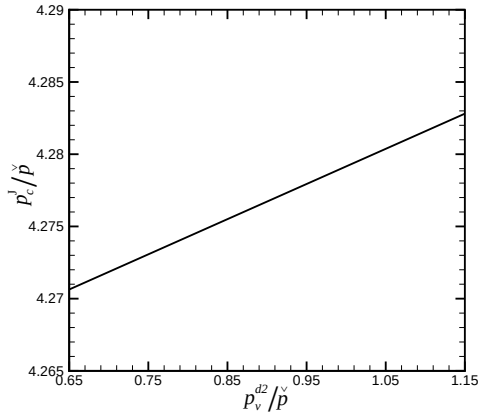

Figure 9.10: Dependence of pressure p_c^{J} on outlet venous pressure $p_v^{d_2}$ of daughter vessel d_2.

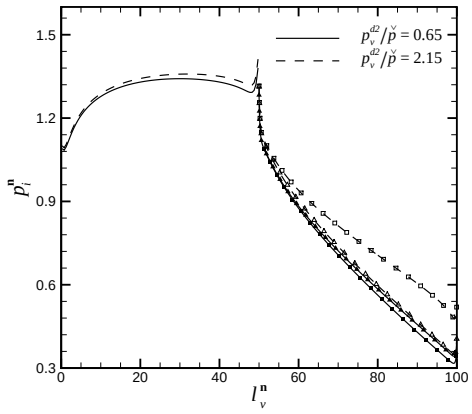

Figure 9.11: Distributions of interstitial pressures on the external vascular surface. Delta symbols: daughter vessel d_1; square symbols: daughter vessel d_2.

indicate that the daughter vessel with higher outlet venous pressure generates higher interstitial pressures around it compared with the interstitial pressures near the daughter vessel with the lower outlet venous pressure. This affects the distributions of the interstitial pressure and the flow fluid in tumour interior, as presented in Fig.9.12. We might be able to obtain the similar flow phenomena

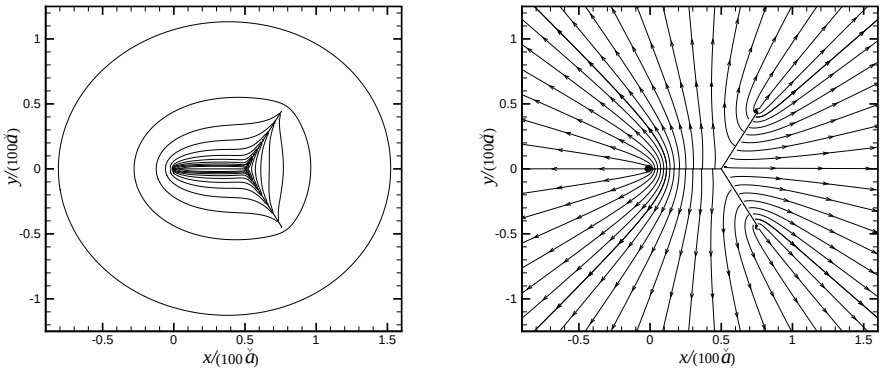

(a) $p_v^{d_1}/\check{p} = 0.9$, $p_v^{d_2}/\check{p} = 0.65$ **(b)** $p_v^{d_1}/\check{p} = 0.9$, $p_v^{d_2}/\check{p} = 0.65$

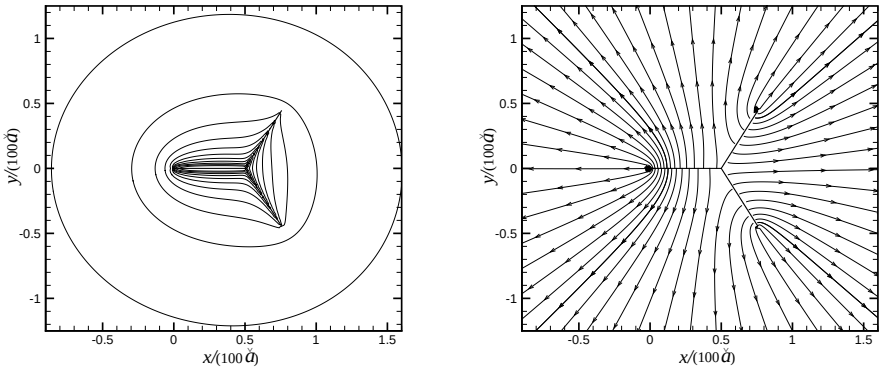

(c) $p_v^{d_1}/\check{p} = 0.9$, $p_v^{d_2}/\check{p} = 2.15$ **(d)** $p_v^{d_1}/\check{p} = 0.9$, $p_v^{d_2}/\check{p} = 2.15$

Figure 9.12: Slides of 3D simulation results for (a, c) pressure contours and (b, d) blood flow velocity streamlines on the vascular network located plane.

based on the results in Section 6.1.1 by regarding that the outlet vascular flow pressure in mother vessel m, the inlet vascular flow pressure in daughter vessel d_1, and both inlet and outlet pressures for the flow in daughter vessel d_2 are increased. However, it is necessary to be noticed that the interstitial pressures obtained here represent the fully coupling effects of all vessels within the entire vascular network, not the simply added-up results when we artificially take part of the vascular network to calculate each vessel individually. According

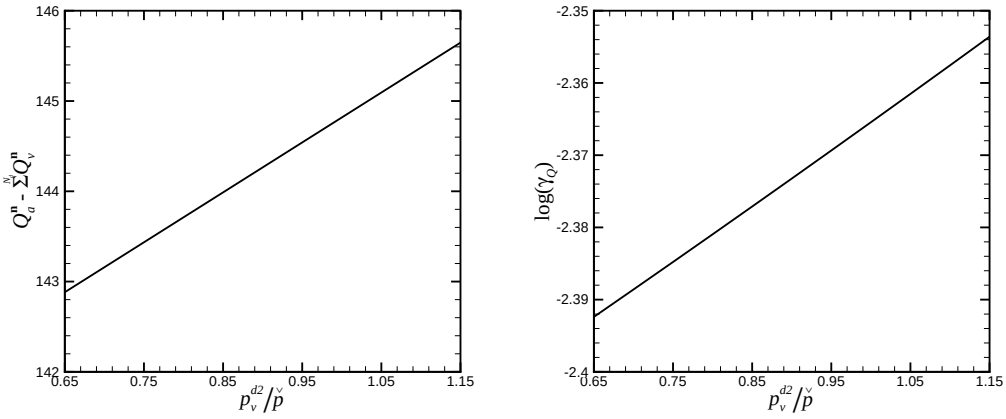

Figure 9.13: Dependence of (a) extravasation flux and (b) the relative flux coefficient γ_Q on outlet venous pressure $p_v^{d_2}$ of daughter vessel d_2.

to the foregoing analysis in Section 6.1.1, when the vasculature is represented by a single vessel, the extravasation flux and the relative flux coefficient γ_Q are both improved if the outlet vascular flow pressure is elevated. The same trends of the variations of the extravasation flux and the relative flux coefficient are presented when we only increase the outlet venous pressure for the flow in daughter vessel d_2 (Fig.9.13). Then, if the tumour vasculature has multiple outlet venous ends, it could be beneficial for the delivery of anti-cancer particles with heavy weight through vascular walls in tumour and the effectiveness of radiotherapy and chemotherapy when we can elevate one or more outlet venous vascular flow pressures.

9.3 Asymmetrical bifurcation

In order to support tumour growth, abnormal branching pattern is induced by angiogenesis which is not usually found in normal tissues [Less *et al.* (1991)]. One of the special tumour vascular structures is an asymmetrical bifurcation. Unlike the vascular configuration with symmetrical dichotomous branching in normal tissues, Less *et al.* (1991) stated that some of the vascular bifurcations in tumour are atypical. For such a kind of vascular bifurcation, the outside angles between the daughter vessels and the mother vessel are unequal. Furthermore, the radius of the daughter vessel with larger outside angle (normally between $8\pi/9$ and π) retains the same order as the radius of the mother vessel, while the radius of the daughter vessel with smaller outside angle (normally less than $8\pi/9$) is one order lower than that of the mother vessel.

We set up a study case for tumour blood flow here, in which an asymmetrically bifurcated vascular network with permeability is embedded in a solid tumour to a large extent. Similar to the investigation case in Section 9.2, all the vessel centre lines are located on one plane (oxy), and the afferent connecting point (inlet point) of mother vessel m is fixed at origin o whose centre line is along axis x. The lengths of all vessels are identical, and set as $l_v^m = l_v^{d_1} = l_v^{d_2} = 0.5$ cm. However, in the present case, the two outside angles are not equal with each other, but assigned as $\beta_1 = 2\pi/3$ and $\beta_2 = 17\pi/18$ respectively. According to the patten of tumour vascular configuration stated above, we let radii $a^m = 0.01$ cm, $a^{d_1} = 0.004$ cm and $a^{d_2} = 0.008$ cm for mother vessel m, daughter vessels d_1 and d_2 respectively. There are two significant differences of the vascular structure between the present study case (Case BaS) and the case investigated in Section 9.2 (Case BS). One is that the radius of daughter vessel d_2 in Case BaS is enlarged significantly relative to that in Case BS. The other is that the two outside angles are unequal to each

other in the current case.

Based on the discussions in Sections 7.1 and 9.2, we notice that vessel radius has strong effects on tumour blood flow, especially on vascular flow. In our current study case (Case BaS), if the inlet vascular flow pressure in the mother vessel is given as $p_a^m = 5.93283 \times 10^4$ g cm^{-1}s^{-2}, and the outlet vascular flow pressures in both daughter vessels as $p_v^{d_1} = p_v^{d_2} = p_v = 1.19990 \times 10^4$ g cm^{-1}s^{-2}, referring to the analogy described in Eqs.(9.2.1) to (9.2.3), we can conclude that resistance $Z_g^{d_2}$ decreases when the radius of daughter vessel d_2 is enlarged while the radii of the other vessels within the vascular network remain unchanged. This leads to the decreasing of the overall geometrical resistance for the vascular flow. As a result, according to Eq.(9.2.1), the flux flowing through the vascular network is increased in Case BaS relative to that in Case BS since pressure difference $p_a - p_v$ of the two cases is identical to each other. Consequently, the pressure gradient along the mother vessel is elevated since resistance Z_g^m remains constant, which indicates that vascular flow pressure p_c^{J} at the junction is lowered as p_a remains unchanged. Fig.9.14 presents the difference of the tumour blood flow between Case BaS and Case BS when we let tumour hydraulic conductivity parameter $\kappa = 10^{-10}$ g^{-1}cm^{3}s, tumour peripheral pressure $p_0 = 6.666 \times 10^2$ g cm^{-1}s^{-2}, and vessel permeability $L_p = 10^{-9}$ g^{-1}cm^{2}s. Fig.9.14a reflects the above analysis that the vascular flow pressure at the junction in Case BaS is lower than that in Case BS. This also leads to that the pressures in vessels are lower under Case BaS than those under Case BS. Meanwhile, we notice that the pressures inside the two daughter vessels in Case BaS are almost the same. This is due to that both the inlet and the outlet vascular flow pressures in these two daughter vessels are respectively identical to each other, and the variation of vessel radius has insignificant effects on the pressures in vessel, as discussed in Section 7.1. The results in

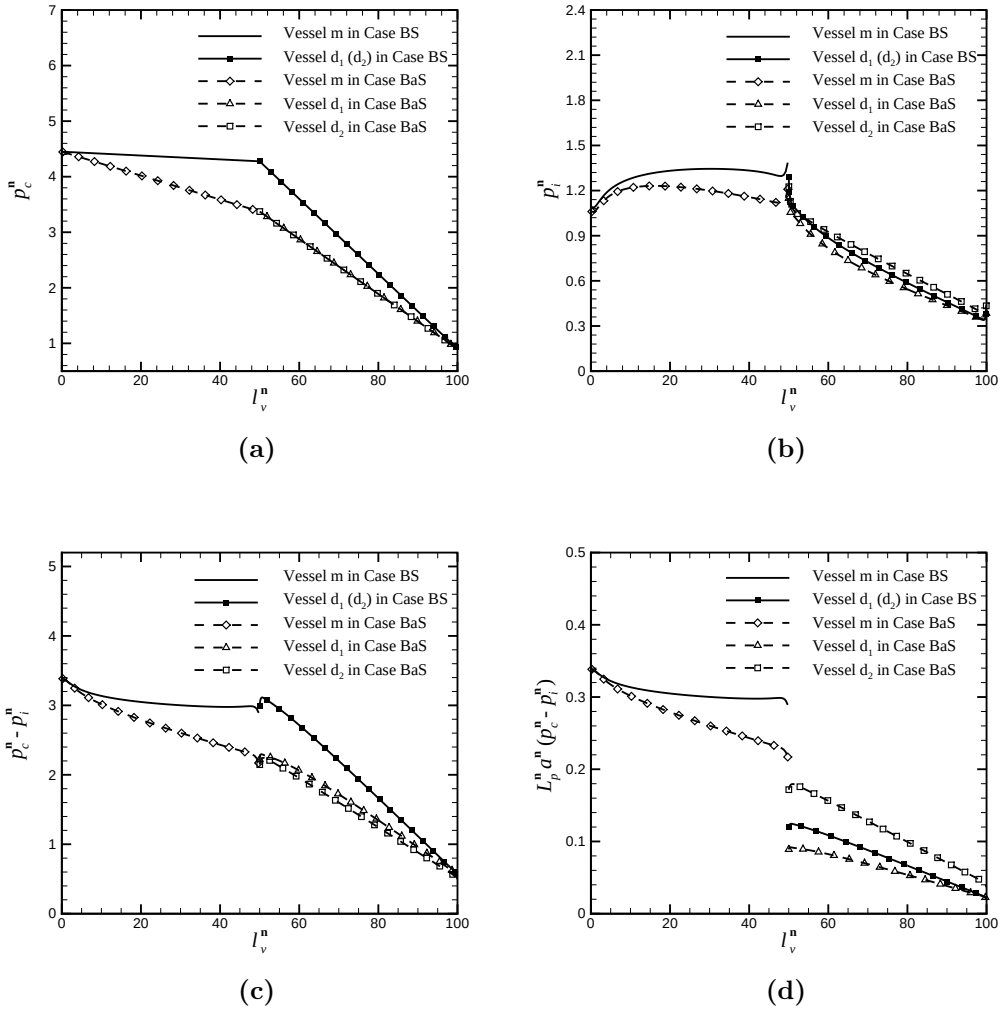

Figure 9.14: Distributions of (a) vascular flow pressures, (b) interstitial pressures on the external vascular surface, (c) transmural pressure differences, and (d) extravasation flux along the vascular network.

Fig.9.14 show that, relative to the daughter vessel with smaller radius, the daughter vessel with larger radius can generate higher interstitial pressures on its external vascular surface (Fig.9.14b) and transport more extravasation flux (Fig.9.14d), even though the transmural pressure difference is reduced (Fig.9.14c). This is due to the broadened vascular surface area caused by the

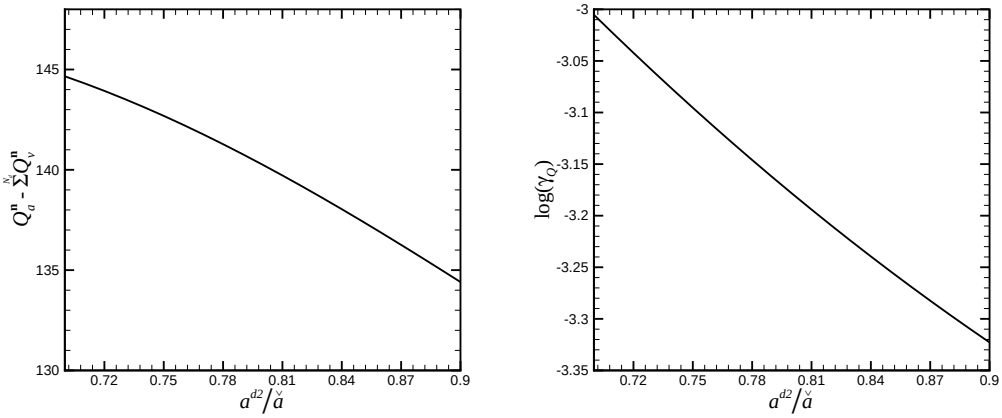

Figure 9.15: Dependence of (a) extravasation flux and (b) the relative flux coefficient γ_Q on radius a^{d_2} of daughter vessel d_2.

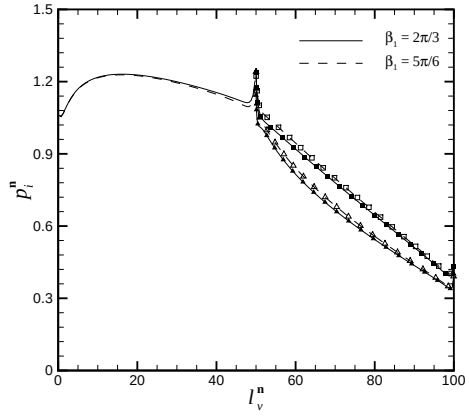

Figure 9.16: Distributions of interstitial pressures on the external vascular surface. Delta symbols: daughter vessel d_1; square symbols: daughter vessel d_2.

enlarged vessel radius. The flow phenomena are consistent with the results in Section 7.1. We have to be aware that the results presented here are not the simple additions of the simulation results obtained via three individual vessels. The fully coupling effects between all the vessels within the whole vascular network are included in this case. The results in Fig.9.15 show that the overall

extravasation flux and the relative flux coefficient $\gamma_{_Q}$ are lowered when the radius of daughter vessel d_2 is enlarged. These results have some difference compared with the case in Section 7.1 when the vasculature is represented by a single straight vessel, in which we have seen that enlarging vessel radius reduces the relative flux coefficient $\gamma_{_Q}$, but improves the overall extravasation flux.

The outside angles between mother vessel and daughter vessels reflect the relative positions of vessels in vascular network. The variation of outside angle has limited effects on the flow through vascular network since the discretised differential equations for vascular flow remain unchanged, whereas it has clear effects on the flow field in tumour interstitium. For Case BaS, when we let $\beta_1 = 2\pi/3, 3\pi/4, 5\pi/6$ orderly, while keep the other geometrical parameters for the vascular structure to remain constant, the vascular flow pressures at the junction almost remain unchanged, which are $p_c^{\mathrm{J}}/\check{p} = 3.373263$, $p_c^{\mathrm{J}}/\check{p} = 3.373263$ and $p_c^{\mathrm{J}}/\check{p} = 3.373264$ respectively. However, the interstitial pressures on the exterior vascular surface are affected by the variation of β_1, as plotted in Fig.9.16. The results in Fig.9.17 show that the variation of β_1 has clear influence on the interstitial pressure contours and the flow field around the vascular network in tumour interior. However, away from the vasculature, the shapes of the interstitial pressure contours tend to be circular and the flow flux over there would be uniform in all the directions.

9.4 Vasculature with three-dimensional centre lines inside tumour

In our previous investigations, we let the vessel centre lines of the entire vascular network locate on one plane. The major purpose of doing so is that

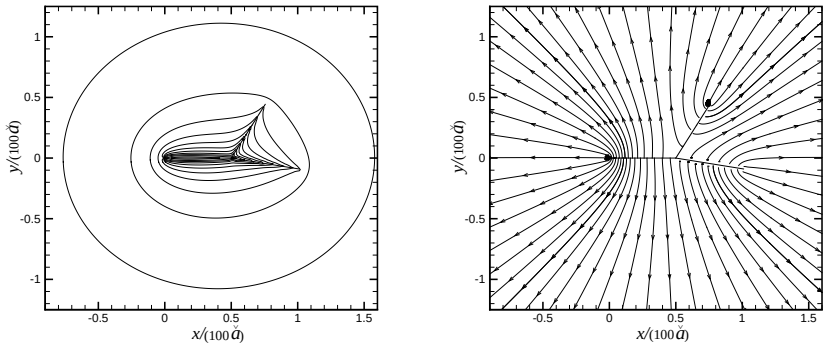

(a) when $\beta_1 = 2\pi/3$ **(b)** when $\beta_1 = 2\pi/3$

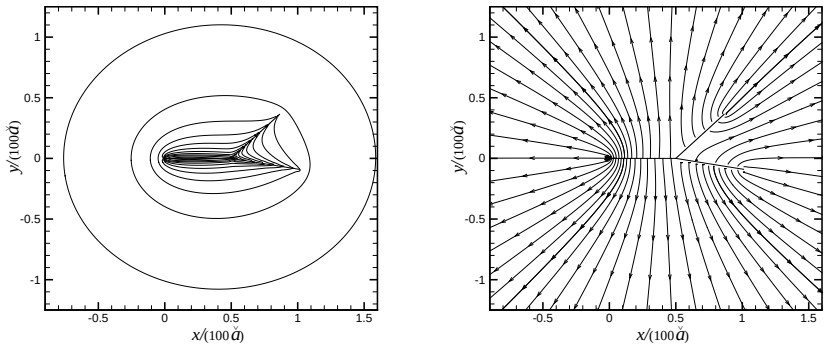

(c) when $\beta_1 = 3\pi/4$ **(d)** when $\beta_1 = 3\pi/4$

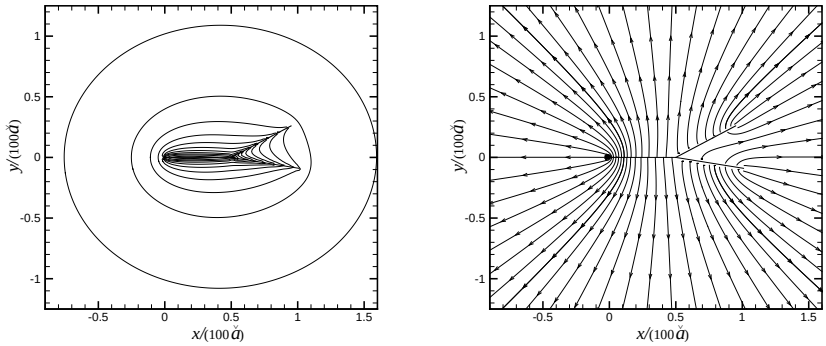

(e) when $\beta_1 = 5\pi/6$ **(f)** when $\beta_1 = 5\pi/6$

Figure 9.17: Slides of 3D simulation results for (a, c, e) pressure contours and (b, d, f) blood flow velocity streamlines on the vascular network located plane.

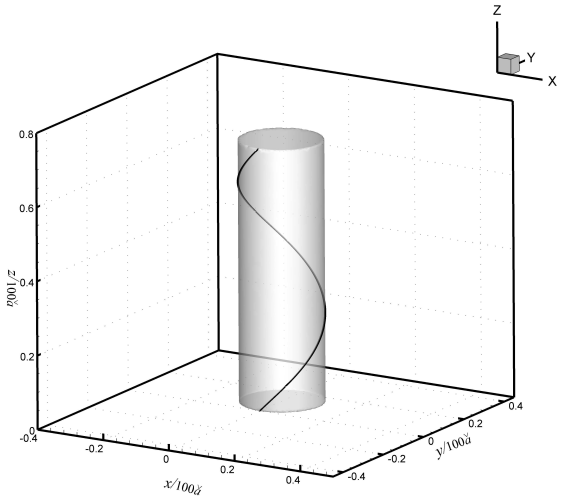

Figure 9.18: Sketch of the shape of a "tortuous" vessel.

it is convenient and illustrative for us to present the simulation results and analyse the features of tumour blood flow. However, it is important to be noticed that our mathematical model is applicable even when the centre lines of tumour vessels are three-dimensional. In this part, we study two special three-dimensional tumour vascular structures which are rarely found in normal tissues. One structure is a "tortuous" vessel, which means that when the vessel is bent, it also rises with a uniform rate in the third dimension, as shown in Fig.9.18. We set up a study case for tumour blood flow when a permeable "tortuous" vessel is embedded in a solid tumour to a large extent. The vessel, whose inlet point locates at origin o of reference frame $o - xyz$, is bent by 2π and rises along axis z. The distance between the arterial and venous points along axis z is $l_v/\sqrt{2}$. According to the analysis in Section 8.2, vessel curvature elevates the interstitial pressures on the external vascular surface, but reduces the value of the relative flux coefficient γ_Q. When the geometrical sizes and physical parameters of the test case in Section 5.2 are adopted, Fig.9.19 plots the distributions of the interstitial pressures along the exterior vascular surface

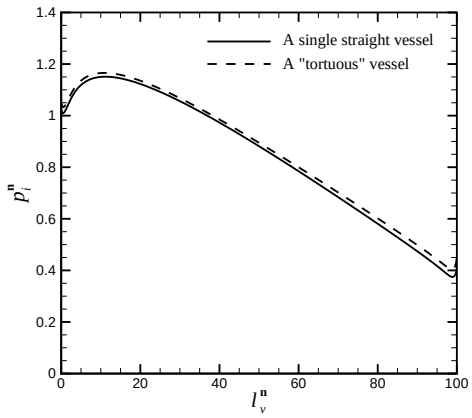

Figure 9.19: Distributions of interstitial pressures on the external vascular surface.

for the present case and the case in Section 5.2. The relative flux coefficients for the current case and for the test case in Section 5.2 are $\log_{10}(\gamma_Q) = -3.4851$ and $\log_{10}(\gamma_Q) = -3.4811$ respectively. These results reflect the foregoing discussions. Moreover, the complex shape of the vessel has significant effects on the tumour interstitial flow, as presented in Fig.9.20.

Another unique structure of tumour vasculature is a vascular network with trifurcation, which represents a mother vessel splits into three daughter vessels. Less *et al.* (1991) stated that within the trifurcation of tumour vascular network, the radius of the daughter vessel with the largest outside angle retains the same order with the radius of the mother vessel, while the radii of the other two daughter vessels are one order lower than that of the mother vessel. We investigate a case for tumour blood flow, in which a permeable vascular network with trifurcation is embedded in a solid tumour to a large extent. The arterial point of the mother vessel is located at origin o of reference coordinate system $o - xyz$ whose centre line is along axis x. Daughter vessel d_2 shares the same centre line with the mother vessel ($\beta_2 = \pi$), and daughter vessels d_1

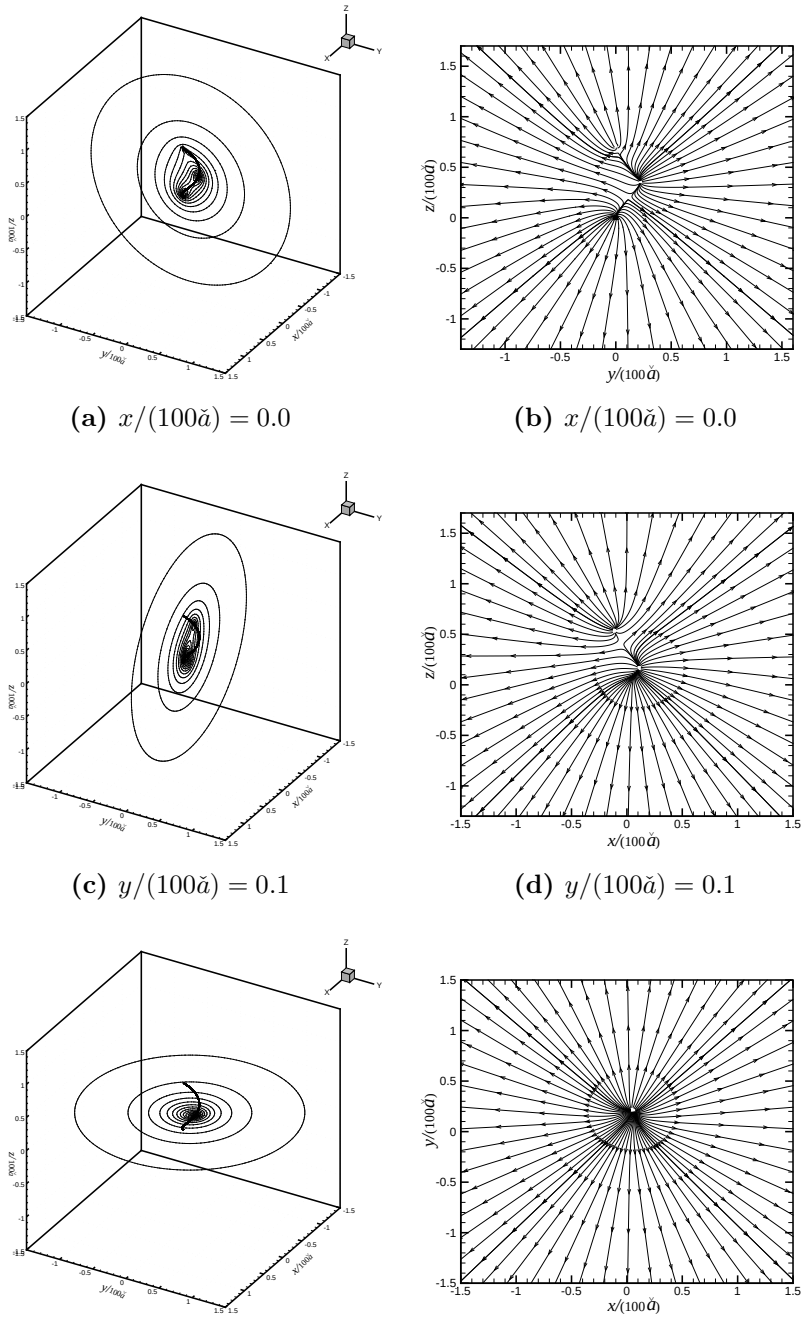

(a) $x/(100\check{a}) = 0.0$ **(b)** $x/(100\check{a}) = 0.0$

(c) $y/(100\check{a}) = 0.1$ **(d)** $y/(100\check{a}) = 0.1$

(e) $z/(100\check{a}) = 0.3$ **(f)** $z/(100\check{a}) = 0.3$

Figure 9.20: Slides of 3D simulation results for (a, c, e) pressure contours and (b, d, f) blood flow velocity streamlines in tumour interstitium.

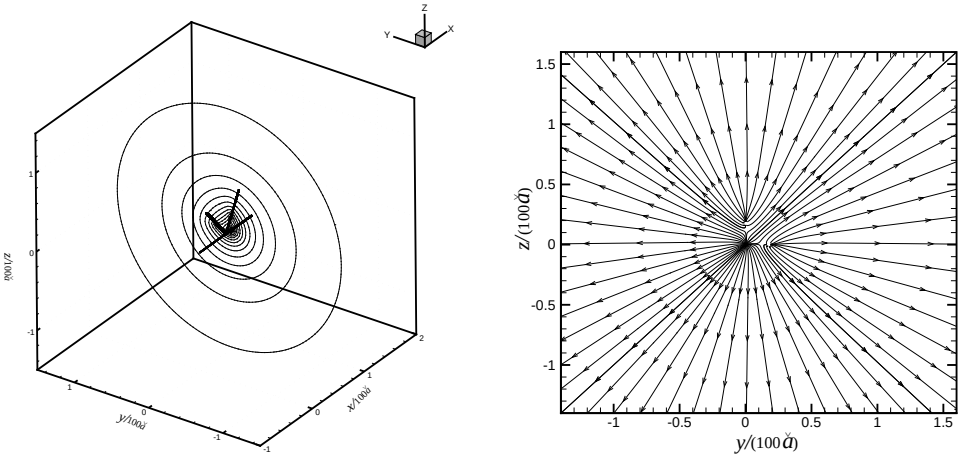

(a) $x/(100\check{a}) = 0.6$ **(b)** $x/(100\check{a}) = 0.6$

Figure 9.21: Slides of 3D simulation results for (a) pressure contours and (b) blood flow velocity streamlines in tumour interstitium.

and d_3 are on plane oyz and oxz with outside angles $\beta_1 = 2\pi/3$ and $\beta_3 = 2\pi/3$ respectively. Based on the patterns of tumour vascular network summarised by Less *et al.* (1991), we set the geometrical sizes of the vascular network in this case as followings: $l_v^m = l_v = l_v^{d_1} = l_v^{d_2} = l_v^{d_3} = 0.5$ cm, $a^m = 0.01$ cm, $a^{d_1} = 0.004$ cm, $a^{d_2} = 0.008$ cm, and $a^{d_3} = 0.004$ cm.

When the physical parameters for the flow in Case BaS are adopted, the junction pressure inside the vascular network in the current case is lower compared with that in Case BaS, which are $p_c^{\mathrm{J}}/\check{p} = 3.3299$ and $p_c^{\mathrm{J}}/\check{p} = 3.3733$ respectively. This is due to that the geometrical resistance for the daughter vessel part in the present case is higher than that in Case BaS, while the resistance for the mother vessel part are identical to each other under these two cases. As a result, based on Eq.(9.2.1), the flux flowing through the vascular network is reduced in the present case compared with that in Case BaS since pressure difference $p_a - p_v$ is the same in both cases, which leads to the vascular flow pressure at the junction lowered in the current case. Meanwhile,

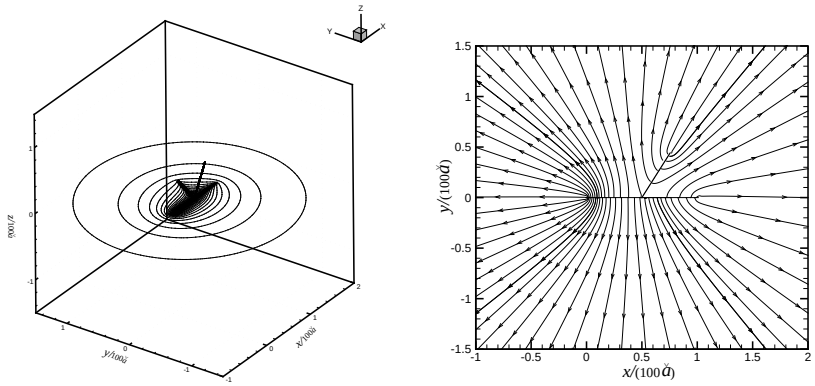

(a) $z/(100\check{a}) = 0.0$ **(b)** $z/(100\check{a}) = 0.0$

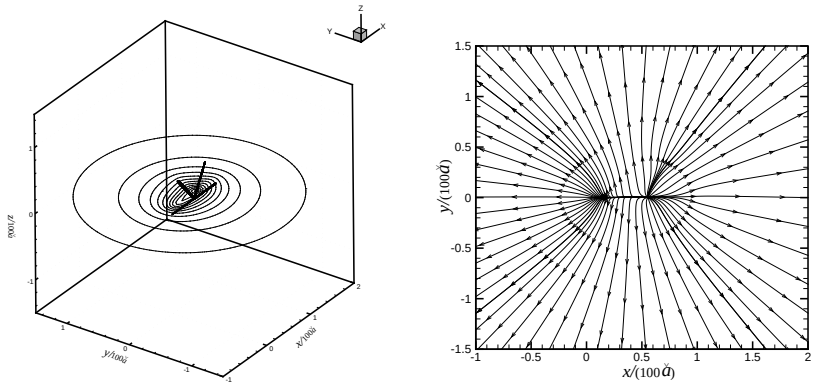

(c) $z/(100\check{a}) = 0.1$ **(d)** $z/(100\check{a}) = 0.1$

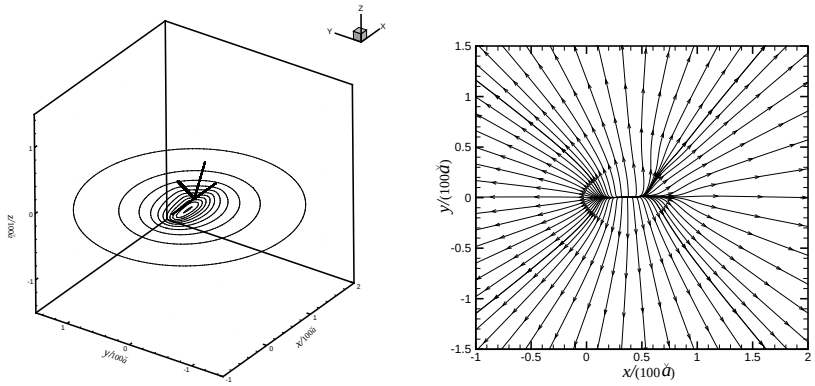

(e) $z/(100\check{a}) = -0.1$ **(f)** $z/(100\check{a}) = -0.1$

Figure 9.22: Slides of 3D simulation results for (a, c, e) pressure contours and (b, d, f) blood flow velocity streamlines in tumour interstitium.

the complicated configuration of the vascular network with trifurcation has clear effects on the flow field in tumour interstitium, as shown in Figs.9.21 and 9.22.

Chapter 10

Approximation Model for Tumour Vascular Flow

10.1 Approximation model for the blood flow through a tumour vessel

In Chapter 4, we have developed a mathematical model for the blood flow through a tumour vessel and the flow field in tumour interstitium based on conservation of mass and momentum. In the meantime, as tumour vessels are permeable, we have included the coupling effect between the vascular flow and the interstitial flow by the Starling's law which is also obtained from mass conservation. We have applied this fully coupling model to investigate how different kinds of physical parameters affect tumour blood flow when tumour vasculature is represented by a single vessel in Chapters 6 to 8. According to the obtained results, we noticed that the vascular flow pressures are almost unaffected by the vessel permeability and the tumour hydraulic conductivity coefficient, as shown in Figs.6.12a and 6.15a respectively. Mathematically, this

indicates that the last term on the left-hand side of mass-conservation equation (4.3.9), or

$$H_b(s)\frac{\mathrm{d}Q_c(s)}{\mathrm{d}s} + 2\pi a(s)L_p(s)\left[p_c(s) - p_i(s)\right] = 0, \tag{10.1.1}$$

is small in value compared with the first term on the left-hand of that equation or Eq.(10.1.1). As a result, it is possible to develop an approximation model through simplifying the above equation by ignoring the last term on its left-hand side, which gives

$$H_b(s)\frac{\mathrm{d}Q_c(s)}{\mathrm{d}s} = 0. \tag{10.1.2}$$

Once the position, shape and geometrical sizes of the vessel are given, we notice that the approximation model in Eq.(10.1.2) is only relevant to vascular flow pressure $p_c(s)$ (flux Q_c). Consequently, if the above formulation is adopted as the governing equation for the flow through tumour vessel, we are able to obtain $p_c(s)$ directly by solving Eq.(10.1.2) analytically or through FDM. We can then introduce $p_c(s)$ into Eq.(4.3.15) to calculate interstitial pressure $p_i(s)$ on the external vascular surface. In this way, the whole numerical simulation procedure of the approximation model is simplified into a one-step forward process instead of the repeated iteration procedure of the fully coupling model as stated in Section 5.1.

10.1.1 Analytical solution of Eq.(10.1.2)

As aforementioned in Sections 8.2 and 9.1, under the usual physical and physiological conditions in a solid tumour, the blood flow through a tumour vessel can be described by the Poiseuille's law in Eq.(5.1.10) even if the vessel is not

straight. Substituting Eq.(5.1.10) into Eq.(10.1.2), we obtain

$$H_b^2(s)\frac{\mathrm{d}^2 p_c}{\mathrm{d}s^2} + \frac{\mathrm{d}p_c}{\mathrm{d}s}\left[\frac{4H_b^2(s)}{a(s)}\frac{\mathrm{d}a(s)}{\mathrm{d}s} + H_c(s)H_b(s)\right] = 0 \tag{10.1.3}$$

which can be solved analytically. Let

$$\frac{\mathrm{d}p_c}{\mathrm{d}s} = f_p, \tag{10.1.4}$$

which gives

$$\frac{\mathrm{d}f_p}{\mathrm{d}s} = \frac{\mathrm{d}^2 p_c}{\mathrm{d}s^2}. \tag{10.1.5}$$

Introducing Eqs.(10.1.4) and (10.1.5) into Eq.(10.1.3), and rearranging the terms, we have

$$\frac{\mathrm{d}f_p}{f_p} = -\left[\frac{4}{a(s)}\frac{\mathrm{d}a(s)}{\mathrm{d}s} + \frac{H_c(s)}{H_b(s)}\right]\mathrm{d}s. \tag{10.1.6}$$

Noticing that $H_c(s) = \mathrm{d}H_b(s)/\mathrm{d}s$ as defined in Eq.(4.1.7), we obtain the solution of the above equation as

$$f_p = \frac{C_p^1}{a^4(s)H_b(s)}, \tag{10.1.7}$$

in which C_p^1 is a positive constant. Substituting Eq.(10.1.7) into Eq.(10.1.4), we have the solution for $p_c(s)$ as

$$p_c(s) = C_p^2 + C_p^1 \int_0^s \frac{1}{a^4(\eta)H_b(\eta)}\mathrm{d}\eta, \tag{10.1.8}$$

where C_p^2 is a constant. If inlet and outlet vascular flow pressures p_a and p_v are given, we have

$$\begin{cases} p_c = p_a & s = 0, \\ p_c = p_v & s = l_v(s). \end{cases} \tag{10.1.9}$$

Introducing Eq.(10.1.9) into Eq.(10.1.8), we obtain

$$\begin{cases} C_p^2 = p_a, \\ C_p^1 = -\dfrac{p_a - p_v}{\displaystyle\int_{l_v(s)} \frac{1}{a^4(\eta) H_b(\eta)} \mathrm{d}\eta}. \end{cases} \tag{10.1.10}$$

Substituting Eq.(10.1.10) into Eq.(10.1.8), and rearranging the terms, we get

$$p_c(s) = p_a - \frac{p_a - p_v}{\displaystyle\int_{l_v(s)} \frac{1}{a^4(\eta) H_b(\eta)} \mathrm{d}\eta} \int_0^s \frac{1}{a^4(\eta) H_b(\eta)} \mathrm{d}\eta. \tag{10.1.11}$$

The integrals in the above equation can be calculated numerically. When the same discretised mesh as described in Section 4.3.4 are adopted, for segment $n = 1$,

$$p_c^{[n]} = p_a - \frac{p_a - p_v}{\displaystyle\sum_{i=1}^{N_E} \frac{\delta s_i}{(a_i)^4 H_b^{[i]}}} \left\{ \frac{\delta s_n}{2 (a_n)^4 H_b^{[n]}} \right\} \qquad n = 1, \tag{10.1.12}$$

and for segment $1 < n \leq N_E$,

$$p_c^{[n]} = p_a - \frac{p_a - p_v}{\displaystyle\sum_{i=1}^{N_E} \frac{\delta s_i}{(a_i)^4 H_b^{[i]}}} \left\{ \sum_{i=1}^{n-1} \frac{\delta s_i}{(a_i)^4 H_b^{[i]}} + \frac{\delta s_n}{2 (a_n)^4 H_b^{[n]}} \right\} \qquad n = 2, 3, \cdots N_E. \tag{10.1.13}$$

Introducing $p_c(s)$ into Eq.(4.3.17) which is discretised from Eq.(4.3.15), we can calculate interstitial pressure $p_i(s)$ on the exterior vascular surface straightforwardly.

10.1.2 Validity of the approximation model

The approximation model is applied to calculate some of the study cases which have been investigated in Sections 6.3, 6.2 and 8.2, and the results are presented in Figs.10.1, 10.2 and 10.3 respectively, when the segment size is set as $\delta s_j = 0.2a$ and the relative round error as $Er = 10^{-6}$. In Fig.10.1d, as $Q_a = Q_v$ under the approximation model, the definition of the relative flux coefficient γ_Q has been modified to

$$\gamma_Q = \frac{\breve{Q}_{ex}}{Q_a} = \frac{\int_{l_v(s)} 2\pi L_p(s) a(s) \left[p_c(s) - p_i(s)\right] \mathrm{d}s}{Q_a}. \tag{10.1.14}$$

The definition in the above equation is equivalent to Eq.(5.0.4) for the fully coupling model. These figures show that the simulation results obtained by the approximation model are in good agreement with the results calculated by the fully coupling model. This indicates that our primary assumption of ignoring the last term on the left-hand side of Eq.(10.1.1) in the approximation model is rational for the above study cases. For the study case in Fig.10.1a, the results of simulation time by the approximation model and by the fully coupling model are listed in Table10.1 under different sizes of discretised segment. Table10.1 shows that the smaller the size of discretised segment is, the more significant the difference of the simulation time between these two models is. This is mainly due to that the numerical procedure of the approximation model is a one-step forward process, while the results pursued by the fully coupling model

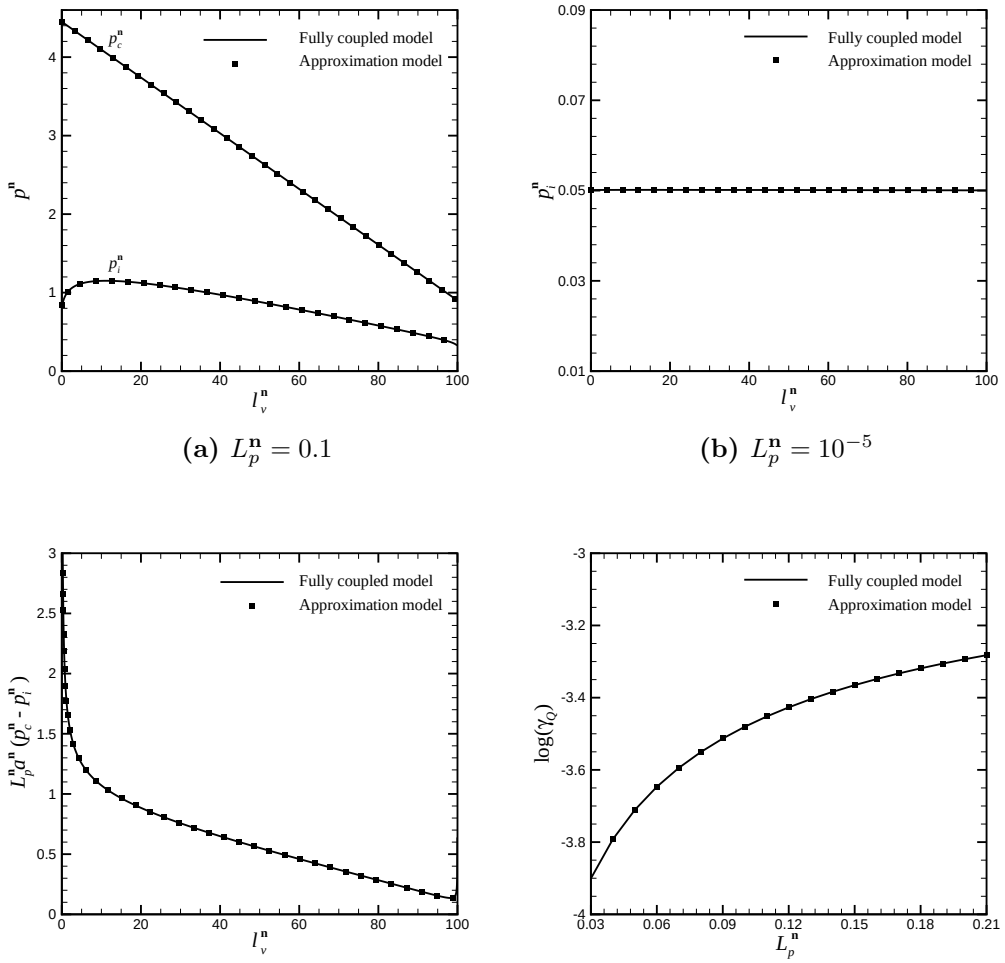

(a) $L_p^{\mathbf{n}} = 0.1$ **(b)** $L_p^{\mathbf{n}} = 10^{-5}$

(c) $L_p^{\mathbf{n}} = 10^3$ **(d)**

Figure 10.1: Comparison of the simulation results obtained by the fully coupling model and by the approximation model for the study cases in Section 6.3.

are through iteration. Generally speaking, the convergent rate of iteration decreases when the segment size becomes smaller, which leads to the increasing of the simulation time by the fully coupling model.

Before the approximation model is applied to further investigations, we have to examine its validity in depth. The approximation model is established

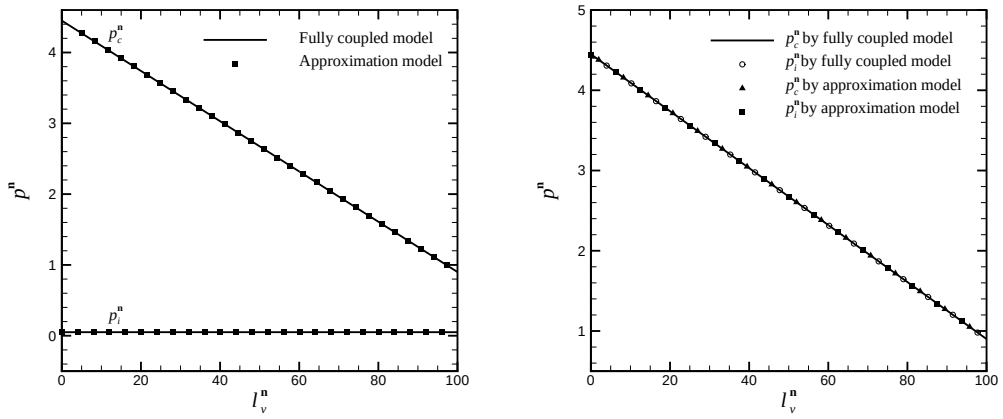

(a) $\kappa^{\mathbf{n}} = 10^4$ **(b)** $\kappa^{\mathbf{n}} = 10^{-4}$

Figure 10.2: Comparison of the simulation results obtained by the fully coupling model and by the approximation model for the study cases in Section 6.2.

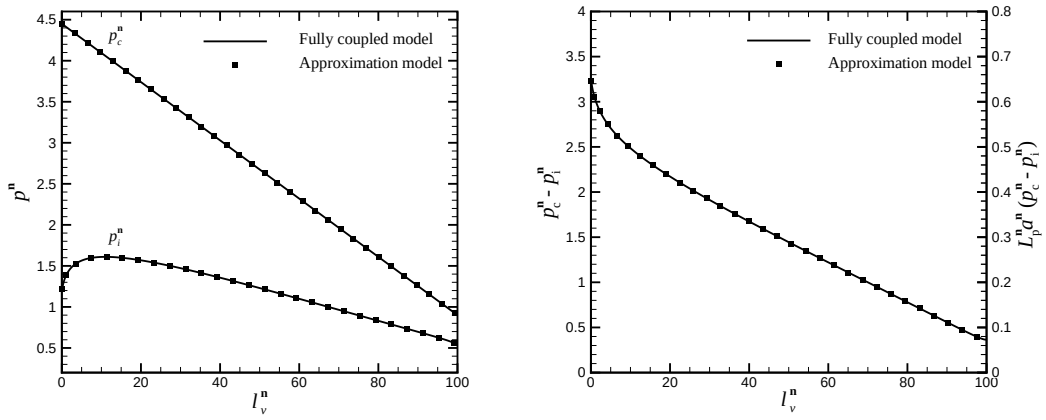

(a) **(b)**

Figure 10.3: Comparison of the simulation results obtained by the fully coupling model and by the approximation model for the study cases in Section 8.2, when $a^{\mathbf{n}} = 0.2$, $l_v/R_c = 4\pi/3$ ($D = 647$).

by ignoring the term with small value from the fully coupling model. Recalling the governing equation for the vascular flow in the fully coupling model, which

Table 10.1: Simulation time by the fully coupling model and approximation model

Size of segment	Fully coupling model Time (s)	Approximation model Time (s)
$\delta s_j = 0.2a$	142	131
$\delta s_j = 0.1a$	662	635
$\delta s_j = 0.05a$	2661	2538

is

$$H_b^2(s)\frac{\mathrm{d}^2 p_c}{\mathrm{d}s^2} + \left[\frac{4H_b^2(s)}{a(s)}\frac{\mathrm{d}a(s)}{\mathrm{d}s} + H_c(s)H_b(s)\right]\frac{\mathrm{d}p_c}{\mathrm{d}s} - \frac{16\mu L_p(s)}{a^3(s)}\left[p_c(s) - p_i(s)\right] = 0, \tag{10.1.15}$$

we notice that the ignored term (Term Ig) is

$$\frac{16\mu L_p(s)}{a^3(s)}\left[p_c(s) - p_i(s)\right] \tag{10.1.16}$$

relative to Eq.(10.1.3) in the approximation model. As we have set that flow dynamic viscosity μ is constant, the value of Term Ig is in direct proportion to vessel permeability $L_p(s)$ and transmural pressure difference $p_c(s) - p_i(s)$, but in inverse proportion to the cube of vessel radius $a(s)$. It is worth to be noticed that the value of Term Ig does not depend on $L_p(s)$, $p_c(s) - p_i(s)$ or $a(s)$ individually, because transmural pressure difference relies on vessel permeability and vessel radius according to the analysis in Sections 6.3 and 7.1. However, though the variation of vessel radius can affect transmural pressure difference $p_c(s) - p_i(s)$, the effects are insignificant as discussed in Section 7.1.

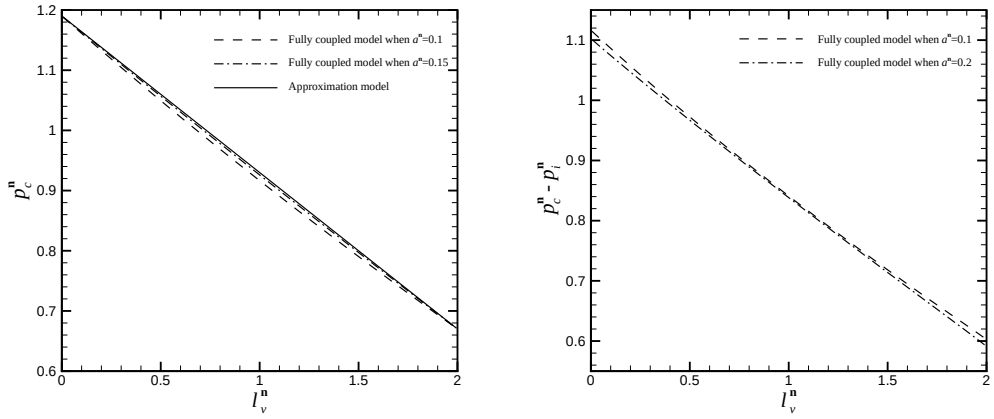

Figure 10.4: Distributions of (a) vascular flow pressures and (b) transmural pressure difference.

Then, we are able to separate vessel radius $a(s)$ for investigation. Since the value of Term Ig is in inverse proportion to the cube of $a(s)$, the variation of $a(s)$ can affect the value of Term Ig significantly. When the size of vessel radius is small, the value of Term Ig can be large, which may make the primary assumption of the approximation model invalid. We set up an investigation case for tumour blood flow, in which a single straight vessel with length $l_v = 0.02$ cm is embedded in a solid tumour to a large extent whose hydraulic conductivity parameter is set as $\kappa = 5 \times 10^{-8}$ g^{-1}cm^{3}s and peripheral pressure as $p_0 = 6.666 \times 10^2$ g cm^{-1}s^{-2}. The vessel permeability is given as $L_p = 5 \times 10^{-7}$ g^{-1}cm^{2}s, and the inlet and outlet vascular flow pressures as $p_a = 1.58653 \times 10^4$ g cm^{-1}s^{-2} and $p_v = 8.9326 \times 10^3$ g cm^{-1}s^{-2} respectively. The simulation results of the current case are presented in Figs.10.4, 10.5 and Table10.2, when the vessel radius varies from $a(s) = 1 \times 10^{-3}$ cm to $a(s) = 3 \times 10^{-3}$ cm. Since the radius is uniform along the vessel in the present case, according to Eq.(10.1.3), pressure $p_c(s)$ inside the vessel declines linearly

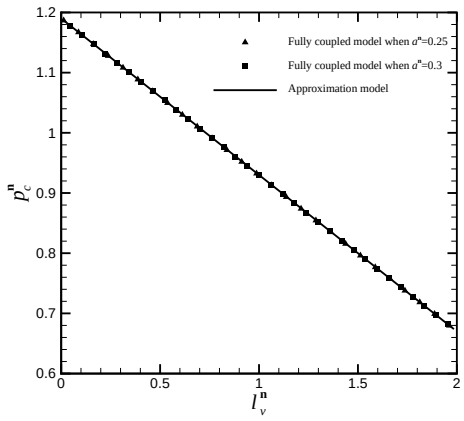

Figure 10.5: Distributions of the pressures in vessel.

from p_a to p_v, as shown in Fig.10.4 by the solid line. However, the results in Fig10.4a show that, when $a(s)$ is small, $p_c(s)$ obtained by the fully coupling model is not linear along the vessel. This is due to that the low value of $a(s)$ leads to the high value of ratio L_p/a^3. As a result, the value of Term Ig is no longer small, since transmural pressure difference $p_c(s) - p_i(s)$ does not tend to zero, as displayed in Fig.10.4b. This indicates that, under such consequences, the approximation model is not rational, and Term Ig cannot be ignored from the fully coupling model. Along the increasing of vessel radius $a(s)$, the value of ratio L_p/a^3 decreases rapidly, which makes the value of Term Ig lowered significantly. When the value of Term Ig is small enough, the results calculated by the approximation model are in good agreement with the results obtained by the fully coupling model, as shown in Fig.10.5 and Table10.2. For these consequences, the approximation model is rational.

Another feature that can affect the value of ratio L_p/a^3 is vessel permeability $L_p(s)$, which consequently has effects on the value of Term Ig. The effects of $L_p(s)$ on the value of Term Ig is relatively complicated because it has strong influence on interstitial pressure $p_i(s)$ on the exterior vascular surface,

Table 10.2: The overall amount of the extravasation flux

a	$L_p/(a^3)$	Original model $Q_{ex}^{\mathbf{n}}$	Approx model $\breve{Q}_{ex}^{\mathbf{n}}$	relative difference $\left\|\breve{Q}_{ex}^{\mathbf{n}} - Q_{ex}^{\mathbf{n}}\right\| / Q_{ex}^{\mathbf{n}}$
0.0010	500.000	53.220	53.770	1.033%
0.0012	289.352	63.909	64.290	0.596%
0.0014	182.148	74.473	74.752	0.374%
0.0016	122.070	84.949	85.161	0.250%
0.0018	85.734	95.355	95.522	0.175%
0.0020	62.500	105.702	105.836	0.127%
0.0025	32.000	131.354	131.439	0.065%
0.0030	18.519	156.750	156.808	0.037%

which can then affect transmural pressure difference $p_c(s) - p_i(s)$ significantly, as aforementioned in Section 6.3. According to the above investigations, when $L_p/a^3 = 500$ as $L_p = 5 \times 10^{-7}$ g^{-1}cm^{2}s and $a = 0.001$ cm, the approximation model is not rational since the value of Term Ig is too large to be ignored. However, if we keep the value of radio L_p/a^3 as $L_p/a^3 = 500$, while let vessel radius $a = 0.005$ cm and vessel permeability $L_p(s) = 6.25 \times 10^{-5}$ g^{-1}cm^{2}s, the results obtained by the approximation model are in good agreement with the results calculated by the fully coupling model, as shown in Fig.10.6. According to the analysis in Section 6.3, when the value of vessel permeability is high, interstitial pressure $p_i(s)$ on the external vascular surface could be elevated even to be equal to vascular flow pressure $p_c(s)$, or $p_i(s) \to p_c(s)$. Under this circumstance, transmural pressure difference $p_c(s) - p_i(s)$ tends to zero, which

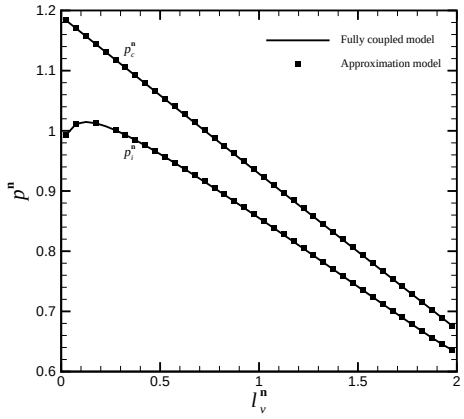

Figure 10.6: Distributions of (a) vascular flow pressures and (b) transmural pressure difference.

makes the value of Term Ig small enough to be ignored even though the value of ratio L_p/a^3 is large ($L_p/a^3 = 500$). Consequently, the approximation model is still rational under such a situation. Based on the foregoing discussions in Section 6.2, when the value of tumour hydraulic conductivity coefficient κ is low, transmural pressure difference $p_c(s) - p_i(s)$ could also tend to zero. According to the coupling effect relationship defined in Eq.(6.1.1), when the value of ratio L_p/κ is high, $p_c(s) - p_i(s) \to 0$ since interstitial pressure gradient $\partial p_i(s)/\partial n$ should be within some reasonable range when inlet vascular flow pressure p_a, outlet vascular flow pressure p_v and tumour peripheral pressure p_0 are given. Under such a circumstance, the approximation model is still reasonable even though the value of ratio L_p/a^3 is high. For the foregoing study case, if vessel radius $a = 0.001$ cm remains constant while κ can be varied, we observe that the results in Table10.3 reflect the above discussions. Therefore, the approximation model is rational when either of the following two conditions is met: 1. the value of ratio L_p/a^3 is low; 2. if the value of ratio L_p/a^3 is not low, the value of ratio L_p/κ should be high. Otherwise, tumour blood flow can only be investigated by the fully coupling model. All the cases that have been investi-

Table 10.3: The overall amount of the extravasation flux along vessel

L_p/κ	Original model $Q_{ex}^{\mathbf{n}}$	Approx model $\breve{Q}_{ex}^{\mathbf{n}}$	relative difference $\left\|\breve{Q}_{ex}^{\mathbf{n}} - Q_{ex}^{\mathbf{n}}\right\| / Q_{ex}^{\mathbf{n}}$
50	47.998	48.442	0.924%
100	42.759	43.108	0.816%
500	22.865	22.961	0.417%
1000	14.477	14.514	0.256%
5000	3.689	3.691	0.0615%

gated in the beginning of this section can be fallen into category 1, except the case in Fig.10.1c, which belongs to condition 2.

10.2 Vasculature with branches

Having been clear with the range of rationality and availability of the approximation model, we can further apply it to simulate tumour blood flow when tumour vasculature contains complicated structures. To take the vascular bifurcation which has been investigated in Section 9.1 as an example, the pressures inside the mother vessel can be expressed in the form of Eqs.(10.1.12) and (10.1.13) through replacing p_v with vascular flow pressure p_c^{J} at the junction of the vascular network, and the pressures inside each daughter vessel are in the form of Eqs.(10.1.12) and (10.1.13) by replacing p_a with p_c^{J}. Substituting the expressions for the vascular flow pressures into the pressure gradient condition at the junction which is defined in Eq.(9.1.6), we have

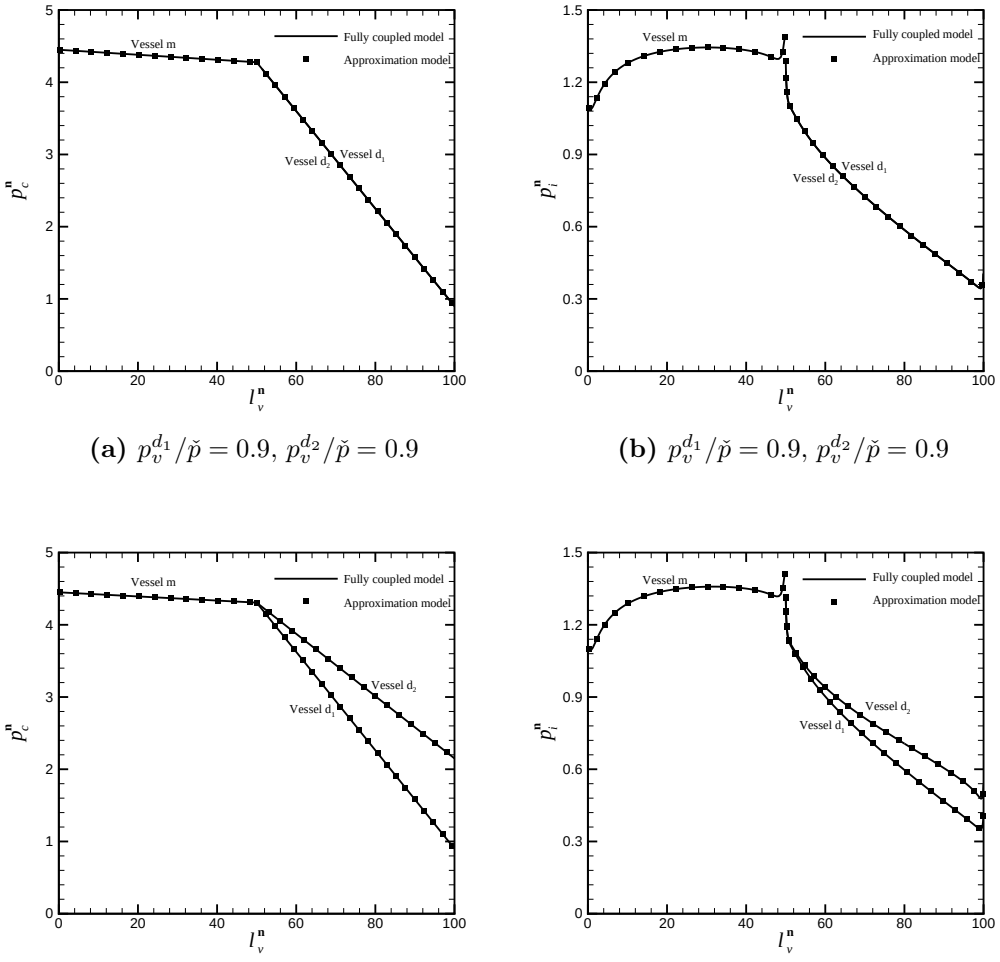

(a) $p_v^{d_1}/\check{p} = 0.9$, $p_v^{d_2}/\check{p} = 0.9$ **(b)** $p_v^{d_1}/\check{p} = 0.9$, $p_v^{d_2}/\check{p} = 0.9$

(c) $p_v^{d_1}/\check{p} = 0.9$, $p_v^{d_2}/\check{p} = 3.0$ **(d)** $p_v^{d_1}/\check{p} = 0.9$, $p_v^{d_2}/\check{p} = 3.0$

Figure 10.7: Distributions of (a, c) vascular flow pressures and (b, d) interstitial pressures on the external vascular surface for Case BS.

$$\frac{p_a^m - p_c^{\mathrm{J}}}{\sum_{i=1}^{N_E} \dfrac{\delta s_i^m}{\left(a_i^m\right)^4 H_b^{m[i]}}} = \sum_{k=1}^{N_d} \frac{p_c^{\mathrm{J}} - p_v^{d_k}}{\sum_{i=1}^{N_E^{d_k}} \dfrac{\delta s_i^{d_k}}{\left(a_i^{d_k}\right)^4 H_b^{d_k[i]}}}. \tag{10.2.1}$$

Then, p_c^{J} can be obtained directly by solving the above linear equation, which allows us to calculate pressure $p_c(s)$ in the vascular network according to

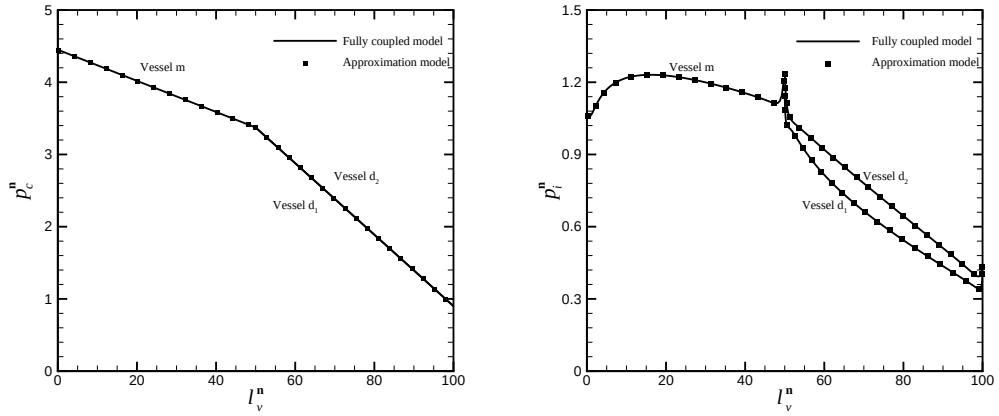

(a) **(b)**

Figure 10.8: Distributions of (a) vascular flow pressures and (b) interstitial pressures on the external vascular surface for Case BaS.

Eqs.(10.1.12) and (10.1.13) straightforwardly. Introducing $p_c(s)$ into Eq.(9.1.7), we are able to obtain interstitial pressure $p_i(s)$ on the exterior vascular surface along the whole vasculature. Compared with the numerical procedure which includes an inner loop to calculate p_c^{J} and an outer loop for $p_c(s)$ and $p_i(s)$ in the fully coupling model as stated in Section 9.1, the whole calculation procedure by the approximation model is a three-step process when tumour vasculature has branches. According to Tables10.2 and 10.3, Case BS and Case BaS in Chapter 9 can be solved by the approximation model. Figs.10.7 and 10.8 show that the simulation results obtained by the approximation model are in good agreement with the results calculated by the fully coupling model. The simulation time for Case BS by the approximation model is 1280s, while it is 1393s by the fully coupling model. The difference of simulation time is mainly due to the simplicity of the numerical procedure of the approximation model.

The approximation model can be further applied to simulate tumour

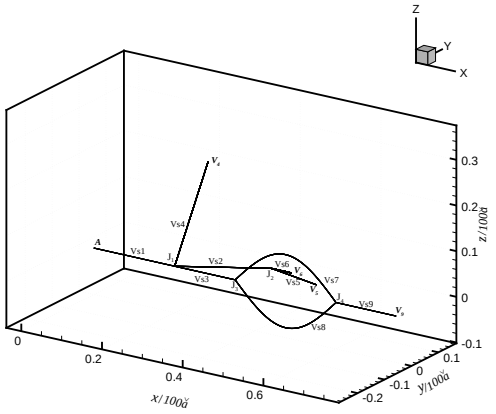

Figure 10.9: Sketch of the configuration of a 3D complex vascular network.

blood flow when tumour vasculature is a more complicated vascular network with multiple generations of daughter vessels. Similar to the procedure which was stated in the beginning of this section, we firstly compose a set of linear equations for vascular flow pressure p_c^{J} at all junctions within the entire vascular network. We then calculate p_c^{J} by solving those linear equations, and obtain the pressures inside vessels based on Eqs.(10.1.12) and (10.1.13). After that, we can get the interstitial pressures on the exterior vascular surface along the entire vascular network through Eq.(9.1.6). Fig.10.9 sketches a study case, in which a complex vascular network with permeability $L_p = 10^{-9}$ g^{-1}cm^{2}s is embedded in a solid tumour to a large extent whose hydraulic conductivity parameter is set as $\kappa = 10^{-10}$ g^{-1}cm^{3}s and peripheral pressure as $p_0 = 6.666 \times 10^2$ g cm^{-1}s^{-2}. The vascular network starts with mother vessel Vs1 splitting into three daughter vessels Vs2, Vs3, Vs4 at junction J_1. Then daughter vessel Vs2 separates into two granddaughter vessels Vs5 and Vs6 at junction J_2, and daughter vessel Vs3 splits into two granddaughter vessels Vs7 and Vs8 at junction J_3. Furthermore, granddaughter vessels Vs7 and Vs8 forms a self loop, which means that they meet with each other at the

downstream ends of those two vessels, and connect with great-granddaughter vessel Vs9 at junction J_4. The shape and geometrical sizes of each vessel within the vascular network are listed in Table10.4. Referring to Tables10.2 and 10.3, we are able to simulate this case by the approximation model. The inlet condition for the vascular flow is $p_a = 5.93283 \times 10^4$ g cm^{-1}s^{-2} at the arterial point of the mother vessel, and the outlet vascular flow conditions are $p_v^4 = 1.19990 \times 10^4$ g cm^{-1}s^{-2}, $p_v^5 = 9.3325 \times 10^3$ g cm^{-1}s^{-2}, $p_v^6 = 6.6661 \times 10^3$ g cm^{-1}s^{-2}, $p_v^9 = 8.6659 \times 10^3$ g cm^{-1}s^{-2} at the venous ends of vessels Vs4, Vs5, Vs6 and Vs9 respectively. We obtain that the junction pressures inside the vascular network are $p_c^{J_1}/\check{p} = 39.29114$, $p_c^{J_2}/\check{p} = 26.76337$, $p_c^{J_3}/\check{p} = 30.52034$ and $p_c^{J_4}/\check{p} = 10.09251$ for junctions J_1, J_2, J_3 and J_4 respectively. Meanwhile, the three-dimensional simulation results for the pressure contours and the flow velocity streamlines in tumour space are presented in Fig.10.10.

Table 10.4: Parametric equation for the vessel centre line and geometrical sizes of every vessel within vascular network.

Vessel	Parametrical equations for the vessel centre line	Length (cm)	Radius (cm)
Vs1	$\begin{cases} x(s) = s, \\ y(s) = 0.0, \quad 0.0 \le s \le 0.2 \\ z(s) = 0.0. \end{cases}$	0.2	0.01
Vs2	$\begin{cases} x(s) = 0.2 + s/2, \\ y(s) = \sqrt{3}\, s/2, \quad 0.0 \le s \le 0.2 \\ z(s) = 0.0. \end{cases}$	0.2	0.004
Vs3	$\begin{cases} x(s) = 0.2 + s, \\ y(s) = 0.0, \quad 0.0 \le s \le 0.15 \\ z(s) = 0.0. \end{cases}$	0.15	0.008
Vs4	$\begin{cases} x(s) = 0.2 + s/2, \\ y(s) = -s/2, \quad 0.0 \le s \le 0.5 \\ z(s) = \sqrt{2}\, s/2. \end{cases}$	0.5	0.003
Vs5	$\begin{cases} x(s) = \sqrt{3}/2 + \sqrt{3}\, s\cos(\pi/9)/2, \\ y(s) = 0.1 + s\cos(\pi/9)/2, \quad 0.0 \le s \le 0.1 \\ z(s) = -s\sin(\pi/9). \end{cases}$	0.1	0.003
Vs6	$\begin{cases} x(s) = \sqrt{3}/2 + s, \\ y(s) = 0.1, \quad 0.0 \le s \le 0.05 \\ z(s) = 0.0. \end{cases}$	0.05	0.0005
Vs7	$\begin{cases} x(s) = 0.35 + s, \\ y(s) = 0.0, \quad 0.0 \le s \le 0.25 \\ z(s) = 0.08\sin(s\pi/0.25). \end{cases}$	0.3045	0.0065
Vs8	$\begin{cases} x(s) = 0.35 + s, \\ y(s) = 0.0, \quad 0.0 \le s \le 0.25 \\ z(s) = -0.08\sin(s\pi/0.25). \end{cases}$	0.3045	0.0065
Vs9	$\begin{cases} x(s) = 0.6 + s, \\ y(s) = 0.0, \quad 0.0 \le s \le 0.15 \\ z(s) = 0.0. \end{cases}$	0.15	0.01

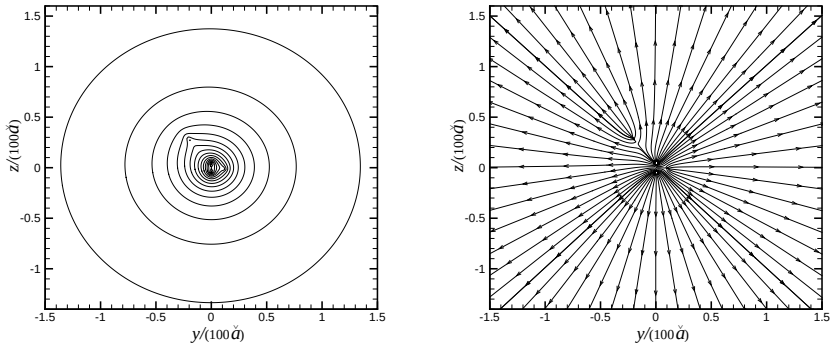

(a) $x/(100\check{a}) = 0.4$

(b) $x/(100\check{a}) = 0.4$

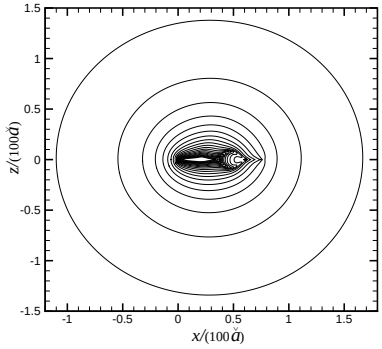

(c) $y/(100\check{a}) = 0.0$

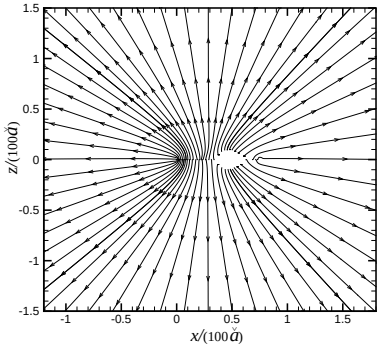

(d) $y/(100\check{a}) = 0.0$

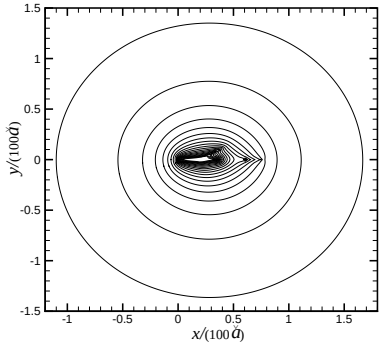

(e) $z/(100\check{a}) = 0.0$

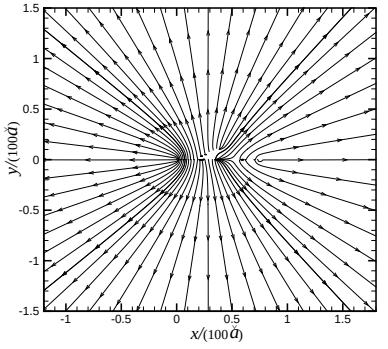

(f) $z/(100\check{a}) = 0.0$

Figure 10.10: Slides of 3D simulation results for (a, c, e) pressure contours and (b, d, f) flow velocity streamlines in tumour interstitium.

Chapter 11

Summary and Discussions

Tumour blood flow is one of the most important factors that can affect tumour growth and cancer therapies. It can be investigated efficiently by computational fluid dynamics through modelling tumour blood flow by numerical simulations. In this thesis, a three-dimensional mathematical model has been developed to investigate the blood flow through a vascular network with permeability which is embedded in a solid tumour. In this model, the vascular network can be three-dimensional in space and with generations of branches. The complex three-dimensional configuration of tumour vasculature is described by the parametric equation in terms of the vessel centre lines. The cross section of each vessel in the vascular network is assumed to be circular, and the length scale in the transverse direction of the vessel is smaller than that in the longitudinal direction. As a result, the flow inside a tumour vessel is dominated by the pressure gradient along its centre line. The mass- and momentum-conservation equations are derived in the local cylindrical coordinate system located on a certain vessel cross section, whose longitudinal axis is along the tangential direction of the vessel centre line at that section. Since the vascular flow is dominated by the leading component in the longitudinal direction of

the vessel, its governing equation becomes an ordinary differential equation, which is converted into one with respect to the parameter of the parametric equation for the vessel centre line. For the vasculature with complex structure, for example a mother vessel splitting into two or more daughter vessels at a junction point, the conditions of pressure continuity and mass conservation are imposed at every junction of the vascular network.

Due to the permeability of tumour vasculature, blood is transmitted from vessels into tumour interstitium. The mathematical relationship for extravasation flux is described by the Starling's law, which indicates that the transvascular flux depends on the vessel permeability and the transmural pressure difference. Based on mass conservation, the flux exceeded from a tumour vessel into interstitium must be equal to the gradient of the flux flowing through the vessel. Combining this relationship with the governing equation for the vascular flow, a one-dimensional differential equation for the flow inside the vessel is obtained, in which the source term contains tumour interstitial pressure. This coupling effect is also included in the governing equation for the blood flow in tumour interstitium. Together with the conditions of pressure continuity and mass conservation at junctions, the governing equations for the flow through entire vascular network are derived.

As tumour interstitium is regarded as porous media, the blood flow in it is described by the Darcy's law, which indicates that the fluid velocity is in direct proportion to the gradient of interstitial pressure. Substituting the Darcy's law into flow continuity equation, the interstitial pressure satisfies the Laplace equation as the tumour tissue hydraulic conductivity is assumed to be constant. The boundary condition for the interstitial flow is derived based on continuity of flow velocity on the vascular surface. Taking this boundary condition into account, the Laplace equation is transformed into a boundary-integral

equation when the Green's function is used. This offers anther equation linking the pressures inside and outside vessels, or the coupling effect. Together with the governing equations for the vascular flow, the mathematical model is completed.

The mathematical model is discretised and solved numerically. There are a number of complications for the numerical procedure. In particular, though the flow inside each vessel has been rationally approximated by the component in the longitudinal direction of the vessel, the interstitial flow on the external vascular surface has other components because its direction is unconstrained. The circumferential average of the interstitial pressure on the exterior vascular surface is adopted to avoid the mismatch between the internal and external vascular pressures. As a result, the original three-dimensional boundary-integral equation is reduced to a one-dimensional integral equation with respect to the parameter of the parametrical equation for the vessel centre line. Moreover, when the vessel shape becomes complex, for example a curved vessel, the governing differential equation for the flow through the vessel could become complicated in terms of the expression of the parametrical equation for the vessel centre line. In the meantime, since the vessel cross sections are no longer parallel with each other, the integral equation derived from the Laplace equation is also significantly modified. The discretised differential and integral equations are solved by finite difference method and boundary element method respectively. The developed model and methodology have first been tested for a single straight vessel. Results are compared with published data, and excellent agreement has been found. The efficiency of the methodology has been analysed.

As the rationality of our mathematical model has been approved, it is applied to study how different types of physical parameters and irregular tumour

vascular structures affect tumour blood flow in context with the transvascular delivery of anti-cancer agents with heavy weight in a solid tumour and the effectiveness of chemotherapy and radiotherapy for cancer. Our simulation results indicate that, when we can elevate one or more venous pressures of the vascular network to reduce the difference between the inlet and outlet vascular flow pressures and to enlarge the difference between the outlet vascular flow pressures and the tumour peripheral pressure, it would be beneficial for the delivery of anti-cancer agents with heavy weight throughout the vascular surface and the effectiveness of radiotherapy and chemotherapy. If the vascular permeability or part of it can be raised, the overall ability of transvascular delivery of anti-cancer macromolecules with large size and effectiveness of radiotherapy and chemotherapy can be improved, while the efficiency would be compromised when the permeability is higher than some level. Increasing the tumour tissue hydraulic conductivity is another option to improve the ability of transporting anti-cancer agents out of the vessels into tumour interior and the effectiveness of chemotherapy and radiotherapy, but the efficiency would be lowered when the value of the tumour tissue hydraulic conductivity is high. The variation of vessel radius has different effects on tumour blood flow under different types of vascular flow conditions. When the perfused flux and the inlet pressure for the vascular flow are given, an increase of tumour vessel radius can improve the efficacy of transporting anti-cancer agents with heavy weight through vascular surface into tumour interstitium and the effectiveness of the chemotherapy and radiotherapy. However, if the perfused flux and the outlet pressure for the vascular flow are fixed, dilated tumour vessel has negative effects on transvascular delivery of the macromolecules with large size in tumour or the effectiveness of the chemotherapy and radiotherapy. On the other hand, if we can control the inlet and outlet pressures for the vascular flow, enlarging

tumour vessel can be beneficial for transporting the anti-cancer agents with heavy weight through vascular surface into tumour interior, but the effectiveness of cancer therapies has to be sacrificed. Moreover, our model is applied to undertake some initial investigations on tumour blood flow when a compliant permeable vessel is embedded in a solid tumour. Our results show that, under the same physical and geometrical conditions, the vessel with compliance can generate more extravasation flux relative to the rigid one.

Meanwhile, the interstitial flow field has been investigated by our model. The interstitial flow near the vessels is affected significantly by the physical parameters and the abnormal complex configuration of tumour vasculature. For example, if a tumour vessel is bent with some curvature, the shapes of interstitial pressure contours vary rapidly near the vessel. The interstitial flow velocity streamlines show that the interstitial blood flow on the concave side of the vessel is less active than the flow on the convex side. This can cause the uneven supply of anti-cancer agents within tumour interstitium. Far away from tumour vasculature, the shapes of interstitial pressure contours tend to be circular and the flux over there is uniform in all directions.

Based on the patterns of the vascular flow, an approximation model is developed by ignoring the term with small value in the fully coupling model. Compared with the fully coupling model, the approximation model neglects the coupling effect between the internal and external vascular pressures in the differential equations for the vascular flow, which simplifies the calculation procedure. The approximation model is valid only if the rational conditions are met. The computation efficiency of the approximation model is higher than the fully coupling model, especially when the structure of vascular network is complicated. Further to this, if the accurate results are required, the solution obtained by the approximation model can be adopted as the initial guess for the

fully coupling model, which should be able to reduce the number of iteration in the fully coupling model.

The present model is derived based on conservation of mass and momentum, which does reflect the true physics of the blood flow through a permeable vascular network embedded in a solid tumour to a large extent. There are nevertheless some approximations within this model, such as the longitudinal flow assumption for the vascular flow and the Darcy's law for the interstitial flow. Also the one-dimensional model for the interstitial flow along the external vascular surface is questionable for the local results near the junctions of tumour vascular network. All of these require further research and investigations. It is therefore unrealistic to expect that the present work has immediate clinical applications, but it nevertheless is one step forward towards the goal of improving the delivery of anti-cancer agents with heavy weight into solid tumours.

Appendix A

Computation of the Complete Elliptic Integrals of the First and Second Kind

The complete elliptic integrals of the first and second kind are defined as

$$F(\hat{m}) = \frac{2}{\pi} \int_0^{\pi/2} (1 - \hat{m} \sin^2 \xi)^{-1/2} d\xi, \tag{A.0.1}$$

and

$$E(\hat{m}) = \frac{2}{\pi} \int_0^{\pi/2} (1 - \hat{m} \sin^2 \xi)^{1/2} d\xi, \tag{A.0.2}$$

respectively, where $\sqrt{\hat{m}}$ is the module of the elliptic integrals.

When $0 \leq \sqrt{\hat{m}} < 1$, an efficient method to calculate $F(\hat{m})$ and $E(\hat{m})$ is through the recursive formulae [Pozrikidis (1997)], which are

$$F(\hat{m}) = (1 + \hat{K}_1)(1 + \hat{K}_2)(1 + \hat{K}_3) \cdots, \tag{A.0.3}$$

and

$$E(\hat{m}) = F\left(1 - \frac{\hat{m}}{2}\hat{P}\right), \tag{A.0.4}$$

where

$$\hat{K}_0 = \hat{m}, \qquad \hat{K}_j = \frac{1 - (1 - \hat{K}_{j-1}^2)^{\frac{1}{2}}}{1 + (1 - \hat{K}_{j-1}^2)^{\frac{1}{2}}} \qquad j \geq 1, \tag{A.0.5}$$

and

$$\hat{P} = 1 + \frac{\hat{K}_1}{2}\left[1 + \frac{\hat{K}_2}{2}\left(1 + \frac{\hat{K}_3}{2}(\cdots)\cdots\right)\right]. \tag{A.0.6}$$

Abramowitz and Stegun (1972) provided the alternative polynomial approximations to calculate $F(\hat{m})$ and $E(\hat{m})$, as stated in Section 4.3.4.

References

Abramowitz, M. and Stegun, I. A. (eds.) (1972), *Handbook of Mathematical Functions with Formulas, Graphs, and Mathematical Tables*, United States Department of Commerce, National Bureau of Standards.

Algire, G. H. (1943), An Adaptation of the Transparent Chamber Technique to the Mouse, *Journal of National Cancer Institute* **4**, 1–11.

Algire, G. H. (1945), Vascular Reactions of Normal and Malignant Tumors *in Vivo*. I. Vascular Reactions of Mice to Wounds and to Normal and Neoplastic Transplants., *Journal of National Cancer Institute* **6**, 73–85.

Anderson, H. and Price, P. (2002), Clinical Measurement of Blood Flow in Tumours Using Positron Emission Tomography: A Review, *Nuclear Medicine Communications* **23**, 131–138.

Anderson, J. D. (1995), *Computational Fluid Dynamics The basics with Applications*, sixth edition, McGraw Hill.

Apelblat, A., Katzir-Katchalsky, A. and Silberberg, A. (1974), A Mathematical Analysis of Capillary-Tissue Fluid Exchange, *Biorheology* **11**, 1–49.

Bacharach, S. L., Libutti, S. K. and Carrasquillo, J. A. (2000), Measuring Tumor Blood Flow with H2 15O: Practical Considerations, *Nuclear Medicine and Biology* **27**, 671–676.

Baish, J. W., Netti, P. A. and Jain, R. K. (1997), Transmural Coupling of Fluid Flow in Microcirculatory Network and Interstitium in Tumors, *Microvascular Research* **53**, 128–141.

Baxter, L. T. and Jain, R. K. (1989), Transport of Fluid and Macromolecules in Tumors I. Role of Interstitial Pressure and Convection, *Microvascular Research* **37**, 77–104.

Baxter, L. T. and Jain, R. K. (1990), Transport of Fluid and Macromolecules in Tumors II. Role of Heterogeneous Perfusion and Lymphatics, *Microvascular Research* **40**, 246–263.

Beardsley, T. (1994), A War Not Won, *Scientific American* **270**, 130 – 138.

Boucher, Y., Brekken, C., Netti, P. A. and Baxter, L. T.and Jain, R. K. (1998), Intratumoral Infusion of Fluid: Estimation of Hydraulic Conductivity and Implications for the Delivery of Therapeutic Agents, *British Journal of Cancer* **78**, 1442–1448.

Boucher, Y. and Jain, R. K. (1992), Microvascular Pressure is the Principal Driving Force for Interstitial Hypertension in Solid Tumors: Implications for Vascular Collapse, *Cancer Research* **52**, 5110–5114.

Boyle, P. and Levin, B. (eds.) (2008), *World Cancer Report 2008*, The International Agency for Research on Cancer, Lyon.

Brebbia, C. A. and Dominguez, J. (1992), *Boundary Elements An Introductory Course*, Computational Mechanics Publication.

Briggs, W. L., Henson, V. E. and McCormick, S. F. (2000), *A Multigrid Tutorial*, second edition, The Society for Industrial and Applied Mathematics, Philadelphia, United States of America.

Bronshtein, I., Semendyayev, K., Musiol, G. and Muehlig, H. (2007), *Handbook of Mathematics*, fifth English edition, Springer.

Carmeliet, P. and Jain, R. K. (2000), Angiogenesis in Cancer and other Diseases, *Nature* **407**(14), 249–257.

Cartmel, B. (1997), Cancer Control and Epidemiology, *in* S. L. Groenwald, M. H. Frogge, M. Goodman and C. H. Yarbro (eds.), *Cancer Nursing: Principles and Practice*, fourth edition, Jones and Bartlett, Boston, MA, pp.50–76.

Chalkley, W. H. (1948), Comments on Algeria GH and Legallais FY. Growth and Vascularization of Transplantable Mouse Melanomas, *Special Publications of the New York Academy of Sciences* **4**, 164.

Chung, T. J. (2002), *Computational Fluid Dynamics*, Cambridge University Press.

Clark, E. R., Kirby-Smith, H. T., Rex, R. O. and Williams, R. G. (1930), Recent Modifications in the Method of Studying Living Cells and Tissues in Transparent Chambers Inserted in the Rabbit's Ear, *The Anatomical Record* **47**, 187–211.

Costantini, L. C., Bakowska, J. C., Breakefield, X. O. and Issacson, O. (2000), Gene Therapy in the CNS, *Gene Therapy* **7**, 93–109.

Curry, F. E. (1984), Mechanics and Themodynamics of Transcapillary Exchange, *in* E. M. Renkin and C. C. Michel (eds.), *Handbook of Physiology*, American Physiological Society, Bethesda, Maryland, pp.309–374.

Dean, W. R. (1928), The Stream-Line Motion of Fluid in a Curved Pipe (second paper), *Philosophical Magazine and Journal of Science* **5**, 673–695.

Dellian, M., Witwer, B. P.and Salehi, H. A., Yuan, F. and Jain, R. K. (1996), Quantitation and Physiological Characterization of Angiogenic Vessels in Mice: Effect of Basic Fibroblast Growth Factor, Vascular Endothelial Growth Factor/Vascular Permeability Factor, and Host Microenvironment, *American Journal of Pathology* **149**, 59–72.

Dvorak, H. F., Brown, L. F., Detmar, M. and Dvorak, A. M. (1995), Vascular Permeability Factor/Vascular Endothelial Growth Factor, Microvascular Hyperpermeability and Angiogenesis, *American Journal of Pathology* **146**, 1029–1039.

Dvorak, H. F., Nagy, J. A., Feng, D., Brown, L. F. and Dvorak, A. M. (1999), Vascular Permeability Factor/Vascular Endothelial Growth Factor and the Significance of Microvascular Hyperpermeabiltiy in Angiogenesis, *Current Topics in Microbiology and Immunology* **237**, 97–132.

Dykes, P. W., Bradwell, A. R., Chapman, C. E. and Vaughan, A. T. M. (1987), Radioimmunotherapy of Cancer: Clinical Studies and Limiting Factors, *Cancer Treatment Review* **14**, 87–106.

Eason, G., Noble, B. and Sneddon, I. N. (1955), On Certain Integrals of Lipschitz-Hankel Type Involving Products of Bessel Functions, *Philosophical Transactions of the Royal Society of London. Series A, Mathematical and Physical Sciences* **247**(935), 529–551.

Eberhart, R., Shitzer, A. and Hernandez, E. (1980), Thermal Dilution Methods: Estimation of Tissue Blood Flow and Metabolism, *The New York Academy of Sciences* **335**, 107–132.

El-Kareh, A. W. and Secomb, T. W. (1995), Effect of Increasing Vascular Hydraulic Conductivity on Delivery of Macromolecular Drugs to Tumor Cells,

*International Journal of Radiation Oncology * Biology * Physics* **32**, 1419–1423.

Evan, G. I. and Vousden, K. H. (2001), Proliferation, Cell Cycle and Apoptosis in Cancer, *Nature* **411**, 342–348.

Evelhoch, J. L. (1992), Measurement of Tumor Blood Flow by Deuterium NMR and the Effects of Modifiers, *NMR in Biomedicine* **5**, 290–295.

Faltinsen, O. M. and Pettersen, B. (1987), Application of a Vortex Tracking Method to Separated Flow around Marine Structures, *Journal of Fluids and Structures* **1**, 217–237.

Fleischman, G. J., Secomb, T. W. and Gross, J. F. (1986a), Effect of Extravascular Pressure Gradients on Capillary Fluid Exchange, *Mathematical Biosciences* **81**, 145–164.

Fleischman, G. J., Secomb, T. W. and Gross, J. F. (1986b), The Interaction of Extravascular Pressure Fields and Fluid Exchange in Capillary Networks, *Mathematical Biosciences* **82**, 141–151.

Folkman, J. (1971), Tumor Angiogenesis: Therapeutic Implications, *The New England Journal of Medicine* **285**, 1182 – 1186.

Folkman, J. (1995), Angiogenesis in Cancer, Vascular, Rheumatoid and Other Disease, *Nature Medicine* **1**, 27 – 31.

Folkman, J. (2006), Angiogenesis, *Annual Review of Medicine* **57**, 1 – 18.

Fukumura, D. and Jain, R. K. (2007a), Tumor Microenvironment Abnormalities: Causes, Consequences, and Strategies to Normalize, *Journal of Cellular Biochemistry* **101**, 937 – 949.

Fukumura, D. and Jain, R. K. (2007b), Tumor Microvasculature and Microenvironment: Targets for Anti-Angiogenesis and Normalization, *Microvascular Research* **74**, 72 – 84.

Fukumura, D., Yuan, F., Monsky, W. L., Chen, Y. and Jain, R. K. (1997), Effect of Host Microenvironment on the Microcirculation of Human Colon Adenocarcinoma, *American Journal of Pathology* **151**, 679–688.

Fung, Y. C. (1981), *A Multigrid Tutorial*, springer-verlag edition, Biomechanics: Mechanical Properties of Living Tissues, PNew York.

Fyles, A. W., Milosevic, M., Wong, R., Kavanagh, M.-C., Pintilie, M., Sun, A., Chapmane, W., Levina, W., Manchula, L., Keanea, T. J. and Hillc, R. P. (1998), Oxygenation Predicts Radiation Response and Survival in Patients with Cervix Cancer, *Radiotherapy and Oncology* **48**, 149–156.

Gabizon, A., Goren, D., Cohen, R. and Barenholz, Y. (1998), Development of Liposomal Anthracyclines: From Basics to Clinical Applications, *Journal of Controlled Release* **53**, 275–279.

Gabriel, J. (2007), Predisposing Factors to Developing Cancer, *in* J. Gabriel (ed.), *The Biology of Cancer*, second edition, John Wiley and Sons Ltd, West Sussex, England, pp.11–22.

Garcia, M., Jemal, A., Ward, E. M., Center, M. M., Hao, Y., Siegel, R. L. and Thun, M. J. (2007), *Global Cancer Facts & Figures 2007*, GA: American Cancer Society, Atlanta.

Gatenby, R. A., Kessler, H. B., Rosenblum, J. S., Coia, L. R., Moldofsky, P. J., Hartz, W. H. and Broder, G. J. (1988), Oxygen Distribution in Squamous Cell Carcinoma Metastases and Its Relationship to Outcome of Radiation Therapy, *International Journal of Radiation Oncology* **14**, 831–838.

Gerlowski, L. E. and Jain, R. K. (1986), Microvascular Permeability of Normal and Neoplastic Tissues, *Microvascular Research* **31**, 288–305.

Gibbs, F. (1933), A Thermoelectric Blood Flow Recorder in the Form of a Needle, *Proceedings of the Society for Experimental Biology and Medicine* **31**, 141–146.

Guillino, P. M. (1975), Extracellular Compartments of Solid Tumors, *in* F. F. Becher (ed.), *Cancer: A Comprehensive Treatise*, Plenum Press, New York, pp.327–334.

Gullino, P. and Grantham, F. (1961), Studies on the Exchange of Fluids between Host and Tumor. I. A method for Growing Tissue-Isolated Tumors in Laboratory Animals, *Journal of National Cancer Institute* **27**, 679–689.

Gullino, P. M., Clark, S. H. and Grantham, F. H. (1964), The Interstitial Fluid of Solid Tumors, *Cancer Research* **24**, 780–797.

Gump, F. and White, R. (1968), Determination of Regional Tumor Blood Flow by Krypton-85, *Cancer* **21**, 871–875.

Hamming, R, W. (1986), *Numerical Methods for Scientists and Engineers*, second edition, Dover Publications, New York, United States of America.

Hanahan, D. and Weinberg, R. A. (2000), The Hallmarks of Cancer, *Cell* **100**, 57–70.

Hashizume, H., Baluk, P., Morikawa, S., McLean, J. W., Thurston, G., Roberge, S., Jain, R. K. and McDonald, D. M. (2000), Openings between Defective Endothelial Cells Explain Tumor Vessel Leakiness, *American Journal of Pathology* **156**, 1363–1380.

Helmlinger, G., Netti, P. A., Lichtenbeld, H. C., Melder, R. J. and Jain, R. K. (1997), Solid Stress Inhibits the Growth of Multicellular Tumor Spheroids, *Nature Biotechnology* **15**, 778–783.

Hobbs, S. K., Monsky, W. L., Yuan, F., Roberts, W. G., Griffith, L., Torchilin, V. P. and Jain, R. K. (1998), Regulation of Transport Pathways in Tumor Vessels: Role of Tumor Type and Microenvironment, *Proceedings of the National Academy of Sciences of The United States of America* **95**, 4607–4612.

Höckel, M., Knoop, C., Schlenger, K., Vorndran, B., Baussmann, E., Mitze, M., Knapstein, P. G. and Vaupel, P. (1993), Intratumoral pO2 Predicts Survival in Advanced Cancer of the Uterine Cervix, *Radiotherapy and Oncology* **26**, 45–50.

Hori, K., Suzuki, M., Saito, S., Tanda, S., Zhang, Q. H. and Li, H. C. (1994), Changes in Vessel Pressure and Interstitial Fluid Pressure of Normal Subcutis and Subcutaneous Tumor in Rats due to Angiotensin II, *Microvascular Research* **48**, 246–256.

IARC (1994), *IARC Monographs on the Evaluation of Carcinogenic Risks to Humans: Hepatitis viruses*, Vol. 59 of *IARC Monographs on the Evaluation of Carcinogenic Risks to Humans*, International Agency for Research on Cancer, World Health Organization, Lyon, France.

IARC (1998), *Tobacco Habits other than Smoking; Betel-Quid and Areca-Nut Chewing; and some Related Nitrosamines*, Vol. 37 of *IARC Monographs on the Evaluation of Carcinogenic Risks to Humans*, International Agency for Research on Cancer, World Health Organization, Lyon, France.

IARC (2004), *Tobacco Smoke and Involuntary Smoking*, Vol. 83 of *IARC*

Monographs on the Evaluation of Carcinogenic Risks to Humans, International Agency for Research on Cancer, World Health Organization, Lyon, France.

IARC (2008), IARC Monographs, `http://monographs.iarc.fr/`.

Jain, R. K. (1987a), Transport of Molecules across Tumor Vasculature, *Cancer and Metastasis Review* **6**, 559–594.

Jain, R. K. (1987b), Transport of Molecules in the Tumor Interstitium: A Review, *Cancer Research* **47**, 3039–3051.

Jain, R. K. (1988), Determinants of Tumor Blood Flow: A Review, *Cancer Research* **48**, 2641–2658.

Jain, R. K. (1989), Delivery of Navel Therapeutic Agents in Tumors: Physiological Barriers and Strategies, *Journal National Cancer Institute* **81**, 570–576.

Jain, R. K. (1994), Barriers to Drug Delivery in Solid Tumors, *Science American* **271**, 42–49.

Jain, R. K. (1996), Delivery of Molecular Medicine to Solid Tumors, *Science* **271**, 1079–1080.

Jain, R. K. (1997), Delivery of Molecular and Cellular Medicine to Solid Tumors, *Microcirculation* **4**, 1–23.

Jain, R. K. (1998a), Delivery of Molecular and Cellular Medicine to Solid Tumors, *Journal of Controlled Release* **53**, 49–67.

Jain, R. K. (1998b), The Next Frontier of Molecular Medicine: Delivery of Therapeutics, *Nature Medicine* **4**(6), 655–657.

Jain, R. K. (1999a), Transport of Molecules, Particles and Cells in Solid Tumors, *Annual Review of Biomedical Engineering* **1**, 241–263.

Jain, R. K. (1999b), Understanding Barriers to Drug Delivery: High Resolution *in Vivo* Imaging Is Key, *Clinical Cancer Research* **5**, 1605–1606.

Jain, R. K. (2001), Delivery of Molecular and Cellular Medicine to Solid Tumors, *Advanced Drug Delivery Reviews* **46**, 149–168.

Jain, R. K. (2002), Angiogenesis and Lymphangiogenesis in Tumors: Insights from Intravital Microscopy, *Cold Spring Harbor Symposia on Quantitative Biology* **67**, 239–248.

Jain, R. K. (2003), Molecular Regulation of Vessel Maturation, *Nature Medicine* **9**, 685–693.

Jain, R. K. (2005), Normalization of Tumor Vasculature: An Emerging Concept in Antiangiogenic Therapy, *Science* **307**, 58–62.

Jain, R. K., Grantham, F. H. and Gullino, P. M. (1979), Blood Flow and Heat Transfer in Walker 256 Mammary Carcinoma, *Journal of the National Cancer Institute* **66**, 927 – 933.

Jain, R. K. and Baxter, L. T. (1988), Mechanisms of Heterogeneous Distribution of Monoclonal Antibodies and Other Macromolecules in Tumors: Significance of Elevated Interstitial Pressure, *Cancer Research* **48**, 7022–7032.

Jain, R. K. and Fenton, B. T. (2002), Intratumoral Lymphatic Vessels: A Case of Mistaken Identity or Malfunction?, *Journal of the National Cancer Institute* **94**, 417–421.

Jain, R. K. and Ward-Hartley, K. (1984), Tumor Blood Flow — Characterization , Modifications, and Role in Hyperthermia, *IEEE Transactions on Sonics and Ultrasonics* **SU-31**, 504 – 526.

Jang, S. H., Wientjes, M. G., Lu, D. and Au, J. L.-S. (2003), Drug Delivery and Transport to Solid Tumors, *Pharmaceutical Research* **20**(9), 1337–1350.

Jung, Y. D., Ahmad, S. A., Akagi, Y., Takahashi, Y., Liu, W., Reinmuth, N., Shaheen, R. M., Fan, F. and Ellis, L. M. (2000), Role of the Tumor Microenvironment in Mediating Response to Anti-angiogenic Therapy, *Cancer and Metastasis Reviews* **9**, 147–157.

Kohler, M. and Milstein, C. (1975), Continuous Culture of Fused Cells Secreting Antibody of Predefined Specificity, *Nature (London)* **256**, 494–497.

Konerding, M. A., Malkusch, W., Klapthor, B., van Ackern, C., Fait, E., Hill, S. A., Parkins, C., Chaplin, D. J., Presta, M. and Denekamp, J. (1999), Evidence for Characteristic Vascular Patterns in Solid Tumours: Quantitative Studies Using Corrosion Casts, *British Journal of Cancer* **80**, 724–732.

Krogh, A. S. (1919), The Rate of Diffusion of Gases through Animal Tissues with Some Remarks on the Coefficient of Invasion, *The Journal of Physiology* **52**, 391–408.

Kroll, R. A., Pagel, M. A., Muldoon, L. L., Roman-Goldstein, S. and Neuwelt, E. A. (1996), Increasing Volume of Distribution to the Brain with Interstitial Infusion: Dose, rather than Convection, Might Be the Most Important Factor, *Neurosurgery* **38**, 746–752.

Ku, D. N. (1997), Blood Flow in Arteries, *Annual Review of Fluid Mechanics* **29**, 399–434.

Kulkarni, S. B., Betageri, G. V. and Singh, M. (1995), Factors Affecting Microencapsulation of Drugs into Liposomes, *Journal of Microencapsulation* **12**, 229–246.

Landis, E. M. (1927), Micro-Injection Studies of Capillary Permeability I. Factors in the Production of Capillary Stasis, *American Journal of Physiology* **81**, 124–142.

Lee, S. and Schmid-Schönbein, G. W. (1996), Biomechanical Model for the Myogenic Response in the Microcirculation: Part I — Formulation and Initial Testing, *Journal of Biomechanical Engineering* **118**, 145–151.

Less, J. R., Skalak, T. C., Sevick, E. M. and Jain, R. K. (1991), Microvascular Architecture in a Mammary Carcinoma: Branching Patterns and Vessel Dimensions, *Cancer Research* **51**, 265–273.

Leu, A. J., Berk, D. A., Lymboussaki, A., Alitalo, K. and Jain, R. K. (2000), Absence of Functional Lymphatics within a Murine Sarcoma: A Molecular and Functional Evaluation, *Cancer Research* **60**, 4324–4327.

Leunig, M., Yuan, F., Menger, M. D., Boucher, Y., Goetz, A. E., Messmer, K. and Jain, R. K. (1992), Angiogenesis, Microvascular Architecture, Microhemodynamics and Interstitial Fluid Pressure during Early Growth of Human Adenocarcinoma LS174T in SCID Mice, *Cancer Research* **52**, 6553–6560.

Lighthill, M. J. (1972), Physiological Fluid Dynamics: A Survey, *Journal of Fluid Dynamics* **52**(3), 475–497.

MacPhee, P. J. and Michel, C. C. (1995), Subatmospheric Closing Pressures in Individual Microvessels of Rats and Frogs, *The Journal of Physiology* **484**(1), 183–187.

Maedaa, H., Wua, J., Sawaa, T., Matsumurab, Y. and Horic, K. (2000), Tumor Vascular Permeability and the EPR Effect in Macromolecular Therapeutics: A Review, *Journal of Controlled Release* **65**, 271–284.

Mason, J. C. (1975), 'Studies on the Permeability of Single Capillaries', Oxford University, Oxford.

McConnell, A. J. (1957), *Application of Tensor Analysis*, Dover Publications, Beijing, China.

Milosevic, M. F., Fyles, A. W. and Hill, R. P. (1999), The Relationship Between Elevated Intertitial Fluid Pressure and Blood Flow in Tumors: A Bioengineering Analysis, *International Journal of Radiation Oncology * Biology * Physics* **43**(5), 1111–1123.

Mollica, F., Jain, R. K. and Netti, P. A. (2003), A Model for Temporal Heterogeneities of Tumor Blood Flow, *Microvascular Research* **65**, 56–60.

Monsky, W. L., Carreira, C. M., Tsuzuki, Y., Gohongi, a., Fukumura, D. and Jain, R. K. (2002), Role of Host Microenvironment in Angiogenesis and Microvascular Functions in Human Breast Cancer Xenografts: Mammary Fat Pad versus Cranial Tumors, *Clinical Cancer Research* **8**, 1008–1013.

Nagy, J. D. (2005), The Ecology and Evolutionary Biology of Cancer: A Review of Mathematical Models of Necrosis and Tumor Cell Diversity, *Mathematical Biosciences and Engineering* **2**(2), 381–418.

Netti, P. A., Baxter, L. T., Boucher, Y., Skalak, R. and Jain, R. K. (1997), Macro- and Microscopic Fluid Transport in Living Tissues: Application to Solid Tumors, *American Institute of Chemical Engineers* **43**, 818–834.

Netti, P. A., Hamberg, L. M., Babich, J. W., Kierstead, D., Graham, W., Hunter, G. J., Wolf, G. L., Fischman, A., Boucher, Y. and Jain, R. K. (1999), Enhancement of Fluid Filtration across Tumor Vessels: Implication for Delivery of Macromolecules, *Proceedings of the National Academy of Sciences* **96**, 3137–3142.

Netti, P. A., Roberge, S., Boucher, Y., Baxter, L. T. and Jain, R. K. (1996), Effect of Transvascular Fluid Exchange on Pressure-Flow Relationship in Tumors: A Proposed Mechanism for Tumor Blood Flow Heterogeneity, *Microvascular Research* **52**, 27–46.

Nichols, W. W. and O'Rourke, M. F. (2005), *McDonald's Blood Flow in Arteries*, fifth edition, Hodder Arnold, a member of the Hodder Headline Group.

Okihara, K., Watanabe, H. and Kojima, M. (1999), Kinetic Study of Tumor Blood Flow in Prostatic Cancer Using Power Doppler Imaging, *Ultrasound in Medicine & Biology* **25**, 89–94.

Parkin, D. M. (2001), Global Cancer Statistics in the Year 2000, *The Lancet Oncology* **2**(9), 533–543.

Parkin, D. M., Bray, F., Ferlay, J. and Pisani, P. (2005), Global Cancer Statistics, 2002, *CA A Cancer Journal for Clinicians* **55**, 74–108.

Parkin, D. M., Läärä, E. and Muir, C. S. (1988), Estimates of the Worldwide Frequency of Sixteen Major Cancers in 1980, *International Journal of Cancer* **41**(2), 184–197.

Parkin, D. M., Pisani, P. and Ferlay, J. (1993), Estimates of the Worldwide Incidence of Eighteen Major Cancers in 1985, *International Journal of Cancer* **54**(4), 594–606.

Parkin, D. M., Pisani, P. and Ferlay, J. (1999), Estimates of the Worldwide Incidence of 25 Major Cancers in 1990, *International Journal of Cancer* **80**(6), 827–841.

Parkin, D. M., Stjernsward, J. and Muir, C. S. (1984), Estimates of the Worldwide Frequency of Twelve Major Cancers, *Bull World Health Organ* **62**(2), 163–182.

Pedley, T. J. (1980), *The Fluid Mechanics of Large Blood Vessels*, Cambridge University Press, Cambridge.

Peters-Engl, C., Frank, W., Leodolter, S. and Medl, M. (1999), Tumor Flow in Malignant Breast Tumors Measured by Doppler Ultrasound: An Independent Predictor of Survival, *Breast Cancer Research and Treatment* **54**, 65–71.

Peters, W., Telxeira, M., Integlietta, M. and Gross, J. F. (1980), Microcirculatory Studies in Rat Mammary Carcinoma. I. Transparent Chamber Method, Development of Microvasculature, and Pressure in Tumor Vessels, *Journal of National Cancer Institute* **65**, 631–642.

Peterso, H. (1979), Tumor Blood Flow Compared with Normal Tissue Blood Flow, *in* B. Raton (ed.), *Tumor Blood Circulation*, CRC Press, pp.103–114.

Ponder, B. A. J. (2001), Cancer Genetics, *Nature* **411**, 336–341.

Pozrikidis, C. (1997), *Introduction to Theoretical and Computational Fluid Dynamics*, Oxford University Press, New York.

Pozrikidis, C. (2002), *A practical guide to boundary element methods with the software library BEMLIB*, Chapman & Hall/CRC.

Pozrikidis, C. and Farrow, D. A. (2003), A Model of Fluid Flow in Solid Tumors, *Annals of Biomedical Engineering* **31**, 181–194.

Robinson, S. P., Howe, F. A., Rodrigues, L. M., Stubbs, M. and Griffiths, J. R. (1998), Magnetic Resonance Imaging Techniques for Monitoring Changes in Tumor Oxygenation and Blood Flow, *Seminars in Radiation Oncology* **8**, 197–207.

Ryschich, E., Schmidt, E., Maksan, S.-M., Klar, E. and Schmidt, J. (2004), Expansion of Endothelial Surface by an Increase of Vessel Diameter during Tumor Angiogenesis in Experimental Hepatocellular and Pancreatic Cancer, *World Journal of Gastroenterology* **10**, 3171–3174.

Sandison, J. C. (1924), A New Method for Microscopic Study of Living Growing Tissues by the Introduction of Transparent Chamber in the Rabbit's Ear, *The Anatomical Record* **28**, 281–287.

Sapirstein, L. (1958), Regional Blood Flow by Fractional Distribution of Indicators, *American Journal of Physiology* **193**, 161–168.

Sarg, M. J. and Gross, A. D. (eds.) (2007), *The Cancer Dictionary*, third edition, Facts on File, New York, USA.

Schilling, R. J. and Harris, S. L. (2000), *Applied Numerical Methods for Engineering Using Matlab and C*, Thomson Learning.

Schmid-Schönbein, G. W. (1999), Biomechanics of Microcirculatory Blood Perfusion, *Annual Review of Biomedical Engineering* **01**, 73–102.

Sevick, E. M. and Jain, R. K. (1989a), Geometric Resistance to Blood Flow in Solid Tumors Perfused *ex Vivo*: Effects of Tumor Size and Perfusion Pressure, *Cancer Research* **49**, 3506–3512.

Sevick, E. M. and Jain, R. K. (1989b), Viscous Resistance to Blood Flow in Solid Tumors: Effect of Hematocrit on Intratumor Blood Viscosity, *Cancer Research* **49**, 3513–3519.

Shubik, P. (1982), Vascularization of Tumors: A Review, *Journal of Cancer Research and Clinical Oncology* **103**, 2117 – 2226.

Starling, E. H. (1896), On the Absorption of Fluids from the Connective Tissue Spaces, *The Journal of Physiology* **19**, 312–326.

Steinberg, F., Konerding, M. A. and Streffer, C. (1990), The Vascular Architecture of Human Xenotransplanted Tumors: Histological, Morphometrical, and Ultrastructural Studies, *Journal of Cancer Research and Clinical Oncology* **116**, 517–524.

Stohrer, M., Boucher, Y., Stangassinger, M. and Jain, R. K. (2000), Oncotic Pressure in Solid Tumors Is Elevated, *Cancer Research* **60**, 4251–4255.

Swabb, E. A., Wei, J. and Gullino, P. M. (1974), Diffusion and Convection in Normal and Neoplastic Tissues, *Cancer Research* **34**, 2814–2822.

Tong, R. T., Boucher, Y., Kozin, S. V., Winkler, F., Hicklin, D. and Jain, R. K. (2004), Vascular Normalization by Vascular Endothelial Growth Factor Receptor 2 Blockade Induces a Pressure Gradient Across the Vasculature and Improves Drug Penetration in Tumors, *Cancer Research* **64**, 3731–3736.

UCL Cancer Institute (2007), Graph Showing Cancer Death Rate in UK, `http://www.ucl.ac.uk/cancer/what-is-cancer/graph/index.htm`.

Walter, J. (1977), Radiation Hazards and Protection Cytotoxic Chemotherapy, *in Cancer and Radiotherapy: A Short Guide for Nurses and Medical Students*, Churchill Livingstone, London.

Wiig, H. (1982), Microvascular Pressure in DMBA-Induced Rat Mammary Tumors, *Scandinavian Journal of Clinical and Laboratory Investigation* **42**, 165–171.

Wogan, G. N., Hecht, S. S., Felton, J. S., Conney, A. H. and Loeb, L. A. (2004), Environmental and Chemical Carcinogenesis, *Seminars in Cancer Biology* **14**, 473–486.

Womersley, J. R. (1955), Method for the Calculation of Velocity, Rate of Flow and Viscous Drag in Arteries when Their Pressure Gradient is Known, *The Journal of Physiology* **127**, 553–563.

Wu, G. X. and Taylor, R. E. (2003), The Coupled Finite Element and Boundary Element Analysis of Nonlinear Interactions between Waves and Bodies, *Ocean Engineering* **30**, 387–400.

Wu, W. Y. (2004), *Fluid Mechanics*, Peking University Press, Beijing, China.

Yuan, F., Leunig, M., Berk, D. A. and Jain, R. K. (1993), Microvascular Permeability of Albumin, Vascular Surface Area, and Vascular Volume Measured in Human Adenocarcinoma LS174T Using Dorsal Chamber in SCID Mice, *Microvascular Research* **45**, 268–289.

Yuan, F., Leunig, M., Huang, S. K., Berk, D. A., Papahadjopoulos, D. and Jain, R. K. (1994a), Microvascular Permeability and Interstitial Penetration of Sterically Stabilized (Stealth) Liposomes in a Human Tumor Xenograft, *Cancer Research* **541**, 3352–3356.

Yuan, F., Salehi, H. A., Boucher, Y., Vasihare, U. S., Tuma, R. F. and Jain, R. K. (1994b), Vascular Permeability and Microcirculation of Gliomas and Mammary Carcinomas Transplanted in Rat and Mouse Cranial Windows, *Cancer Research* **54**, 4564–4568.

Zhang, X.-Y., Luck, Janson, Dewhirst, M. W. and Yuan, F. (2000), Interstitial Hydraulic Conductivity in a Fibrosarcoma, *American Journal of Physiology - Heart and Circulatory Physiology* **279**, H2726–H2734.

Ziomek, L. J. (1995), *Fundamentals of Acoustic Field Theory and Space-Time Signal Processing*, CRC Press, United States of America.

Zwillinger, D. (ed.) (2003), *Mathematical Tables and Formulae*, 31st edition, CHAPMAN & HALL/CRC.